A STUDY OF SLOW-WAVE PROPAGATION IN A LOSSY DIELECTRIC/FERRITE-LINED WAVEGUIDE

A THESIS

SUBMITTED TO THE DEPARTMENT OF ELECTRICAL ENGINEERING

AND THE COMMITTEE ON GRADUATE STUDIES

OF STANFORD UNIVERSITY

IN PARTIAL FULFILLMENT OF THE REQUIREMENTS

FOR THE DEGREE OF

ENGINEER

By

Edward J. Rothwell

April 1982

Approved for the Department:

Marvin Chodorow

Approved for the University Committee
on Graduate Studies:

Gerald J. Lieberman

PREFACE

This study considers the effects of adding loss to a dielectrically-lined circular waveguide slow-wave structure. Two types of loss are considered: 1) losses exhibited by materials such as graphite, which can be modelled by a frequency-dependent complex scalar permittivity; and, 2) losses exhibited by ferrite materials, which can be modelled by a tensor permeability with frequency dependent complex entries.

The appropriate waveguide dispersion relation is derived for each case and solved numerically for the azimuthally symmetric modes. This solution yields values for the attenuation constant, α, and the phase constant, β, for a wave propagating in the lossy guide.

Results obtained by solving the dispersion relations are applied to the case of the cyclotron slow-wave amplifier. The two goals of this study are to: 1) determine the amount of loss necessary to prevent oscillations in the amplifier; and, 2) find the relative effects on the interaction in the amplifier of adding a thin lossy layer to the slow wave structure in order to prevent charge build-up on the dielectric liner.

TABLE OF CONTENTS

TABLE OF CONTENTS (Continued)

LIST OF TABLES

LIST OF ILLUSTRATIONS

LIST OF ILLUSTRATIONS (Continued)

LIST OF ILLUSTRATIONS (Continued)

LIST OF ILLUSTRATIONS (Continued)

LIST OF ILLUSTRATIONS (Continued)

LIST OF ILLUSTRATIONS (Continued)

I. INTRODUCTION

An increasing need for high power millimeter-wave devices has encouraged much new interest in amplifiers employing the cyclotron maser instability. Theoretical work done by Chu, Hirshfield, and others [3], [4], [5] has demonstrated the potential value of the gyrotron or "fast-wave" interaction in producing amplification at unprecedented power levels. Experimental work done at the Naval Research Laboratories in 1979 and 1980 has provided a considerable amount of favorable evidence. Record power levels at millimeter-wave frequencies have been attained by the NRL's gyrotron traveling-wave amplifier (gyro-TWA). An experimental gyro-TWA in 1980 produced an output of 10 kW with 32 dB gain at 35.1 GHz and a 3 dB bandwidth of 1.4% [2].

The experiments at NRL discovered that unwanted oscillations prevented the amplifier from operating in its optimum regime. Some oscillations as large as 10 kW were reported just above the cutoff frequency of the empty waveguide circuit. These were ascribed to reflections from the input/output couplers. The addition of loss has been the usual means of suppression for such oscillations in a microwave tube amplifier. In his analysis of the effects of wall resistivity on gyrotron gain, Lau [11] suggests that wall loss, added either in the form of distributed or lumped loss, will reduce the chance of oscillations due to reflections. Preliminary experimental evidence from a graphite-lined lossy-waveguide gyro-TWA has led Baird [2] to suggest that such a lossy guide may be essential in obtaining stable operation.

Although the high power output of the NRL gyro-TWA is encouraging, its small (1.4%) bandwidth is somewhat disappointing. The gyro-TWA is by the nature of its interaction a narrow-band device, and so cannot be hoped to provide the large amount of bandwidth demanded by today's millimeter wave applications. Methods for making a wide-band amplifier employing the cyclotron maser instability, however, have been devised. Adding a slow-wave circuit to the gyro-TWA will allow the Weibel or "slow-wave" interaction to be used. Analysis of this interaction by Chu for a dielectrically-loaded waveguide slow-wave structure [3] shows the potential for a very wide bandwidth. Preliminary numerical results suggest bandwidths as high as 60%.

Implementation of this wide-band cyclotron slow-wave amplifier requires significant reduction of the oscillation problems discovered in the NRL experiments with the gyro-TWA. Oscillation is even more of a hazard in the cyclotron slow-wave amplifier since the presence of the dielectric lining complicates the coupling of the wave to and from the waveguide. Oscillations can be suppressed by adding a layer of lossy material, such as a ferrite or graphite, to the inside of the dielectric liner. Analysis of this structure could determine the correct amount of loss to add to produce the required attenuation of the reflected wave.

Although a very good analysis has been performed by Park [2] on a lossless N-layer dielectrically-loaded waveguide, no attempt has yet been made to analyze the lossy three-layer, dielectrically-loaded, slow-wave structure suitable for use in the cyclotron slow-wave amplifier. This study will present such an analysis, the importance

of which is compounded by the necessity of analyzing the effect of a lossy layer applied to prevent deleterious accumulation of charges on the dielectric liner.

II. SLOW-WAVE CYCLOTRON INTERACTION

Increasing interest in millimeter wave applications has led to renewed investigations into electron devices employing cyclotron interaction. The well known gyrotron and Weibel interactions occur when a rotating hollow beam of electrons is projected along an axial magnetic field down a circular waveguide. The RF fields in the guide act on the electrons causing them to bunch in the azimuthal direction along each electron guiding center. This bunching results in a net transfer of energy from the electrons to the RF fields and the wave propagating in the guide is amplified.

Chu and Hirshfield have shown [5] that two bunching mechanisms compete with each other, resulting in two separate regions of amplification. Fast-wave, or gyrotron, interaction results from azimuthal bunching and dominates when:

$$\frac{\omega \Omega_e}{\gamma_o k_z^2 C^2} > 1 . \qquad (2.1)$$

Slow-wave, or Weibel, interaction results from axial bunching and dominates when:

$$\frac{\omega \Omega_e}{\gamma_o k_z^2 C^2} < 1. \qquad (2.2)$$

Here ω is the radian frequency of the wave; C, the velocity of light; k_z, the axial propagation constant; Ω_e, the non-relativistic electron cyclotron frequency; and γ_o, the relativistic mass correction factor pertaining to the electron beam. Figure 2-1 shows how a typical gain plot would appear for a device employing cyclotron interaction. Here gain is plotted against relative frquency, where ωc is the cutoff frequency of the empty waveguide. The left curve results

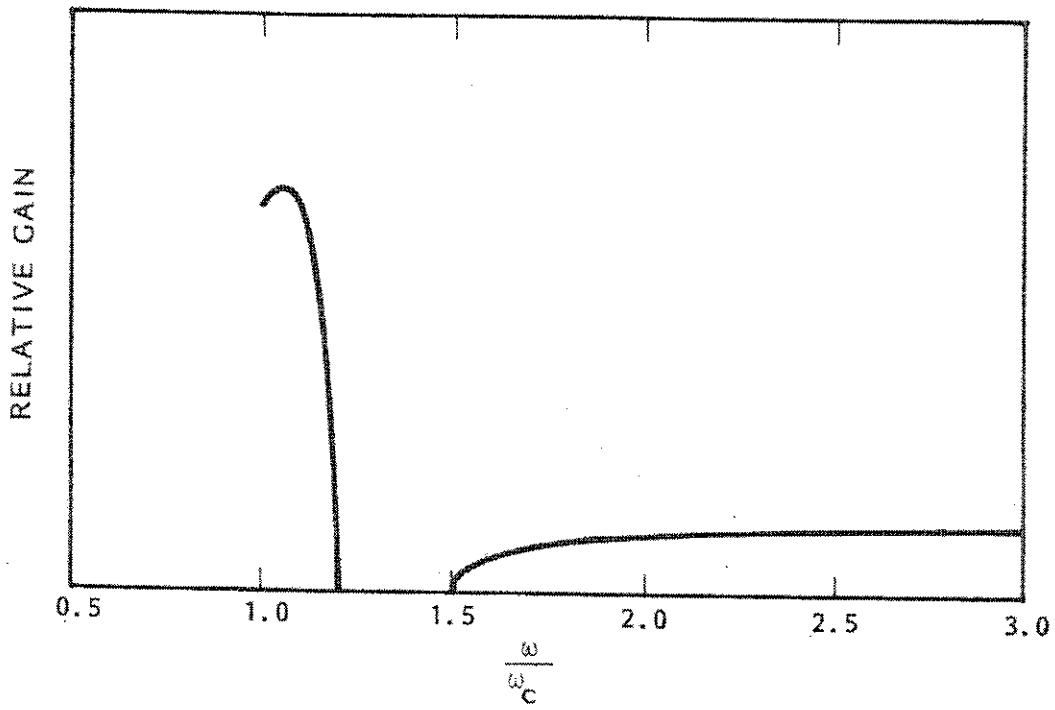

Figure 2-1. Typical Gain vs Frequency Plot for a Device Employing Cyclotron Interaction. ω_c = Waveguide Cutoff Frequency.

from the gyrotron portion of the interaction. In this region condition (2.1) holds. The right curve arises from the Weibel interaction. Here condition (2.2) holds. In the normalized frequency range from 1.2 to 1.4 the two interactions cancel and a region of stability results. This corresponds roughly to the point where the phase velocity of the guided wave approaches the velocity of light.

The gyrotron region is characterized by relatively high gain with narrow bandwidth. In direct contrast, the Weibel region demonstrates significantly lower gain but with considerably larger bandwidth. It is this region which is of most interest for use in wide-band millimeter wave devices. An amplifier working under condition (2.2) is termed a slow-wave cyclotron amplifier.

Chu et. al. [4] have derived the dispersion relation for cyclotron interaction between a rotating electron beam and a wave propagating down a circular waveguide in the TE_{0m} mode. This equation, derived from the linearized Vlasov equation and Maxwell's equations, gives a relationship between wave frequency and complex propagation coefficient (and thus gain). Although its exact form is not important to this study, it does give the appropriate condition for synchronism between the beam and the RF wave. For gain to result in the fast wave region the wave frequency must obey:

$$\omega \gtrsim k_z v_z + s\Omega . \tag{2.3}$$

Here v_z is the axial beam velocity; s, the cyclotron harmonic number; and Ω, the relativistic cyclotron frequency given by:

$$\Omega = \frac{eB_o}{\gamma m_o} \tag{2.4}$$

where Bo is the axial magnetic field, e is the electronic charge, and mo is the electron rest mass. In the slow-wave region the synchronism condition is:

$$\omega \lesssim k_z v_z + s\Omega. \tag{2.5}$$

Figure 2-2 shows how synchronism between the s = 1 beam mode and the TE_{0m} mode in an empty waveguide would appear on an $\omega - \beta$ diagram. Since condition (2.1) holds and $\omega > k_z V_z + \Omega$, the fast wave interaction will predominate. It can be seen that synchronism occurs over only a very narrow frequency range, resulting in a device with small bandwidth.

Synchronism can be achieved over a much broader band if the TE_{0m} mode line is lowered to coincide more with the s = 1 beam line. This reduction in phase velocity is made possible by adding a slow-wave structure to the waveguide. The simplest way of achieving a slow-wave is to line the waveguide with a dielectric. The waveguide then becomes a two-layer dielectric propagating structure where the beam hole is viewed as a dielectric with permittivity ϵo. For such a waveguide Chu has shown [3] that the synchronism condition between the TE_{0m} mode and the beam remains the same. Synchronism between the s = 1 beam line and the TE_{0m} dielectric waveguide mode is indicated in Figure 2-3.

It is apparent that a device operating under the conditions shown in Figure 2-3 can have a potentially large bandwidth, obeying the slow-wave condition (2.2). The dielectric loaded waveguide appears, then, to be a viable slow-wave structure for use in a cyclotron slow-wave amplifier. Its design and operating properties are considered in the next section.

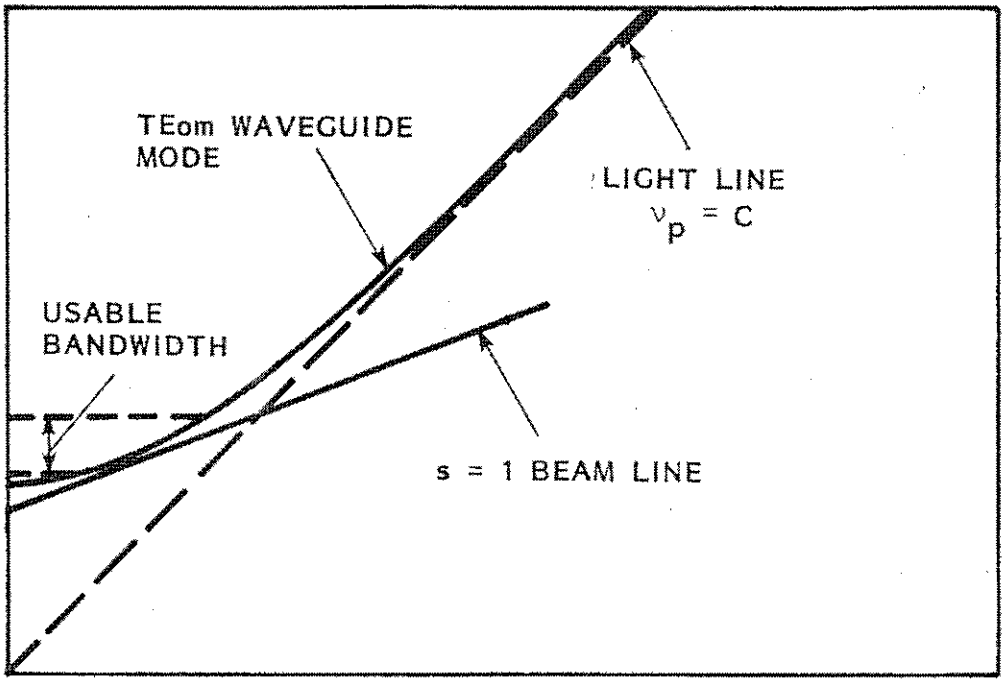

Figure 2-2. Synchronism Between the TE_{0m} Empty Waveguide and s = 1 Beam Modes for Fast Wave Interaction.

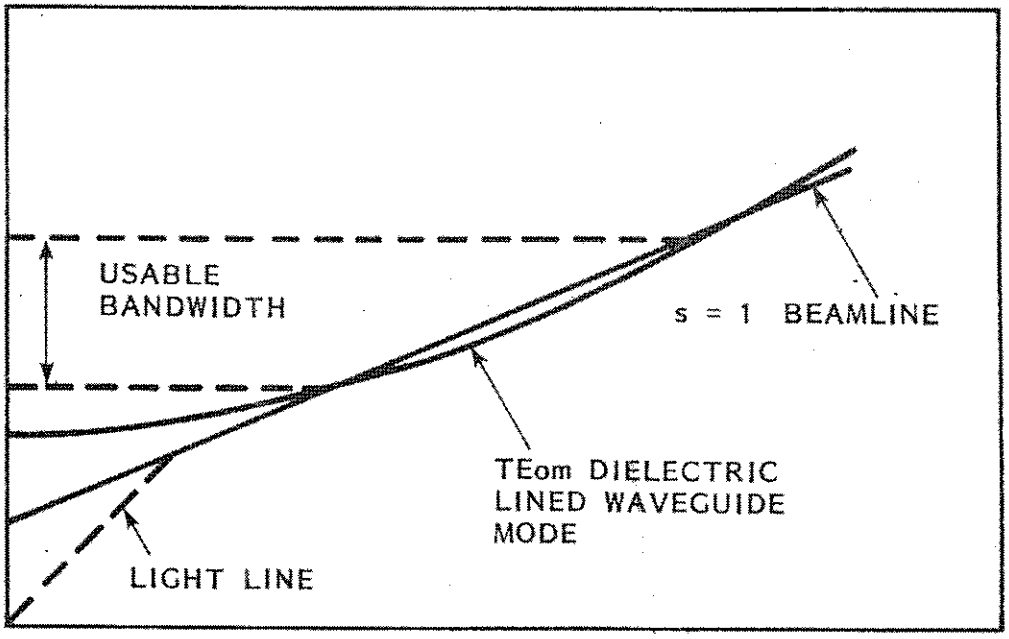

Figure 2-3. Synchronism Between the TE_{0m} Dielectric-Loaded Waveguide and s = 1 Beam Modes for Slow-Wave Interaction.

III. DESIGN AND BEHAVIOR OF THE DIELECTRIC LOADED WAVEGUIDE SLOW-WAVE STRUCTURE

The number of parameters which can be varied in analyzing the two-layer dielectric slow-wave structure is very large. It would prove much too time-consuming to examine every possible combination of waveguide dimensions, dielectric properties, etc. For this study it is sufficient to decide on a certain waveguide design and determine how varying a few important parameters affects the nominal operation of the slow-wave structure. The design case decided on should be typical of slow-wave cyclotron applications. A good place to start the design is to decide on the frequency band used. Current activity in the millimeter region commonly resides in the 40 gigahertz area. Thus, this study will consider an operating band from 36 to 46 GHz, centered on 41 GHz. This assumes a reasonable 3 dB bandwidth of 10 GHz, or about 24% of the center frequency. Next, the properties of the dielectric liner should be chosen. It is assumed that the liner should have a high dielectric constant and small loss tangent (so that the thickness of the dielectric and thus the power loss can be kept to a minimum). The dielectric also must be vacuum compatible so that no particles enter into the beam region and interfere with interaction or focusing. The compound barium tetratitinate ($BaTi_4O_9$) is a dielectric that satisfies all of these requirements. It has a fairly high dielectric constant of 38 and a loss tangent of approximately 6.5×10^{-4}.

Now, the waveguide dimensions are to be chosen. The diameter of the waveguide and the thickness of the dielectric are selected to make the TE_{01} waveguide mode reside in the frequency band of interest.

Here the m = 1 mode is used, since it represents the fundamental waveguide mode. It has the largest fields and lowest cutoff of any azimuthally-symmetric mode. With the dimensions chosen, the beamline is constructed to match the waveguide mode line over the desired frequency range.

This method of choosing waveguide parameters and beam dimensions is actually only a rough first estimate. In the final design, the most important criterion is the resulting gain and gain flatness across the band. A range of acceptable parameters should be tested to produce the combination of gain and bandwidth desired. This requires the use of some sort of small-signal analysis for interaction between a gyrating electron beam and the TE_{01} waveguide mode.

Use of a recently developed, small-signal computer program leads to the optimized waveguide and beam parameters shown in Table 3-1. Analysis of these parameters yields a very flat small signal gain of 2.8 dB/cm over a 3 dB band of 36.3 to 45.8 GHz. For an active circuit length of 15 cm, this gives a very reasonable overall small signal gain of 43 dB for the amplifier.

It is this set of parameters that determines the standard case amplifier analyzed throughout this study. Figure 3-1 shows the waveguide structure.

The information in Table 3-1, equation (2.5), and the additional relations:

$$\Omega = \frac{v_\perp}{r_L} \tag{3.1}$$

$$v_{||}^2 + v_\perp^2 = 2\,\frac{eV}{mo}$$

Table 3-1: Standard Case Parameters of the Cyclotron Slow-Wave Amplifier.

Waveguide Inner Radius, b	0.390 cm
Dielectric Inner Radius, a	0.348 cm
Dielectric constant, ε_{2R}	38.0
Dielectric Loss Tangent, δ	6.5×10^{-4}
Axial Magnetic Field, Bo	10.3 kG
Beam Potential, V	19 kV
Beam Current, I	3.3 A
Orbit Guding Center, Rg	0.2076 cm
Larmor Radius, r_L	0.0424 cm
Velocity Ratio, $v_\perp/v\|\|$	2.0
Active Circuit Length	15.0 cm

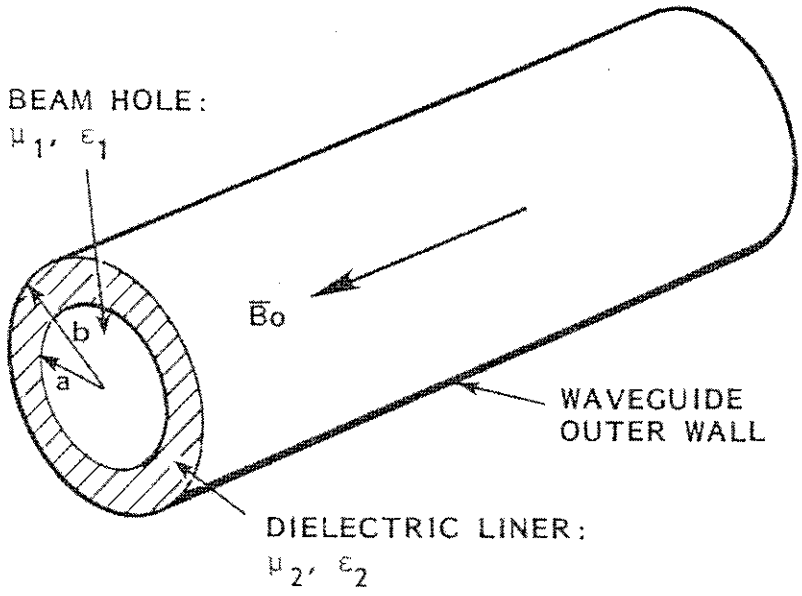

Figure 3-1. Dielectric-Loaded Waveguide Structure.

can be used to obtain the equation (non-relativisitic) for the beam line:

$$\frac{\omega b}{C} = 0.1235\ k_z b + 2.272\ s\ . \qquad (3.2)$$

Here, ω and k_z are normalized using the guide wall inner radius and the velocity of light. (Dimensionally-normalized parameters are used throughout this study to provide maximum flexibility of results.) Thus, neither the axial propagation constant nor the guide inner radius needs to be specified separately, but only their product, $k_z b$. The same applies to the frequency, speed of light, and guide inner radius. Using this convenient system, the relative thickness of the dielectric, a/b, is the only waveguide dimension needed.

The dispersion equation relating ω and k_z for the case of the two-layer dielectric lined waveguide is derived in detail in appendices one and two. For the structure shown in Figure 3-1, equation (A2.6) can be written as:

$$\frac{n^2 k_z^2}{\omega^2 \mu_1 \varepsilon_1 a^2} \frac{(k_{\rho 1}^2 - k_{\rho 2}^2)}{k_{\rho 1}^2 k_{\rho 2}^4} = \left[\frac{k_{\rho 1} \mu_2 f_4}{k_{\rho 2} \mu_1 f_3} - \frac{Jn'(k_{\rho 1} a)}{Jn(k_{\rho 1} a)}\right]\left[\frac{k_{\rho 1} \varepsilon_2 f_2}{k_{\rho 2} \varepsilon_1 f_1} - \frac{Jn'(k_{\rho 1} a)}{Jn(k_{\rho 1} a)}\right] \qquad (3.3)$$

TE TM

where: $k_{\rho 1}^2 = \omega^2 \mu_1 \varepsilon_1 - k_z^2$

$k_{\rho 2}^2 = \omega^2 \mu_2 \varepsilon_2 - k_z^2$

$f_1 = Jn(k_{\rho 2} a)\, Yn(k_{\rho 2} b) - Yn(k_{\rho 2} a)\, Jn(k_{\rho 2} b)$

$f_2 = Jn'(k_{\rho 2} a)\, Yn(k_{\rho 2} b) - Yn'(k_{\rho 2} a)\, Jn(k_{\rho 2} b)$

$f_3 = Jn(k_{\rho 2} a)\, Yn'(k_{\rho 2} b) - Yn(k_{\rho 2} a)\, Jn'(k_{\rho 2} b)$

$f_4 = Jn'(k_{\rho 2 a})\, Yn'(k_{\rho 2} b) - Yn'(k_{\rho 2 a})\, Jn'(k_{\rho 2} b)$.

Here Jn (z) is the nth order Bessel function of the first kind, with argument z, and Yn (z) is the nth order Bessel function of the second kind, with argument z. This equation describes the relationship between ω and k_z for every mode which can exist in the waveguide. When n = 0 (azimuthally symmetric case), the left hand side becomes zero and the right hand side splits into two sets of solutions, one for pure TE modes and one for pure TM modes. When $n \neq 0$ the modes are termed "hybrid" since the fields in the guide have both TE and TM components.

The TE_{01} mode is the mode selected for RF interaction. Setting n = 0 in (3.3) yields the TE_{0m} dispersion relation:

$$\frac{k_{\rho 1}\ \mu_2\ f_4}{k_{\rho 2}\ \mu_1\ f_3} = \frac{Jo'\ (k_{\rho 1}a)}{Jo\ \ (k_{\rho 1}a)} \quad . \tag{3.4}$$

Here the m refers to the m'th solution of (3.4). This equation can be solved numerically, on a computer, for various values of k_z. Solving for the first root gives a plot of the TE_{01} waveguide mode. Letting $\mu_1 = \mu_2 = \mu_0$, $\varepsilon_1 = \varepsilon_0$, $\varepsilon_2 = 38\ \varepsilon_0$, and a/b = 0.892, the curve shown in Figure 3-2 is obtained. Also plotted in this figure is the beam line from equation (3.2) for s = 1. It is seen from this figure that the wave and the beam should be nearly synchronized for fast-wave interaction from about $\frac{\omega b}{c} = 2.30$ to 2.35 and for slow-wave interaction from approximately $\frac{\omega b}{c} = 2.5$ to 4.0 and beyond.

The TE_{01} mode is the only desired mode of operation. Other modes present in the waveguide can be detrimental to TE_{01} interaction. Thus, it is important to know of all possible modes of propagation which can exist in the operating band. Equation (3.3) can be solved

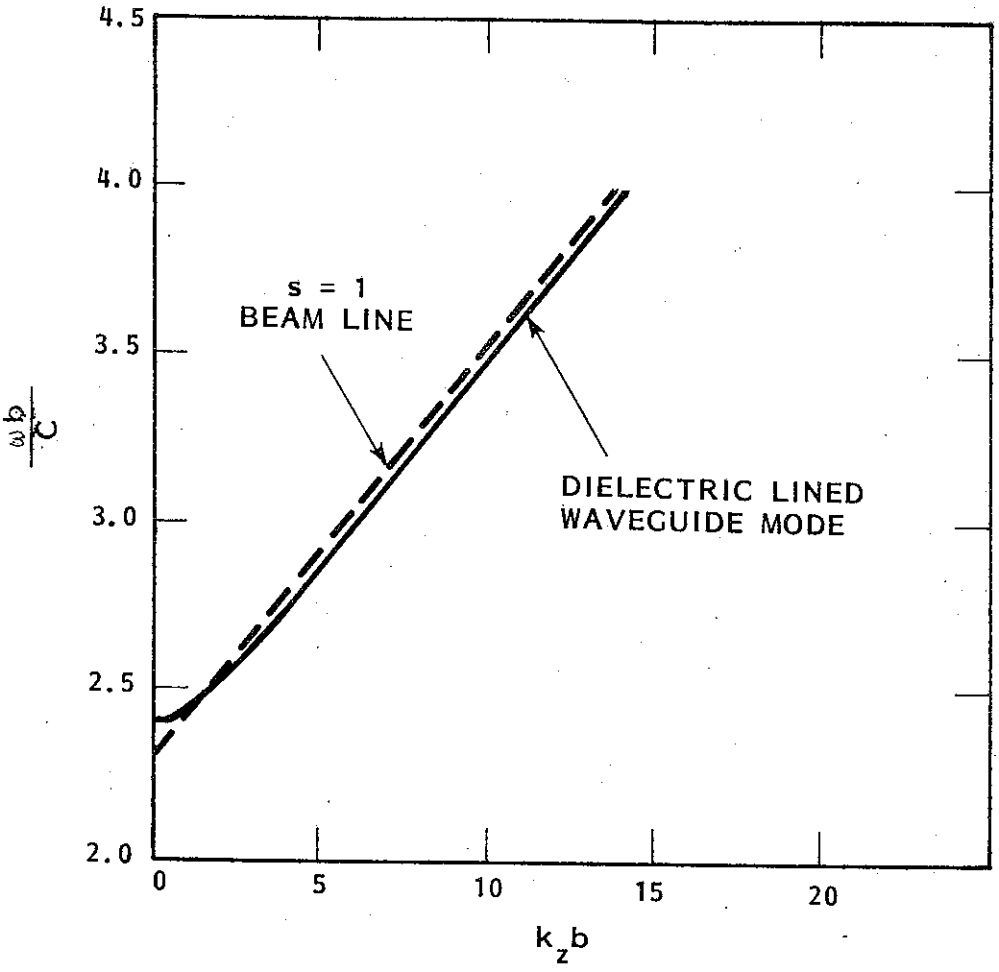

Figure 3-2. Synchronism Between TE_{01} Dielectric-Loaded Waveguide and (s = 1) Beam Modes for Standard Case Parameters.

on the computer for all combinations of m and n which result in solutions near the TE_{01} mode. (Full details of the method of solution are given in Appendix five.) Figure 3-3 is a plot of many of these modes. The $n \neq 0$ hybrid modes are termed "TE" or "TM" by how they act near cutoff (i.e., as $k_z \to 0$). It is seen from equation (3.3) that letting k_z become zero also causes a splitting into pure TE and TM modes.

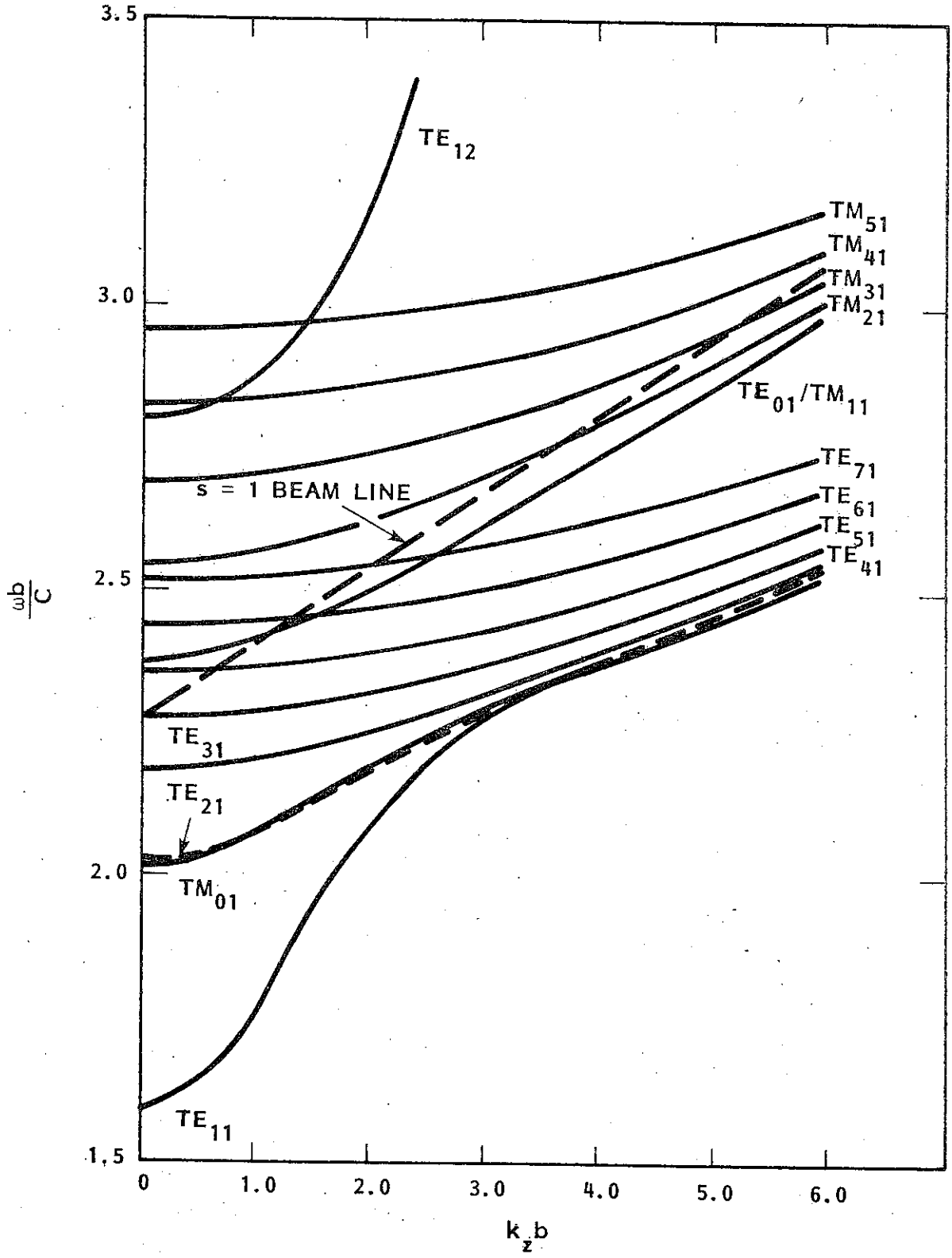

Figure 3-3. Various TE and TM Modes Present in the Dielectric-Loaded Waveguide.

IV. APPLICATION OF LOSS TO THE SLOW-WAVE CYCLOTRON AMPLIFIER

It is common practice in the design and production of microwave tubes to add lossy sections at certain points along the length of an amplifying device. At first glance this may seem self defeating since amplifiers are usually designed for maximum gain or maximum power output. However, certain problems can arise in the operation of the slow-wave cyclotron amplifier which deem the addition of loss a necessary cure.

Two basic problems are considered here, either of which can be of sufficient severity to prevent the device from operating properly. The first of these, charging of the dielectric by the electron beam, is a problem encountered only in the dielectric lined waveguide type of slow-wave structure. The second, parasitic oscillations due to input/output reflections, is common to most all types of microwave tube amplifiers. Each of these problems is discussed in detail below.

A. Charging of the Dielectric Liner

The most efficient slow-wave interaction between a gyrating electron beam and a traveling wave occurs when the guiding centers of the electron orbits are located near peak radial magnetic fields. This is where bunching is most enhanced. Later considerations of the field distributions in the dielectric-lined waveguide (see equations (A3.18) and Figures 6-14 through 6-16) determine that maximum radial magnetic field in a guide propagating the TE_{01} mode occurs very near the vacuum/dielectric interface. Thus, an efficient slow-wave cyclotron amplifier will have a hollow electron stream passing very

near its dielectric liner. This close proximity of high electron concentration results in a significant build up of charges on the surface of the dielectric.

High charge concentration in the dielectric can have very undesirable effects. Electric field fluctuations due to localized surface charges may destabilize interaction by interfering with proper electron bunching. Worse, if these electric fields become too large, dielectric breakdown might occur and the resulting stresses could shatter the fragile liner.

Charge buildup can be controlled by adding a very thin lossy layer to the inside of the dielectric liner. This provides a conductive path through which the charges can leak away before they build to intolerable levels. Since the purpose of the layer in this case is not to add loss to the circuit, it is desired to keep it as thin as possible. Little is gained by having this lossy layer thicker than a fraction of a skin depth.

B. Parasitic Oscillations

Parasitic oscillations will occur in the slow-wave cyclotron amplifier if the loop gain of the circuit is greater than unity. Figure 4-1 shows a schematic representation of the loop gain in a lossless circuit. A wave of amplitude "A" is launched at the input port and propagates down the length of the circuit. Interaction with the electron beam causes amplification of the wave and it emerges at the output port with an amplitude of $G \cdot A$, where G is the gain of the circuit. Since the output port is not perfectly matched to the

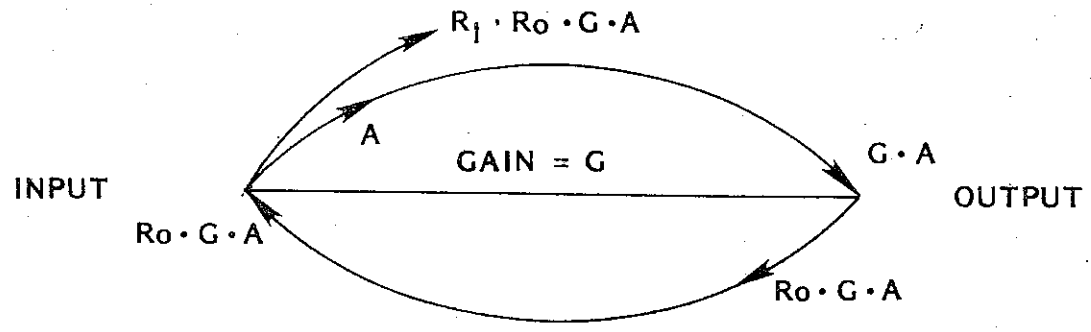

Figure 4-1. Loop Gain in a Lossless Circuit. Input Reflection Coefficient = R_I, Output Reflection Coefficient = R_O.

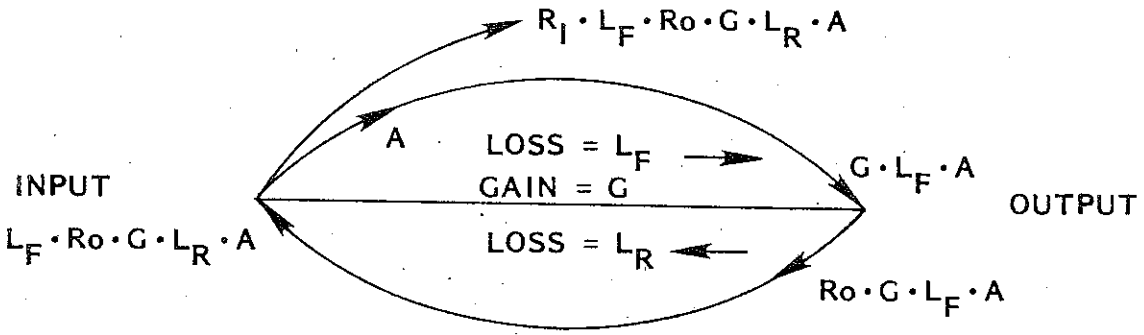

Figure 4-2. Loop Gain in a Circuit with Forward Loss L_F and Reverse Loss L_R. Input Reflection Coefficient = R_I, Output Coefficient = R_O.

circuit it can be characterized by a reflection coefficient, Ro, and a portion of the wave, Ro·G·A, is reflected back toward the input. No gain occurs in the reverse direction and the wave arrives at the input port with the same amplitude Ro·G·A. Here it experiences a second reflection and completes its loop of the circuit with an amplitude of $R_I \cdot Ro \cdot G \cdot A$, R_I being the input reflection coefficient. The loop gain is therefore expressed as:

$$\text{Loop Gain} = \frac{R_I \cdot Ro \cdot G \cdot A}{A} = R_I \cdot Ro \cdot G \ . \qquad (4.1)$$

If this loop gain is greater than one, the wave will continue to propagate up and down the circuit, growing larger and larger until the amplifier saturates. If the loop gain is less than one, the wave will decay and there will be no oscillation. Thus, the condition for stable operation can be written as:

$$R_I \cdot Ro \cdot G < 1 \ . \qquad (4.2)$$

Letting R_I and Ro take on reasonable values, 1.0 and 0.3 respectively, the maximum stable gain is found to be $G_{max} = 3.33$, or 5 dB. This level is insufficient to be considered useful amplification for most applications.

Figure 4-2 shows the same circuit modified to represent lossy wave propagation. Because the wave is attenuated in both directions the loop gain can be written as:

$$\text{Loop Gain} = \frac{R_I \cdot L_F \cdot Ro \cdot G \cdot L_R \cdot A}{A} = L_F \cdot L_R \cdot R_I \cdot Ro \cdot G, \qquad (4.3)$$

and the condition for stable operation is:

$$L_F L_R R_I R_O \, G < 1. \tag{4.4}$$

Written in terms of decibels, this becomes:

$$L_F + L_R + R_I + R_O + G < 0 \text{ dB}. \tag{4.5}$$

The loss L_R in equation (4.5) is the loss experienced by the wave while traveling in the reverse direction. This is equal to the cold circuit loss L. The loss L_F can be viewed as the amount by which the lossless gain is reduced during interaction of the wave and the electron beam (i.e. in the forward direction). Lau, Chu, and Barnett [11] have shown that under fast wave conditions the lossless gain in dB is reduced by approximately 1/3 the cold circuit loss in dB. Although the validity of adapting these results to the slow-wave region may be questionable, it represents the best estimate available at this time. Equation (4.5) then becomes:

$$R_I + R_O + 1.3L + G < 0 \text{ dB}. \tag{4.6}$$

In section III the lossless gain for the 15 cm long cyclotron slow-wave amplifier was found to be 43 dB. Substituting G = 43 dB, R_I = 1.0, and Ro = 0.3 into (4.6) and allowing for a loop gain margin of 12 dB yields:

$$0 - 10.5 \text{ dB} + 1.3L + 43 \text{ dB} = -12 \text{ dB} \tag{4.7}$$

which gives a cold circuit loss of L = -34 dB. The gain of the lossy circuit becomes: $G_{lossy} = G + 0.3L = 43 - 10 = 33$ dB. Thus the stable gain has been increased from 5 to 33 dB by adding 34 dB of loss to the circuit.

Parasitic oscillations are usually assumed to result from the fundamental interaction of the s = 1 beam line with the TE_{01} waveguide mode. However, there are at least two other possible interaction

conditions which could give rise to oscillations. The first is the interaction of the s = 1 beam line with other waveguide modes in the vicinity of the TE_{01} mode. In Figure 3-3 many TE_{n1} modes can be seen to intersect with the s = 1 beam line. Also, many TM_{n1} modes approach the beam line assymptotically for larger values of k_z. Either of these conditions can lead to alternate mode amplification, and thus to oscillations. Adding loss to the circuit may not be sufficient to end this problem, depending on how the loss affects these other modes. The same amount of loss might not attenuate the TM_{21} mode, for example, as effectively as it does the TE_{01} mode. Thus it may be much more expedient to use a mode filter to remove all but the n = 0 (symmetrical) modes.

The second condition results from the interaction of higher harmonics of the beam line with higher order waveguide modes. The s = 2 beam line is of primary concern since it intersects both the TE_{02} and TM_{02} waveguide modes, as shown in Figure 4-3. As m becomes larger (i.e. TE_{03}, TE_{04}, etc.) the RF fields near the dielectric lessen and likelihood of interaction in these modes diminishes. It should be remembered that mode filtration, selective against the hybrid modes, would be ineffectual in removing any of these n = 0 modes.

An interesting idea for suppressing these higher order interactions is the use of frequency dependent loss, such as that exhibited by ferrite materials. The loss distribution could be adjusted so that maximum attenuation would occur at the frequency most subject to interaction (probably near the $s = 2/TE_{02}$ crossover.) At lower frequencies where the fundamental interaction occurs, the loss

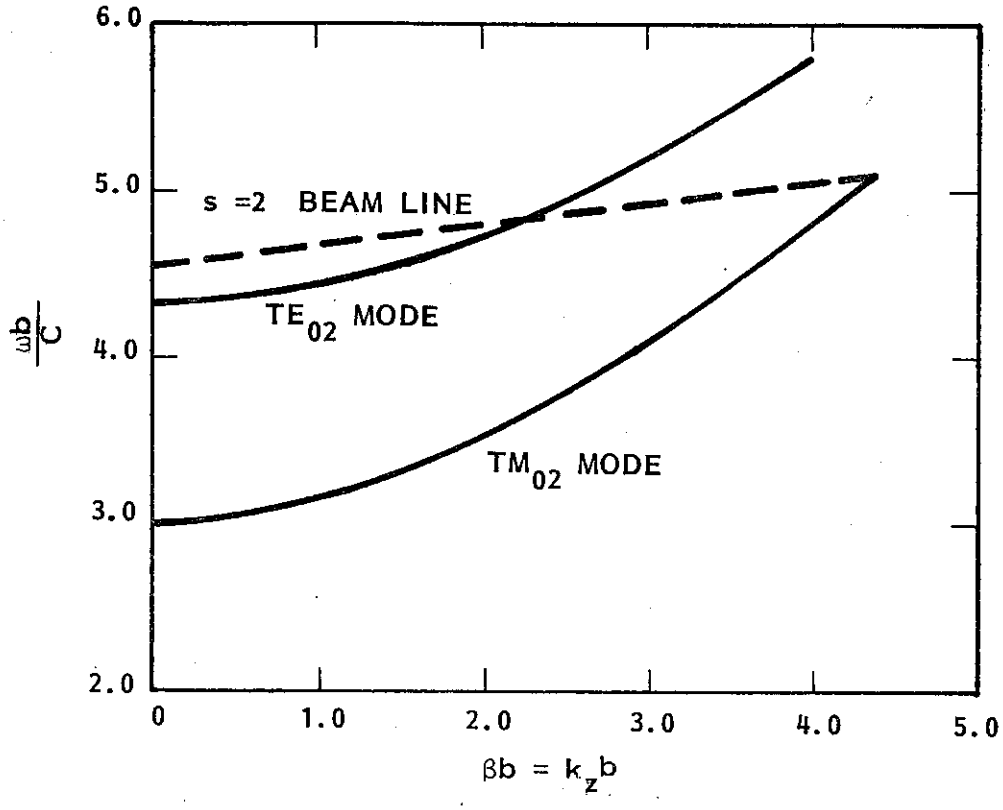

Figure 4-3. Synchronism Between TE_{02} and TM_{02} Dielectric-Loaded Waveguide Modes and the s = 2 Beam Mode.

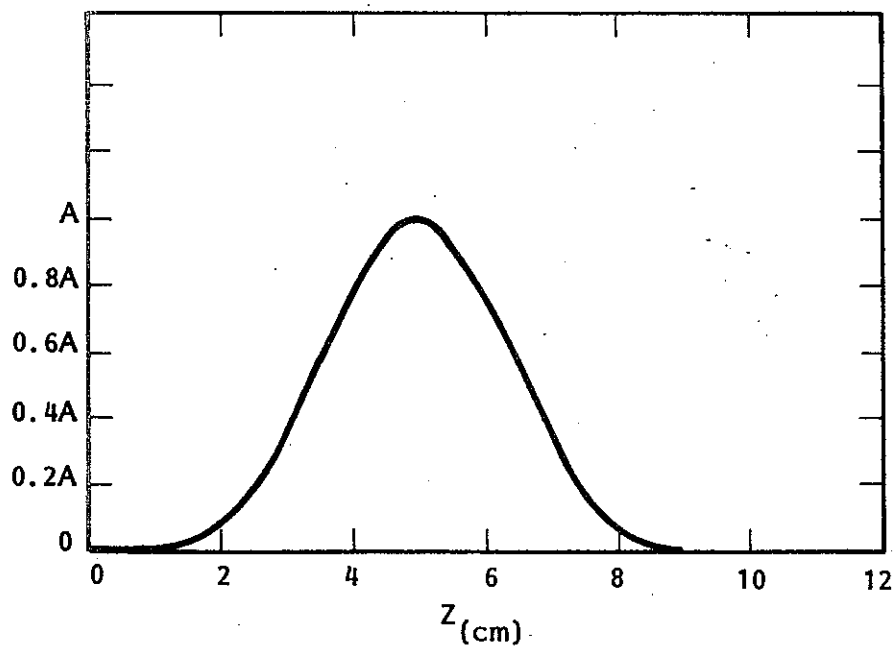

Figure 4-4. Loss Distribution Patterned After the Function $\sin^4 (\frac{z}{10} \pi)$.

would be much less. Thus, unwanted interactions could be attenuated without severe degradation of fundamental gain.

When adding loss to the circuit to dispel charge build up, it is desirable to apply a thin layer of lossy material evenly distributed over the entire length of the amplifier. In contrast, loss designed for suppressing oscillations is usually applied in a pattern over a smaller area. This allows the wave to begin its interaction before a significant amount of attenuation takes place. In addition, such localized loss prevents degradation of device efficiency which would occur if significant attenuation was present near the output. The drawback to patterned loss is that it represents a discontinuity in the circuit, which might cause reflections and generation of spurious modes.

Discontinuities due to patterned loss can be minimized by making the pattern as smooth as possible. Analysis has shown that the smallest reflections occur for loss applied in the shape of a gaussian distribution. However, the finite size of the slow-wave cyclotron amplifier requires that the loss pattern be negligible at the ends. This can be achieved by simulating the gaussian by a $\sin^n (\pi z/\ell)$ function, where ℓ is the length of the loss pattern. Integer values of n on the order of 4 or 5 give good approximations of a gaussian over much of ℓ. Figure 4-4 shows a loss distribution, patterned after the $\sin^4 (\pi z/10)$ function. Here it is assumed that the loss pattern will occupy the first 10 cm of the circuit's 15 cm active length. The peak value of the loss per unit length, A, can be calculated by remembering that 34 dB of total loss is required to give 33 dB of stable gain. Thus, the average loss/unit length times

the length of the loss pattern should be 34 dB. The loss pattern cofactor can be evaluated from:

$$A = \frac{34 \text{ dB}}{\ell\left[\frac{1}{\ell}\int_0^{\ell} \sin^4\left(\frac{z}{\ell}\pi\right) dz\right]} ,$$

or

$$A = \frac{34 \text{ dB}}{(10 \text{ cm})\ [3/8]} = 9.07 \text{ dB/cm.} \qquad (4.8)$$

Therefore, a function for the loss pattern is given by:

$$L(z) = 9.07 \sin^4\left(\frac{z}{10}\pi\right) \text{ dB/cm.} \qquad (4.9)$$

This result will be employed in the following sections.

V. SIMULATION OF THE LOSSY DIELECTRIC AND FERRITE-LINED WAVEGUIDE SLOW-WAVE STRUCTURES

The preceeding sections have provided ample motivation for analyzing the dielectric-lined waveguide slow-wave structure in the presence of loss. First, it is desired to calculate the amount of attenuation which would result from a thin lossy charge suppression layer. From this an optimum trade off between low attenuation and high charge bleed-off can be deduced. It is also necessary to determine if this layer will affect the real part (β) of the propagation constant to the extent that synchronism between the beam and the waveguide mode is reduced.

In addition, an investigation needs to be made to determine the proper thickness of a lossy layer used to suppress oscillations. It is desirable to find some sort of relationship between the lossy nature of the material used, the layer's thickness, and the resulting attenuation. This would allow the formulation of a scheme to apply the amplifier loss pattern of Figure 4-4 to the dielectric-lined waveguide. The resulting effect of this liner on β is also an important consideration. As above, it is hoped that the waveguide mode line and the electron beam line remain in synchronism after the loss is added.

Two groups of materials are candidates for use in the lossy oscillation suppression layer. The first group includes graphite and the graphite-like materials such as aquadag, which are now in common use. These materials are characterized by a high conductivity and can be modeled as an extremely lossy dielectric. The second group is the ferrites. These materials provide a unique frequency dependent

loss which can be used to produce localized attenuation. The attenuation can be made to peak near the fundamental interaction, or at the $s = 2/TE_{02}$ intersection, or at nearly any desired frequency.

It is assumed that the material used for the charge suppression layer is graphite. Graphite's high conductivity provides a path for the charges to quickly escape. This also allows for only a very thin layer to be used, perturbing the fields in the guide as little as possible.

Three different models of the lossy waveguide are considered in this study. Each is described briefly below and then analyzed in detail in Sections 6-8. Each of the analyses, and thus the results obtained, were previously unknown to this author. Although the results are applied to the cyclotron slow-wave amplifier they are useful in themselves, as they merely describe the behavior of a wave propagating in a lossy dielectric-lined waveguide.

A. Two-Layer Model

Here, a thin lossy graphite-like layer added to the dielectric-lined waveguide is modeled using a two-layer approach. The added layer is analyzed assuming the loss to be uniformly distributed throughout the dielectric liner. This approach will probably not give the most accurate representation of the structure, but it does simplify a difficult problem. Its most useful application lies in analyzing the lossy behavior inherent to the dielectric liner itself.

B. Three-Layer Graphite Model

In this approach the thin lossy layer is viewed as a discrete element. The material is assumed to be graphite which has

been added to suppress either charge buildup or oscillations. This is a more complicated version of the above two-layer model.

C. Three-Layer Ferrite Model

This case is much the same as the graphite three-layer model except that the thin layer is represented as a ferrite. This case differs from the two preceeding in that it makes the added assumption that a static magnetic field exists in the guide (as there will be when used as a cyclotron slow-wave circuit).

VI. TWO-LAYER MODEL

A. Formulation

A thin layer of lossy dielectric is added to the inside of the dielectric loaded waveguide shown in Figure 3-1. Its purpose is to either suppress charge buildup in the dielectric or to suppress the onset of oscillation due to mismatches on the circuit. This three-layer waveguide will actually be analyzed, in this section, as if it were a two-layer structure, as shown in Figure 6-1. The loss due to the thin layer is modeled as a loss uniformly distributed throughout the dielectric layer.

The lossy dielectric layer is characterized by a complex scalar permittivity: $\varepsilon_2 = (\varepsilon' - j\,\varepsilon'')\,\varepsilon_o$. It is assumed that the real part of the dielectric constant, ε', does not change with the addition of loss. Thus, $\varepsilon' = 38$ is used throughout the analysis. The loss, then, appears only through the imaginary part of the dielectric constant, ε''. This allows the calculation of attenuation as a function of the single parameter ε''. If ε'' is set equal to $\delta\varepsilon'$, where δ is the loss tangent of the dielectric layer, then this same analysis can be used to model the loss intrinsic to the dielectric. This would be a true two-layer analysis of a two-layer structure.

It should be remembered that equation (3.3) describes a relationship between the wave frequency, ω, and the wave axial propagation constant, k_z, for a structure equivalant to that shown in Figure 6-1b. For the case being analyzed, it is assumed that $\mu_1 = \mu_2 = \mu_o$, $\varepsilon_1 = \varepsilon_o$, and $\varepsilon_2 = (38 - j\varepsilon'')\,\varepsilon_o$. Since ε_2 is represented as a complex permittivity, equation (3.3) becomes a function of a complex variable, and thus its solution is necessarily complex. Using

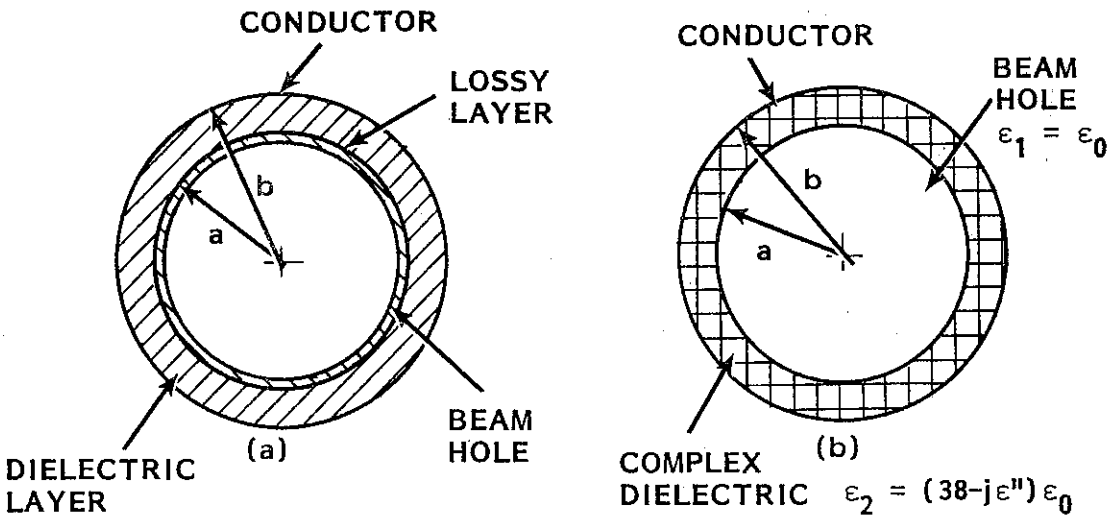

Figure 6-1. Two-Layer Model. a) Actual Three-Layer Structure. b) Two-Layer Model Used in Analysis.

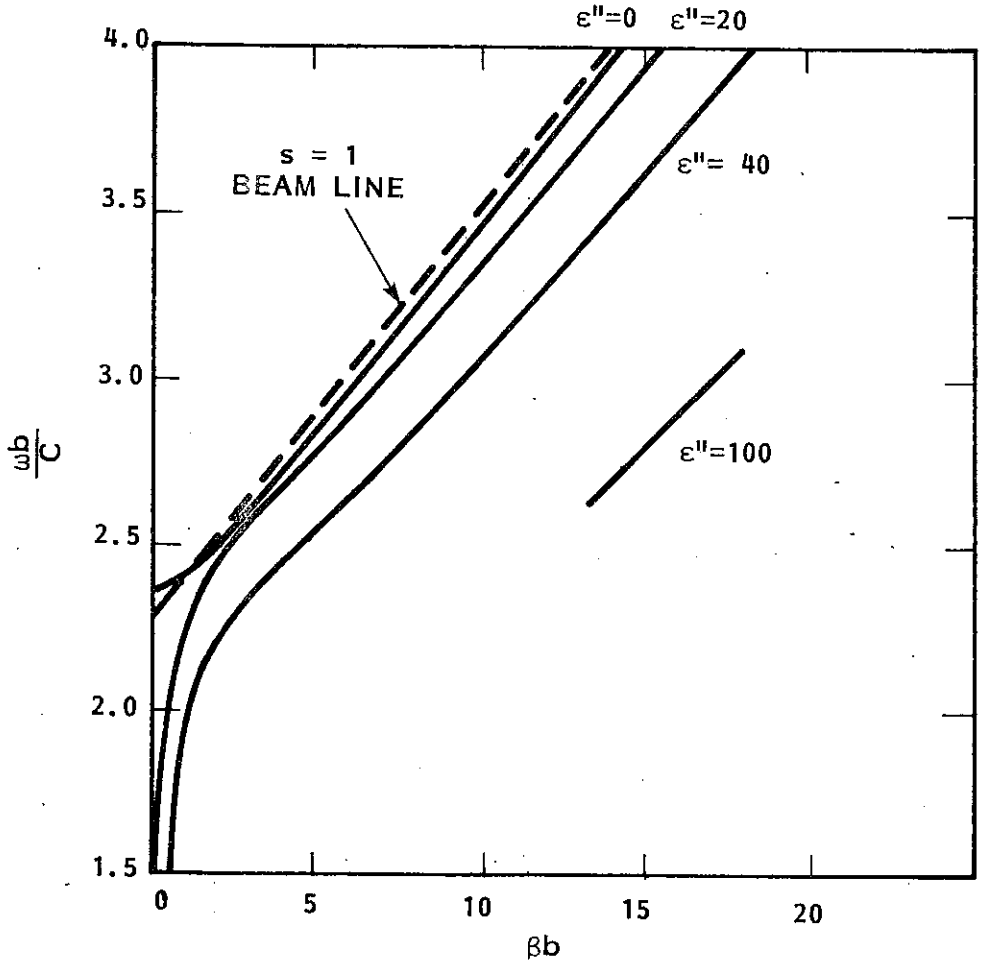

Figure 6-2. Two-Layer TE_{01} $\omega - \beta$ Plot for Various Values of ε''.

the methods in appendix five, this dispersion equation is solved for complex k_z at various real values of frequency. Letting $k_z = \beta - j\alpha$ the wave will vary as:

$$\sim e^{j\omega t - j k_z z} = e^{j\omega t}\, e^{-j(\beta - j\alpha)z} = e^{j\omega t}\, e^{-j\beta z}\, e^{-\alpha z}. \qquad (6.1)$$

Thus, β describes the phase and α describes the attenuation of the wave per unit length, respectively.

A complete solution of (3.3) can be achieved entirely in terms of dimensionally normalized parameters. Values of αb and βb are computed from $\frac{\omega b}{C}$ and a/b, where a and b are the waveguide radii shown in Figure 6-1 and C is the speed of light. A modified version of the dispersion equation can be written in normalized units as:

$$\frac{n^2 (k_z b)^2}{\left(\frac{\omega b}{C}\right)^2 \mu_{1R}\, \varepsilon_{1R} \left(\frac{a}{b}\right)^2} \frac{(k_{\rho 1} b)^2 - (k_{\rho 2} b)^2}{(k_{\rho 1} b)^2 \quad (k_{\rho 2} b)^4} = \left(\frac{k_{\rho 1} b\, \mu_{2R}\, f_4}{k_{\rho 2} b\, \mu_{1R}\, f_3} - \frac{Jn'\left(k_{\rho 1} b \frac{a}{b}\right)}{Jn\left(k_{\rho 1} b \frac{a}{b}\right)} \right) \cdot$$

$$\cdot \left(\frac{k_{\rho 1} b\, \varepsilon_{2R}\, f_2}{k_{\rho 2} b\, \varepsilon_{1R}\, f_1} - \frac{Jn'\left(k_{\rho 1} b \frac{a}{b}\right)}{Jn\left(k_{\rho 1} b \frac{a}{b}\right)} \right) \qquad (6.2)$$

where: $\mu_{1R} = \frac{\mu_1}{\mu_o} \qquad \mu_{2R} = \frac{\mu_2}{\mu_o}$

$$\varepsilon_{1R} = \frac{\varepsilon_1}{\varepsilon_o} \qquad \varepsilon_{2R} = \varepsilon' - j\,\varepsilon''$$

$$k_z b = \alpha b - j\beta b$$

$$(k_{\rho 1} b)^2 = \left(\frac{\omega b}{C}\right)^2 \mu_{1R}\, \mu_{1R} - (k_z b)^2$$

$$(k_{\rho 2} b)^2 = \left(\frac{\omega b}{C}\right)^2 \mu_{2R}\, \varepsilon_{2R} - (k_z b)^2$$

$$f_1 = Jn\ (k\rho_2 b\ \tfrac{a}{b})\ Yn\ (k\rho_2 b) - Yn\ (k\rho_2 b\ \tfrac{a}{b})\ Jn\ (k\rho_2\ b)$$

$$f_2 = Jn'\ (k\rho_2 b\ \tfrac{a}{b})\ Yn\ (k\rho_2 b) - Yn'\ (k\rho_2 b\ \tfrac{a}{b})\ Jn\ (k\rho_2 b)$$

$$f_3 = Jn\ (k\rho_2 b\ \tfrac{a}{b})\ Yn'\ (k\rho_2 b) - Yn\ (k\rho_2 b\ \tfrac{a}{b})\ Jn'\ (k\rho_2 b)$$

$$f_4 = Jn'\ (k\rho_2 b\ \tfrac{a}{b})\ Yn'\ (k\rho_2 b) - Yn'\ (k\rho_2 b\ \tfrac{a}{b})\ Jn'\ (k\rho_2 b).$$

Equation (6.2) and the three-layer dispersion equation (A1.29) are valid in the presence of loss for all modes. However, because of their immediate importance and their intrinsic simplicity, only the azimuthally symmetric (n = 0) modes are considered in this study.

The solution of (6.2) assumes the normalized values: $\mu_{1R} = \mu_{2R} = 1$, $\varepsilon_{1R} = 1$, $\varepsilon_{2R} = 38 - j\,\varepsilon''$, and $a/b = 0.892$.

B. Solution for the TE_{01} Mode

The TE_{01} mode is the most important mode to be analyzed since it is the one involved in the fundamental interaction. Solving for α will determine the necessary amount of loss to prevent oscillations in the amplifier. It will also describe the effect of the charge suppression layer. Solving for β will determine whether synchronism between the beam and the wave has been affected by the addition of loss.

Letting n = 0 in equation (6.2) and solving for the first root results in the TE_{01} ω-β plot shown in Figure 6-2. This graph describes how the mode line changes with various values of ε''. Because k_z is involved in equation (6.2) only as k_z^2, all of the $\omega - \beta$ plots are symmetrical about the ω axis. Figure 6-3 is a continuation

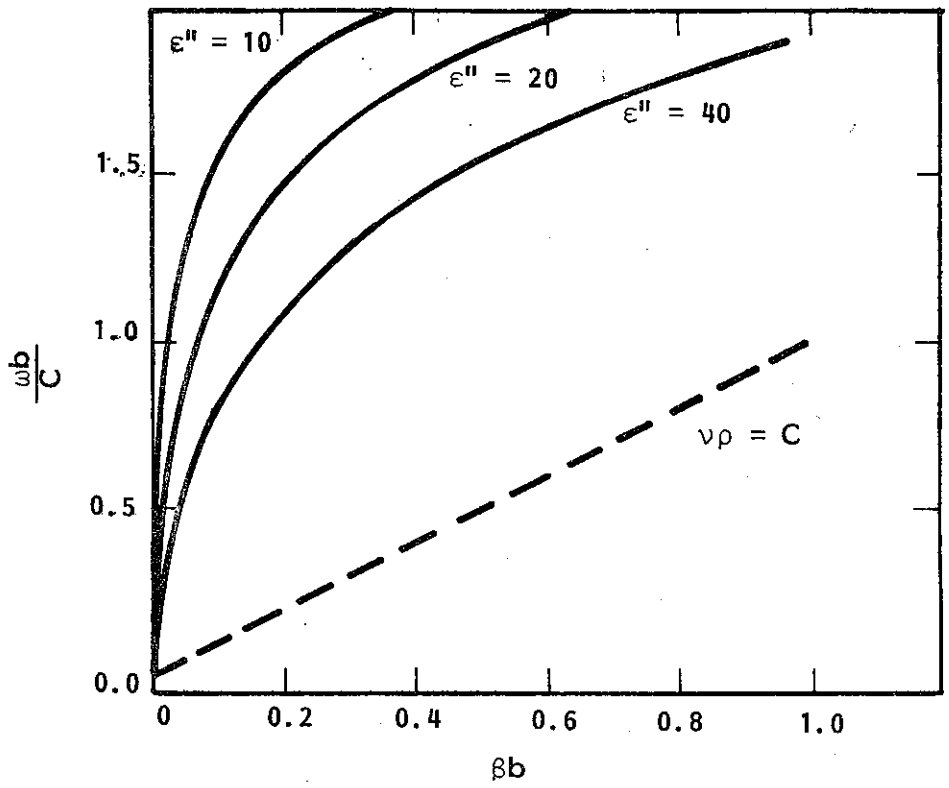

Figure 6-3. Continuation of Figure 6-2.

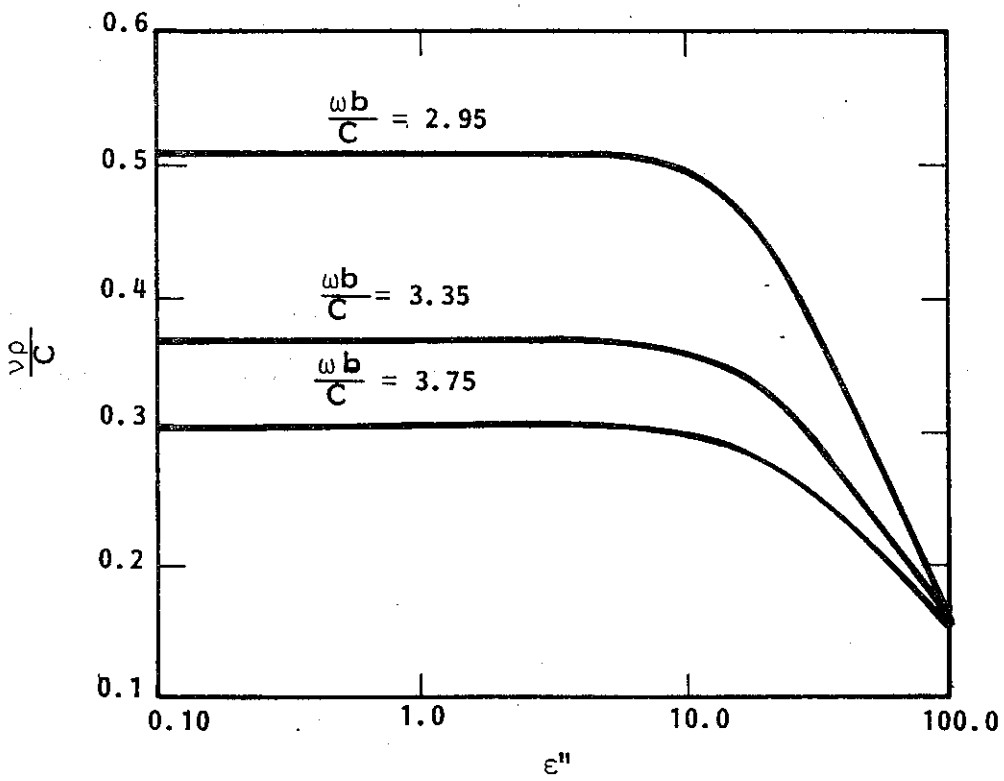

Figure 6-4. TE_{01} Phase Velocity vs ε" for Various Values of Frequency.

of Figure 6-2, down to $\omega = 0$. As ε'' increases, the $\omega - \beta$ line shifts to the right, and synchronism with the beam line is reduced. If the shift in β corresponding to the value of α desired is relatively large, the interaction, and thus the gain, will decrease. This would necessitate a re-evaluation of the small signal gain of the circuit. The desired value of loop gain could then be calculated by finding the proper combination of gain decrease due to β shift (reduced interaction) and gain decrease due to attenuation. It is hoped that the value of ε'' which produces sufficient attenuation to suppress oscillations creates a shift in β that is small enough to be ignored.

Perhaps the best way to see how β changes with the addition of loss is to examine the wave's phase velocity: $v_p = \frac{\omega}{\beta}$. Figure 6-4 is a graph of $v_p/C = (\frac{\omega b}{C})/(\beta b)$ versus ε'', where ε'' is plotted on a log scale to give a full range of values. Three frequencies are shown: the band edges $\frac{\omega b}{C} = 2.95$ and $\frac{\omega b}{C} = 3.75$, and the center frequency $\frac{\omega b}{C} = 3.35$. This plot vividly displays the information desired. Up to about $\varepsilon'' = 5.0$, the phase velocity of the wave at all frequencies departs very little from the lossless case. At this point v_p begins a sharp decrease with additional loss and all three values approach a common assymptotic value of $v_p = 0$. Thus, $\varepsilon'' = 5.0$ can be considered as an indicator point, below which any shift in β will be considered small enough to be ignored (in the frequency band of interest).

The attenuation resulting from the lossy dielectric is shown in Figures 6-5, 6-6, and 6-7. Here αb has been plotted against relative frequency for values of ε'' ranging from 0.25 to 40.0. The arrows shown in the plots correspond to $\frac{\omega b}{c} = 2.37$, which is the cutoff frequency of the lossless waveguide. It is evident from these graphs that as ε'' approaches zero (i.e. the lossless case), the attenuation quickly increases at frequencies approaching lossless cutoff. This indicates that while a wave will not propagate below cutoff in the lossless case (since $\beta = 0$), propagation is possible below this frequency in the lossy case. The penalty is that the attenuation will be much more severe in this region.

The phase constant, β, also exhibits interesting behavior near the lossless cutoff. As mentioned before, β is zero below cutoff in the lossless case. In the lossy case, β approaches zero but does not quite reach it until the point $\omega = 0$. This was seen in Figure 6-3. It can also be seen in Figure 6-3 that as $\varepsilon'' \to 0$, the $\omega - \beta$ line moves much closer to the $\beta = 0$ axis. The same effect is displayed more vividly in Figure 6-8. Here, phase velocity has been plotted against frequency for various values of ε''. As ε'' becomes smaller, the phase velocity at a given frequency below lossless cutoff becomes much larger, approaching the lossless case of $v_p = \infty$. This effect is again shown in Figure 6-9 where phase velocity is plotted vs ε'' at the lossless cutoff frequency. Here phase velocity is seen to get very large as $\varepsilon'' \to 0$. It is a reasonable conclusion from the behavior of both α and β that as ε'' goes to zero, a true lossless cutoff is approached.

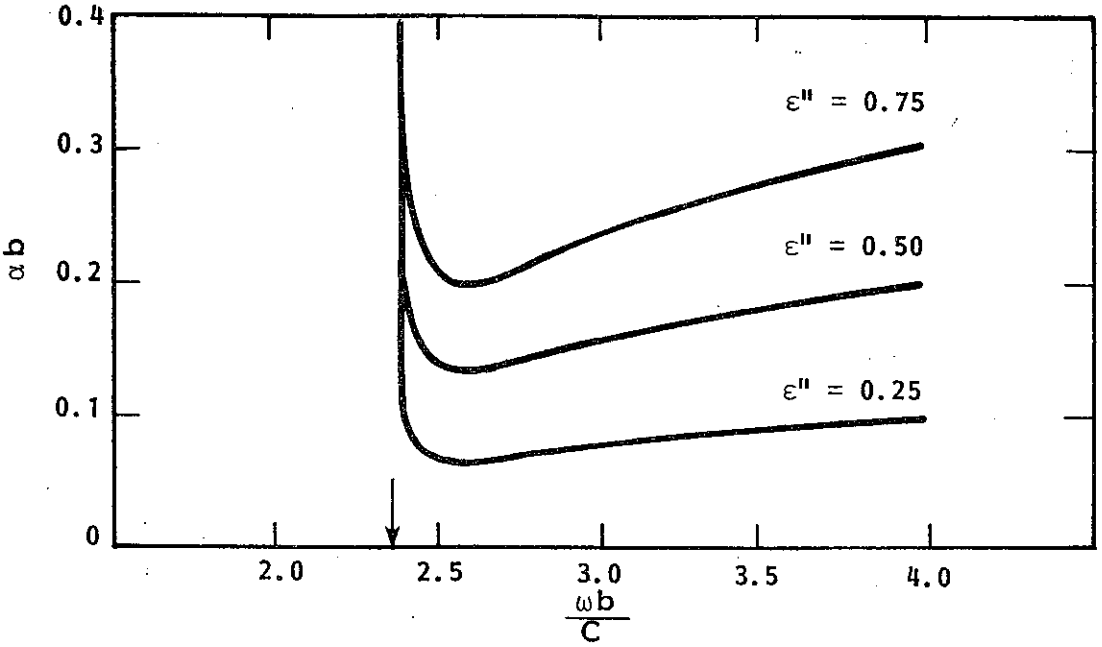

Figure 6-5. TE_{01} Attenuation vs Frequency for Small Values of ε". Arrow Indicates Frequency of Lossless Cutoff.

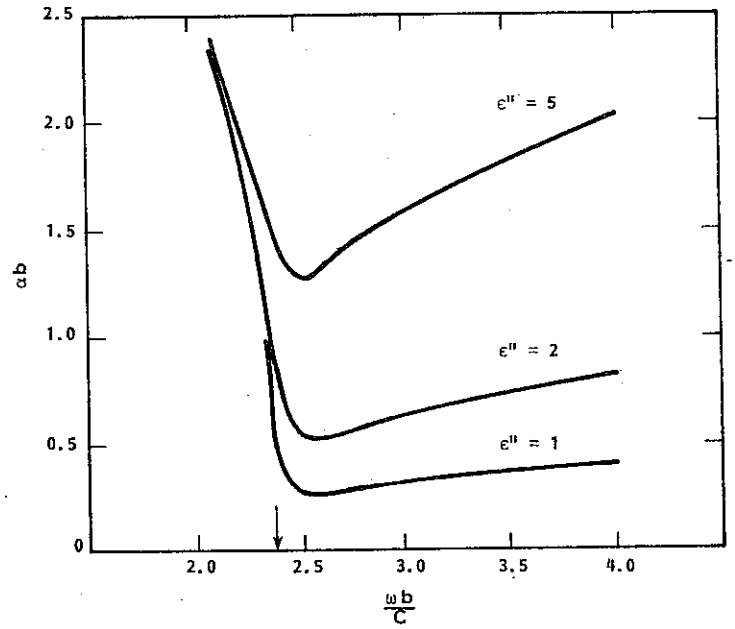

Figure 6-6 TE_{01} Attenuation vs Frequency for Moderate Values of ε". Arrow Indicates Frequency of Lossless Cutoff.

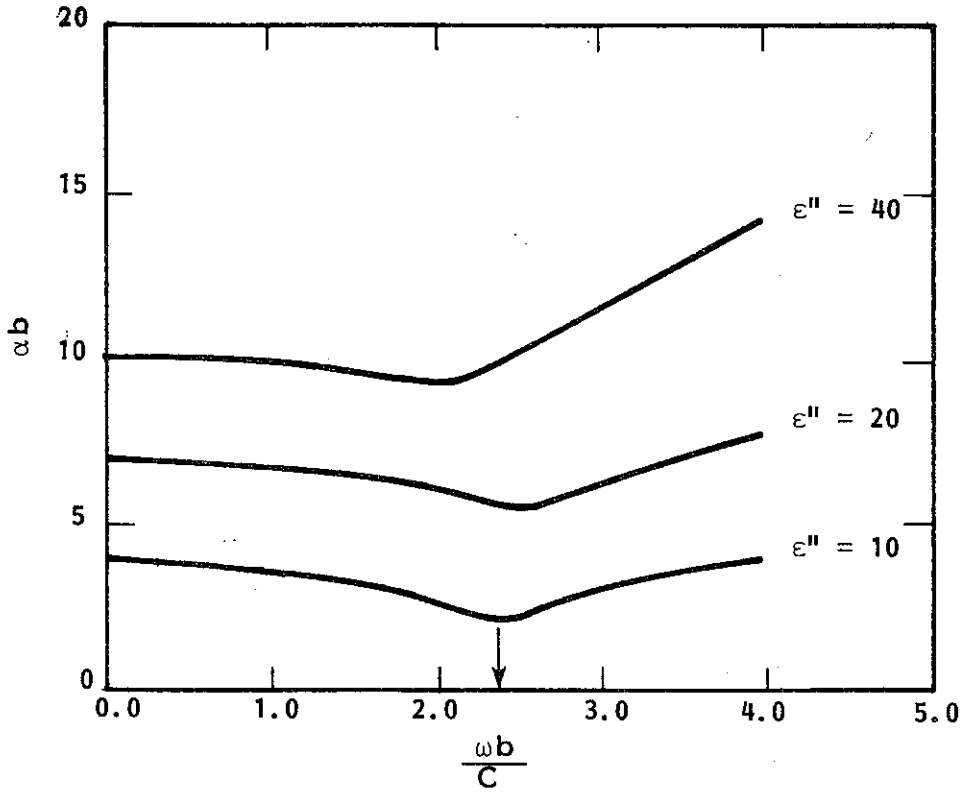

Figure 6-7. TE_{01} Attenuation vs Frequency for Large Values of ε". Arrow Indicates Frequency of Lossless Cutoff.

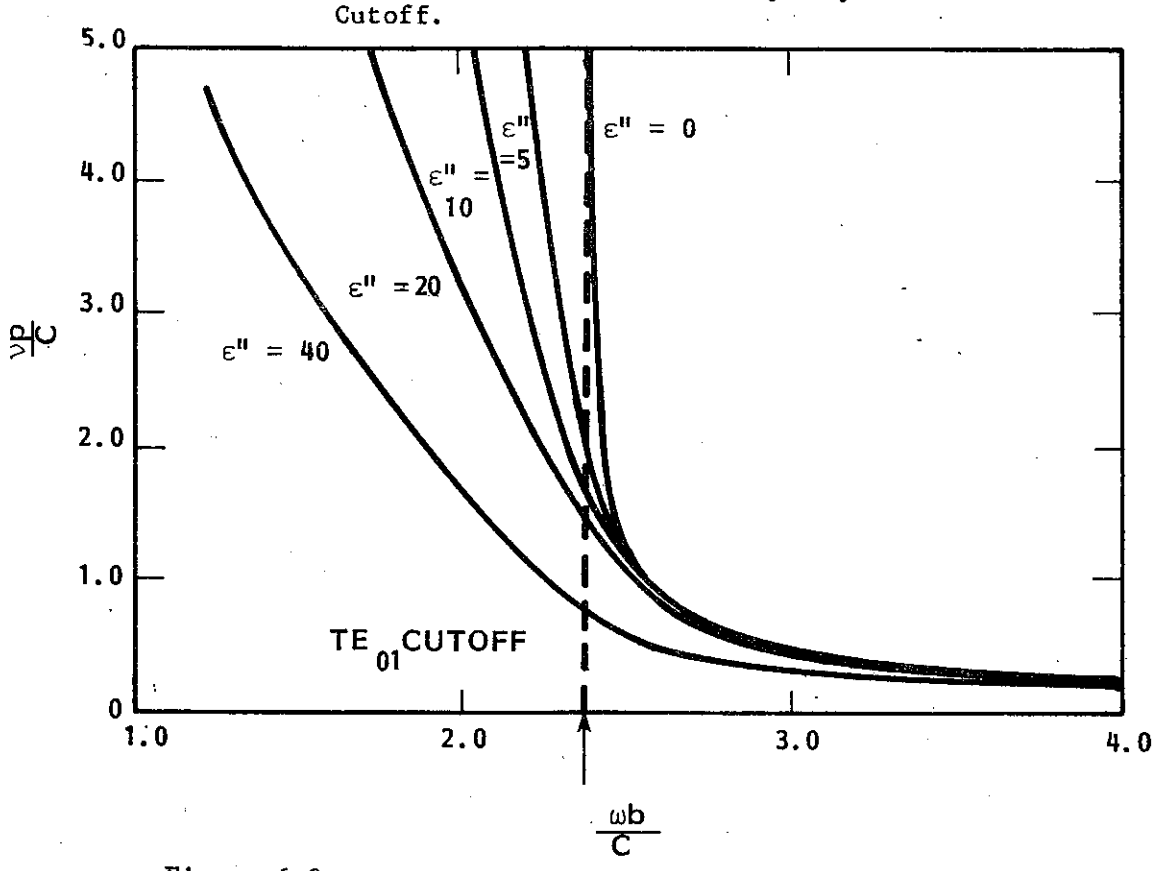

Figure 6-8. TE_{01} Phase Velocity vs Frequency for Various Values of ε".

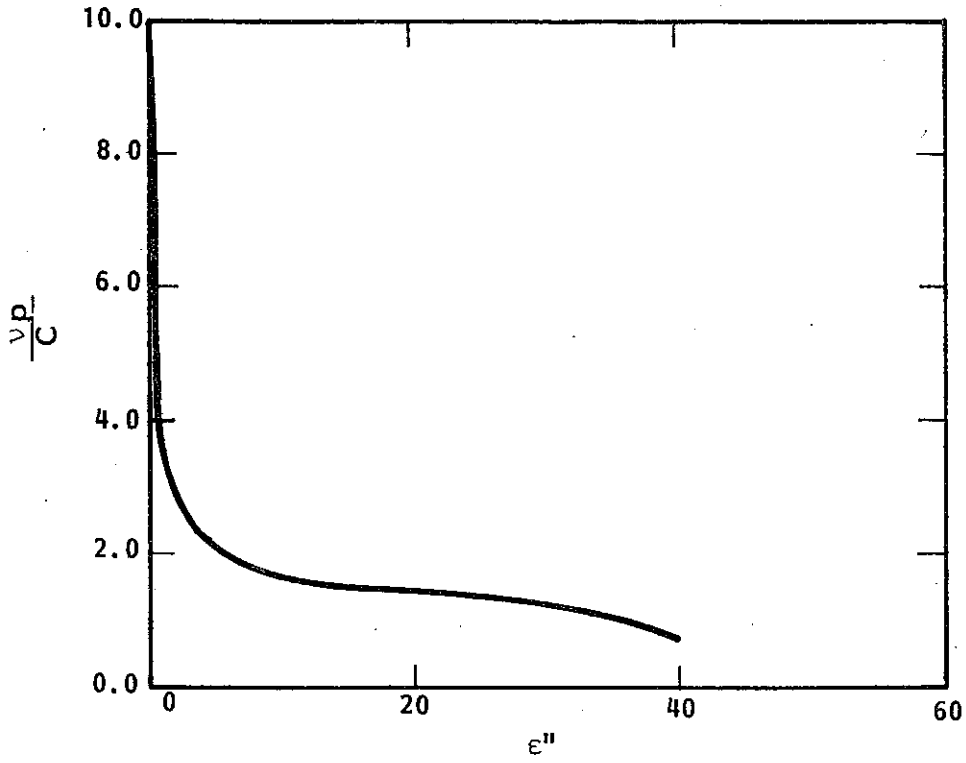

Figure 6-9. TE_{01} Phase Velocity vs ε" at the Lossless Cutoff Frequency.

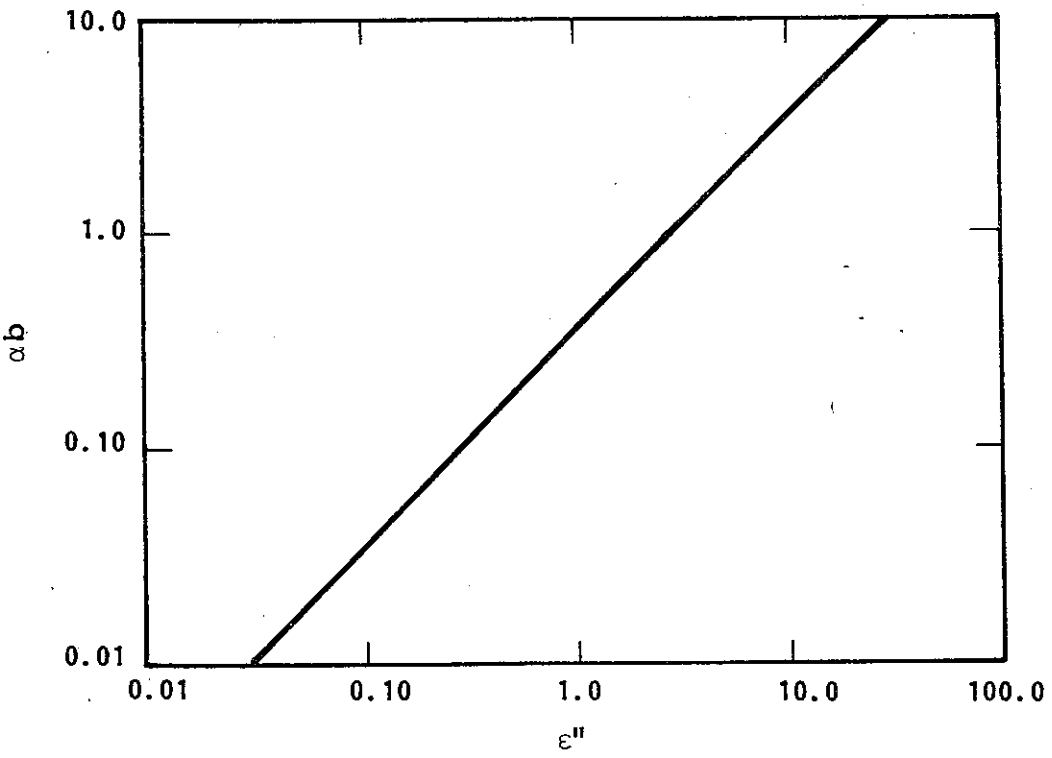

Figure 6-10. TE_{01} Attenuation vs ε" for $\frac{\omega b}{c} = 3.35$.

A useful representation of attenuation results is shown in Figure 6-10. Here αb has been plotted vs ε'' for the center frequency, $\frac{\omega b}{C} = 3.35$, on a log-log scale. For values of ε'' below about 20.0, αb is found to be related to ε'' in a linear fashion. A regression analysis on these results indicates that the first order term is by far the most important, and thus the relationship can be written as:

$$\alpha b\ (\varepsilon'') \cong K_{\alpha 2L}\ (\frac{\omega b}{C})\ \varepsilon''. \qquad (6.3)$$

There is no constant term since $\varepsilon'' = 0$ results in zero attenuation. It is found that, at the other frequency in the operating band, αb and ε'' have nearly the same linear relationship. At the three most important frequencies, $K_{\alpha 2L}$ is found to be:

$$K_{\alpha 2L}\ (2.95) = 3.23,$$

$$K_{\alpha 2L}\ (3.35) = 2.85,$$

$$K_{\alpha 2L}\ (3.75) = 2.58.$$

Equation (6.3) provides a very simple means by which ε'' can be calculated for any value of attenuation desired.

Figures 6-11 and 6-12 examine further the manner in which α varies with frequency and ε''. Each is a plot of:

$$\Delta\ \alpha\ (\omega) = \frac{\alpha\ (\omega) - \alpha\ (\omega_o)}{\alpha\ (\omega_o)}$$

which describes the relative change in α from that at a given frequency. It is important to know how α differs from frequency to frequency since a loop gain margin of 0 dB (as shown in equation (4.7)) should not be exceeded at any frequency. Figure 6-11 shows this parameter vs

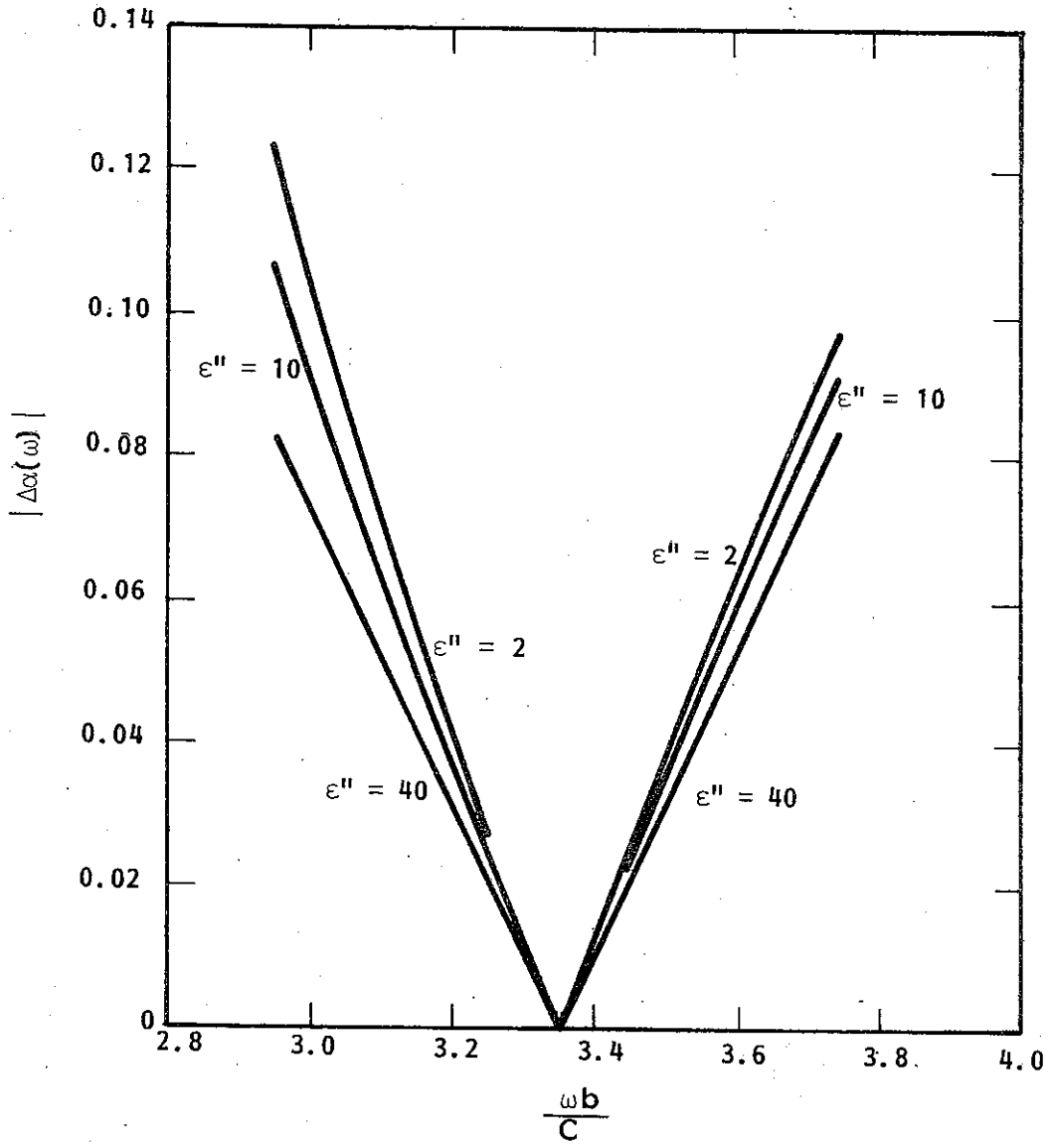

Figure 6-11. $\Delta\alpha\ (\omega) = \frac{\alpha b\ (\omega) - \alpha b\ (\omega o)}{\alpha b\ (\omega)}$ vs Frequency for Various ε'' and $\frac{\omega o b}{C} = 3.35$.

frequency for values of ε'' and $\frac{\omega_o b}{c} = 3.35$, the center frequency. This curve is actually an amplification of Figures 6-7 to 6-9 showing how αb varies with frequency over a narrower range. The linear relationship between αb and $\frac{\omega b}{c}$ is clearly evident. Figure 6-12 describes how $\Delta\alpha(\omega)$ varies with ε'' at various frequencies. As before, $\frac{\omega_o b}{c}$ is taken as 3.35. It is apparent that below about $\varepsilon'' = 2$, $\Delta\alpha(\omega)$ is fairly constant. This means that the relative slopes of the αb vs $\frac{\omega b}{c}$ curve are about the same for all smaller values of ε''.

The foregoing information about αb can be used to obtain the value of ε'' required to suppress oscillations resulting from the fundamental interaction. It was calculated in Section IV that the peak value of the waveguide loss pattern should be 9.07 dB/cm (at mid-band). This corresponds to an αb of: αb = (9.07 dB/cm) (0.39 cm) (0.1151 N^p/dB) = 0.407. As shown in Figure 6-10 or equation (6.3), an attenuation of $\alpha b = 0.407$ occurs when $\varepsilon'' = 1.15$. In other words, 9.07 dB/cm of attenuation will be experienced by a TE_{01} wave propagating in a two-layer waveguide with $\varepsilon_2 = (38 - j\ 1.15)\ \varepsilon_o$. Returning to Figure 6-4, it is found that $\varepsilon'' = 1.15$ falls below the 5.0 indicator point. This is an important observation, leading to the conclusion that the addition of sufficient loss to prevent oscillations due to the fundamental interaction will not adversely affect the synchronism of the beam and the TE_{01} mode. Thus, no parameter modification in the initial small signal analysis is necessary.

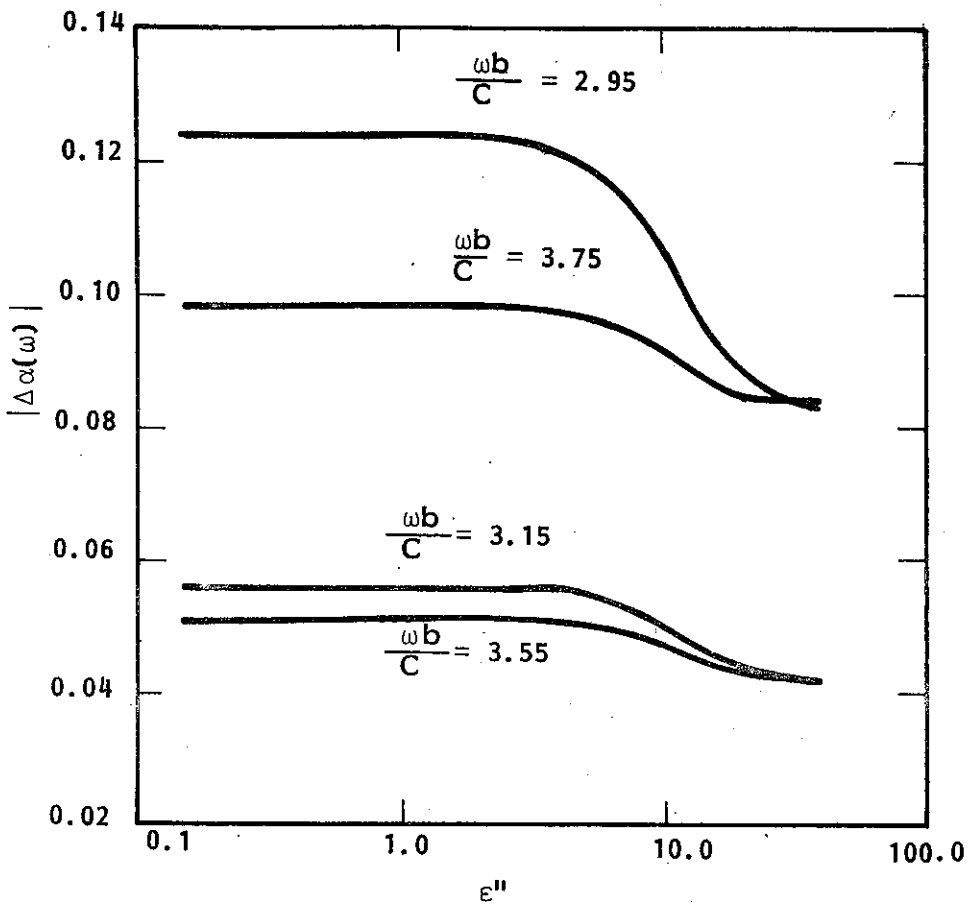

Figure 6-12. $\Delta\alpha\ (\omega) = \frac{\alpha_b\ (\omega) - \alpha_b\ (\omega_o)}{\alpha_b\ (\omega)}$ vs ε'' for Various Frequencies and $\frac{\omega ob}{C} = 3.35$.

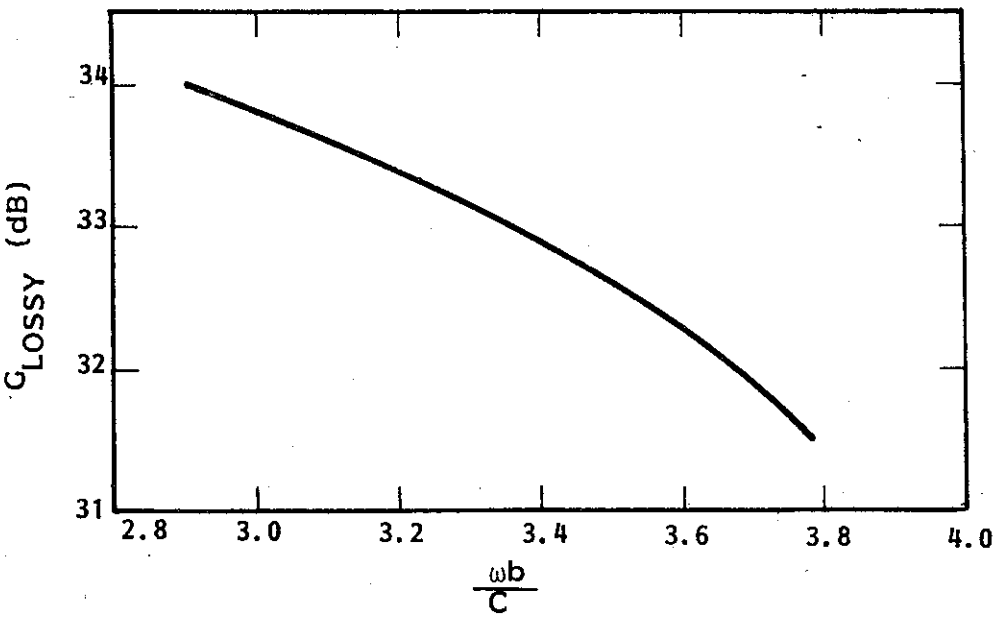

Figure 6-13. Lossy Gain vs Frequency for $\varepsilon'' = 1.15$.

The frequency response of the gain of the amplifier with the lossy dielectric can be found knowing the lossless theoretical gain and how the loss varies with frequency. Remembering that the lossless theoretical gain was found to be a relatively flat 43 dB across the band, and that this gain is reduced by about one-third of the added loss, the lossy gain can be written as:

$$G_{lossy} = 43 \text{ dB} + 0.3 \, L(\omega) \qquad (6.4)$$

where: $L(\omega) = -3.26 \frac{\alpha b(\omega)}{b} \ell$.

Letting: $\ell = 10$ cm, $b = 0.39$ cm, $\varepsilon'' = 1.15$ and using Figures 6-6 and 6-11, a plot of G_{lossy} vs frequency is obtained. This is shown in Figure 6-13. The lossy gain is seen to vary from about 34 dB at the low frequency end to 31.5 dB at the high end of the band. The merit of setting the loop gain margin in equation (4.7) to a sufficiently large value is evident. While the gain at midband may be low enough to prevent oscillations, the gain at $\frac{\omega b}{C} = 2.95$ may be too high. In this case the loop gain at $\frac{\omega b}{C} = 2.95$ is:

$$\text{Loop Gain} = -10.5 + 43 + 1.3 \, (-30.1) = -6.6 \text{ dB} < 0.$$

So, in the reference application, there are no oscillations to be expected from the fundamental interaction.

C. Two-Layer Field Patterns

It has been mentioned that in order to get strong interaction, it is necessary to put the electron beam in the vicinity of highest-strength RF magnetic field. It is advantageous, then, to

obtain a perspective concerning the distributions of the waveguide fields and how they are affected by the addition of loss.

Equations for the values of the TE_{01} fields in each of the two regions have been derived in appendix three. Equations (A3.18) and (A3.19) give values for the fields which have been normalized to make $H_z = 1$ on the axis ($\rho = 0$). These equations are evaluated by choosing a value of $\frac{\omega b}{C}$, solving the TE_{01} dispersion equation for $k_z b$, and substituting these values into (A3.18) and (A3.19).

Figures 6-14, 6-15, and 6-16 are plots of these normalized field components for the lossless waveguide at frequencies of $\frac{\omega b}{C}$ = 2.95, 3.35, and 3.75 respectively. The arrows indicate the vacuum/dielectric interface. The peak value of the relative field strength is seen to be a strong function of frequency, varying by more than two orders of magnitude between $\frac{\omega b}{C} = 2.95$ and $\frac{\omega b}{C} = 3.75$. For all frequencies, the radial magnetic field component, H_ρ, and the azimuthal electric field component, E_ϕ, peak near the boundary of the dielectric and the vacuum. In contrast, the longitudinal magnetic field component, H_z, peaks at the outer waveguide wall, as well as near the dielectric boundary. The behavior of H_ρ justifies the use of a hollow electron beam placed as near the dielectric liner as possible. This puts a maximum amount of the gyrating electrons in the vicinity of peak radial magnetic field.

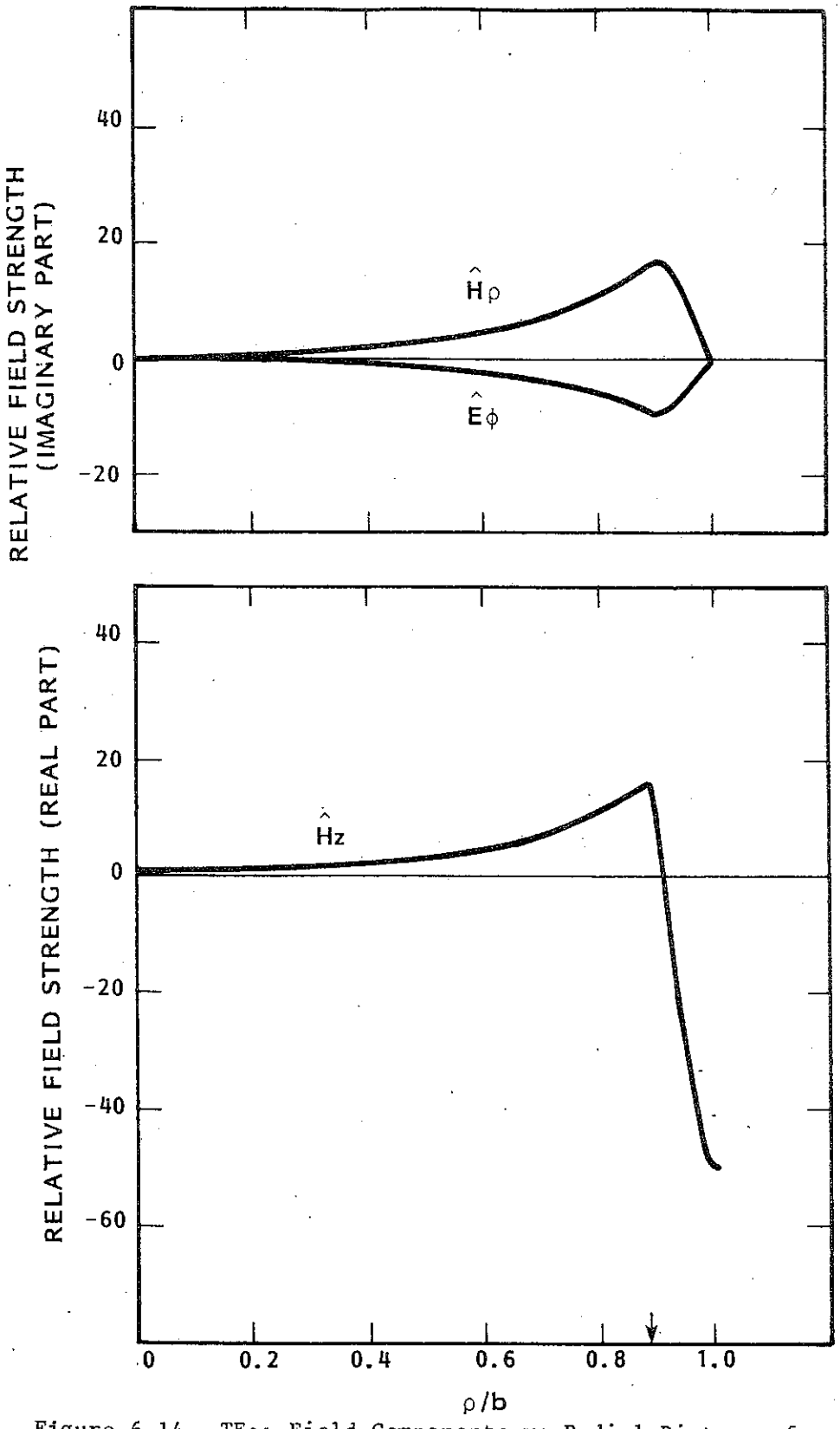

Figure 6-14. TE_{01} Field Components vs Radial Distance for $\varepsilon'' = 0$, $\frac{\omega b}{C} = 2.95$. Arrow Indicates Vacuum/ Dielectric Interface.

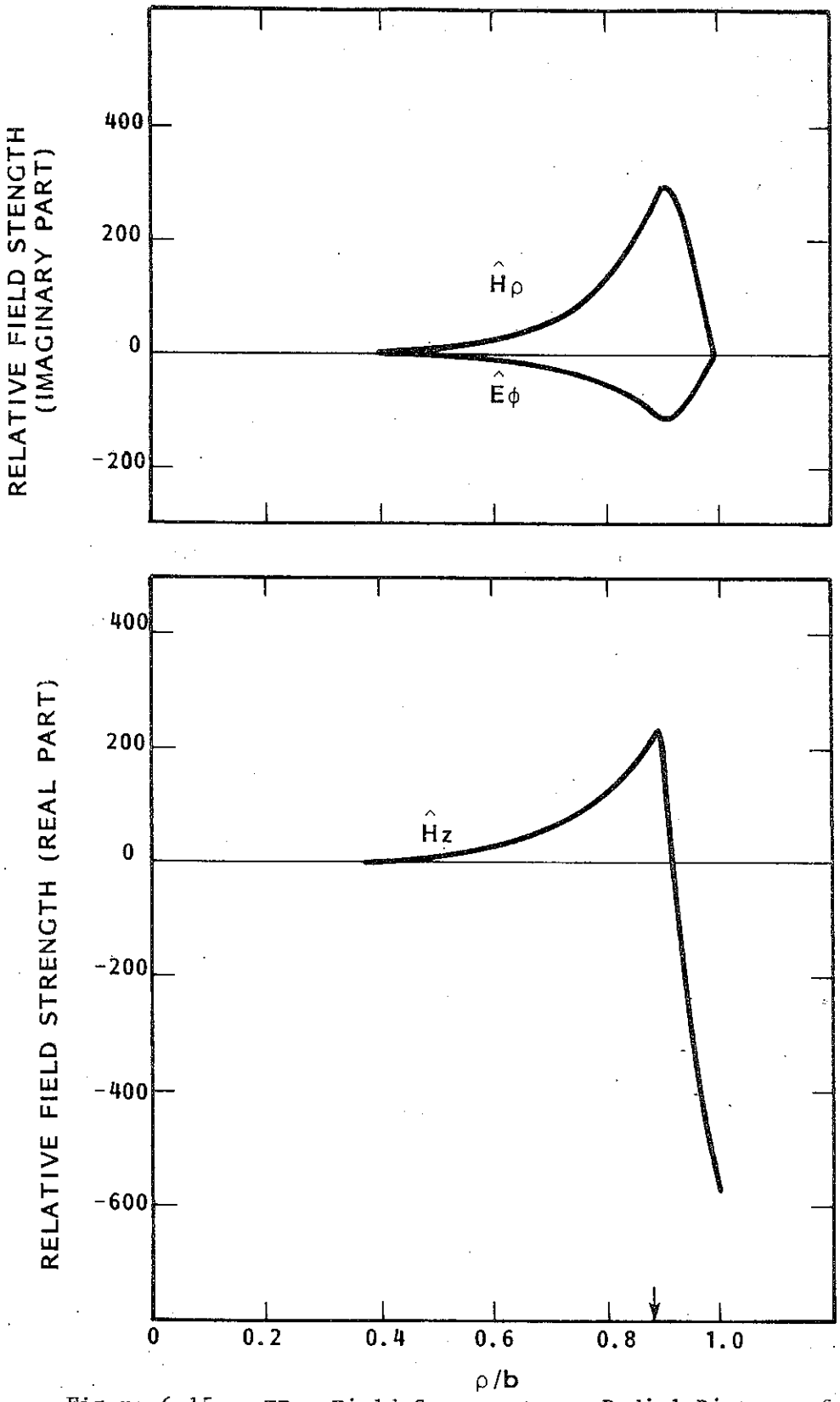

Figure 6-15. TE_{01} Field Components vs Radial Distance for $\varepsilon'' = 0$, $\frac{\omega b}{c} = 3.35$. Arrow Indicates Vacuum/Dielectric Interface.

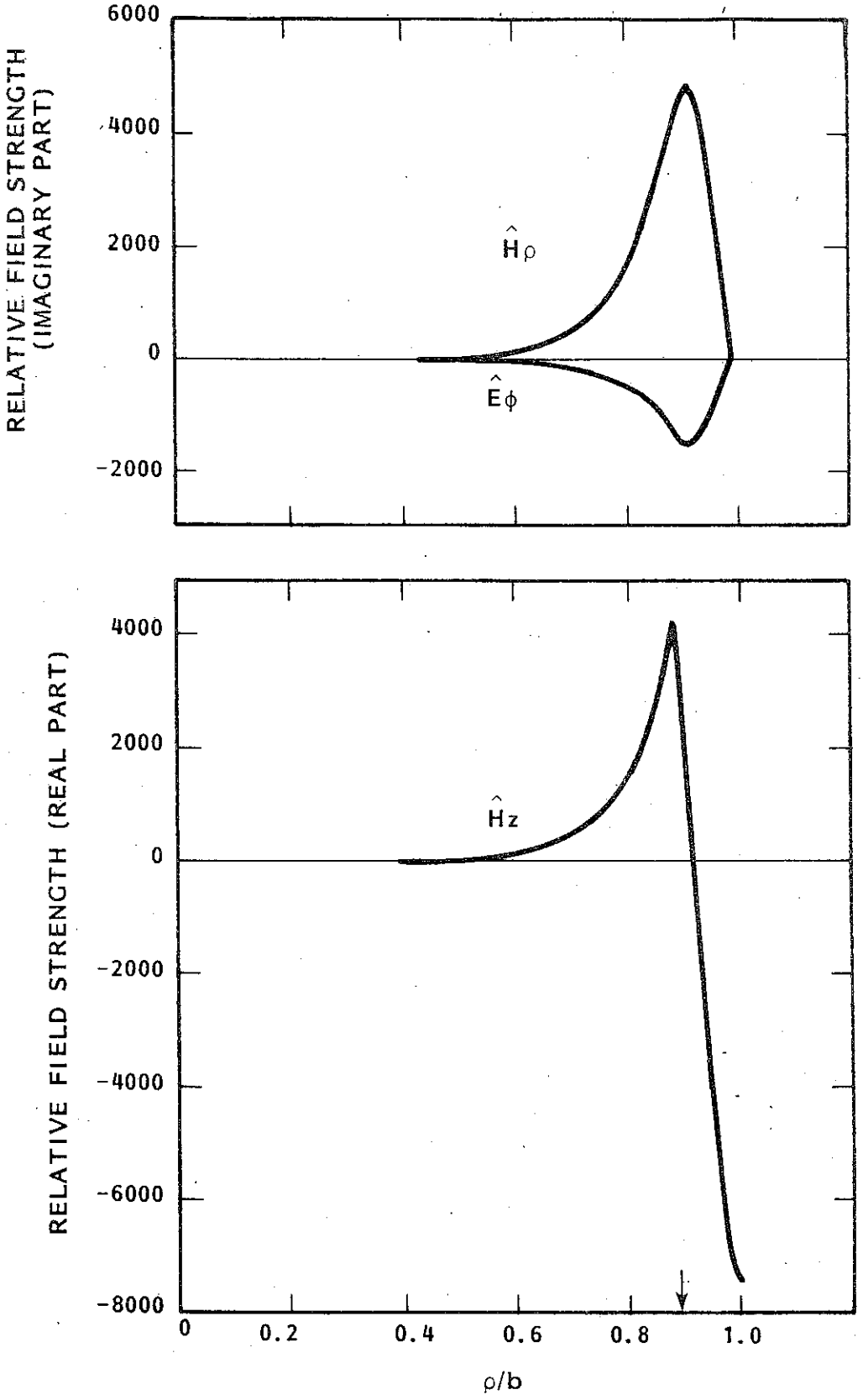

Figure 6-16. TE_{01} Field Components vs Radial Distance for $\varepsilon'' = 0$, $\frac{\omega b}{C} = 3.75$. Arrow Indicates Vacuum/Dielectric Interface.

One worry, discussed earlier, is that the addition of loss would cause a shift in β which would reduce the fundamental interaction. In a similar vein, it is important to consider how the addition of loss affects the radial magnetic field. If H_ρ is reduced or redistributed the electron bunching might be diminished and interaction decreased. Figures 6-17, 6-18, and 6-19 show the normalized field components for values of ε'' of 0.5, 1.15, and 5.0 respectively, where $\frac{\omega b}{c} = 3.35$. Figure 6-18 reveals that for $\varepsilon'' = 1.15$ the real part of H_ρ has decreased slightly, while a small imaginary part has been created. The overall magnitude of H_ρ is about the same, but its phase has changed. Note also that H_ρ and H_z still have about a 90° phase difference while H_ρ and E_ϕ are out of phase by around 180°. Thus, it appears that, at least for $\varepsilon'' = 1.15$, there is no significant decrease in the value of H_ρ. In addition, no redistribution of field peaks is apparent and thus beam localization near the dielectric liner remains valid.

D. Solution for the TM_{01} Mode

The TM_{01} mode should be of little concern regarding unwanted interactions. Figure 3-3 suggests that its mode line is too far from the beam line to allow synchronism to take place. Nevertheless, it is important to analyze how loss affects the TM_{01} mode. There are two reasons for this. First, the potential exists for using the TM_{01} mode for interaction in a slow-wave amplifier. If such a project is undertaken, it is good to have some preliminary analysis of the behavior of the lossy waveguide. Second, it is useful to have the TM_{01} mode as a comparison to the results obtained for the TE_{01} mode.

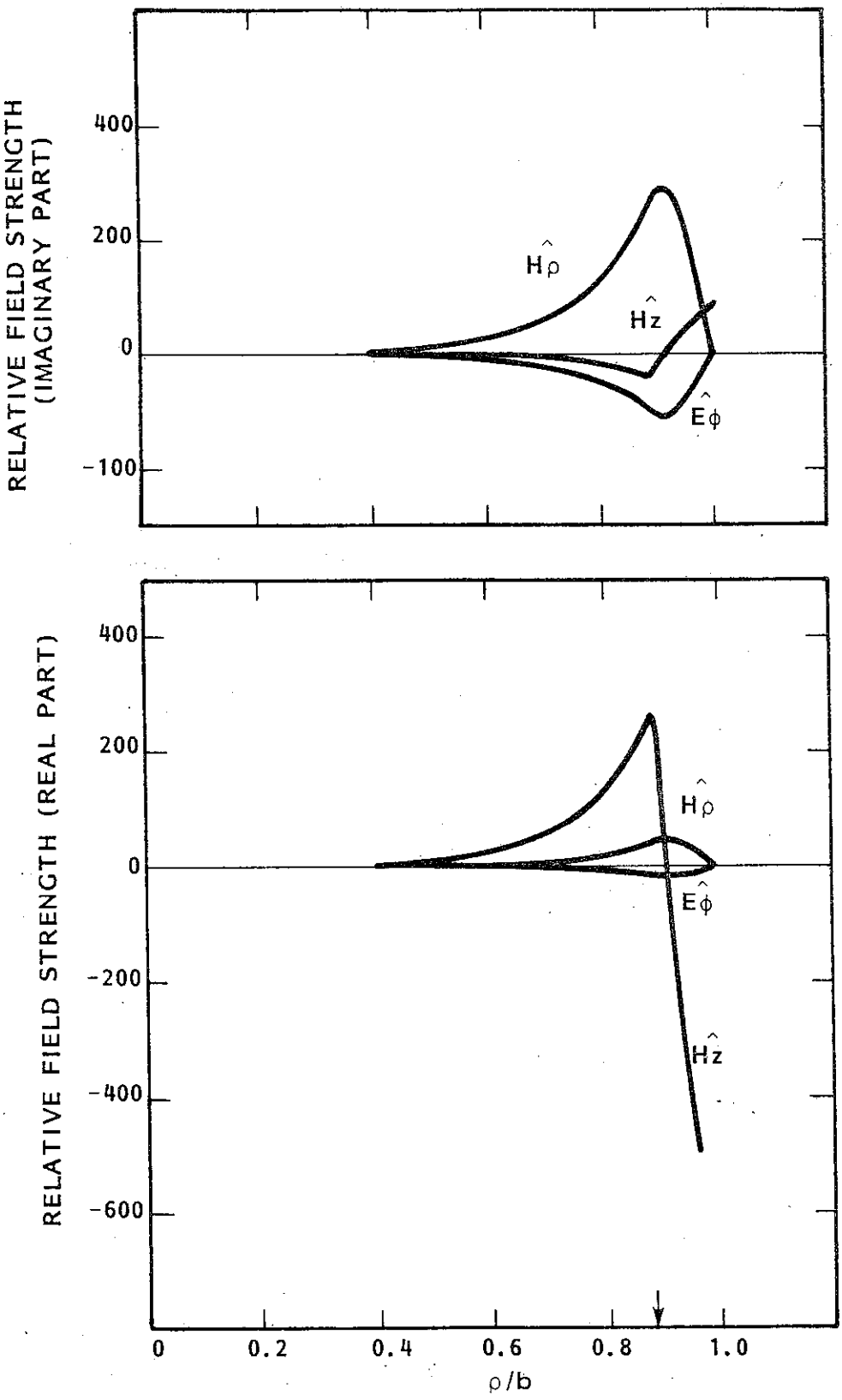

Figure 6-17. TE_{01} Field Components vs Radial Distance for $\varepsilon'' = 0.5$, $\frac{\omega b}{C} = 3.35$. Arrow Indicates Vacuum/Dielectric Interface.

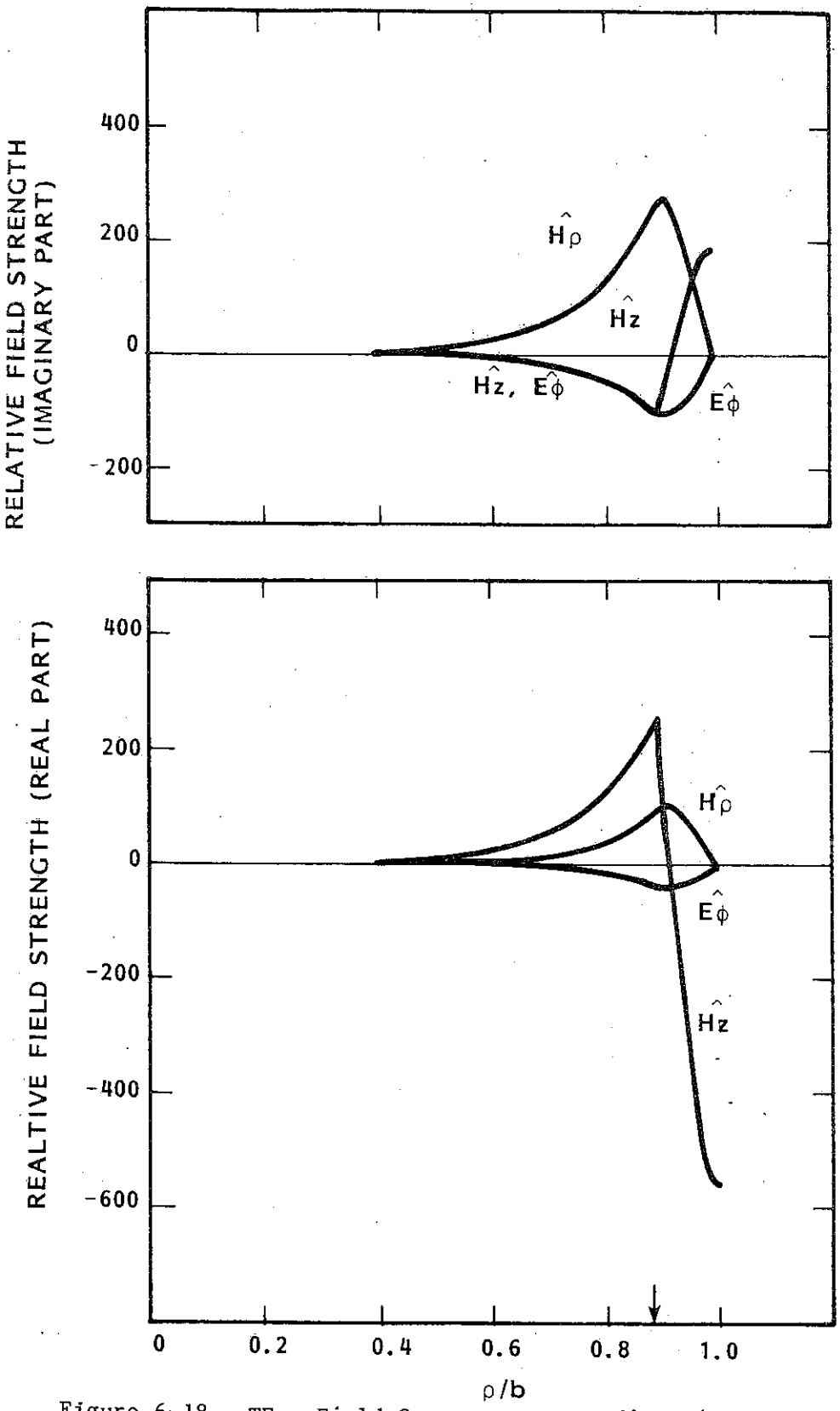

Figure 6-18. TE_{01} Field Components vs Radial Distance for $\varepsilon'' = 1.15, \frac{\omega b}{C} = 3.35$. Arrow Indicates Vacuum/Dielectric Interface.

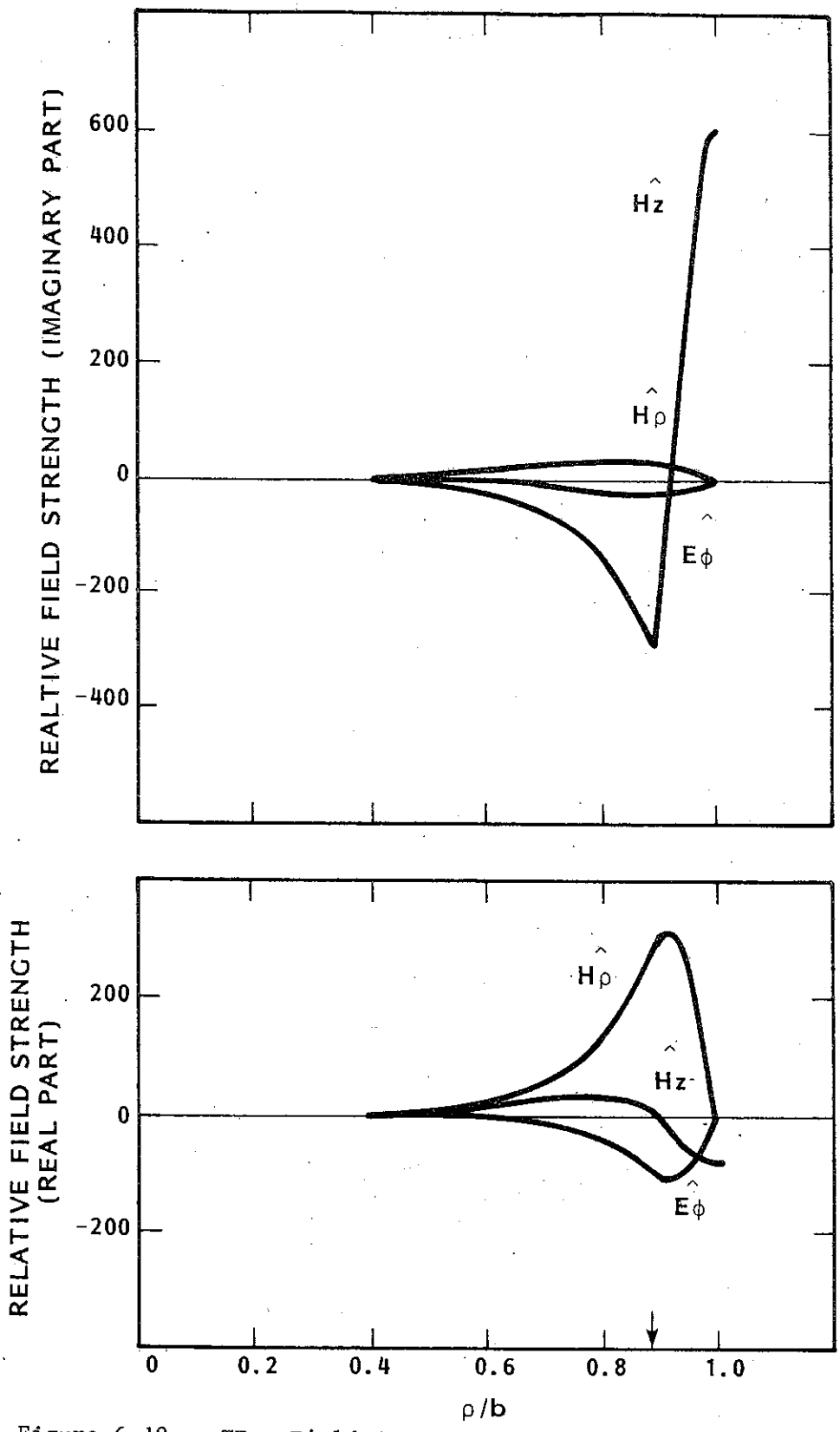

Figure 6-19. TE_{01} Field Components vs Radial Distance for $\varepsilon'' = 5.0$, $\frac{\omega b}{C} = 3.35$. Arrow Indicates Vacuum/Dielectric Interface.

The dispersion relation for the TM_{01} mode is obtained by substituting n = 0 into equation (6.2) and taking the second multiplying term. Solving for the first root yields complex values of the axial propagation coefficient $k_z b = \beta b - j\alpha b$. As with the TE_{01} case, it is assumed that $\mu_{1R} = \mu_{2R} = 1$, $\varepsilon_{1R} = 1$, $\varepsilon_{2R} = 38 - j\varepsilon''$, and $a/b = 0.892$.

Figure 6-20 shows the TM_{01} $\omega - \beta$ diagram for four different values of ε''. It is seen that as ε'' is increased the $\omega-\beta$ curve moves to the right, exhibiting the same effect observed with the TE_{01} mode. This shift seems to be larger in the TM_{01} case, however, yielding a change in βb from the lossless case of about 5.1, against 2.1 for the TE_{01} case (for $\varepsilon'' = 40$ and $\frac{\omega b}{c} = 2.5$). Whereas this shift was undesirable when considering fundamental interaction, here it is a benefit. The addition of loss increases the distance between the TM_{01} mode line and the beam line and thus lessens the chance for unwanted interactions.

The shift in βb with changing ε'' is more dramatically illustrated in Figure 6-21, where the wave's phase velocity is plotted against the log of ε''. This graph appears very similar to the one obtained from the TE_{01} case (Figure 6-4) except at the frequency $\frac{\omega b}{c} = 2.3$. Here an interesting "bump" is seen for ε'' around 4 or 5. At the other frequencies the phase velocity decreases with increasing ε'' and the $\omega - \beta$ curve shifts to the right. At $\frac{\omega b}{c} = 2.3$ the phase velocity first increases with increasing ε'', peaks out at $\varepsilon'' = 5.0$,

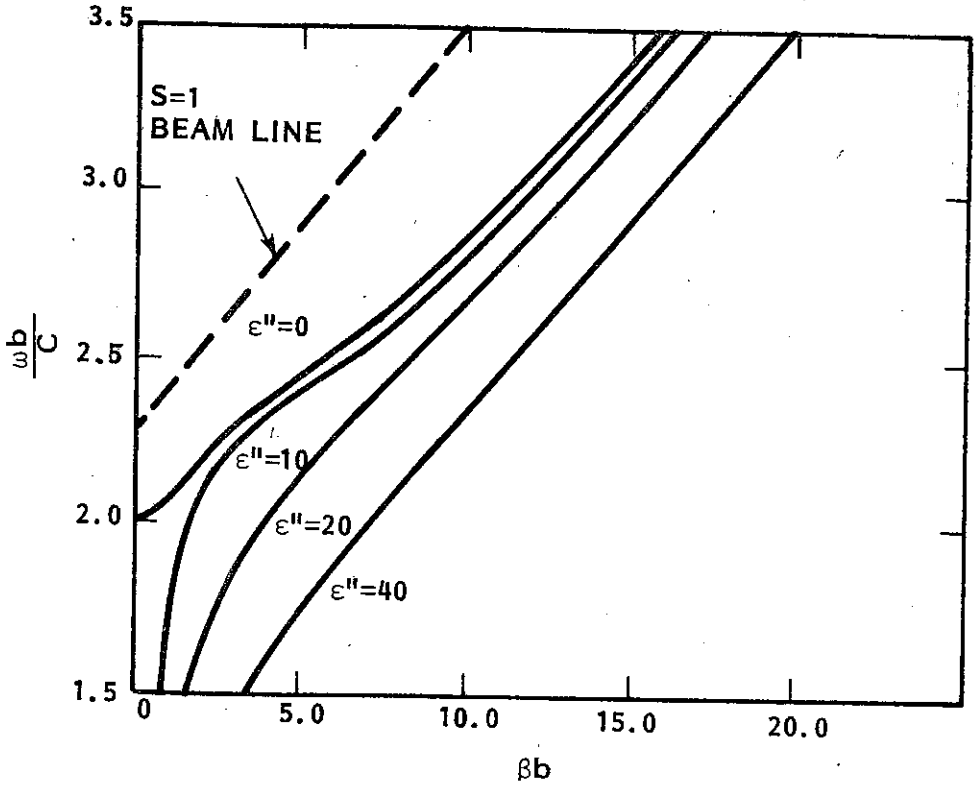

Figure 6-20. Two-Layer TM_{01} $\omega - \beta$ Plot for Various Values of ε''.

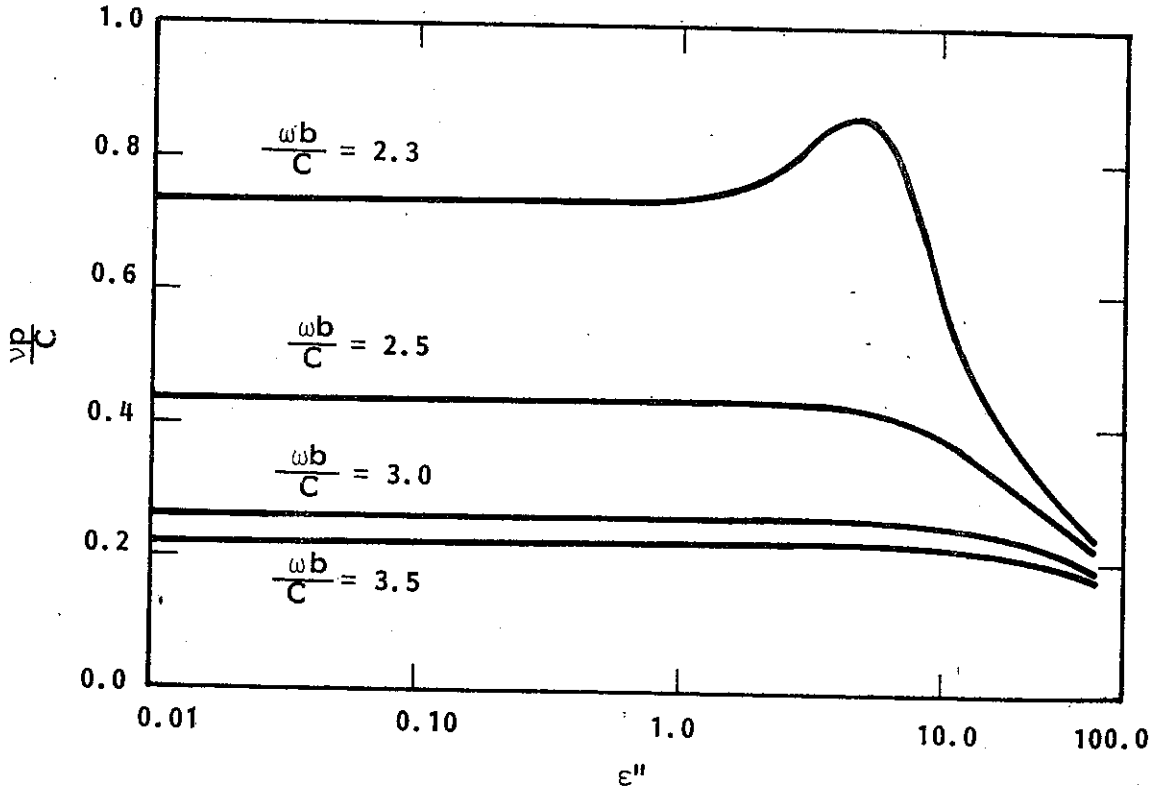

Figure 6-21. TM_{01} Phase Velocity vs ε'' for Various Values of Frequency.

then decreases in much the same manner as the other curves. This corresponds to that point on the $\omega-\beta$ diagram shifting left, stopping, then shifting to the right. In other words, the $\varepsilon'' = 5$, TM_{01} mode line will cross the $\varepsilon'' = 0$ line in the vicinity of $\frac{\omega b}{c} = 2.3$.

Interestingly, the lossless TM_{01} mode line has a peculiarity of its own in the vicinity of $\frac{\omega b}{c} = 2.3$. As β is decreased, the TM_{01} mode is apparently heading for cutoff in the same manner as the TE_{01} mode. However, at a point near $\frac{\omega b}{c} = 2.3$ ($\beta b = 3.0$) the curve makes an abrupt little dip and affects cutoff at a lower frequency. This behavior is not seen in the TE_{01} mode line, and thus certain differences in this region are not entirely surprising.

The attenuation of the TM_{01} wave resulting from the lossy nature of the waveguide is plotted in Figures 6-22 and 6-23. The curves in Figure 6-23, for $\varepsilon'' = 10$, 20, and 40, are somewhat similar to those found for the TE_{01} mode (shown in Figure 6-7). In both cases the attenuation decreases with decreasing frequency until a point near the lossless cutoff (indicated by an arrow) is reached. Below this frequency the attenuation increases with decreasing frequency. With the exception indicated below, the only major difference between the two modes is that the curvature of the attenuation plots appears to be concave down in the TE_{01} mode and concave up in the TM_{01} mode in the region above lossless cutoff.

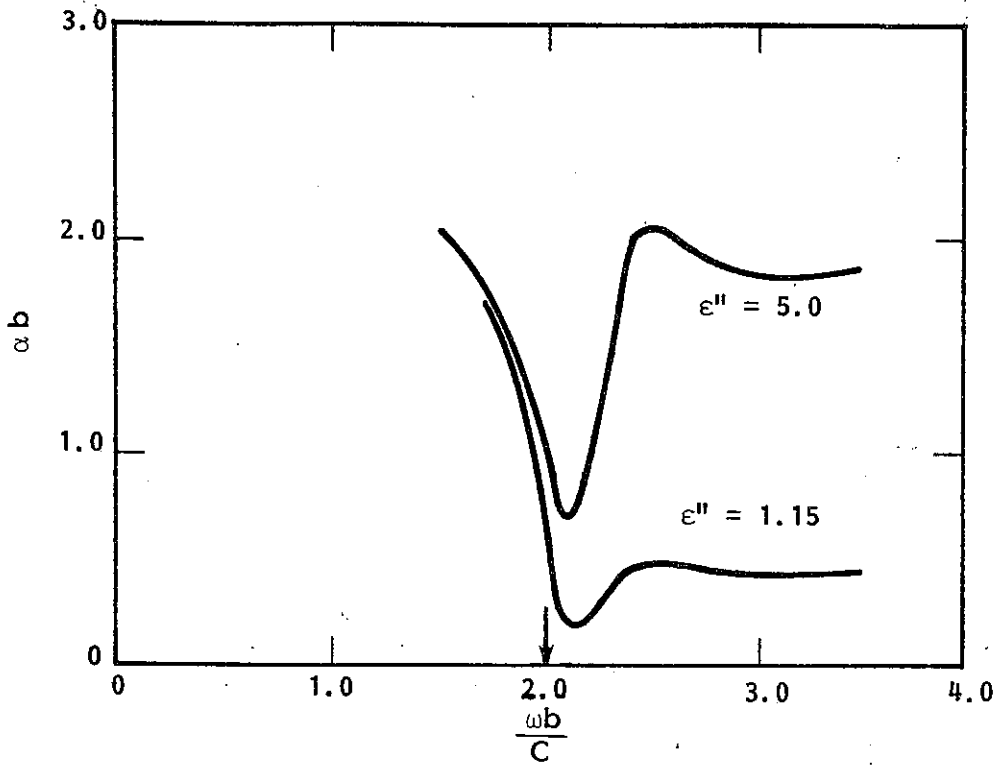

Figure 6-22. TM_{01} Attenuation vs Frequency for Moderate Values of ε". Arrow Indicates Lossless Cutoff.

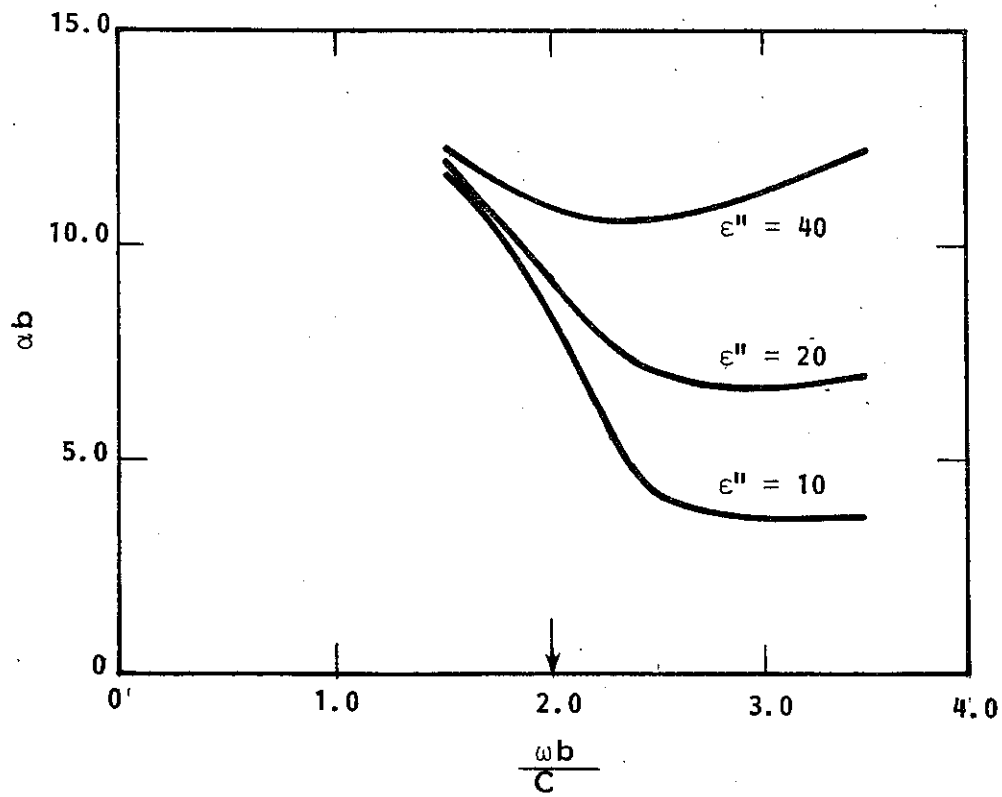

Figure 6-23. TM_{01} Attenuation vs Frequency for Large Values of ε". Arrow Indicates Lossless Cutoff.

The curves shown in Figure 6-22 show striking differences to those in Figure 6-6. In the TE_{01} case there is no change in the basic shape of the curve as ε'' is reduced. However, as ε'' is changed from 10.0 to 5.0 there is a drastic change in the TM_{01} curve. Figure 6-22 shows a huge dip for the $\varepsilon'' = 5.0$ curve at about $\frac{\omega b}{c} = 2.3$. When $\varepsilon'' = 1.15$ the dip is smaller but still noticeable. This drop in attenuation is apparently connected to the interesting behavior of βb described previously. When $\varepsilon'' = 1.15$, the bump in Figure 6-21 is just beginning to develop, and the dip in Figure 6-22 is fairly small. At $\varepsilon'' = 5.0$ the bump is at its peak and the dip in attenuation is very large. At $\varepsilon'' = 10.0$ the bump in the phase velocity curve has disappeared, and so has the dip in attenuation.

For higher values of frequency the "bump-and-dip" behavior is not present, and the TM_{01} attenuation acts much the same as in the TE_{01} case. Figure 6-24 is a log-log plot of attenuation vs ε'' for $\frac{\omega b}{c} = 3.4$. The linear nature of this curve is very much like that shown in Figure 6-10 for the TE_{01} mode. In both cases the curves have a slope of one until about $\varepsilon'' = 10$.

As stated before, when the beam is synchronized with the TE_{01} mode, the chances of interaction between the beam and the TM_{01} mode are fairly small. Oscillation due to this interaction should be even less likely when loss in the form of $\varepsilon'' = 1.15$ is added and the TM_{01} mode is attenuated. Such should be the case at all frequencies

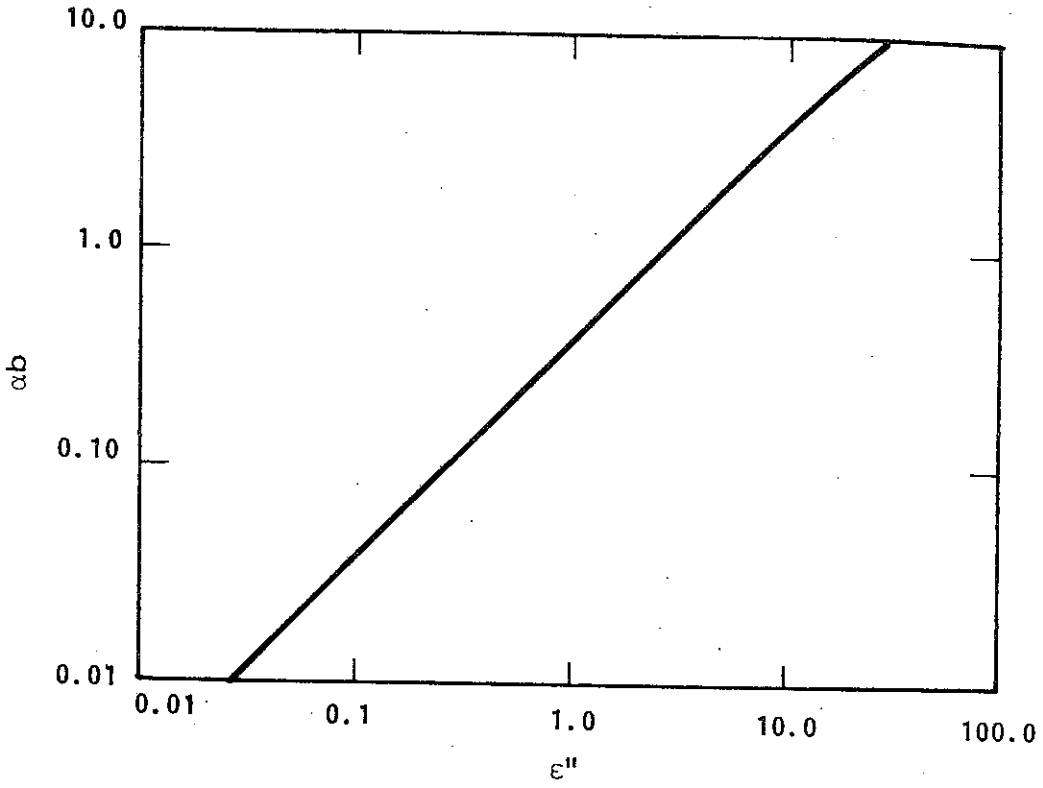

Figure 6-24. TM_{01} Attenuation vs ε'' for $\frac{\omega b}{c} = 3.4$.

except, possibly, near the troublesome $\frac{\omega b}{c} = 2.3$. This frequency is characterized by three important differences. First, Figure 6-20 shows that this is the point at which the TM_{01} mode line passes closest to the beam line. Second, Figure 6-21 indicates that when a loss of $\varepsilon'' = 1.15$ is added to the waveguide the TM_{01} mode line actually moves a bit closer to the beam line. Third, Figure 6-22 shows that the attenuation at $\frac{\omega b}{c} = 2.3$ is only about half of its value at higher frequencies.

Oscillation at $\frac{\omega b}{c} = 2.3$ would represent a much more worrisome problem if the TM_{01} mode were ever used for fundamental interaction. This is due mainly to the dip in the attenuation curve. An amount of loss sufficient to prevent oscillations at $\frac{\omega b}{c} = 2.5$ would probably be only a third of that necessary at $\frac{\omega b}{c} = 2.3$. Thus, if the right amount of loss were added to suppress oscillations at $\frac{\omega b}{c} = 2.3$, the higher frequencies would be subjected to an attenuation about three times larger than necessary. This would prove detrimental to the lossy gain of the amplifier.

E. Solution for the TE_{02} and TM_{02} Modes

The TE_{02} and TM_{02} modes must be considered potential sources of oscillation since they both intersect the s = 2 beamline. If a mode filter is used to remove all but the azimuthally symmetric

modes, the TE_{02} and TM_{02} modes will remain as the most bothersome. They are considered together here because, unlike the TE_{01} and TM_{01} modes, their attenuation characteristics are very similar.

The TE_{02} and TM_{02} modes are calculated by substituting $n = 0$ into equation (6.2) and solving for the second set of roots. Figures 6-25 and 6-26 show the resulting $\omega - \beta$ curves for the TE_{02} and TM_{02} modes. Also plotted in these figures is the $s = 2$ beam line, which is found by substituting $s = 2$ into equation (3.2). Figure 6-25 shows that the shift in βb for the TE_{02} case is much less and very different than that in the TE_{01} case. In fact, for $\varepsilon'' = 40$, the shift is to the right at lower frequencies and to the left at higher frequencies, resulting in a crossing of the lossless line. Differing behavior is also exhibited in Figure 6-26 for the TM_{02} mode. The shifts are much smaller than in the TM_{01} case, and the $\varepsilon'' = 20$ and $\varepsilon'' = 40$ lines are seen to cross at about $\frac{\omega b}{c} = 2.7$. An interesting result of the reduced shift in β is that the intersection point of the TE_{02} or TM_{02} mode line and the $s = 2$ beam line should remain fairly constant over a wide range of ε''.

The phase velocity of the TE_{02} and TM_{02} modes is plotted against ε'' in Figures 6-27 and 6-28. Figure 6-28 reveals that the TM_{02} phase velocity exhibits decreasing $\frac{v_p}{c}$ with increasing ε'', as seen before. Figure 6-27 is more interesting: at $\frac{\omega b}{c} = 4.8$ the phase velocity of the TE_{02} wave decreases with increasing ε'' while at

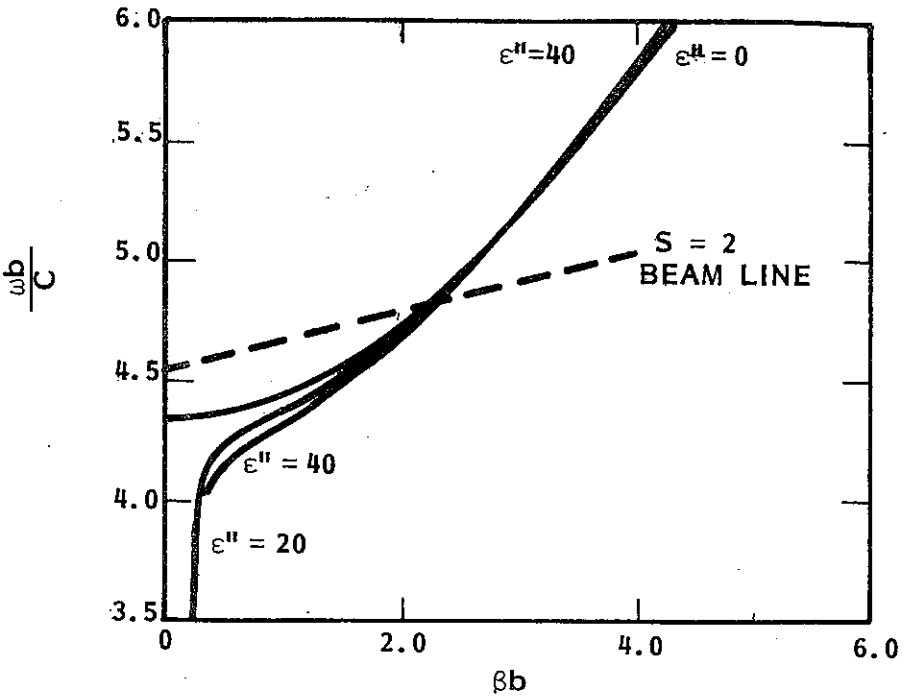

Figure 6-25. Two-Layer TE_{02} $\omega - \beta$ Plot for Various Values of ε''.

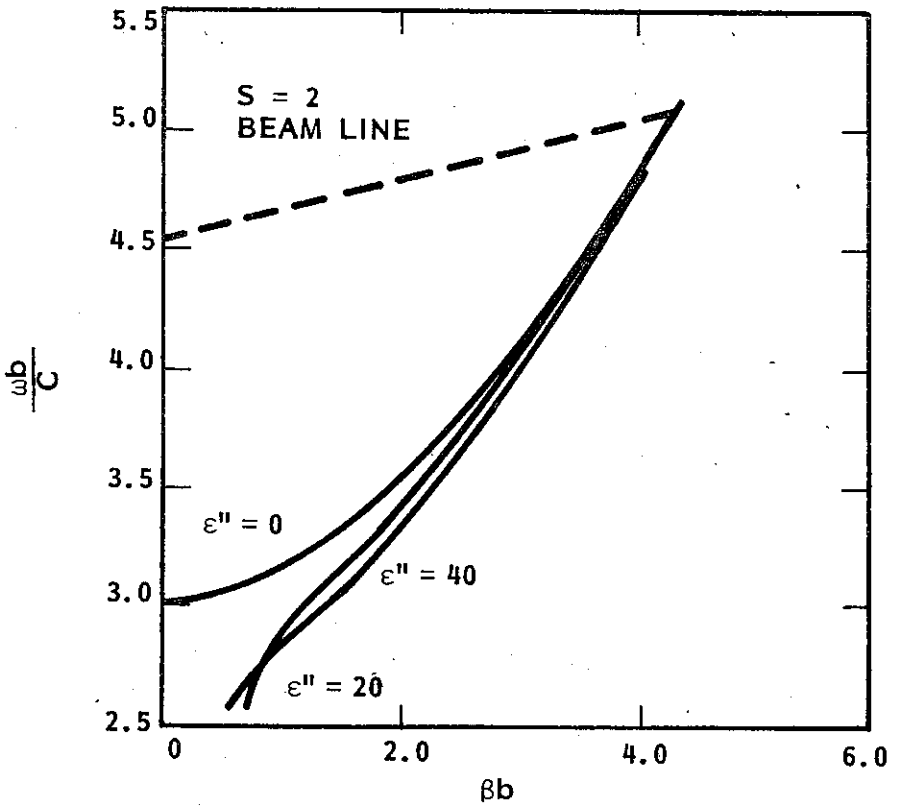

Figure 6-26. Two-Layer TM_{02} $\omega - \beta$ Plot for Various Values of ε''.

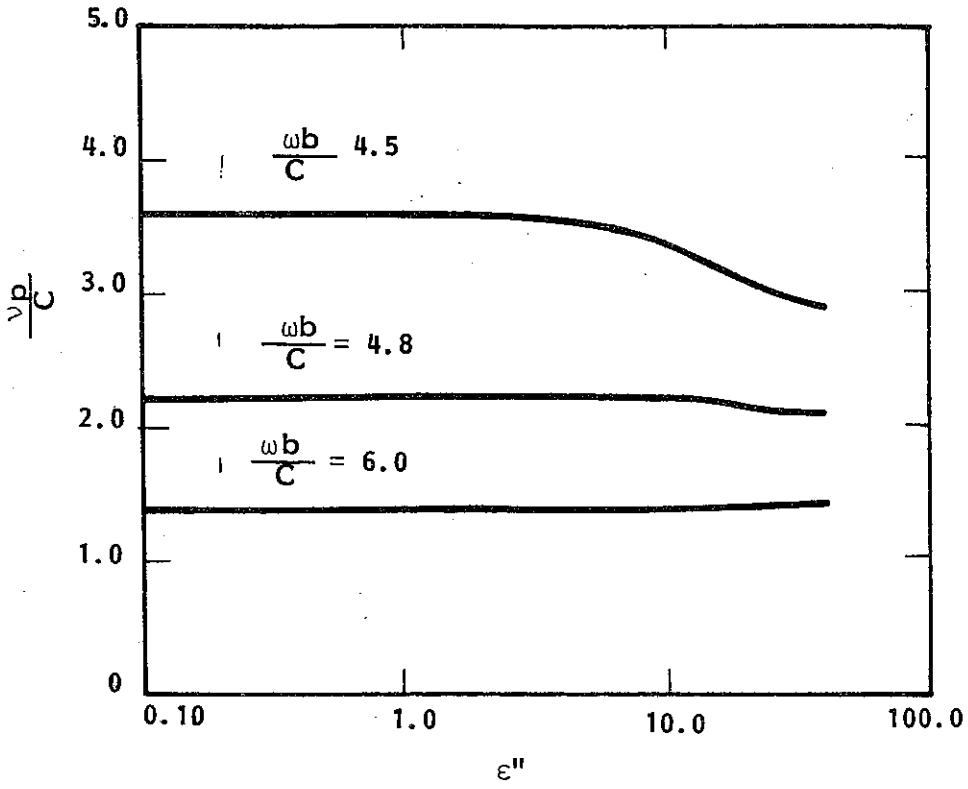

Figure 6-27. TE_{02} Phase Velocity vs ε" for Various Frequencies.

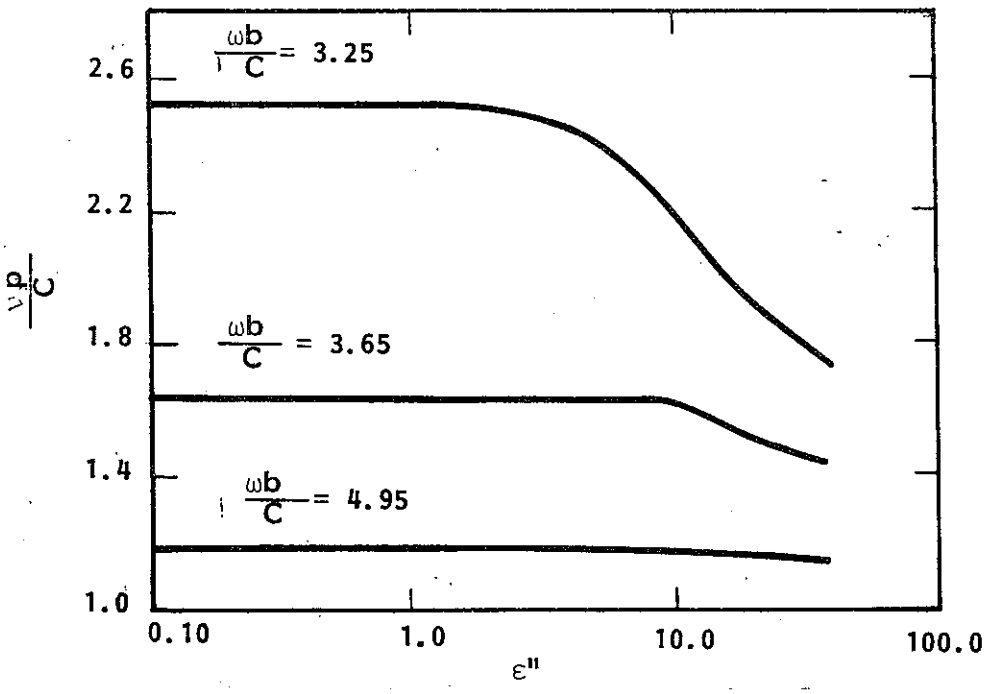

Figure 6-28. TM_{02} Phase Velocity vs ε" for Various Frequencies.

$\frac{\omega b}{C}$ = 6.0 it increases slightly. This results in the crossover effect seen in Figure 6-25.

Figures 6-29 and 6-30 show the attenuation resulting from various values of ε'' for the TE_{02} and TM_{02} modes. The basic shape of these curves is much the same as that of the TM_{01} mode with higher ε'' -- slow decreasing attenuation with decreasing frequency until a point near lossless cutoff is reached, then increasing rapidly. A more important observation is that the TE_{02} and TM_{02} waves are attenuated much less, by nearly two orders of magnitude, than are their TE_{01} and TM_{01} counterparts. The exception is near lossless cutoff (shown by the arrow) where the attenuation is nearly as great.

An interesting characteristic of both figures 6-29 and 6-30 is that the ε'' = 40 curve intersects other curves. This is not intuitively expected. For example, at $\frac{\omega b}{C}$ = 6.0 the TE_{02} wave will experience more attenuation with ε'' = 20 than with ε'' = 40 (αb = 0.115 as opposed to αb = 0.100). This also means that certain values of attenuation can be obtained from more than one value of ε''. Figures 6-31 and 6-32 show this more clearly, plotting attenuation against ε''. In both figures the usual linear relationship between ε'' and αb is seen to hold up to about ε'' = 5.0. However, at this point the curves begin to flatten out and, for certain frequencies, bend back down. For the TE_{02} mode at $\frac{\alpha b}{C}$ = 6.0, a value of αb = 0.10 can be obtained at either ε'' = 11.5 or at ε'' = 39.

A qualitative understanding of why the higher order modes are attenuated less than the TE_{01} and TM_{01} modes can be gained by

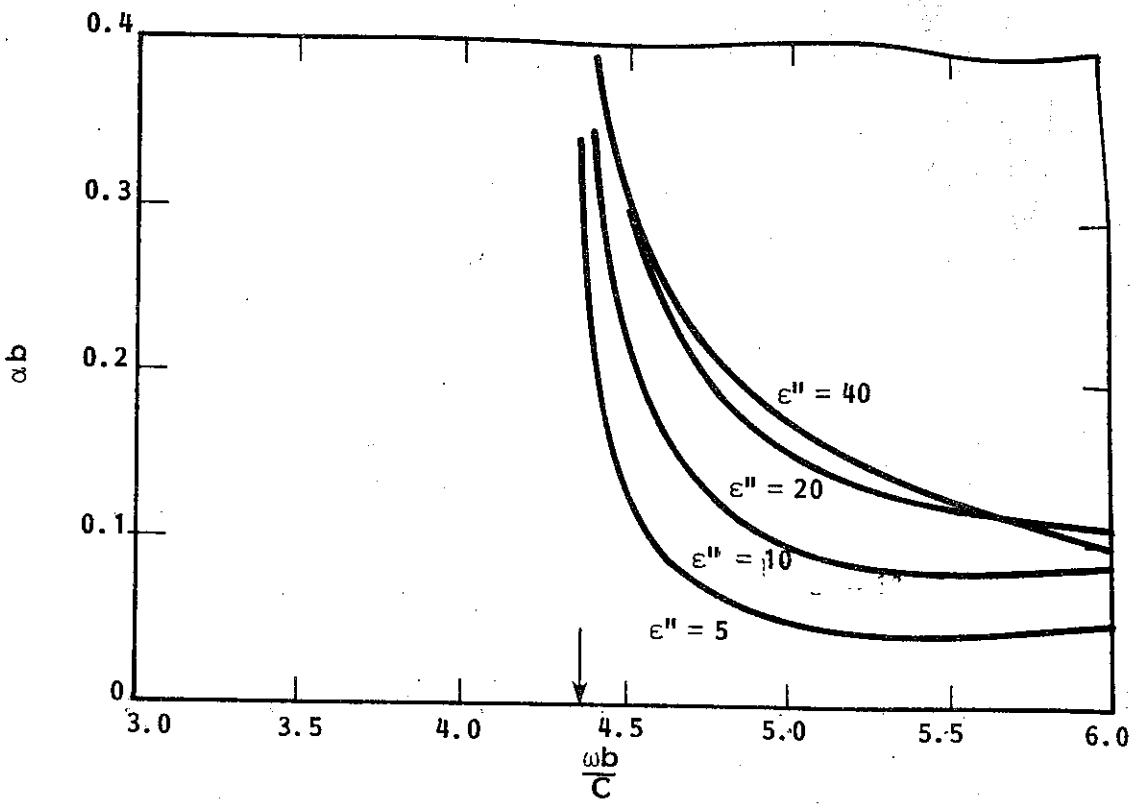

Figure 6-29. TE_{02} Attenuation vs Frequency for Various ε". Arrow Indicates Lossless Cutoff.

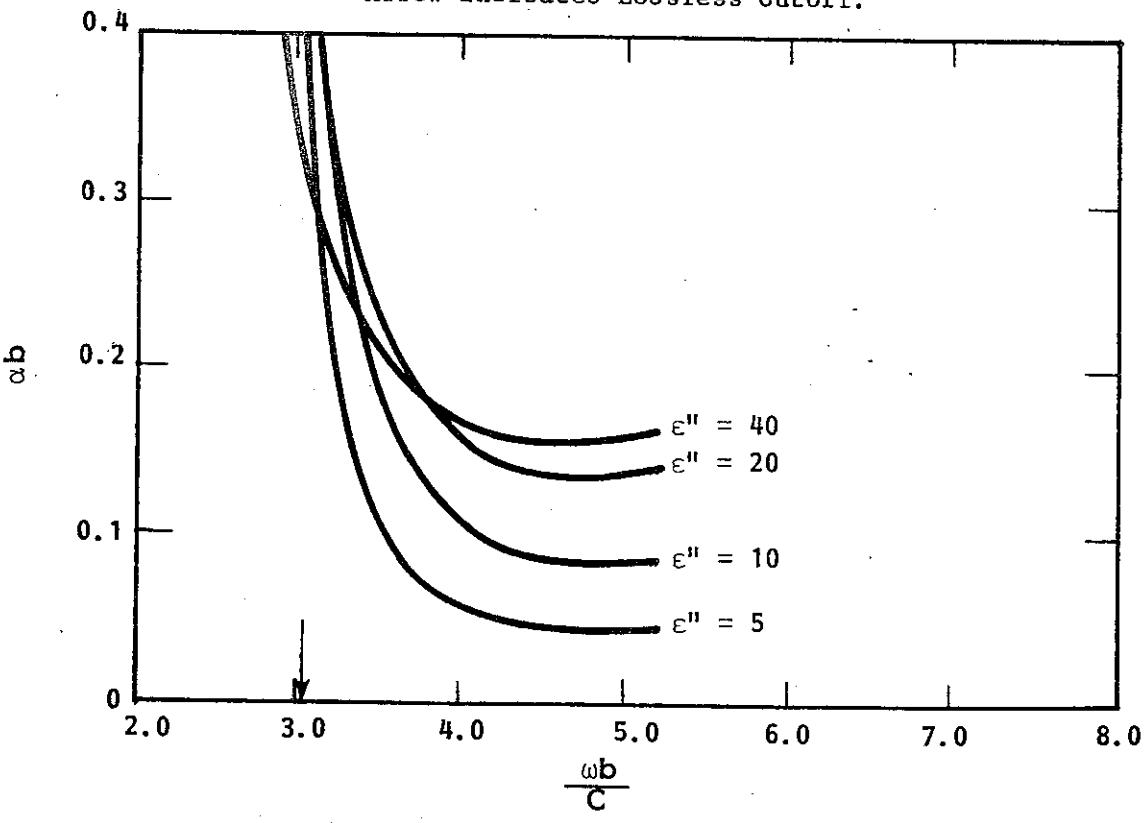

Figure 6-30. TM_{02} Attenuation vs Frequency for Various ε". Arrow Indicates Lossless Cutoff.

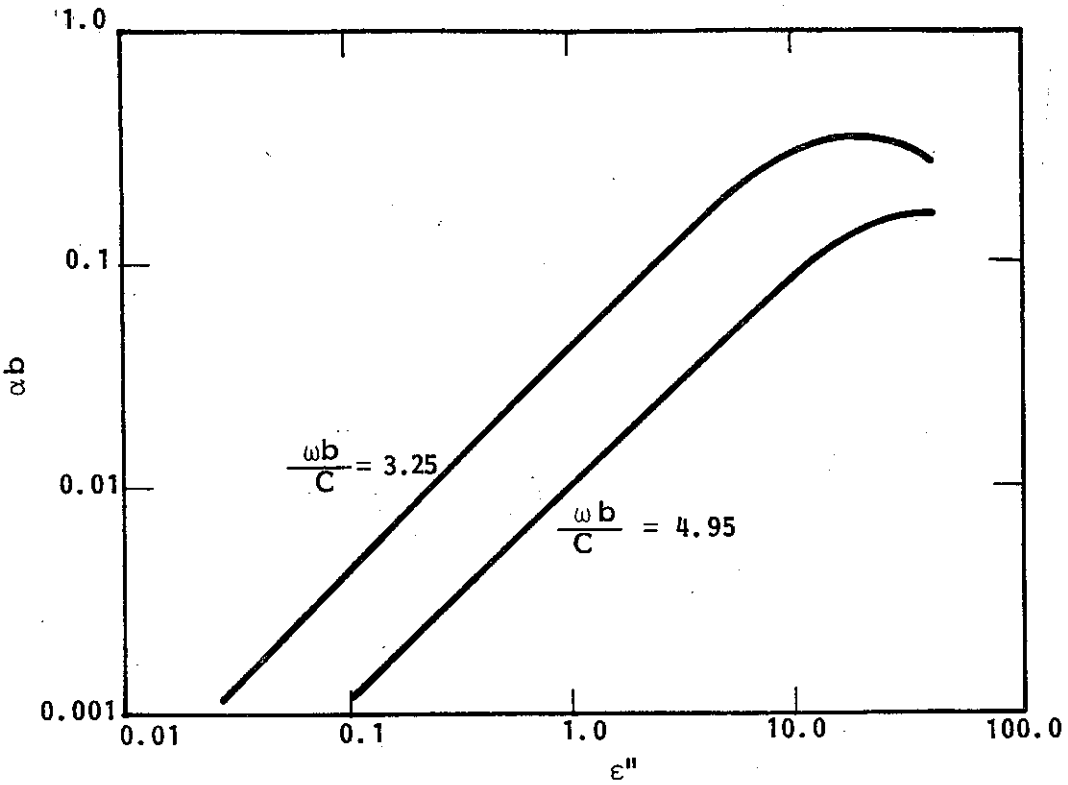

Figure 6-31. TM_{02} Attenuation vs ε" for Various Frequencies.

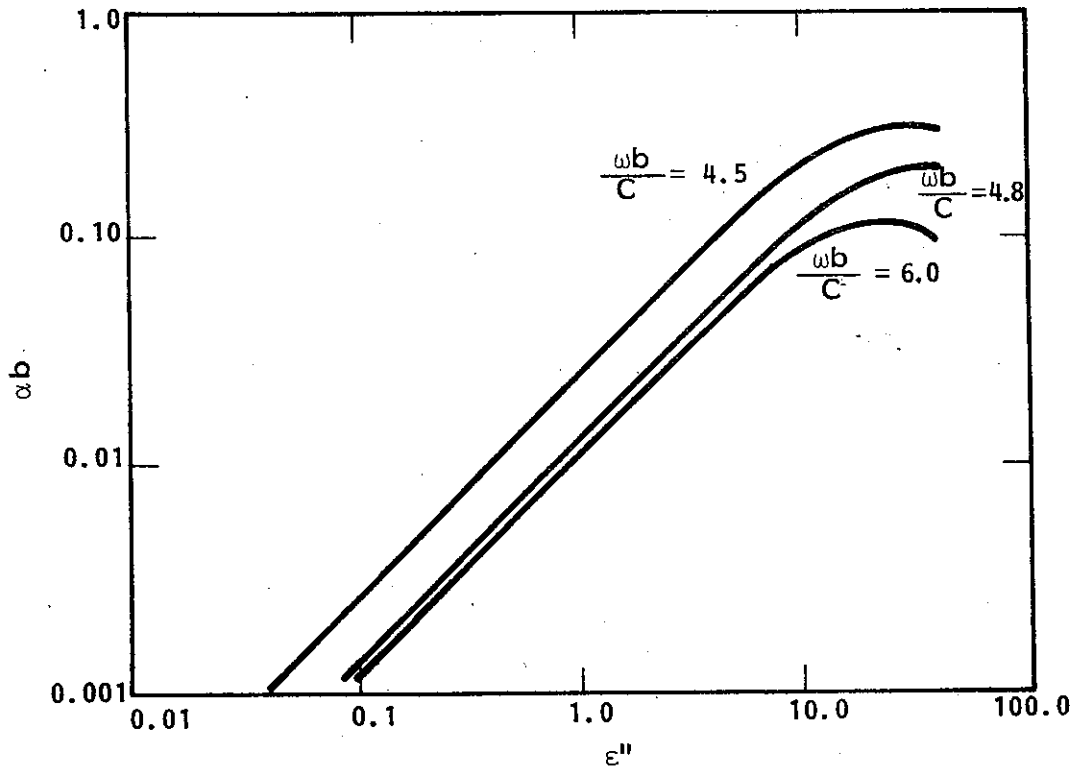

Figure 6-32. TE_{02} Attenuation vs ε" for Various Frequencies.

comparing the distributions of their waveguide fields. In Figure 6-14 the TE_{01} electric field was seen to peak inside the dielectric region. In Figure 6-33 the electric field is largest at $\rho/b = 0.4$, inside the vacuum region, and is much smaller in the dielectric. Thus, since the loss is added to a region of high field strength, the TE_{01} mode is greatly attenuated. Likewise, since the loss is added to a region of relatively low TE_{02} field strength, the TE_{02} mode is attenuated much less.

For the selected case of $\varepsilon'' = 1.15$, the TE_{02} mode experiences an attenuation of about $\alpha b = 0.016$ at $\frac{\omega b}{C} = 4.8$ (the $TE_{02}/s = 2$ intersection). This corresponds to a TE_{02} loss of 1.34 dB over the 10 cm length of the amplifier. At $\frac{\omega b}{C} = 5.1$ ($TM_{02}/s = 2$ intersection) the TM_{02} mode experiences $\alpha b = 0.01$ or about 0.84 dB of loss over the length of the amplifier. How effective this amout of loss is in suppressing oscillations depends on how much interaction occurs between the beam and these higher order modes. It is a fortunate consequence that positioning the electron beam to maximize TE_{01} interaction reduces TE_{02} interaction. The hollow beam is placed as close to the dielectric as possible, so that the electrons will experience the maximum level of the TE_{01} field strength. However, Figure 6-33 shows that this is a region of small TE_{02} field strength and so the TE_{02} interaction is correspondingly smaller.

Atlhough there is only about a 30% reflection at the output at midband ($\frac{\omega b}{C} = 3.35$), the match at higher frequencies (e.g.

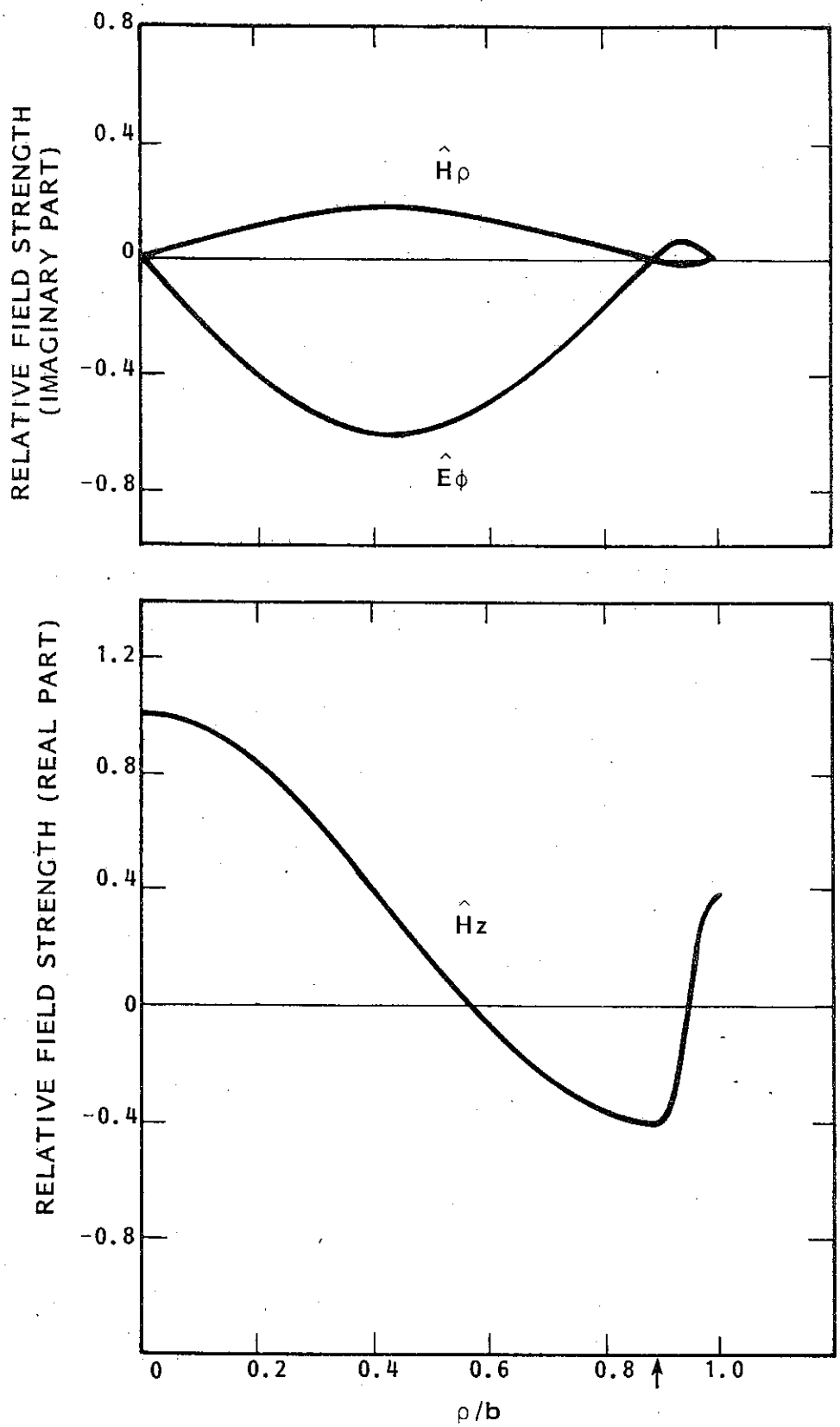

Figure 6-33. TE_{02} Field Components vs Radial Distance for $\frac{\omega b}{C} = 4.50$, $\varepsilon'' = 0$.

$\frac{\omega b}{C} = 4.8$) can be much worse. Such a situation would increase the chances of higher mode oscillation. To accurately determine if the loss experienced by the TE_{02} and TM_{02} modes will prevent their oscillating, a small signal analysis should be conducted that includes the effects of the second harmonic beamline.

F. Solution for Inherent Losses

A realistic application of the two-layer dielectric-loaded waveguide theory is to determine the amount of attenuation resulting from loss inherent to the dielectric. It is assumed that all loss is represented by the imaginary part of the dielectric constant and that it is distributed evenly throughout. The barium tetratitinate considered here has a real dielectric constant of $\varepsilon' = 38$ and a loss tangent of $\delta = \frac{\varepsilon''}{\varepsilon'} \cong 6.5 \times 10^{-4}$. Thus, a two-layer analysis can be performed with $\varepsilon_2 = \varepsilon_o (38 - j0.025)$.

Figures 6-34 and 6-35 show the attenuation which result from $\varepsilon'' = 0.025$. The curves are similar to those found for larger values of ε''. One interesting observation is that the jump in attenuation as the lossless cutoff is approached has become much steeper for this small ε''. As pointed out before, this frequency behaves more like a "true" cutoff as ε'' becomes smaller.

At midband ($\frac{\omega b}{C} = 3.35$) the TE_{01} mode has $\alpha b = 0.00905$. This corresponds to a cold circuit loss of 3.0 dB over the 15 cm total length of the amplifier (as opposed to the 10 cm length of the loss pattern). For the TM_{01} mode the loss is about 3.1 dB at the same

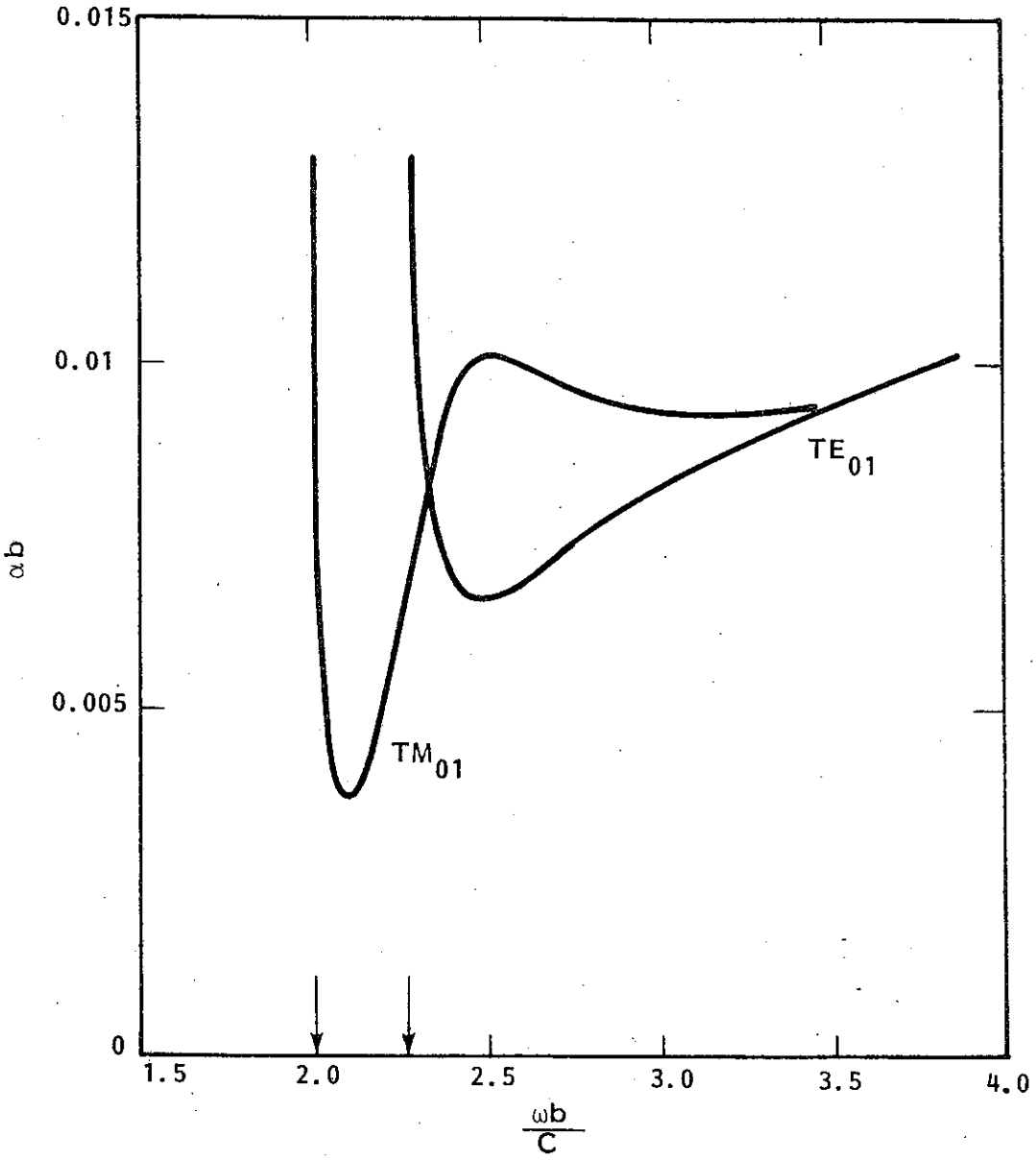

Figure 6-34. TM_{01} and TE_{01} Attenuation vs Frequency for $\varepsilon'' = 0.025$. Arrows Indicate Cutoff Frequencies.

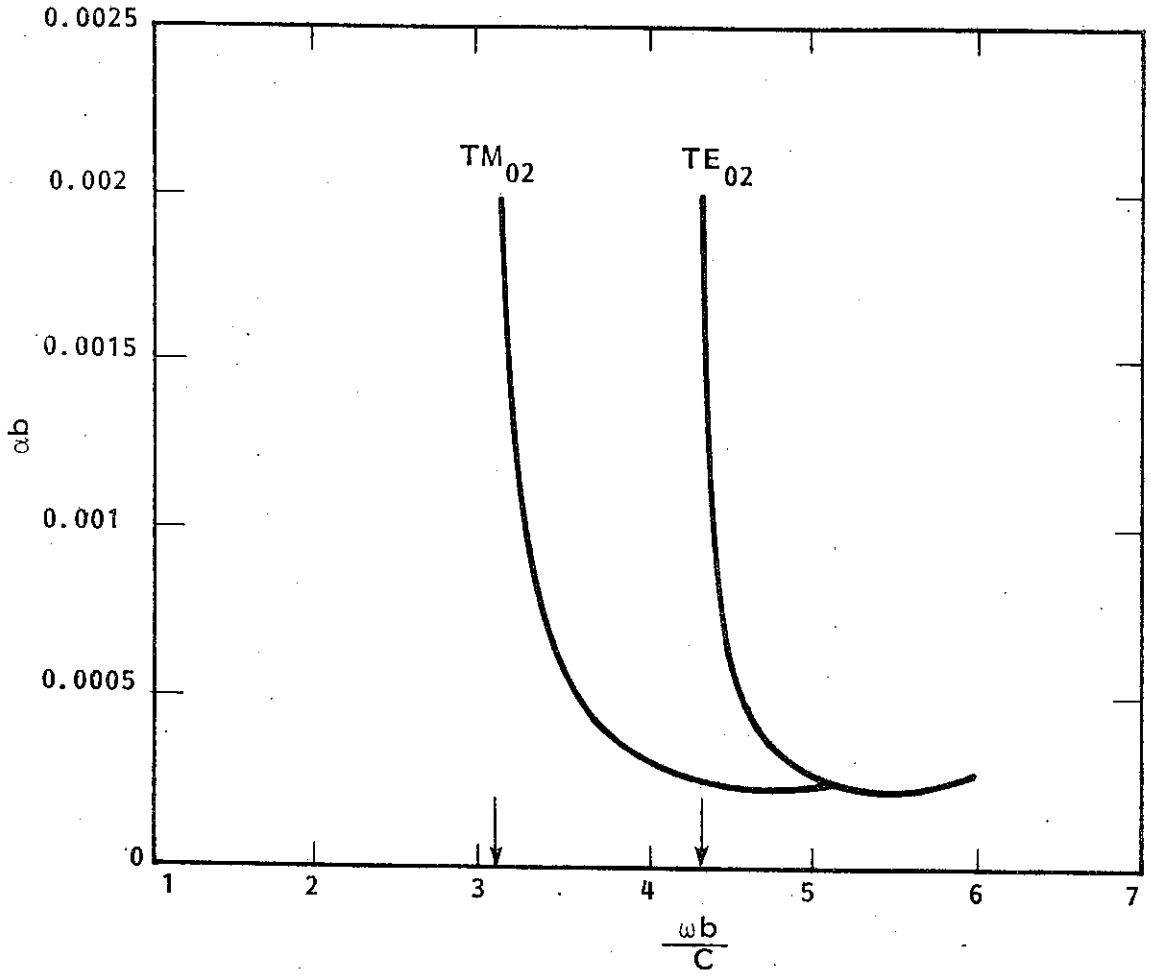

Figure 6-35. TM_{02} and TE_{02} Attenuation vs Frequency for $\varepsilon'' = 0.025$. Arrows Indicate Cutoff Frequencies.

frequency. This is a surprisingly large amount of loss for those accustomed to dealing with losses associated with an empty waveguide. As expected, the TE_{02} and TM_{02} modes experience much smaller losses. At $\frac{\omega b}{C} = 5.0$, the TE_{02} mode will have a loss of 0.09 dB and the TM_{02} mode 0.08 dB, each over a length of 15 cm.

G. Validity of the Two-Layer Model

The two-layer model makes many assumptions which are necessary to make a complicated problem tractable. Some of these are fairly standard, such as assuming an infinite length waveguide with perfectly-conducting, infinitely-thin walls. Others seem to be less justified. It was assumed that a third, very thin, highly conductive layer added to the inside of the dielectric could be modelled as if all of its loss where distributed evely throughout the dielectric layer. This simplified the problem a great deal, but only at the cost of losing all knowledge of the physical structure of the third layer. So even though it was learned that a dielectric layer with $\varepsilon'' = 1.15$ will adequately prevent oscillations, there is no way to translate this into a thickness and conductivity of the third layer. Experimental evidence might be helpful here, but it is evident that a true three-layer analysis is needed.

A second problem arises from the simplistic assumption that ε'' does not vary with frequency. Although this may be more or less true when considering a narrow range of frequencies, as ω gets smaller ε'' is certain to be quite different. This actual dependence on frequency, though, is not easily seen. This is because ε'' is not a true physical quantity but rather an invented factor -- the result of

combining two very different layers. The thin lossy layer would probably be composed of a graphite-like substance and, thus, would have its own ε'' of $\frac{\sigma}{\omega\varepsilon_o}$, where σ (the conductivity of the substance) is also a function of frequency. The dielectric layer has its own intrinsic loss, and its ε' and ε'' must obey the Kronig-Kramers relations. How these factors all combine to give a single ε'' and how this ε'' varies with frequency is not immediately evident. Perhaps it is best, then, to consider only the results from the frequency band of interest, $\frac{\omega b}{c}$ = 2.95 to 3.75, where ε'' should not have a strong dependence on frequency.

Although it is true that the two-layer model is not the most accurate way to present a three-layer lossy waveguide, its analysis does provide a wealth of qualitative information. It has been learned that the addition of loss in a sufficient amount to suppress TE_{01}-mode oscillations does not seriously affect either the phase constant of the wave or the rf magnetic fields in the guide. Thus, interaction between the beam and the wave is not seriously threatened. It has been learned that the TE_{02} and TM_{02} waves are not as strongly attenuated as the TE_{01} wave for a given amount of loss. Also, the manner in which the attenuation varies with relative changes in loss has been determined.

The two-layer model must be viewed in the appropriate manner. It is an easy, simplistic, but not highly accurate way to gain a great deal of insight into the behavior of wave propagating in the three-layer lossy dielectric waveguide.

VII. THREE-LAYER GRAPHITE MODEL

A. Formulation

A thin, very lossy layer of material is added to the inside of the dielectric loaded waveguide shown in Figure 3-1. This layer will most likely be composed of graphite or some graphite-like substance and so can be modelled as a lossy dielectric having a complex scalar permittivity $\varepsilon = (\varepsilon' - j\,\varepsilon'')\,\varepsilon_o$. The real part of $\varepsilon/\varepsilon_o$ is assumed to be unity, while the imaginary part is a function of σ, the conductivity of the material:

$$\varepsilon'' = \frac{\sigma}{\omega\varepsilon_o} \quad . \tag{7.1}$$

The geometry of this model is shown in Figure 7-1.

Analysis of the three-layer model has two important goals. First, it is desired to find the attenuation that would result from a thin lossy charge suppression layer, and the layer's affect on the phase constant of a propagating wave. Second, the necessary thickness and conductivity of a layer used to prevent oscillations need to be determined.

Due to the complex nature of the three-layer analysis only the TE_{01} mode will be considered in detail, though some abbreviated results for the TE_{02} mode will also be presented. A complete derivation of the three-layer dispersion equation, relating the axial propagation constant and the frequency, is given in Appendix One. As with the two-layer dispersion equation only the azimuthally symmetric

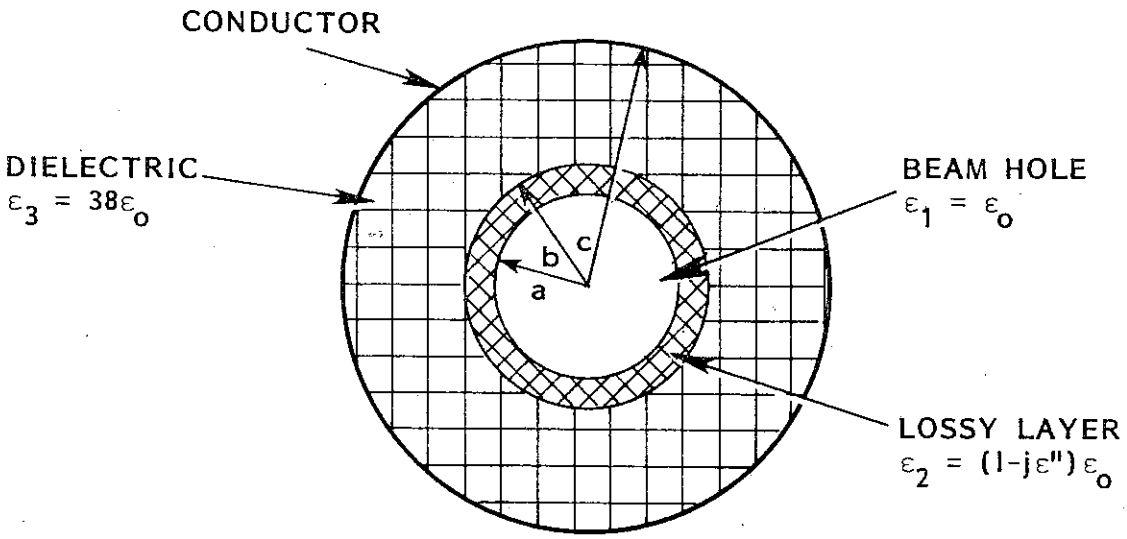

Figure 7-1. Geometry of the Three-Layer Dielectric Loaded Waveguide Model.

(n = 0) modes are considered. For the TE_{0m} modes equation (A1.31) can be rearranged to yield the dispersion relation:

$$\left[\frac{k\rho_2\ \mu_1\ U_1'}{k\rho_1\ \mu_2\ U_1}\ U_2-U_2'\right]\left[\frac{k\rho_3\ \mu_2\ f_3}{k\rho_2\ \mu_3\ f_4}\ U_5-U_5'\right]-\left[\frac{k\rho_2\ \mu_1\ U_1'}{k\rho_1\ \mu_2\ U_1}\ U_3-U_3'\right]\cdot$$

$$\cdot\left[\frac{k\rho_3\ \mu_2\ f_3}{k\rho_2\ \mu_3\ f_4}\ U_4-U_4'\right]=0 \qquad (7.2)$$

where: $k\rho_1 = \omega^2\ \mu_1\ \varepsilon_1 - k_z^2$

$k\rho_2 = \omega^2\ \mu_2\ \varepsilon_2 - k_z^2$

$k\rho_3 = \omega^2\ \mu_3\ \varepsilon_3 - k_z^2$

$U_1 = J_o\ (k\rho_1\ a) \quad U_1' = J_o'\ (k\rho_1\ a)$

$U_2 = J_o\ (k\rho_2\ a)$ etc.

$U_3 = Y_o\ (k\rho_2\ a)$

$U_4 = J_o\ (k\rho_2\ b)$

$U_5 = Y_o\ (k\rho_2\ b)$

$f_3 = J_o\ (k\rho_3\ b)\ Y_o'\ (k\rho_3\ c) - Y_o\ (k\rho_3\ b)\ J_o'\ (k\rho_3\ c).$

$f_4 = J_o'\ (k\rho_3\ b)\ Y_o'\ (k\rho_3\ c) - Y_o'\ (k\rho_3\ b)\ J_o'\ (k\rho_3\ c).$

This equation is solved for the complex propagation constant at a given real value of frequency. Normalized parameters are again used: αc and βc are computed from values of $\frac{\omega c}{C}$, $\frac{a}{c}$, and $\frac{b}{c}$. In this analysis it is assumed that $\mu_{1R} = \mu_{2R} = \mu_{3R} = 1$, $\varepsilon_{2R} = 1 - j\,\varepsilon''$, and $\varepsilon_{3R} = 38$. The thickness of the dielectric is determined by $\frac{b}{c} = 0.892$ while $\frac{a}{c}$ and ε'' are allowed to vary.

The conductivity of a typical graphite sample at microwave frequencies is about $\sigma = 7 \times 10^4$ $\mho$/m. For a frequency of 41 GHz, equation (7.1) yields a relative dielectric constant of $\varepsilon_{2R} = (1 - j31000)$. This extremely large value of ε_2 can lead to severe computational problems when trying to solve (7.2). Evaluation of $J_o\ (a + jb)$ gives an answer roughly proportional to exp (b). Thus, having a dielectric constant on the order of 3×10^4 risks computer overflow, roundoff errors, and serious difficulty in the convergence of complex root-finding routines. In fact, the computer may be asked to handle numbers as large as exp (1000) $\cong 10^{434}$ and as small as 1 at the same time.

These problems can be avoided by not calculating $J_o\ (a + jb)$ directly. Instead, the asymptotic expansions for J_o and Y_o can be substituted directly into the dispersion relation, and it can be manipulated algebraically until a more computer-oriented form is obtained.

The asymptotic expansions for Bessel functions of large argument are given by:

$$J_n\ (z) \cong \sqrt{\frac{2}{\pi z}}\ [P\cos\ (\chi) - Q\sin\ (\chi)]$$

$$Y_n\ (z) \cong \sqrt{\frac{2}{\pi z}}\ [P\sin\ (\chi) - Q\cos\ (\chi)] \qquad (7.3)$$

where: $\chi = z - (2n + 1)\ \frac{\pi}{4} = x + jy.$

The terms P and Q are found from the infinite series:

$$P = \sum_{\ell=0}^{\infty} P_\ell \qquad Q = \sum_{\ell=0}^{\infty} Q_\ell \tag{7.4}$$

where: $P_o = 1,\ P_i = -P_{i-1} \cdot \dfrac{\left(\mu_n - [4i-3]^2\right)\left(\mu_n - [4i-1]^2\right)}{(2i)\ (2i-1)\ (8z)^2}$

$$Q_o = \frac{\mu_n - 1}{8z},\ Q_i = -Q_{i-1} \cdot \frac{\left(\mu_n - [4i-1]^2\right)\left(\mu_n - [4i+1]^2\right)}{(2i)\ (2i+1)\ (8z)^2}$$

and: $\mu_n = 4\ n^2.$

The sines and cosines in equation (7.3) can be written as:

$$\begin{aligned} \sin(\chi) &= \sin(x)\cosh(y) + j\cos(x)\sinh(y) \\ \cos(\chi) &= \cos(x)\cosh(y) - j\sin(x)\sinh(y), \end{aligned} \tag{7.5}$$

and thus the Bessel function expansions become:

$$\begin{aligned} J_n(z) &\cong \sqrt{\frac{2}{\pi z}}\ [CA - j\ SB] \\ Y_n(z) &\cong \sqrt{\frac{2}{\pi z}}\ [CB + j\ SA] \end{aligned} \tag{7.6}$$

where: $A = P\cos(x) - Q\sin(y) \qquad C = \cosh(y)$

$B = P\sin(x) + Q\cos(y) \qquad S = \sinh(y).$

The dispersion equation (7.2) can be written as:

$$[M_1\ U_2 - U_2']\ [M_2\ U_5 - U_5'] - [M_2\ U_3 - U_3']\ [M_2\ U_4 - U_4'] = 0 \tag{7.7}$$

where: $M_1 = \dfrac{k_{\rho 2}\ \mu_1\ U_1'}{k_{\rho 1}\ \mu_2\ U_1}$

$$M_2 = \frac{k_{\rho 3}\ \mu_2\ f_3}{k_{\rho 2}\ \mu_3\ f_4}.$$

Now, letting:

$$z_1 = k\rho_2\, a = x_1 + j\, y_1$$
$$z_2 = k\rho_2\, b = x_2 + j\, y_2 \qquad (7.8)$$

and:

$$A_1 = P_1 \cos(x_1) - Q_1 \sin(x_1) \qquad A_2 = P_2 \cos(x_2) - Q_2 \sin(x_2)$$
$$B_1 = P_1 \sin(x_1) + Q_1 \cos(x_1) \qquad B_2 = P_2 \sin(x_2) + Q_2 \cos(x_2) \qquad (7.9)$$
$$C_1 = \cosh(y_1) \qquad C_2 = \cosh(y_2)$$
$$S_1 = \sinh(y_1) \qquad S_2 = \sinh(y_2)$$

Then:

$$U_2 \cong \sqrt{\frac{2}{\pi z_1}}\,[C_1 A_1 - j\, S_1 B_1] \qquad U_4 \cong \sqrt{\frac{2}{\pi z_2}}\,[C_2 A_2 - j\, S_2 B_2]$$
$$U_3 \cong \sqrt{\frac{2}{\pi z_1}}\,[C_1 B_1 + j\, S_1 A_1] \qquad U_5 \cong \sqrt{\frac{2}{\pi z_2}}\,[C_2 B_2 + j\, S_2 A_2]. \qquad (7.10)$$

The Bessel function derivatives U_2', U_3', U_4', and U_5' can be found by employing the recursion relations for J_n and Y_n. From these it is found that:

$$J_n'(z) \cong \sqrt{\frac{2}{\pi z}}\,[CA' - j\, SB']$$
$$Y_n'(z) \cong \sqrt{\frac{2}{\pi z}}\,[CB' + j\, SA'] \qquad (7.11)$$

where:
$$A'(n, z) = \frac{n}{z} A(n, z) - A(n + 1, z)$$
$$B'(n, z) = \frac{n}{z} B(n, z) - B(n + 1, z).$$

These asymptotic expansions for the Bessel functions and their derivatives can now be substituted into the dispersion equation (7.7). Multiplying this out and using the relations:

$$\sinh (y_1 - y_2) = S_1 C_2 - C_1 S_2 \qquad (7.12)$$

$$\cosh (y_1 - y_2) = C_1 C_2 - S_1 S_2$$

yields the new form of the TE_{0m} dispersion equation:

$$\begin{aligned} &M_1 M_2 [(A_1 B_2' - A_2' B_1) - j (A_1 A_2' + B_1 B_2') \tanh (y_1 - Y_2)] \\ &+ M_1 [(A_2 B_1 - A_1 B_2) + j (A_1 A_2 + B_1 B_2) \tanh (y_1 - y_2)] \\ &+ M_2 [(A_2' B_1' - A_1' B_2') + j (A_1' A_2' + B_1' B_2') \tanh (y_1 - y_2)] \\ &+ \quad [(A_1' B_2 - B_1' A_2) - j (A_1' A_2 + B_1' B_2) \tanh (y_1 - y_2)] = 0 \end{aligned} \qquad (7.13)$$

with the new values of M_1 and M_2:

$$M_1 = \frac{k\rho_2 \mu_1}{k\rho_1 \mu_2} \cdot \frac{A_o' - j B_o' \tanh (y_o)}{A_o - j B_o \tanh (y_o)} \qquad (7.14)$$

$$M_2 = \frac{k\rho_3 \mu_2}{k\rho_2 \mu_3} \cdot \frac{(A_3 B_4' - B_3 A_4') - j (A_3 A_4' + B_3 B_4') \tanh (y_3 - y_4)}{(A_3' B_4' - B_3' A_4') - j (A_3' A_4' + B_3' B_4') \tanh (y_3 - y_4)}$$

where: $z_o = k\rho_1 a = x_o + j y_o$

$z_3 = k\rho_3 b = x_3 + j y_3$

$z_4 = k\rho_3 c = x_4 + j y_4$

Although equation (7.13) seems much more complicated than (7.2), it is far easier to implement on the computer. The tanh function is readily available on most systems and as long as all fractions are cleared of their denominators, (7.13) should not be prone to overflow or roundoff errors. Equation (7.13) also has the added benefit of extremely rapid convergence.

B. Solution for TE_{01} Mode

Equation (7.13) has been solved numerically (as described in Appendix Five) for the case of m = 1, giving solutions for the TE_{01} mode. Figures 7-2, 7-3, and 7-4 plot resulting values of attenuation against the relative thickness of the lossy layer for various ε'' at frequencies of $\frac{\omega c}{C}$ = 2.95, 3.35, and 3.75. The general trend of these curves is for attenuation to rise sharply as the lossy thickness is increased from zero, then slowly level off. As the thickness is increased much further, it appears to reach a point beyond which attenuation does not increase appreciably. This point is a definite function of frequency, being reached sooner at higher $\frac{\omega c}{C}$. Some insight into this effect can be gained by looking at the field plots of the lossless two-layer waveguide shown in Figures 6-14, 6-15, and 6-16.

The electric field in the two-layer guide, E_ϕ, is seen to be largest near the dielectric liner and then to fall rapidly to zero at the axis. When a thin lossy sleeve is placed inside the dielectric, it is exposed to maximum electric field. As its thickness is increased the layer encompasses more and more electric field until any further increase takes in relatively little field. This point corresponds to the thickness at which the attenuation levels out. The field plots also show a dependence of E_ϕ shape on frequency. The higher the frequency, the quicker E_ϕ falls toward zero and the sooner the attenuation levels off.

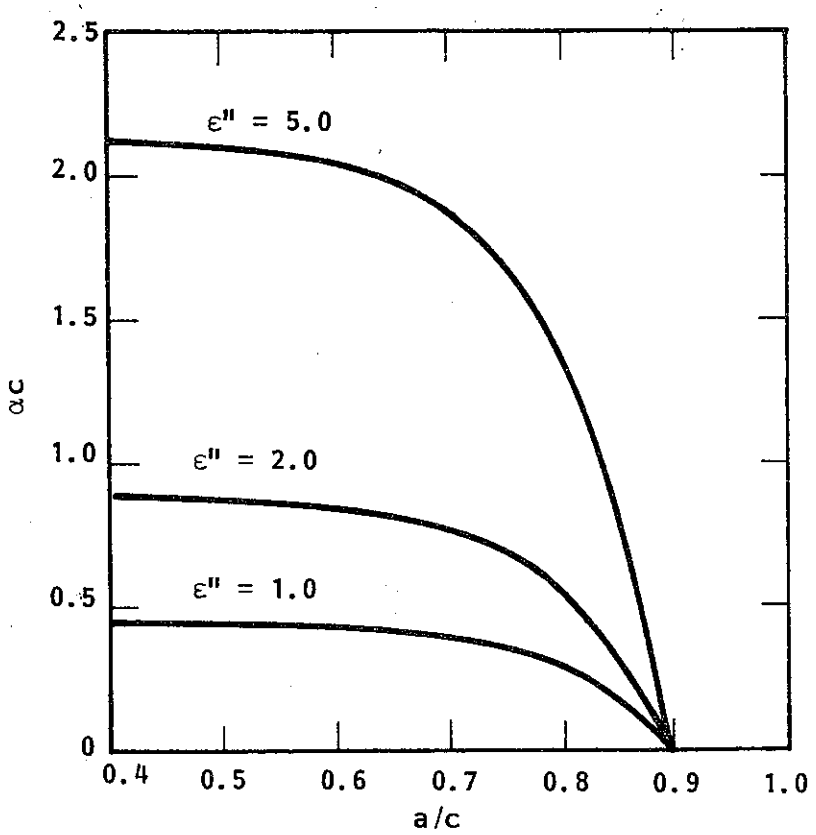

Figure 7-2. TE_{01} Attenuation vs Relative Thickness for $\frac{\omega c}{C}$ = 2.95 and various ε".

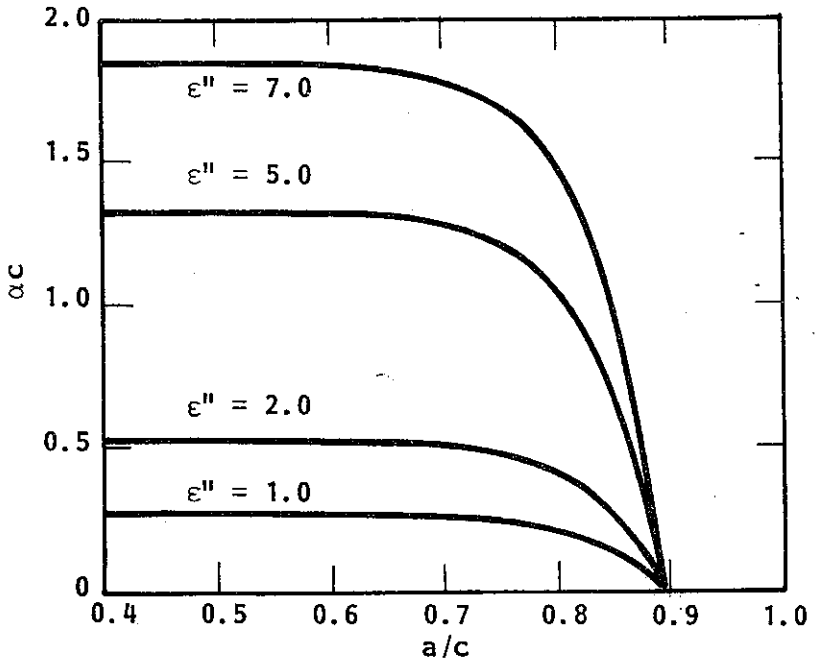

Figure 7-3. TE_{01} Attenuation vs Relative Thickness for $\frac{\omega c}{C}$ = 3.35 and various ε".

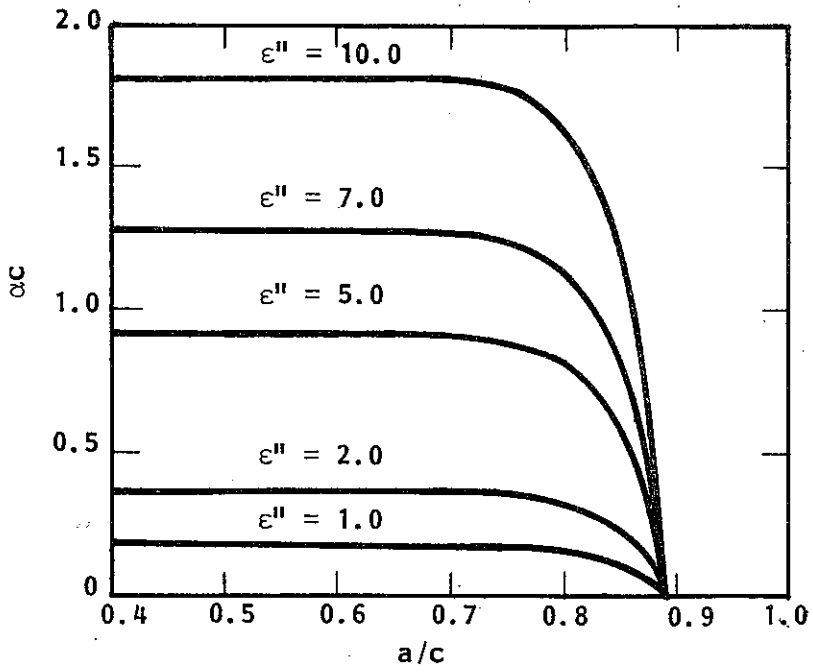

Figure 7-4. TE_{01} Attenuation vs Relative Thickness for $\frac{\omega c}{C}$ = 3.75 and Various ε".

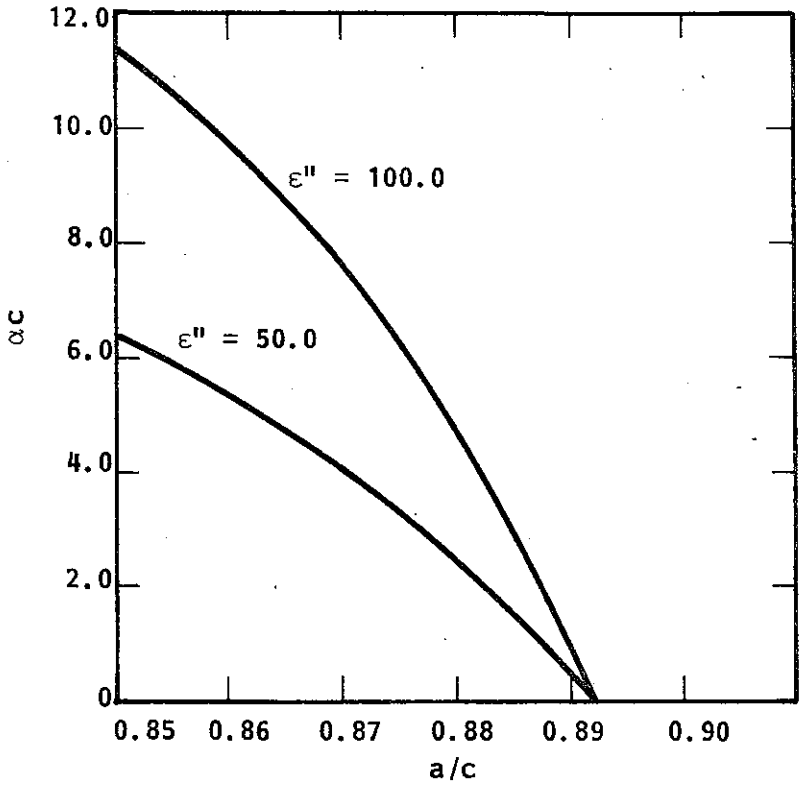

Figure 7-5. TE_{01} Attenuation vs Relative Thickness for $\frac{\omega c}{C}$ = 2.95 and ε" = 50, 100.

Figures 7-2, 7-3, and 7-4 show a definite dependence of attenuation on frequency. For a given value of ε'', the maximum attenuation decreases with increasing frequency. This is contrary to what was found using the two-layer theory. The two-layer case showed a trend of slightly increasing attenuation with increasing frequency.

Figures 7-5, 7-6, and 7-7 show plots of attenuation vs relative thickness for values of $\varepsilon'' = 50$ and 100. It is apparent that a/c is becoming a very cumbersome parameter at higher ε''. Thus, a new parameter is defined: $w = \frac{b}{c} - \frac{a}{c}$. Here w is actually the width (thickness) of the lossy layer normalized to the outer guide radius. This is much easier to visualize than a/c.

Figures 7-8 through 7-16 are plots of attenuation vs w for a wide variety of ε'' up to 50,000. In the range of $\varepsilon'' = 200$ or greater it appears that, for $\alpha c < 5.0$, w and αc are related in a nearly linear manner. Looking back at Figure 7-2 it is seen that this region corresponds to the portion of the graph very near a/c = 0.892. At this point αc is rapdily increasing with a/c, and has not yet begun to level out. This can be viewed as the "linear" region of the attenuation, where the slope $\frac{\partial(\alpha c)}{\partial(a/c)}$ is relatively constant.

Figures 7-8 through 7-16 also show a linear relationship between ε'' and αc. Doubling ε'' at a given frequency and thickness in the linear region also doubles αc. The overall relationship between αc, w, and ε'' is shown in a very convenient form in Figure 7-17. Here values of w and ε'' are plotted to give a certain αc.

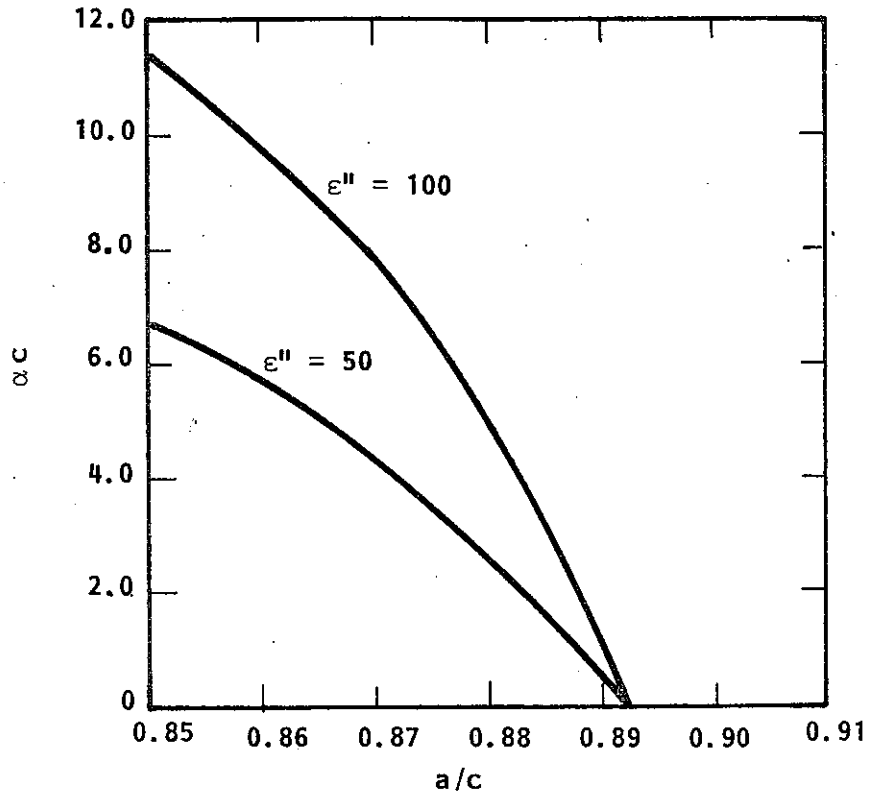

Figure 7-6. TE_{01} Attenuation vs Relative Thickness for $\frac{\omega c}{C} = 3.35$ and $\varepsilon'' = 50, 100$.

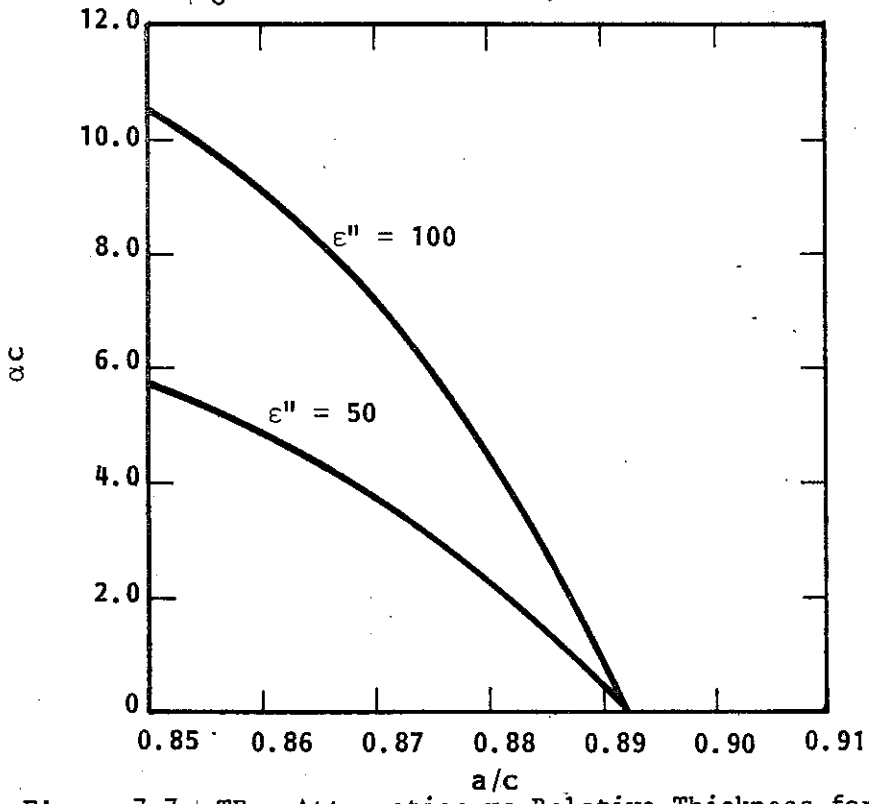

Figure 7-7. TE_{01} Attenuation vs Relative Thickness for $\frac{\omega c}{C} = 3.75$ and $\varepsilon'' = 50, 100$.

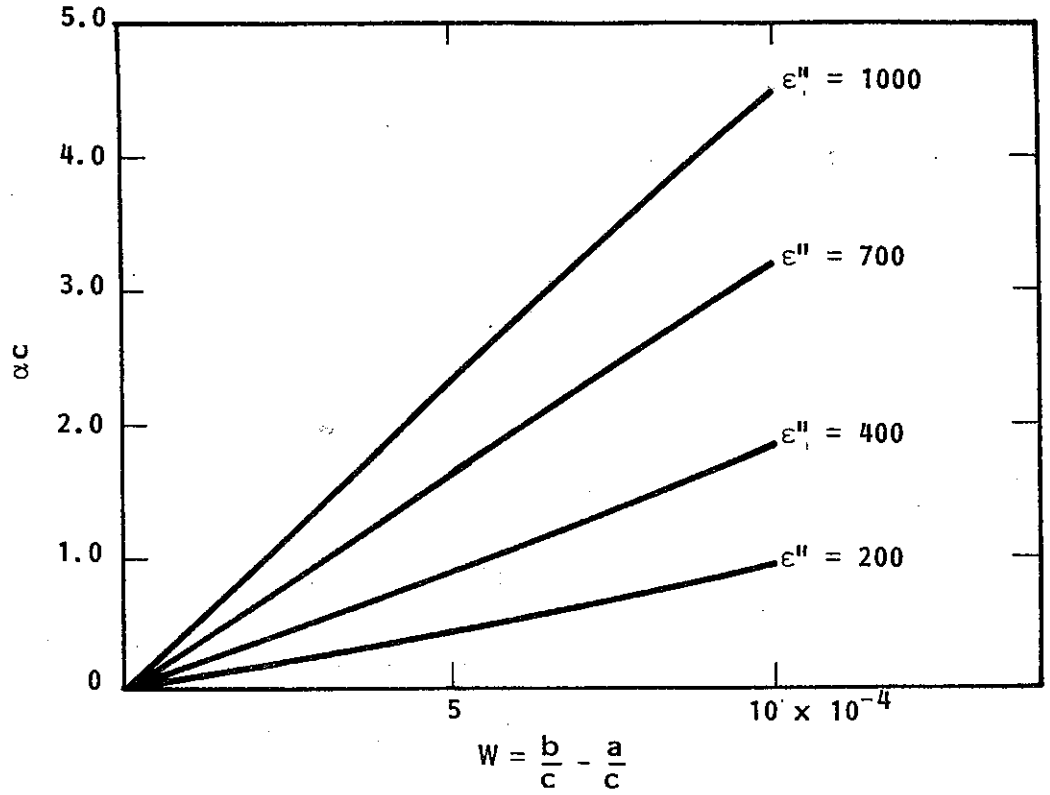

Figure 7-8. TE_{01} Attenuation vs Relative Thickness for $\frac{\omega c}{C}$ = 2.95 and Various ε".

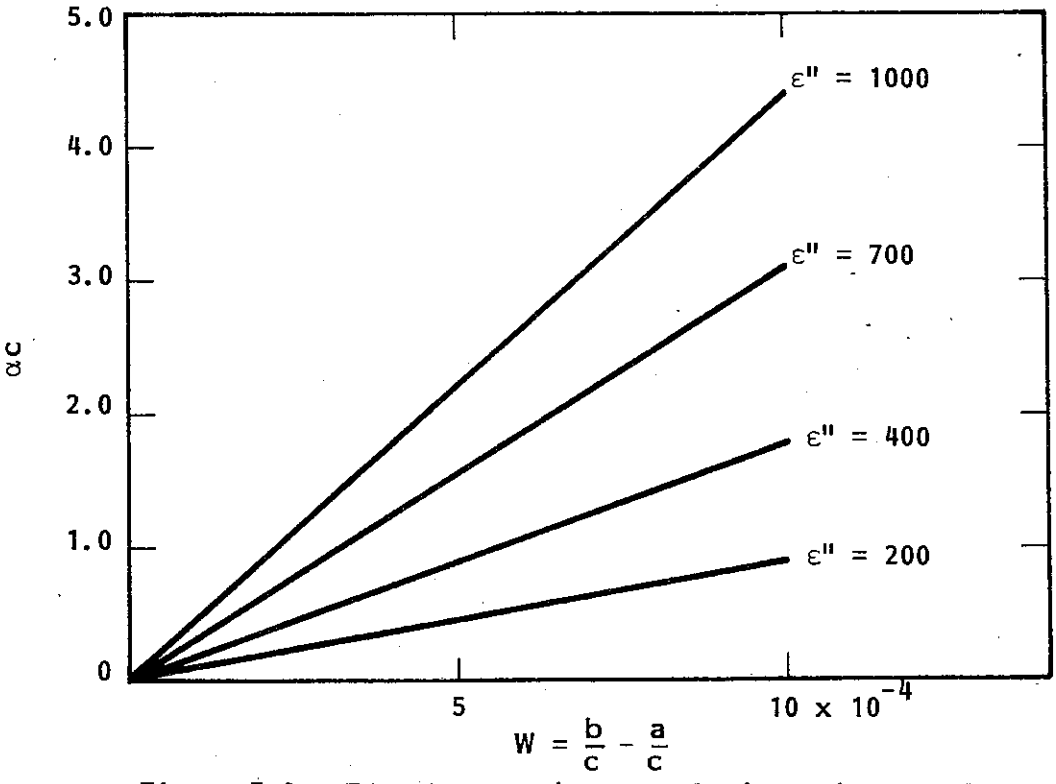

Figure 7-9. TE_{01} Attenuation vs Relative Thickness for $\frac{\omega c}{C}$ = 3.35 and Various ε".

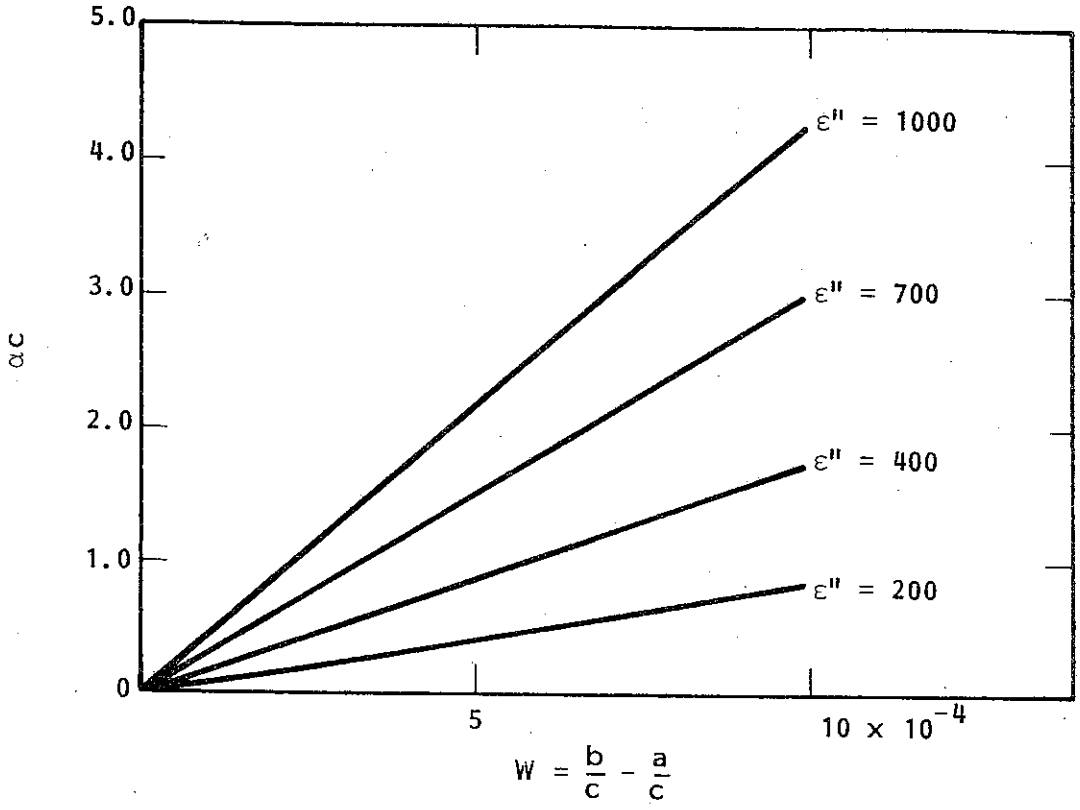

Figure 7-10. TE_{01} Attenuation vs Relative Thickness for $\frac{\omega c}{C} = 3.75$ and Various ε''.

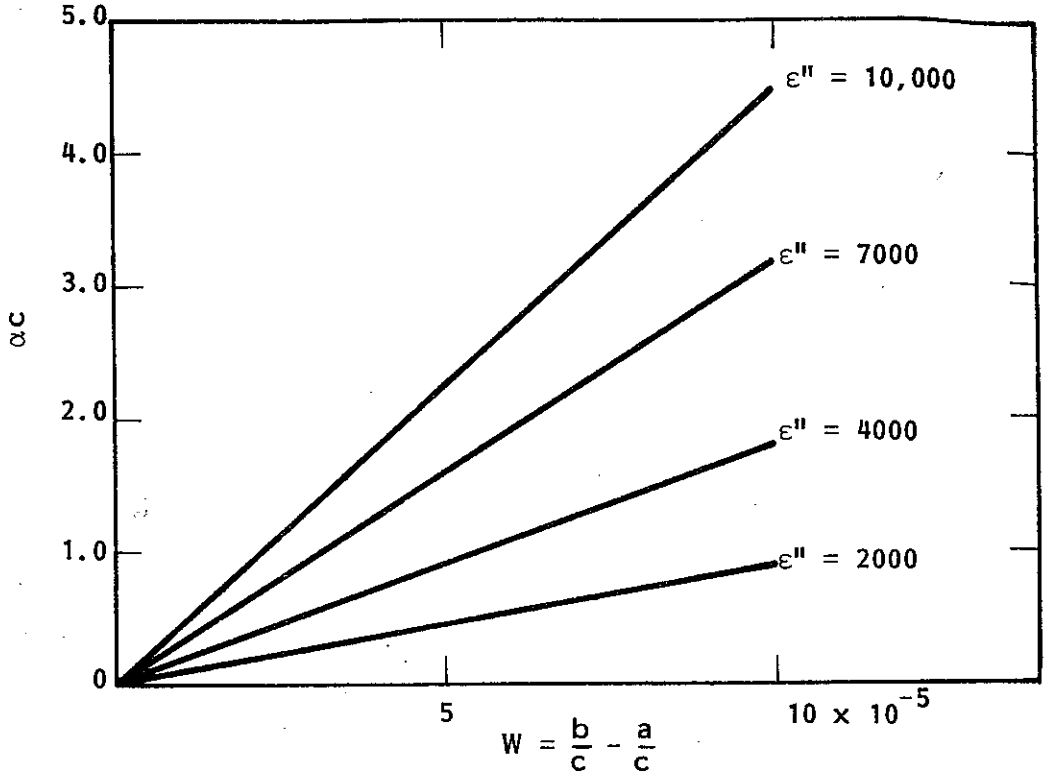

Figure 7-11. TE_{01} Attenuation vs Relative Thickness for $\frac{\omega c}{C}$ = 2.95 and Various ε".

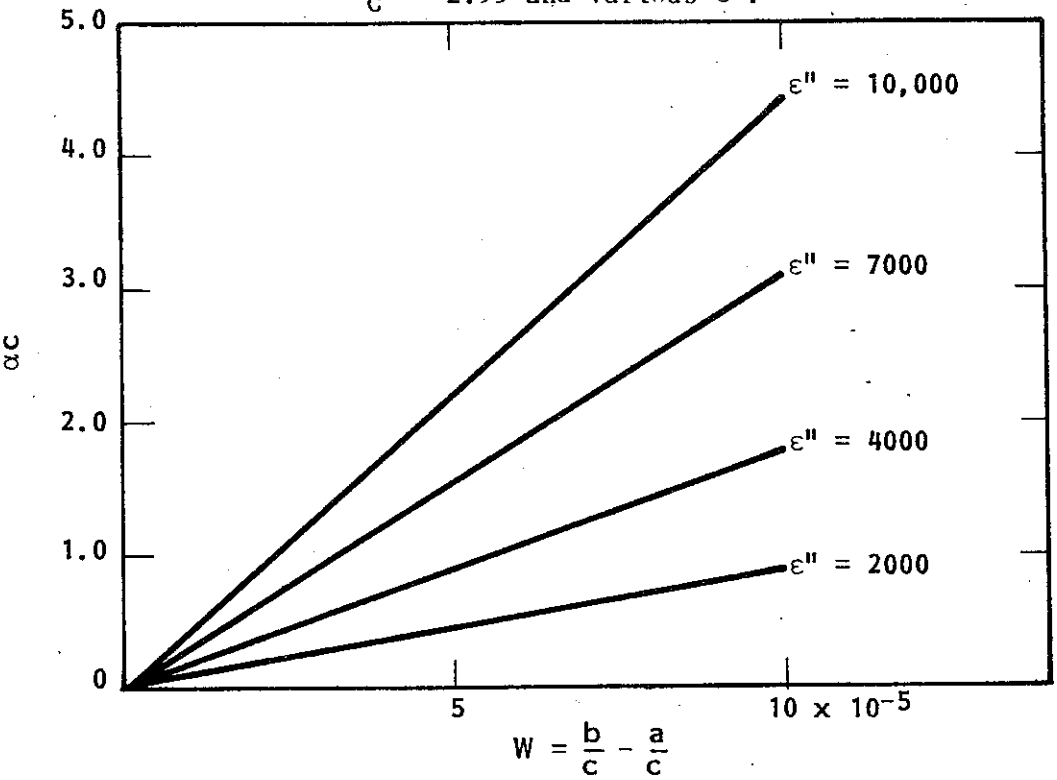

Figure 7-12. TE_{01} Attenuation vs Relative Thickness for $\frac{\omega c}{C}$ = 3.35 and Various ε".

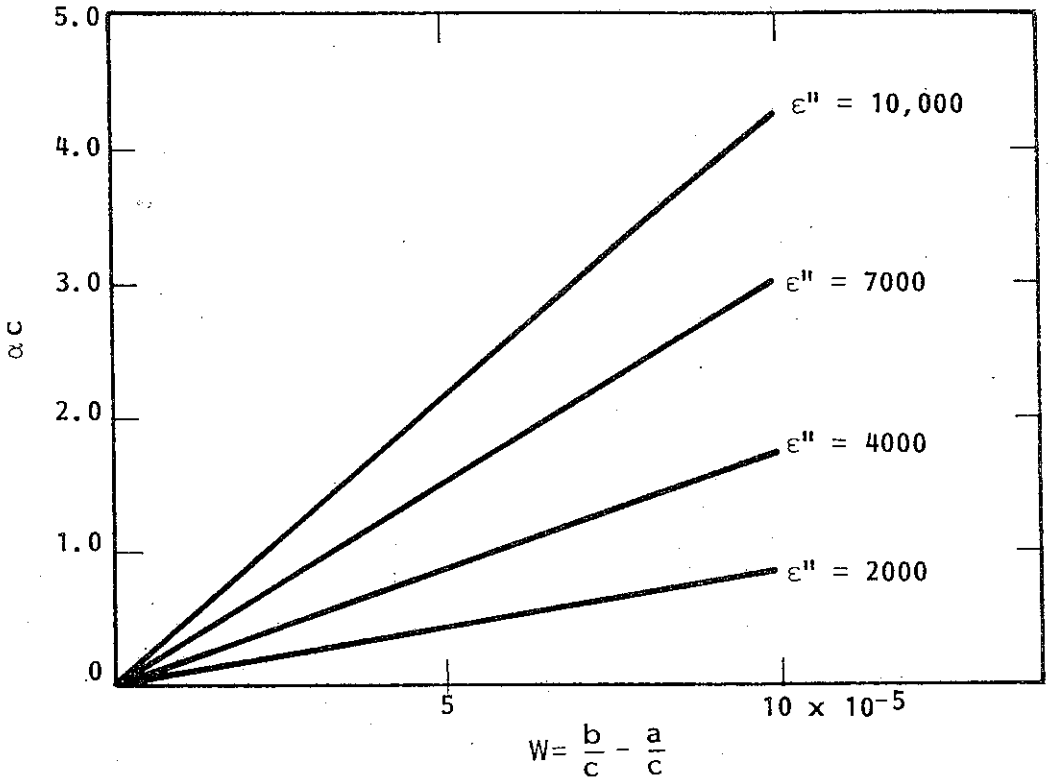

Figure 7-13. TE_{01} Attenuation vs Relative Thickness for $\frac{\omega c}{C}$ = 3.75 and Various ε".

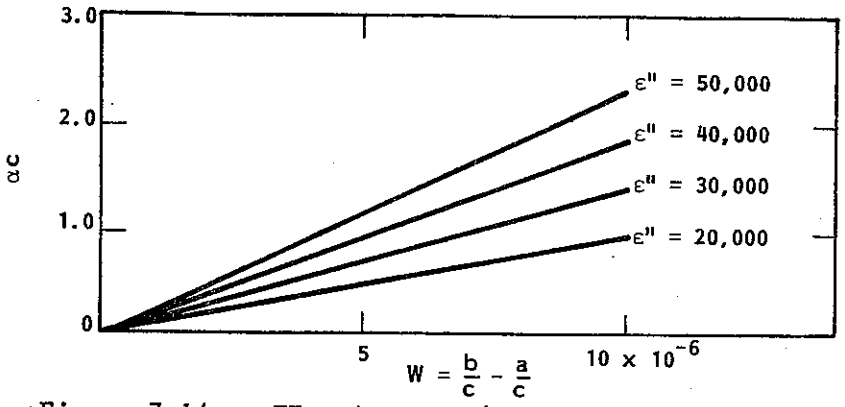

Figure 7-14. TE_{01} Attenuation vs Relative Thickness for $\frac{\omega c}{C}$ = 2.95 and Various ε".

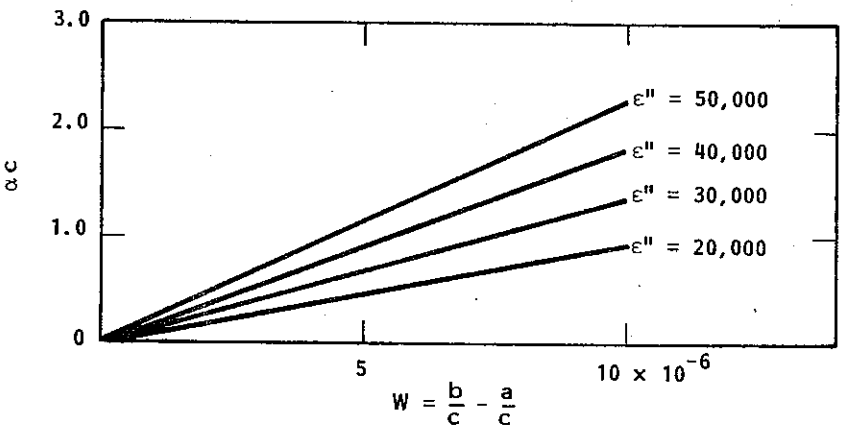

Figure 7-15. TE_{01} Attenuation vs Relative Thickness for $\frac{\omega c}{C}$ = 3.35 and Various ε".

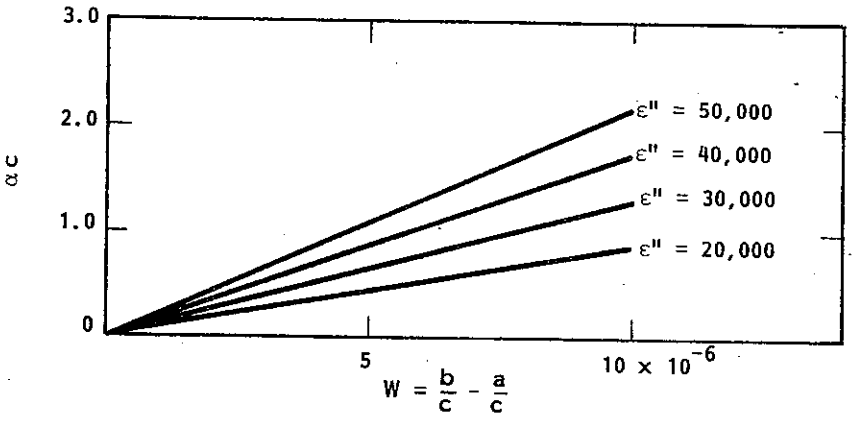

Figure 7-16. TE_{01} Attenuation vs Relative Thickness for $\frac{\omega c}{C}$ = 3.75 and Various ε".

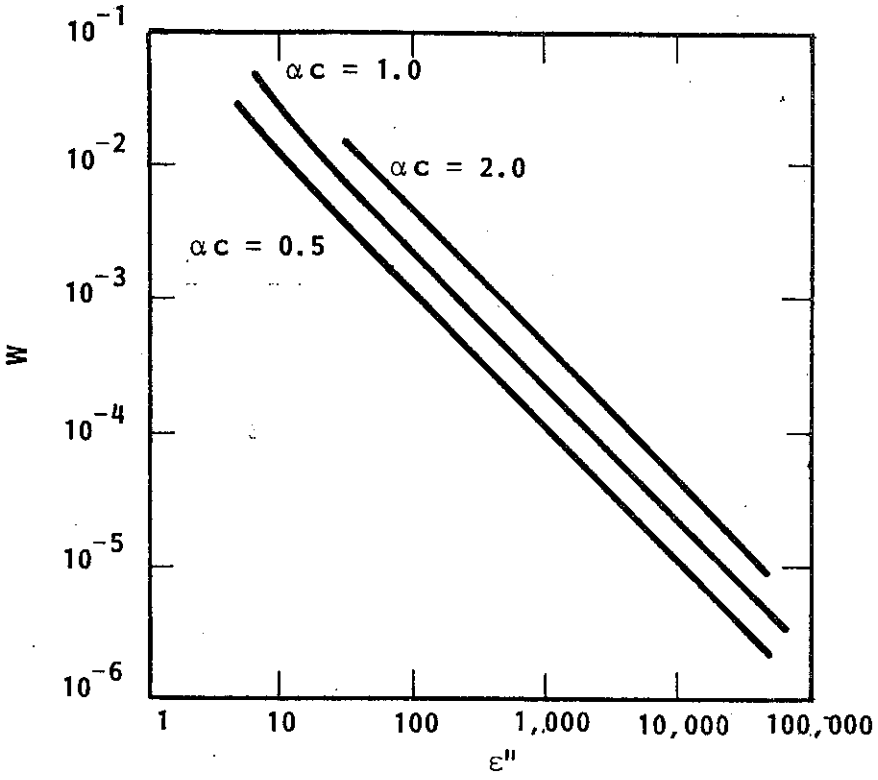

Figure 7-17. Proper Choice of w and ε" to Give a Certain Value of TE_{01} Attenuation. $\frac{\omega c}{C} = 3.35$.

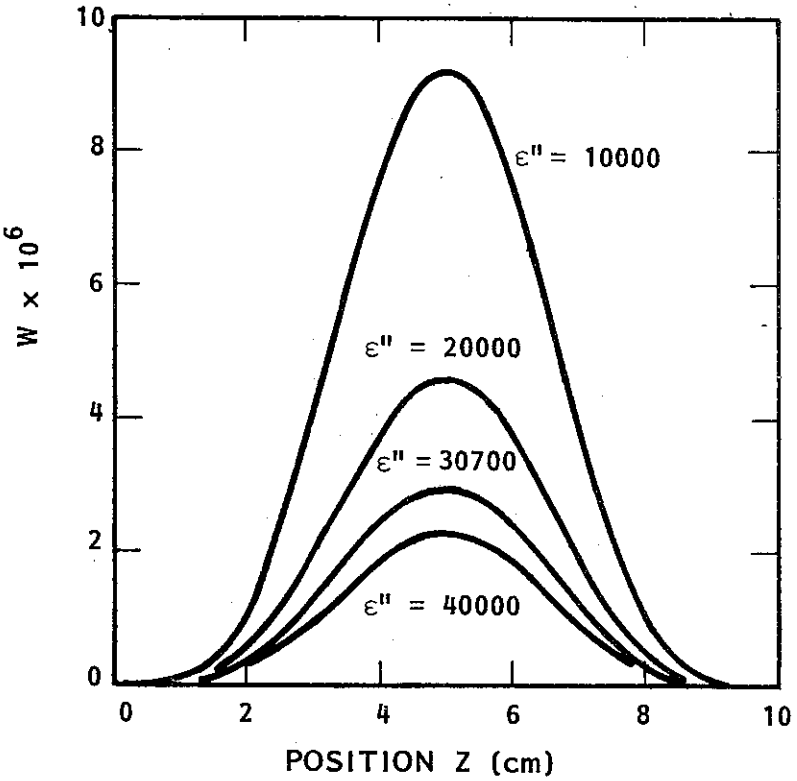

Figure 7-18. Geometry of the TE_{01} Loss Pattern for Various ε".

From these curves a choice of ε'' and w can be made which would give the value of attenuation desired for a particular need. It is seen from this plot that the curves do not depart from straight lines until about $\varepsilon'' < 30$ or $w > 10^{-2}$. This further defines the "linear region" for those values of αc.

Figure 7-17 allows for αc to be represented in a very useful fashion:

$$\alpha c \cong K_{\alpha c01}(\omega) \cdot w \cdot \varepsilon'' \qquad (7\text{-}15)$$

when αc is in the linear region. A three-dimensional regression analysis done on αc, w, and ε'' over the region of interest gives the values of $K_{\alpha c01}$ shown in Table 7-1. These values of $K_{\alpha c01}$

$\frac{\omega c}{C}$	$K_{\alpha c01}$
2.95	4.50
3.35	4.41
3.75	4.27

Table 7-1. Average Value of K_{ac01} Calculated for Various Values of Frequency.

will give αc to an accuracy of at least two figures in the linear region. The dependence of attenuation on frequency can now be viewed as resulting from $K_{\alpha c01}(\omega)$, a non-linear function of frequency.

Equation (7-15) can be employed directly to calculate the properties of a charge-suppression layer. For example, assume that a layer of graphite is added to the amplifier to bleed off excess charge. It is desired that this layer be of such a thickness so as to produce an attenuation of less than $\alpha c = 0.01$ (3.3 dB over 15 cm). From equation (7-15) it is found that:

$$w = \frac{0.01}{4.41 \times 31000} = 7.4 \times 10^{-8} .$$

This is less than a thousandth of a skin dept at this frequency. By similar reasoning, a lossy-layer thickness of one skin depth will result in an attenuation of more than 3300 dB over the 15-cm length of the amplifier.

Remember that the physical process by which the loss is applied to the waveguide will put a lower limit on the thickness of the lossy layer. As a layer of metal or graphite is applied by common techniques such as vapor deposition or carbon arcing, at first a little bit of the material must stick to the dielectric. Since the sticking coefficient of the graphite to the dielectric is less than the self-sticking coefficient of graphite to graphite, the material will adhere easier to previously deposited graphite than to the dielectric. Thus, the material deposits in islands, or clumps. The applied lossy layer won't be good for D.C. conduction (i.e. charge bleed-off) until the clumps fuse together to form a continuous layer. Thus, there exists a minimum depth below which D.C. conduction will not take place. For graphite this depth has been found to be about 100-200 Å. From equation (7-15) it is determined that an average thickness of $w = 2.56 \times 10^{-6}$ (100 Å) produces a normalized attenuation of $\alpha c = 0.3505$ which is about 117 dB over the 15 cm total length of the amplifier. It appears, then, that it will probably be necessary to reduce the conductivity of the lossy material to prevent excessive attenuation. Thus, pure graphite appears to be a poor choice.

Equation (7-15) can also be used to calculate the geometry of the loss pattern required to suppress TE_{01} oscillations. It was determined earlier that a loss pattern with the form: $L(z) = 9.07 \sin^4 (\frac{z}{10} \pi)$ dB/cm would be sufficient. This corresponds to an

attenuation of: $\alpha c\ (z) = 0.407 \sin^4 (\frac{z}{10} \pi)$. Since equation (7-15) describes a linear relationship between αc and w, the thickness of the applied lossy layer, w (z), will be of the same algebraic form. This thickness is plotted in Figure 7-18 for various values of ε''. The figure shows how a cross section of the lossy layer would appear if cut along the z-axis.

As with the two-layer case, it is important to determine how the real part of the propagation constant changes with the addition of loss. In Figures 7-19, 7-20, and 7-21 a factor $\Delta\beta c = \beta c\ (\varepsilon'') - \beta c\ (\varepsilon'' = 0)$ has been plotted atainst the thickness of the lossy layer. $\Delta\beta c$ is a measure of the amount by which βc has departed from the lossless βc. These figures behave much the same as did the ones showing the attenuation. As the thickness is increased, $\Delta\beta c$ shifts around until a point is reached where it levels off. For small values of w (i.e. the linear region of the attenuation curves), $\Delta\beta c$ appears to be fairly well behaved. This is again shown in Figures 7-22, 7-23, and 7-24 which are log-log plots of $\Delta\beta c$ vs w for a wide range of ε''. These curves are again very straight but have a slope of two rather than one. Thus, in this region of small w, $\Delta\beta c$ is proportional to w^2. It is also apparent from these curves that $\Delta\beta c$ is proportional to ε''^2. Therefore, in this region, $\Delta\beta c$ can be written as:

$$\Delta\beta_c \cong K_{\beta c01}\ (\omega) \cdot w^2 \cdot \varepsilon''^2. \qquad (7\text{-}16)$$

Values of $K_{\beta c01}$ at various frequencies are given in Table 7-2.

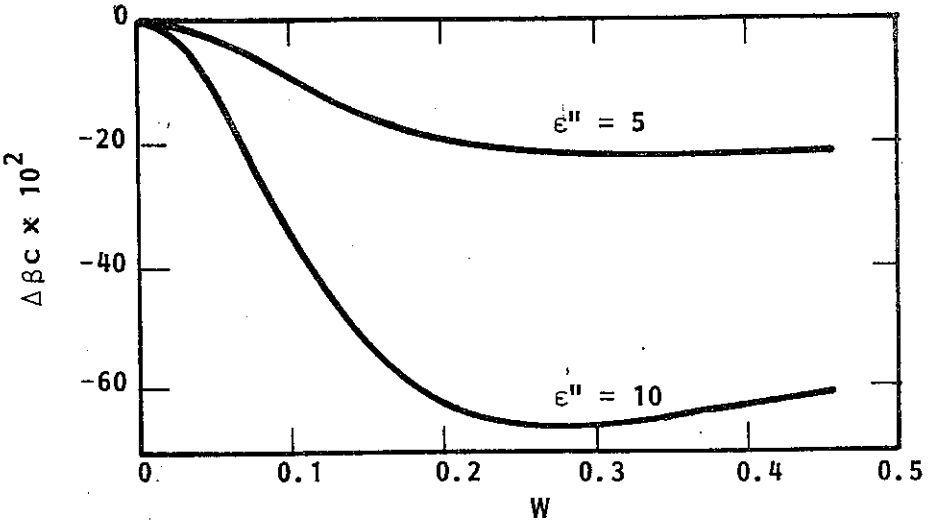

Figure 7-19. TE_{01} $\Delta\beta c = \beta c\ (\varepsilon'') - \beta c\ (\varepsilon'' = 0)$ vs w at $\frac{\omega c}{C} = 2.95$ for $\varepsilon'' = 5, 10$.

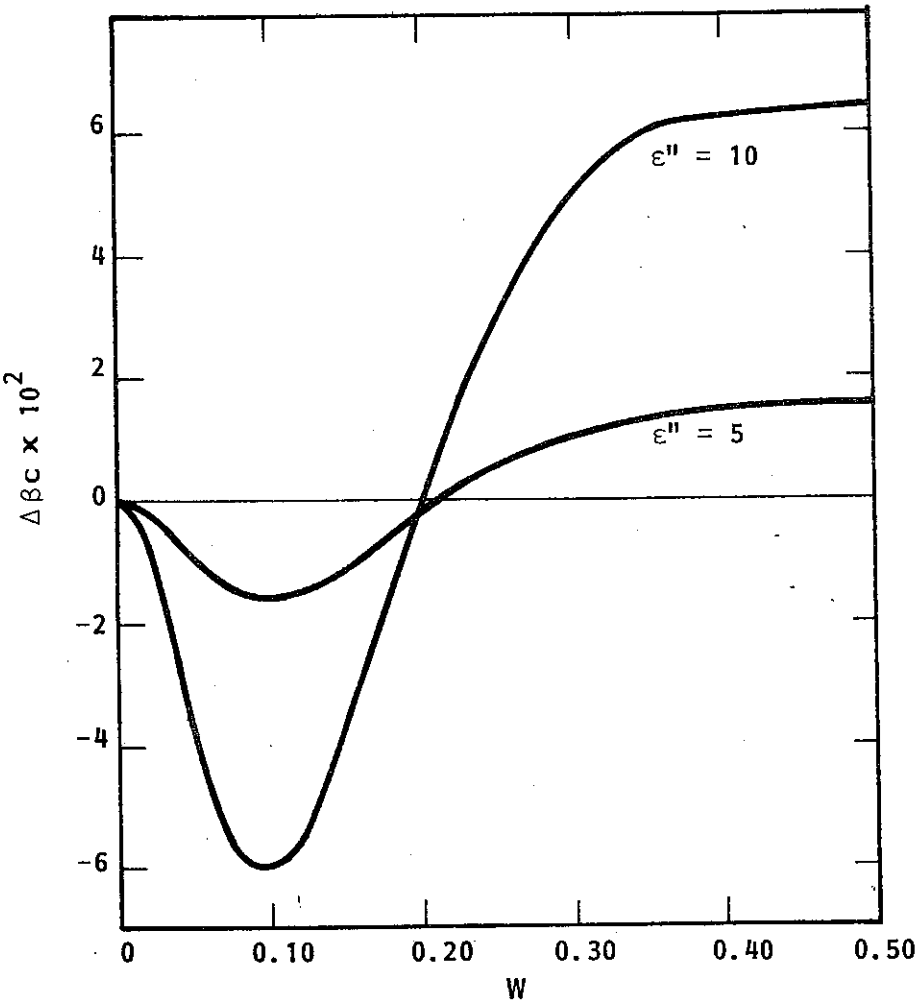

Figure 7-20. TE_{01} $\Delta\beta c = \beta c\ (\varepsilon'') - \beta c\ (\varepsilon'' = 0)$ vs w at $\frac{\omega c}{C} = 3,35$ for $\varepsilon'' = 5, 10$.

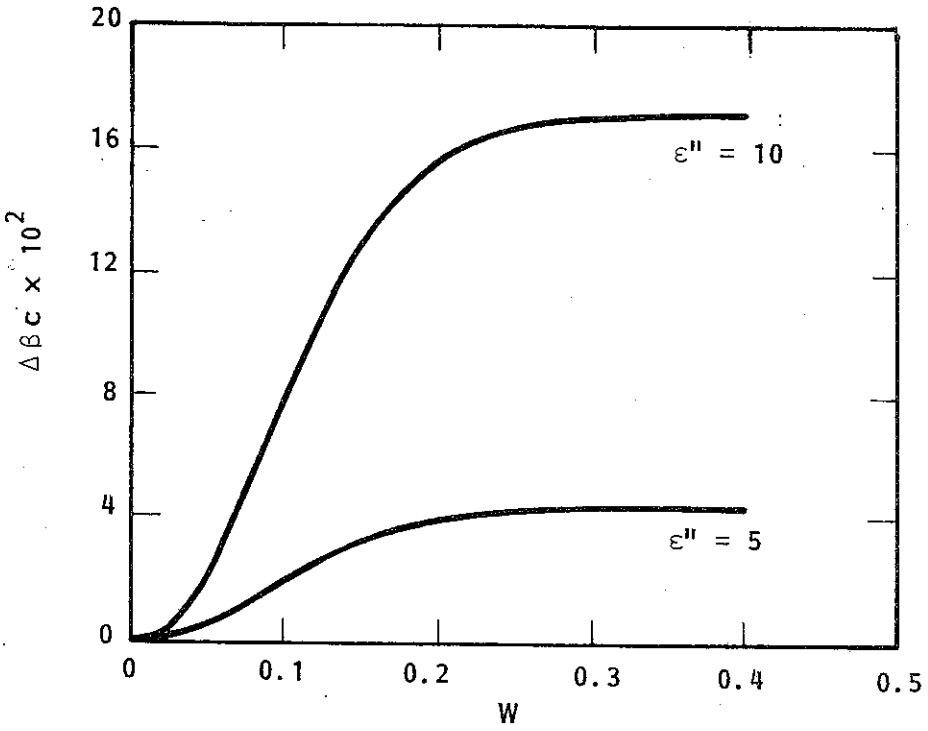

Figure 7-21. TE_{01} $\Delta\beta c = \beta c\ (\varepsilon'') - \beta c\ (\varepsilon'' = 0)$ vs w at $\frac{\omega c}{C} = 3.75$ for $\varepsilon'' = 5, 10$.

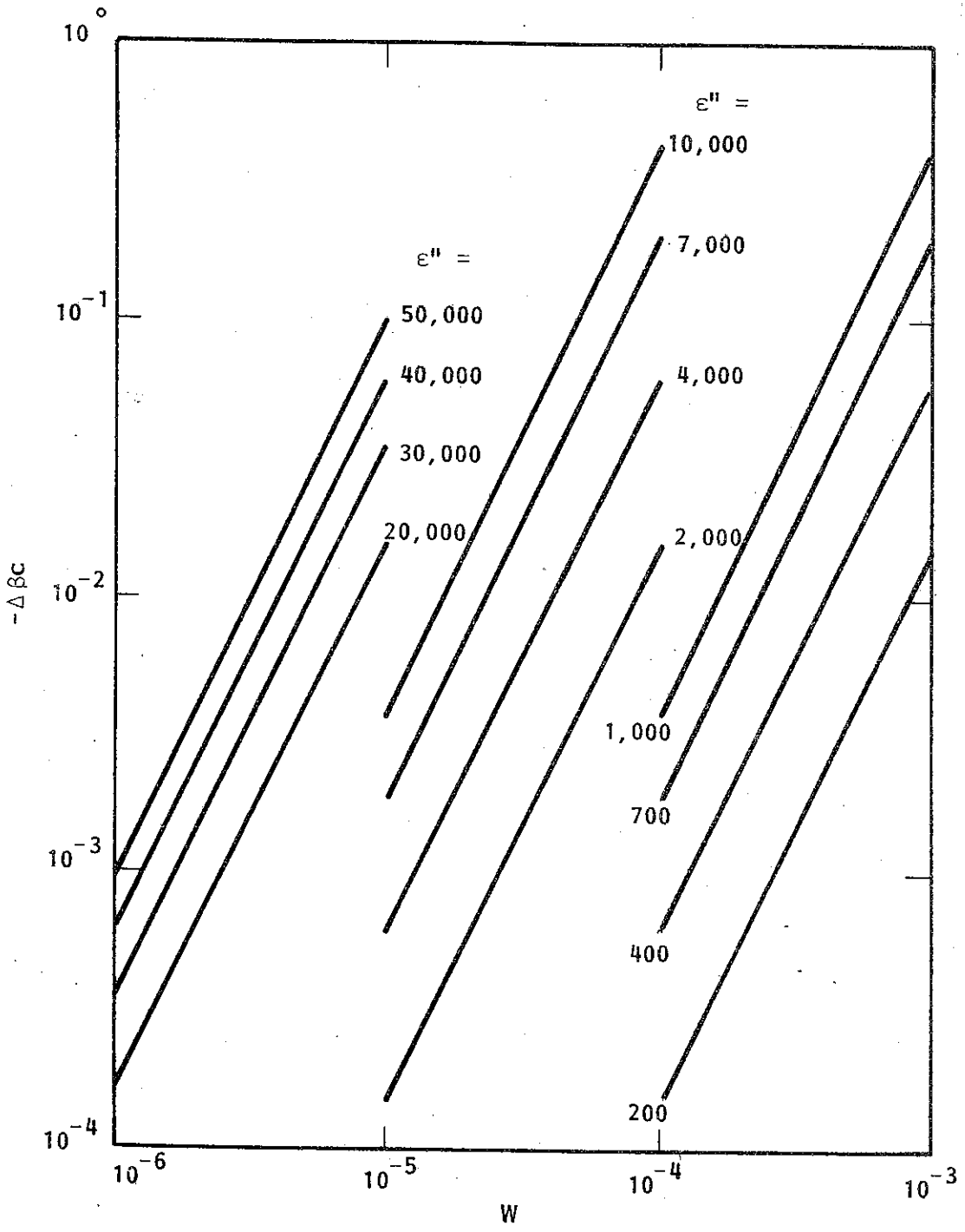

Figure 7-22. TE_{01} $\Delta\beta c$ vs w at $\frac{\omega c}{C} = 2.95$ for various ε''.

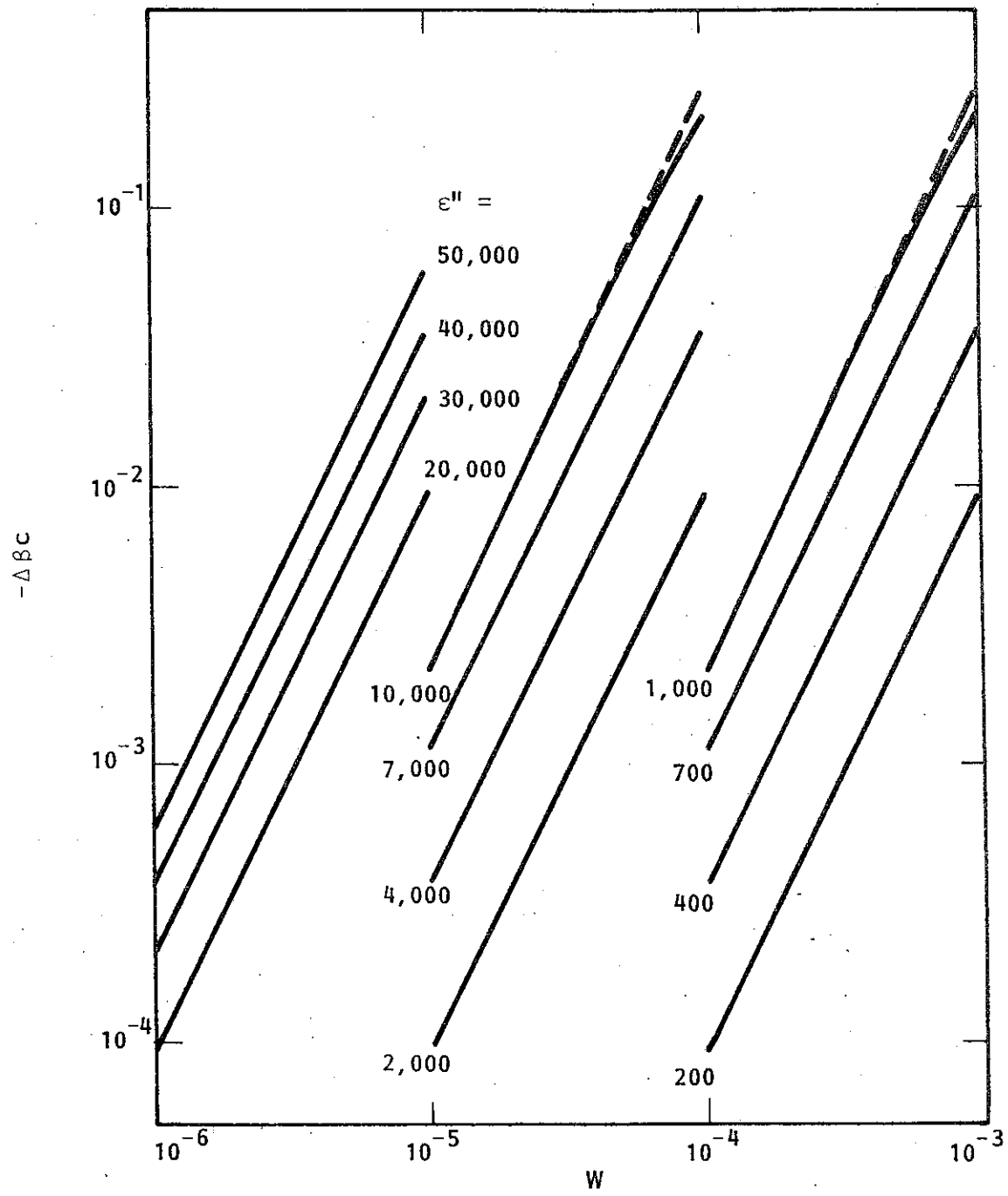

Figure 7-23. TE_{01} $\Delta\beta c$ vs w at $\frac{\omega c}{C}$ = 3.35 for Various ε''.

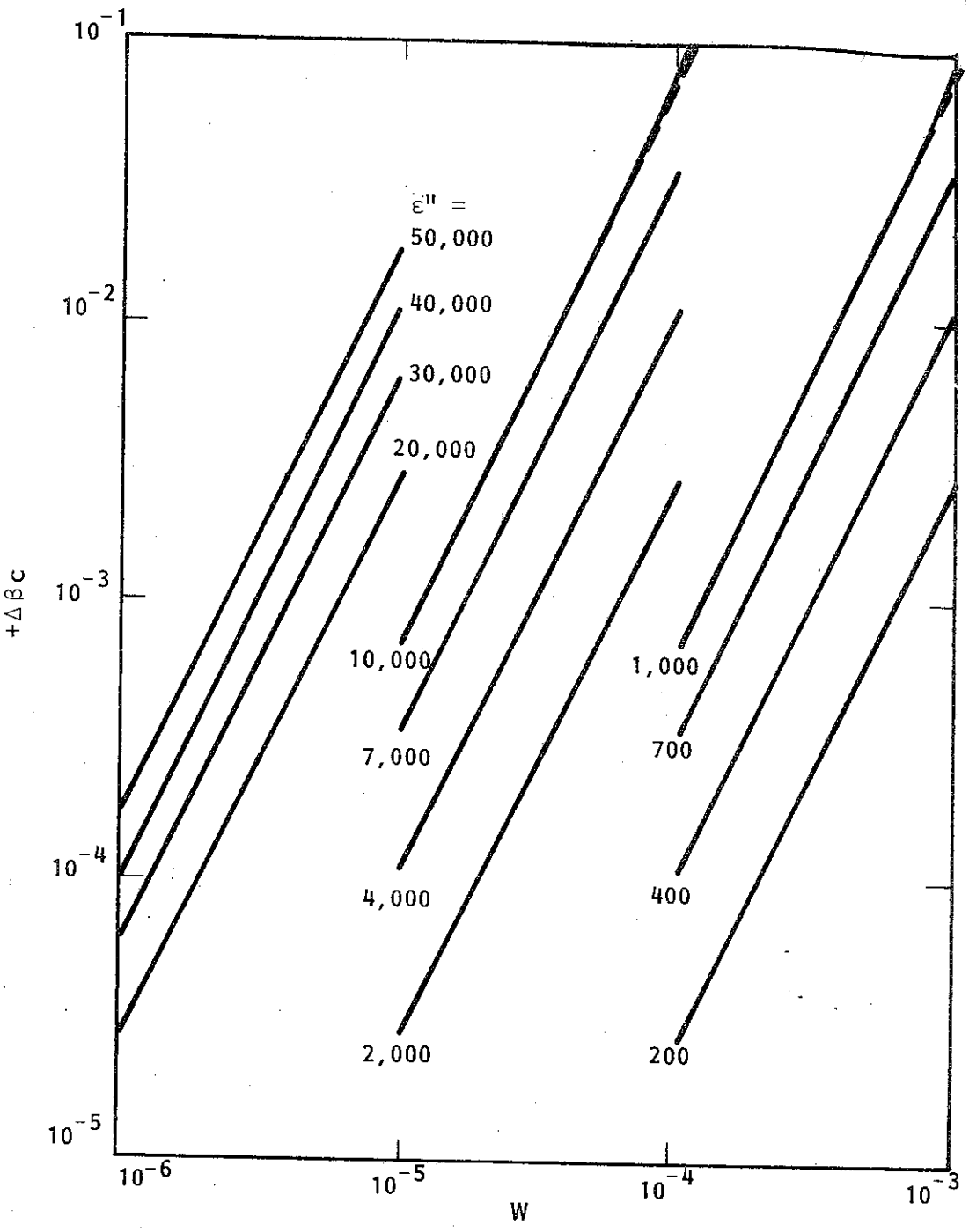

Figure 7-24. TE_{01} $\Delta\beta c$ vs w at $\frac{\omega c}{C}$ = 3.75 for Various ε''.

$\frac{\omega c}{C}$	$K_{\beta c01}$
2.95	-0.386
3.35	-0.230
3.75	0.069

Table 7-2. Average Value of $K_{\beta c01}$ Calculated for Various Values of Frequency.

Equation (7-16) can be used to calcualte the shift in β for a desired amount of attenuation. For example, to get an attenuation of αc = 0.407 at $\frac{\omega c}{C}$ = 3.35, values of $w = 2.3 \times 10^{-6}$ and $\varepsilon'' = 31000$ can be used. This would then result in $\Delta\beta c = (-0.230)\ (2.3 \times 10^{-6})^2\ (31000)^2 =$ 0.0012. Such a shift would probably not produce any significant reduction in the interaction with the electron beam, agreeing with the predictions of the two-layer analysis. For the loss pattern in Figure 7-18, this would be the maximum shift in βc. Since equation (7-16) states that $\Delta\beta c$ is proportional to w^2, the shift in βc as a function of position on the z-axis can be written as: $\Delta\beta c\ (z) =$ $0.0012 \sin^8 (\frac{z}{10} \pi)$.

C. Solution for the TE_{02} Mode

A solution for the TE_{02} mode can be found by solving for the second root of equation (7.13). Figure 7-25 shows the attenuation a TE_{02} wave would experience as a function of normalized layer thickness. The curves shown are for large values of ε'' ranging from 10,000 to 50,000, which are most likely to characterize a very lossy

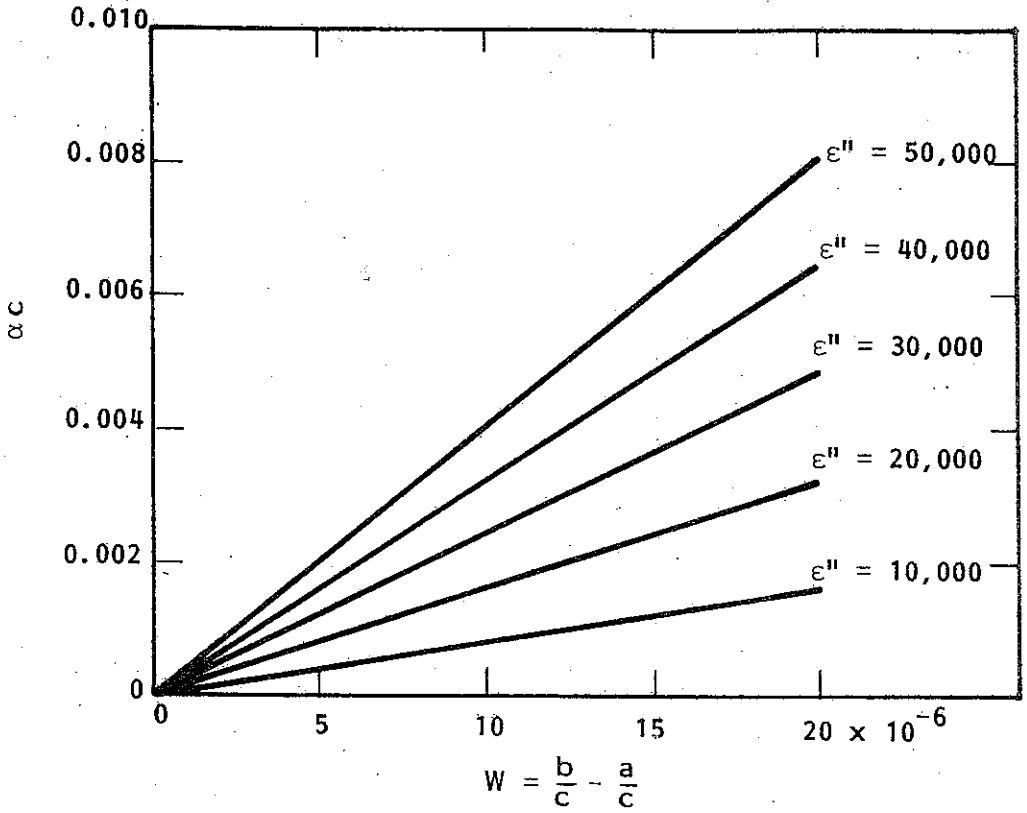

Figure 7-25. TE_{02} Attenuation vs w at $\frac{\omega c}{C} = 4.82$ for Various ε''.

material. The frequency is $\frac{\omega c}{C} = 4.82$, the intersection point of the s = 2 beam line and the TE_{02} mode line. It is near this frequency that TE_{02} oscillation is most likely to occur. A linear relationship between αc, w, and ε'' is again seen and can be written as:

$$\alpha c \cong K_{\beta c02}(\omega) \cdot \varepsilon'' \cdot w \qquad (7\text{-}17)$$

where $K_{\alpha c02}(4.82) = 0.00806$. Comparing Figure 7-25 with a similar TE_{01} drawing, such as Figure 7-15, reveals that for a given ε'' and w, a TE_{02} wave is attenuated much less than a TE_{01} wave. This is more easily seen by comparing the values of $K_{\alpha c01}(3.35)$ and $K_{\alpha c02}(4.82)$:

$$\frac{K_{\alpha c01}(3.35)}{K_{\alpha c02}(4.82)} \qquad \frac{4.41}{0.00806} \cong 547.$$

Thus, an equivalent w and ε'' in the linear region will attenuate the TE_{01} wave about 500 times more than the TE_{02} wave, at the given frequencies. This large difference in attenuation is very much the same as was predicted by the two-layer theory. The shift in βc has not been plotted here since it is almost negligible. At $\varepsilon'' = 50{,}000$ βc changes by at most 0.0016%.

It is very interesting to examine the behavior of the TE_{02} mode outside its linear region. Figure 7-26 is a plot of attenuation vs thickness for a fairly large range of w. It is seen that near w = 0.1 the attenuation takes a sharp upward jump, growing by nearly two orders of magnitude. A limited amount of insight into this behavior is gained by looking at Figure 6-33 (which is a plot of the two-layer lossless fields for the TE_{02} mode). These curves show that the electric field E_ϕ starts very small near the dielectric and rises sharply, peaking about halfway between the center of the guide and the dielectric.

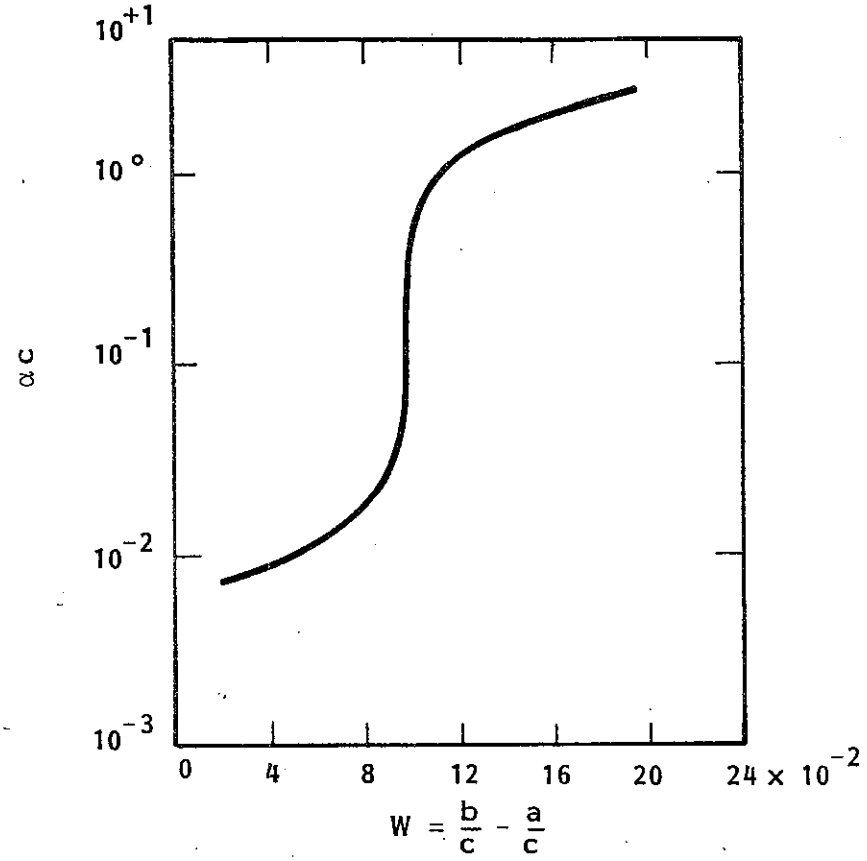

Figure 7-26. TE_{02} Attenuation vs Large w at $\frac{\omega c}{C} = 4.82$ and $\varepsilon'' = 50{,}000$.

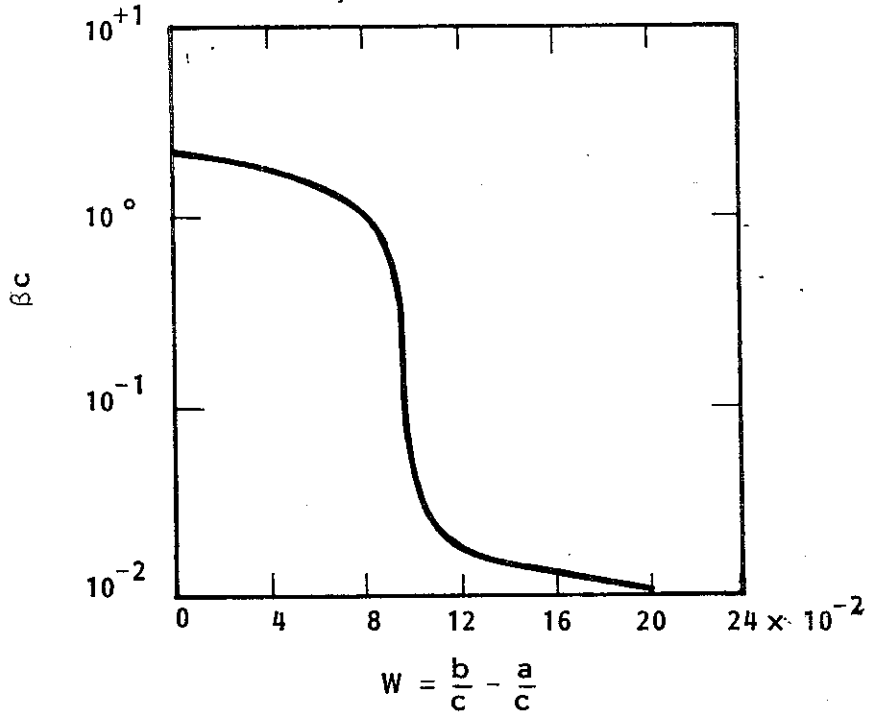

Figure 7-27. TE_{02} Phase Constant vs Large w at $\frac{\omega c}{C} = 4.82$ and $\varepsilon'' = 50{,}000$

When a thin lossy sleeve is placed inside the dielectric liner it will not intercept much of the electric field. However, as its thickness is increased, more and more field is encompassed. This explains the general trend of Figure 7-26 but not the reason for such an abrupt jump. It should be remembered, though, that adding the lossy layer perturbs the fields in the waveguide. Widening the layer increases the perturbation. To fully understand Figure 7-26 it would be of value to investigate the three-layer fields, which have not been treated in this study.

The phase of the TE_{02} wave at $\frac{\omega c}{C} = 4.82$ and $\varepsilon'' = 50{,}000$ is plotted in Figure 7-27 for larger values of w. It is interesting to note that at roughly the place that αc abruptly increases, βc abruptly decreases. In fact, βc falls by about two orders of magnitude -- the same amount αc rises. Under these conditions the point, $w \cong 10 \times 10^{-2}$, can be viewed as a type of pseudo-cutoff point, where TE_{02} propagation is markedly reduced.

D. Solution for the TE_{01} Mode with Frequency Variable ε''

When the manner in which attenuation varies with frequency was discussed earlier, the fact that ε'' is a function of frequency was not taken into account. That is why no plots of attenuation vs frequency were made. This dependence can be easily incorporated into the analysis by recalling equation (7.1):

$$\varepsilon'' = \frac{\sigma}{\omega \varepsilon_o} \qquad (7.1)$$

where σ is assumed to be constant with frequency. Assuming further that $\sigma = 7 \times 10^4$, which is the conductivity or graphite in the

microwave range, ε'' has been plotted against true frequency in Figure 7-28. The dotted lines show the frequency band of the amplifier: f = 36 to 46 GHz. These values of ε'' can be used in the dispersion equation to solve for αc and βc which will then have a more accurate dependence on frequency.

The results of the solution for the TE_{01} mode with frequency dependent ε'' are shown in Figure 7-29 and 7-30. Figure 7-29 is a plot of attenuation vs frequency for three different values of layer thickness. Attenuation is again seen to be decreasing with increasing frequency. The arrow shows the lossless cutoff frequency, and, as with the two-layer case, the attenuation shows a fast-rising increase as this value is approached.

Figure 7-30 plots $\Delta\beta c = \beta c\ (\varepsilon'' = 0) - \beta c\ (\varepsilon'')$ against frequency for four values of thickness. (It should be noted that the positive portion of the $\Delta\beta c$ axis employs a different scale than the negative portion.) Two interesting points are found from Figure 7-30. First, there is a point -- at $f \cong 44.5$ GHz -- where $\Delta\beta c$ is zero for all thicknesses. At this frequency βc does not change with the addition of the lossy layer, regardless of the layer's thickness. Second, as the frequency approaches lossless cutoff, $\Delta\beta c$ increases rapidly in the negative direction. This is as was found in the two-layer analysis; that is, although βc goes to zero at cutoff in the lossless case, it remains finite, but very small, in the lossy case.

E. Comparison of the Two-Layer and Three-Layer Analyses

When used to analyze the same three-layer waveguide, there is certainly little doubt that the three-layer model gives more accurate and useful results than the two-layer model. The failings

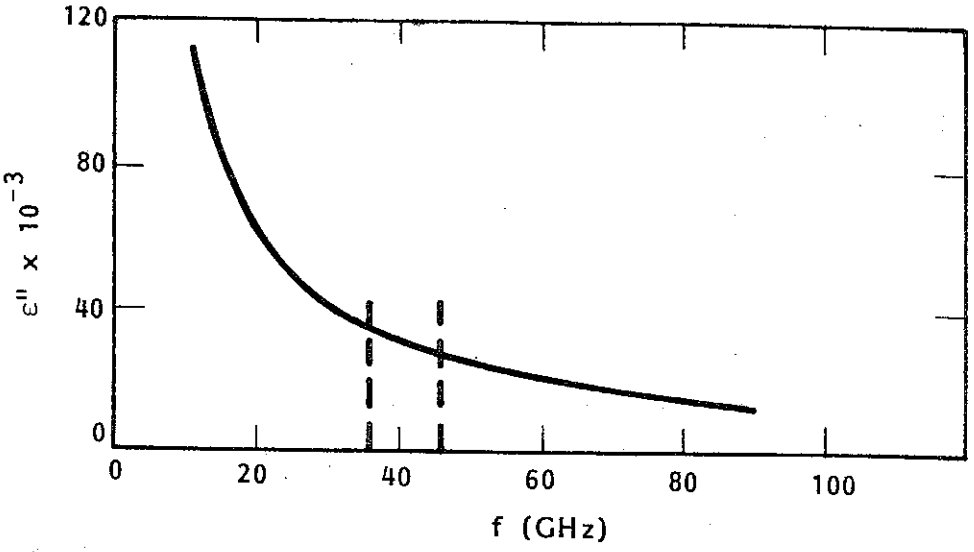

Figure 7-28. $\varepsilon'' = \frac{\sigma}{\omega\varepsilon_o}$ vs Frequency for $\sigma = 7 \times 10^4$ ℧/m. Dotted Lines Indicate the Frequency Band of Operation.

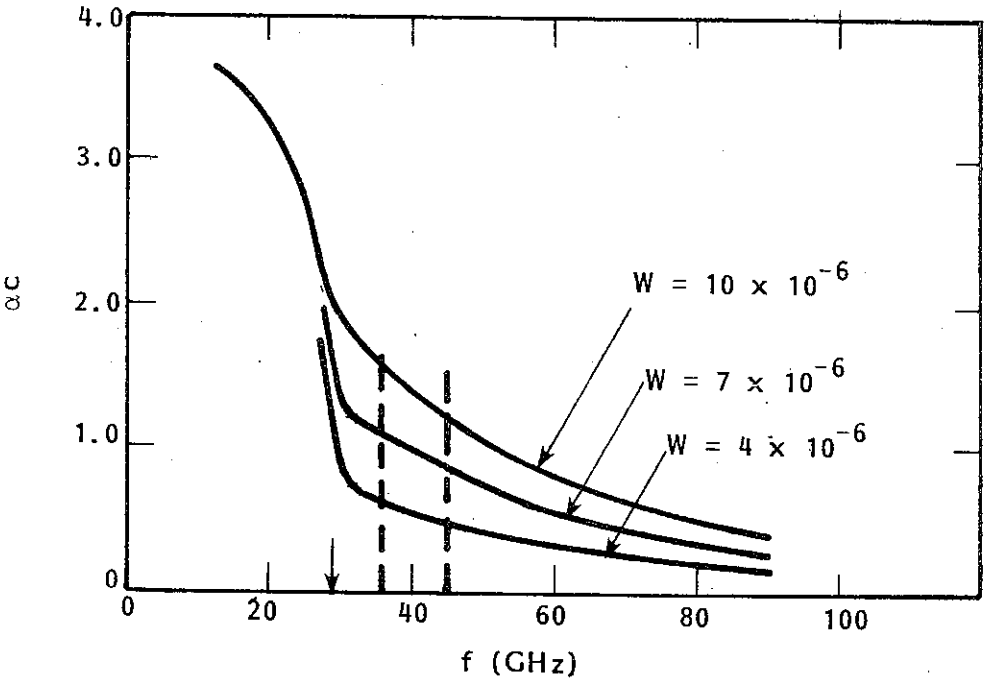

Figure 7-29. TE_{01} Attenuation vs Frequency for $\varepsilon'' = \frac{\sigma}{\omega\varepsilon_o}$ and Various w. Arrow Indicates Lossless Cutoff.

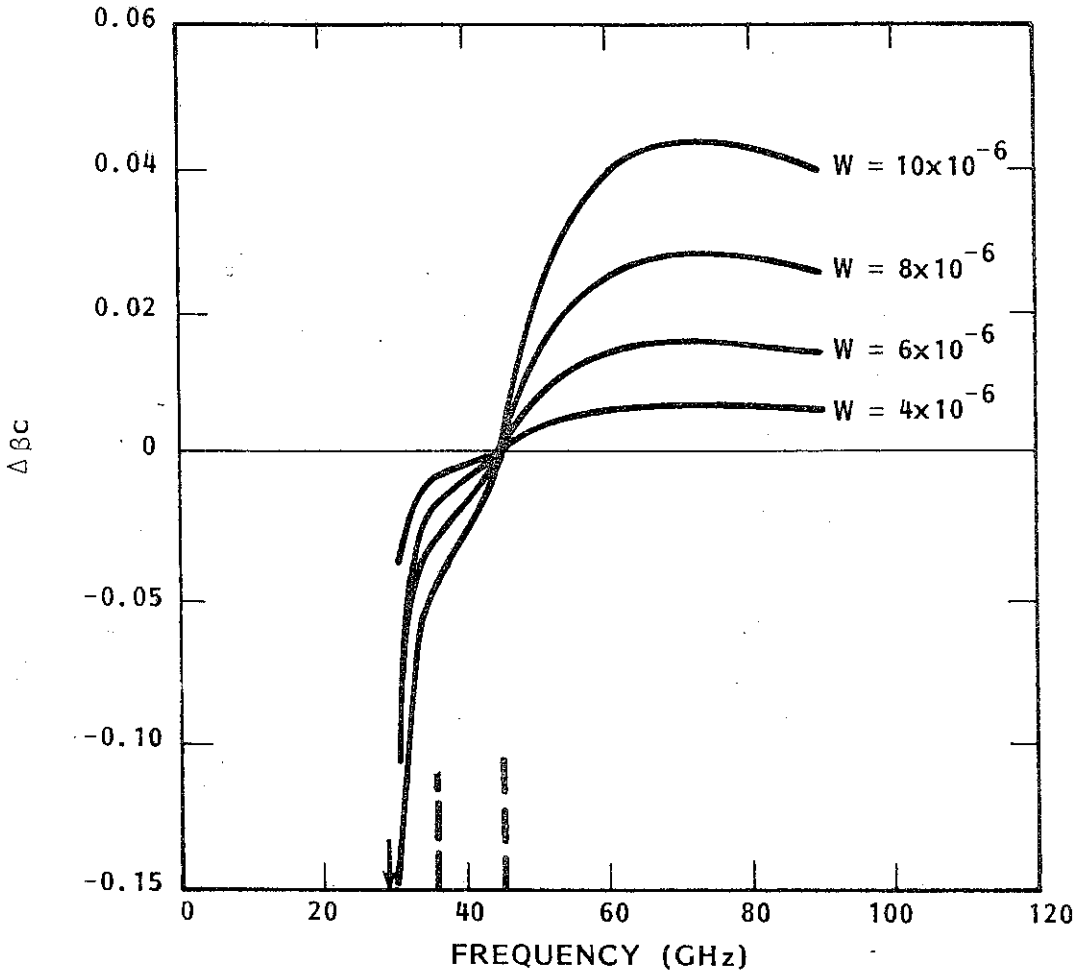

Figure 7-30. TE_{01} $\Delta\beta c = \beta c\ (\varepsilon'' = 0) - \beta c\ (\varepsilon'')$ vs Frequency for $\varepsilon'' = \frac{\sigma}{\omega\varepsilon_o}$ and Various w. Note the Different Scale Above and Below $\Delta\beta c = 0$. Arrow Indicates Lossless Cutoff.

of the two-layer model are made evident by some marked discrepancies between two- and three-layer results. Among these are the differences in how attenuation varies with frequency and the relative differences between the magnitude of TE_{01} and TE_{02} attenuation.

There were, happily, also some important agreements. Both models found linear relationships between α_c and ε'' and so a relation could be drawn between $K_{\alpha 2L}$ and $K_{\alpha c01}$. Also, both models came to the important conclusion that the addition of a lossy layer, thick enough to suppress TE_{01} oscillations, will not perturb β to the extent that interaction is jeopardized.

The importance of the two-layer model lies in its simplicity; that of the three-layer model in its accuracy. The two-layer dispersion equation is very simple and presents little computational difficulty due to its low values of ε''. The three-layer equation is much more complex and necessitates some clever algebra to make it computer compatible. The two-layer model gives quick and easy views of the field patterns, whereas the three-layer fields are much more complex and are not treated in this study. Perhaps the two-layer model's most accurate and useful application is in calculating the attenuation and phase constant due to losses inherent to the dielectric liner. On the other hand, the three-layer model is best used as a design tool. Given a desired attenuation, it can find an appropriate value of the conductivity and thickness of the required lossy layer.

VIII. THREE-LAYER FERRITE MODEL

A. Formulation

A thin layer of a ferrite material can be added to the waveguide of Figure 3-1 for the purpose of suppressing either fundamental or higher order mode oscillations in the amplifier. The frequency dependent lossy characteristics of ferrites are well known and provide an interesting means of adding attenuation to the amplifier circuit. The ferrite would be applied in much the same manner as graphite -- as a thin layer just inside the dielectric. The geometry of this ferrite/dielectric-loaded waveguide is shown in Figure 8-1.

The ferrite layer is modelled as having a complex scalar permittivity $\varepsilon_2 = (\varepsilon_2' - j\,\varepsilon_2'')\,\varepsilon_o$ and a tensor permeability:

$$\overleftrightarrow{\mu_2} = \begin{bmatrix} \mu & j\,\mu_a & 0 \\ -j\,\mu_a & \mu & 0 \\ 0 & 0 & \mu_{11} \end{bmatrix} \tag{8.1}$$

where μ and μ_a are complex functions of frequency. Although μ_{11} can vary somewhat, it is assumed to be constant and equal to unity throughout this analysis. Losses in the ferrite are represented both by the imaginary part of ε_2 and the imaginary parts of the entries of $\overleftrightarrow{\mu_2}$. Clarricoats [6] suggests a very useful way to express the entries of $\overleftrightarrow{\mu_2}$ in a mathematical form. He derives the phenomenological relationships:

$$\begin{aligned}
\mu' &= 1 + \frac{1}{2}\left[\frac{P_m\,(\sigma_m - 1)}{(\sigma_m - 1)^2 + \alpha_m^2} + \frac{P_m\,(\sigma_m + 1)}{(\sigma_m + 1)^2 + \alpha_m^2}\right] \\
\mu_a' &= -\frac{1}{2}\left[\frac{P_m\,(\sigma_m - 1)}{(\sigma_m - 1)^2 + \alpha_m^2} - \frac{P_m\,(\sigma_m + 1)}{(\sigma_m + 1)^2 + \alpha_m^2}\right] \\
\mu'' &= \frac{1}{2}\left[\frac{P_m\,\alpha_m}{(\sigma_m - 1)^2 + \alpha_m^2} + \frac{P_m\,\alpha_m}{(\sigma_m + 1)^2 + \alpha_m^2}\right]
\end{aligned} \tag{8.2}$$

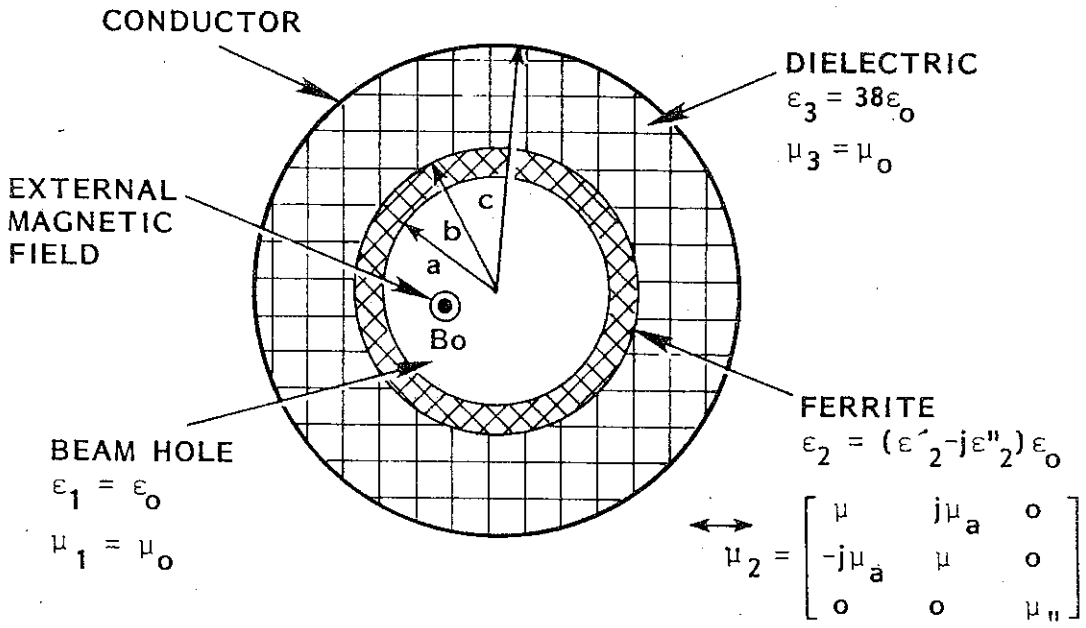

Figure 8-1. Geometry of Ferrite/Dielectric-Loaded Waveguide Model.

$$\mu_a'' = -\frac{1}{2}\left[\frac{P_m \alpha_m}{(\sigma_m - 1)^2 + \alpha_m^2} - \frac{P_m \alpha_m}{(\sigma_m + 1)^2 + \alpha_m^2}\right]$$

where: $\mu = \mu' - j\mu''$

$\mu_a = \mu_a' - j\,\mu_a''$.

The dimensionless parameters P_m, σ_m, and α_m are determined by the wave frequency, external magnetic field in the waveguide, and the magnetic and geometric properties of the ferrite. The factors σ_m and α_m should not be confused with conductivity or attenuation. The ferrite parameters are given by:

$$\sigma_m = \frac{\gamma H_{res}}{\omega}$$

$$P_m = \frac{\gamma 4\pi M_s}{\omega} \qquad (8.3)$$

$$\alpha_m = \frac{\gamma \Delta H}{2\omega}.$$

Here, M_s is the magnetization of the ferrite, ΔH is the linewidth, and H_{res} is the resonant magnetic field. The gyromagnetic ratio, γ, is taken to be $2\pi \times 2.8 \times 10^6$ in MKS units. The resonant magnetic field is found from:

$$H_{res} = [H_{ex} + H_{an} + (N_x - N_z)\,4\pi M_s]^{1/2}\,[H_{ex} + H_{an} + (N_y - N_z)\,4\pi M_s]^{1/2}. \qquad (8.4)$$

In this formula, H_{ex} is the external magnetic field along the axis in the waveguide, H_{an} is the anisotropy field, and N_x, N_y, and N_z are shape demagnetizing factors determined by the geometry of the ferrite. The ferrite sleeve is assumed to have the shape factors $N_y = N_z = 0$, $N_x = 1$ throughout the analysis. It is found that varying these factors by small amounts does not drastically alter the results.

The number of variables in this three-layer waveguide problem is quite large. To examine all possible combinations would prove a time-consuming task indeed. Thus, a single set of parameters will be established, with one of these variables allowed to vary in each of the cases examined. The choice of a standard set of ferrite parameters should be made from a range of realistically achievable values. In the microwave region, commonly available ferrites will have parameters falling into the ranges listed in Table 8-1. Of these, the parameters chosen to represent the standard case are shown in Table 8-2. Ferrite materials are very versatile in the large range of parameters that can be obtained. A material can be manufactured which exhibits the desired parameters by manipulating the metallurgy of the ferrite: particle composition, grain size, mixture ratios, etc. A value of $\varepsilon'' = 0$ was chosen so that the loss due to the imaginary components of $\overleftrightarrow{\mu}_2$ would be more apparent. The value of H_{an} is determined by maximizing μ'' at a desired frequency. It can be shown that maximum μ'' (which is nearly equal to μ_a'') occurs for:

$$\sigma_m^2 = 2\sqrt{(\alpha_m^2 + 1)} - (\alpha_m^2 + 1) \qquad (8.5)$$

where: $0 \leq \alpha_m \leq \sqrt{3}$.

This value of σ_m is substituted (8.3) to obtain a value of H_{res}. This in turn gives the necessary value of H_{an} from equation (8.4). Thus, H_{an} is used to control the frequency at which peak μ'' occurs.

To provide maximum flexibility of results, normalized values are used throughout the analysis. All field values are

Table 8-1: Available Range of Ferrite Parameters

Parameter	Min. Value	Max. Value	Units
ε_2'	12.0	18.0	
ε_2''	0.01	1.0	
H_{an}	0	30,000	oe
$4\pi M_s$	2,000	4,000	oe
ΔH	2,000	6,000	oe

Table 8-2: Chosen Standard Case Parameter.

Paramater	Value	Units
ε_2'	12.0	
ε_2''	0.0	
a/c	0.865	
$4\pi M_s$	4,000	oe
ΔH	5,000	oe
H_{an}	2,477	oe
H_{ex}	10,300	oe

Table 8-3: Normalized Standard Case Parameters.

Normalized Parameter	Value
$\frac{4\pi M_s}{H_{ex}}$	0.38835
$\frac{H_{an}}{H_{ex}}$	0.24051
$\left(\frac{\omega c}{C}\right)$ peak μ''	3.35
$\frac{\Delta H}{H_{ex}}$	0.48544
$\frac{\gamma c}{C} H_{ex}$	2.35726

normalized by H_{ex}, the external magnetic field in the waveguide. This allows the use of the following formulas:

$$\sigma_m = \frac{\left(\frac{\gamma c}{C} H_{ex}\right)\left(\frac{H_{res}}{H_{ex}}\right)}{\left(\frac{\omega c}{C}\right)}$$

$$P = \left(\frac{\gamma c}{C} H_{ex}\right)\left(\frac{4\pi M_s}{H_{ex}}\right) \Big/ \left(\frac{\omega c}{C}\right) \qquad (8.6)$$

$$\alpha_m = \frac{\left(\frac{\gamma c}{C} H_{ex}\right)\left(\frac{\Delta H}{H_{ex}}\right)}{2\left(\frac{\omega c}{C}\right)}$$

$$\frac{H_{res}}{H_{ex}} = \left[1 + \frac{H_{an}}{H_{ex}} + (N_x - N_z)\frac{4\pi M_s}{H_{ex}}\right]^{1/2}\left[1 + \frac{H_{an}}{H_{ex}} + (N_y - N_z)\frac{4\pi M_s}{H_{ex}}\right]^{1/2}.$$

Table 8-3 lists the equivelant normalized values of the standard case parameters.

B. Investigation of Ferrite Parameters

Much insight into the behavior of the ferrite-loaded waveguide can be gained by examining the behavior of μ', μ'', μ_a', and μ_a''. Equations (8.2) have been plotted against frequency for the parameters of Table 8-3. This is shown in Figure 8-2. The frequency dependence of these factors is easily seen. The shape of the μ'' curve suggests that attenuation will be limited to a band of frequencies

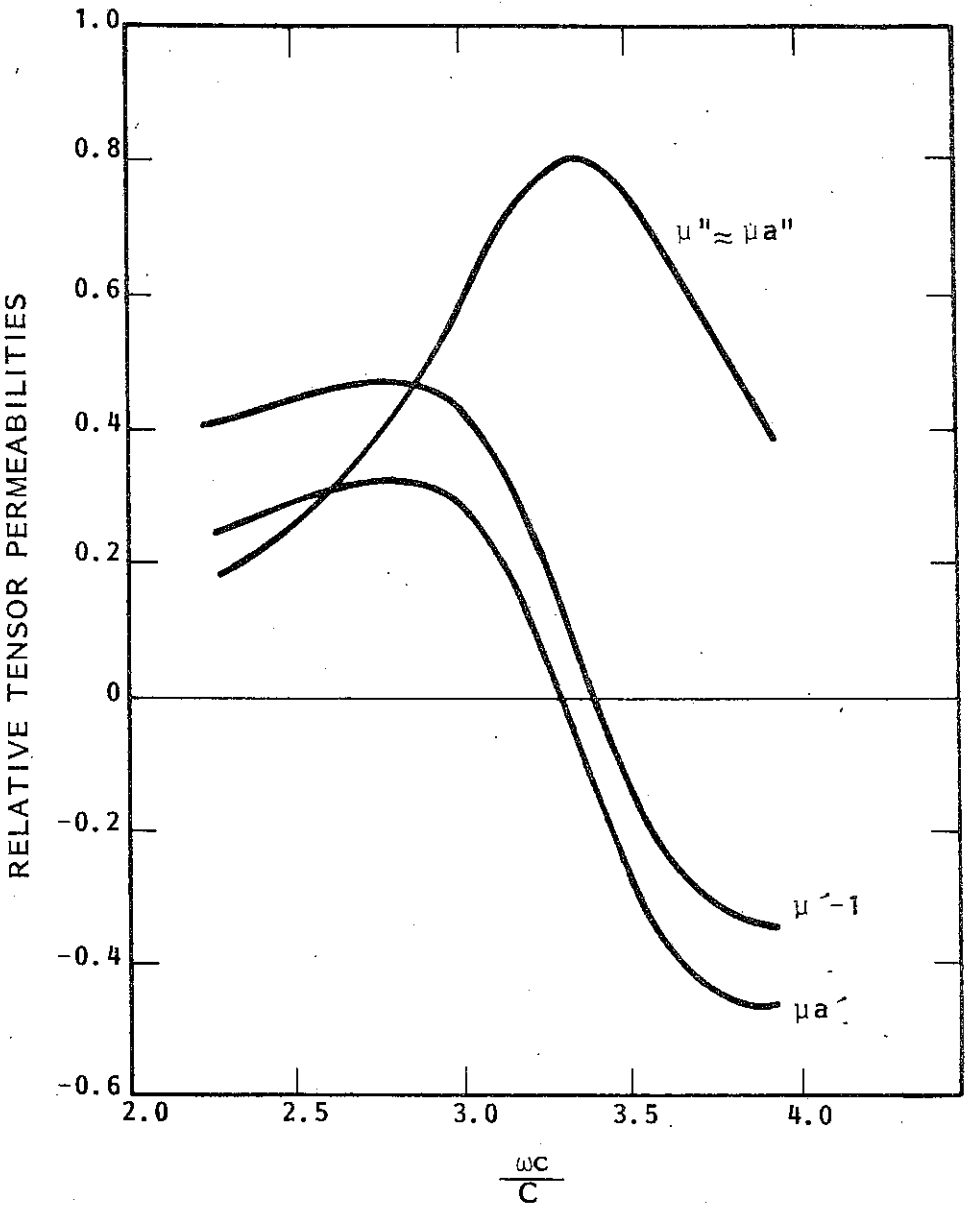

Figure 8-2. $\mu'-1$, μ_a', and μ'' vs Frequency for the Standard Case.

centered on or near $\left(\frac{\omega c}{C}\right)$ peak μ''. This "notch-like" behavior could have very useful applications. For instance, $\left(\frac{\omega c}{C}\right)$ peak μ'' could be centered on the frequency at which the s = 2 beam line intersects the TE_{02} waveguide mode, thus attenuating these higher frequencies but not affecting the fundamental interaction.

It was mentioned before that the frequency at which μ'' reaches its peak is determined by the anisotropy field, H_{an}. This relationship is shown graphically in Figure 8-3 for $\frac{4\pi M_s}{H_{ex}} = 0.39$. In this plot, a value for H_{an} can be chosen to give the desired value of $\left(\frac{\omega c}{C}\right)$ peak μ''. Since H_{an} can't be negative, it is seen that $\left(\frac{\omega c}{C}\right)$ peak μ'' cannot be made smaller than about 2.8, using the standard case parameters. Figure 8-4 shows how this choice of H_{an} varies with $\frac{4\pi M_s}{H_{ex}}$, assuming $\left(\frac{\omega c}{C}\right)$ peak μ'' is set at 3.35

The effects of other parameters have also been examined. Figure 8-5 demonstrates how the choice of ΔH, the linewidth, changes the shape of the μ'' curve. As ΔH is increased, the peak value of μ'' becomes smaller, and the curve widens out. Thus, the value of ΔH helps determine the band of frequencies over which the attenuation will be effective.

Figure 8-6 shows how the peak value of μ'' depends on both ΔH and $4\pi M_s$. As just mentioned, μ'' is largest for smallest ΔH. It is also seen that μ''_{max} is a function of $4\pi M_s$. As $4\pi M_s$ is made large, μ''_{max} increases.

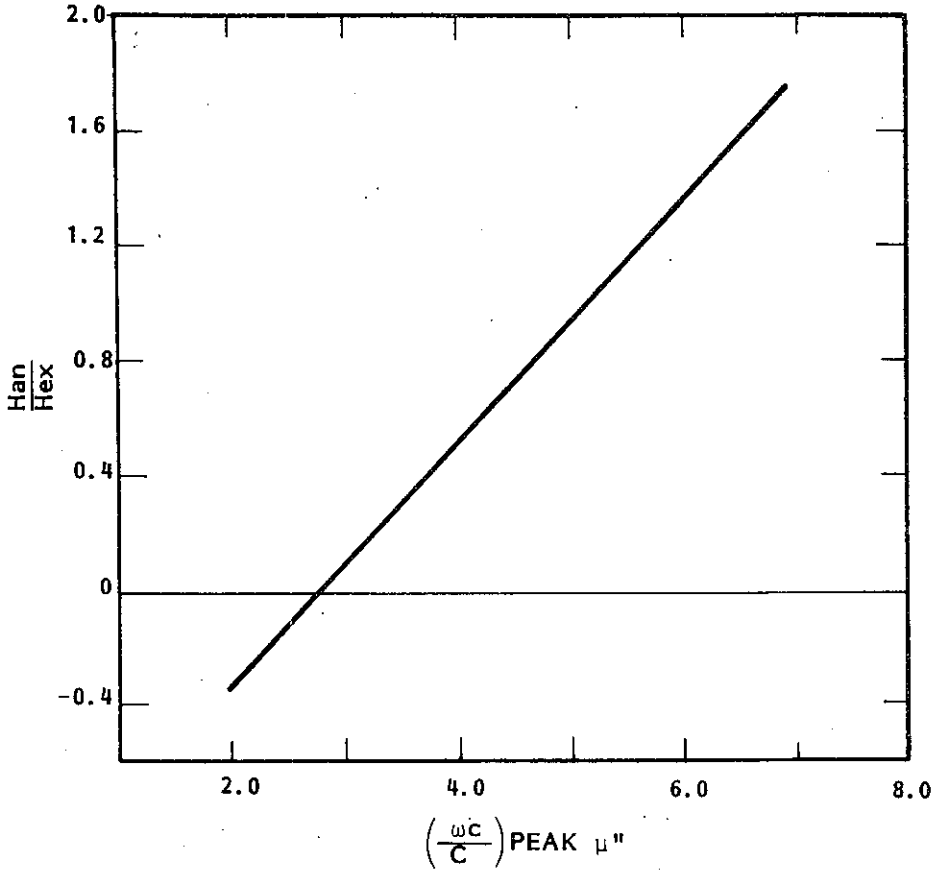

Figure 8-3. Anisotropy Field vs Frequency of Peak μ" for the Standard Case Parameters.

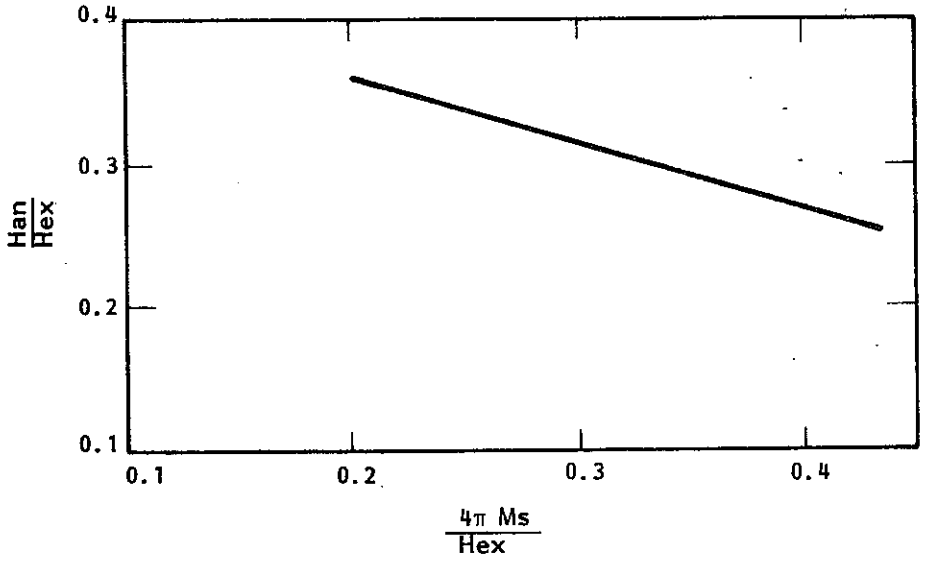

Figure 8-4. Anisotropy Field vs Magnetization to Give Peak μ" at $\frac{\omega_c}{C} = 3.35$.

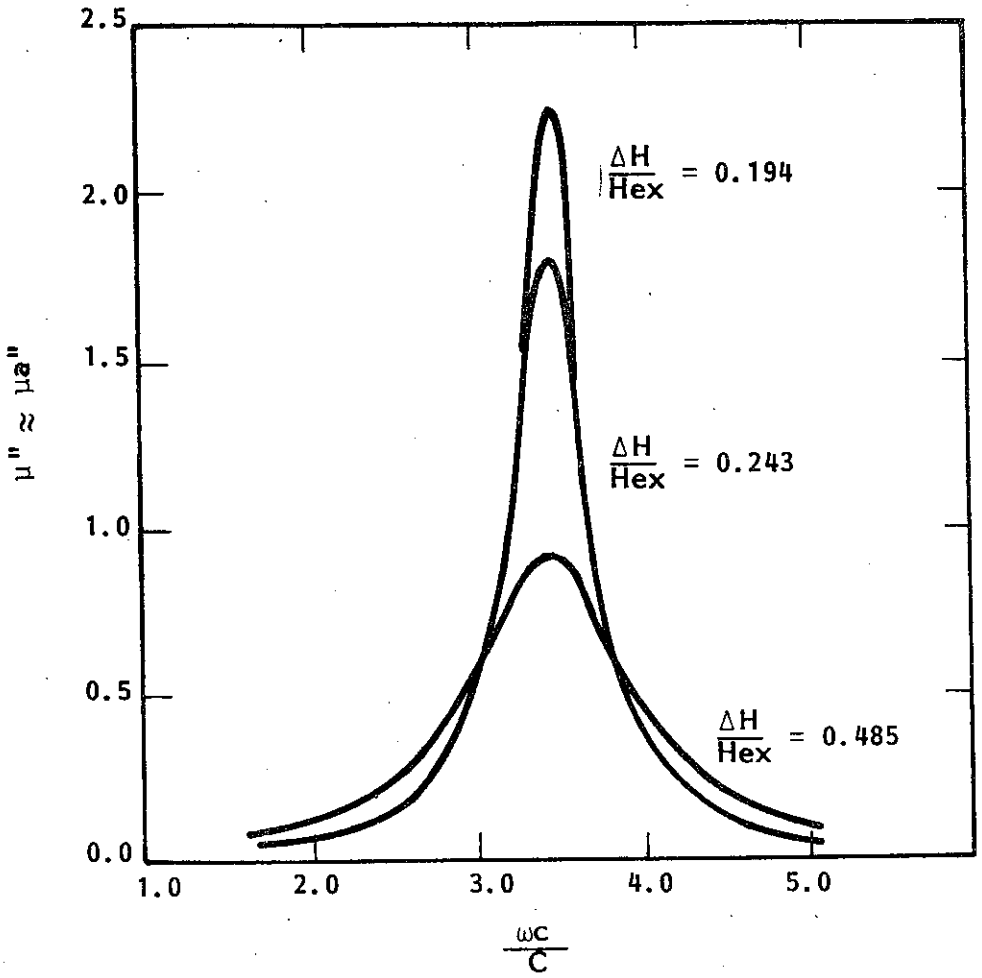

Figure 8-5. μ" vs Frequency for Various Linewidths and the Standard Case.

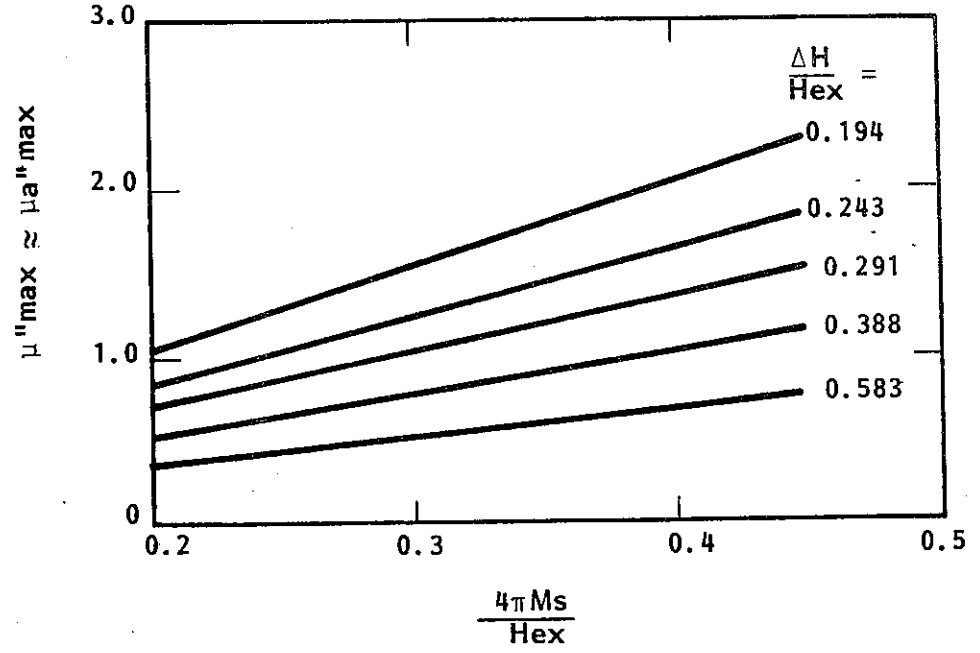

Figure 8-6. Peak Value of μ" vs Magnetization for Various Linewidths. $\left(\frac{\omega c}{c}\right)$ Peak μ" = 3.35.

Using these preliminary results, an early design criterion can be hypothesized. First, a choice of H_{an} is made to position maximum loss at the frequency desired. Next, a value of ΔH is picked depending on whether highest loss is desired, or largest frequency spread. This should be done with a certain logical value of $4\pi M_s$ in mind. The major problem with this system is, of course, that there may not be a real material with the chosen properties. Practicality will probably necessitate a compromise in the final choice of ferrite parameters and, thus, in the frequency response of the attenuation.

C. Solution for the TE_{01} Mode

A complete derivation of the n = 0 three-layer ferrite-loaded waveguide dispersion relation is given in Appendix IV. Its solution is considered here for the TE_{01} mode. This mode is the first root of equation (A4.17) and is found by beginning with the two-layer lossless TE_{01} mode and slowly increasing the lossy layer until the desired thickness is reached. That is, w is increased from 0.0 (the lossless, two-layer case) to, for example, 0.027 (the standard parameter case) so that convergence at this thickness can be more easily obtained. Modes propagating in a ferrite are named TE and TM by how they act as the ferrite approaches a dielectric; that is, as $\mu_a \to 0$.

As before, a value of $k_z c = \alpha c - j\beta c$ is determined from a value of $\frac{\omega c}{C}$ by solving the dispersion equation. (Full details of the method of solution are given in Appendix Five.) Figure 8-7 and 8-8 show the solution of (A4.17) for the standard case parameters. The expected dependency of attenuation on frequency is clearly seen

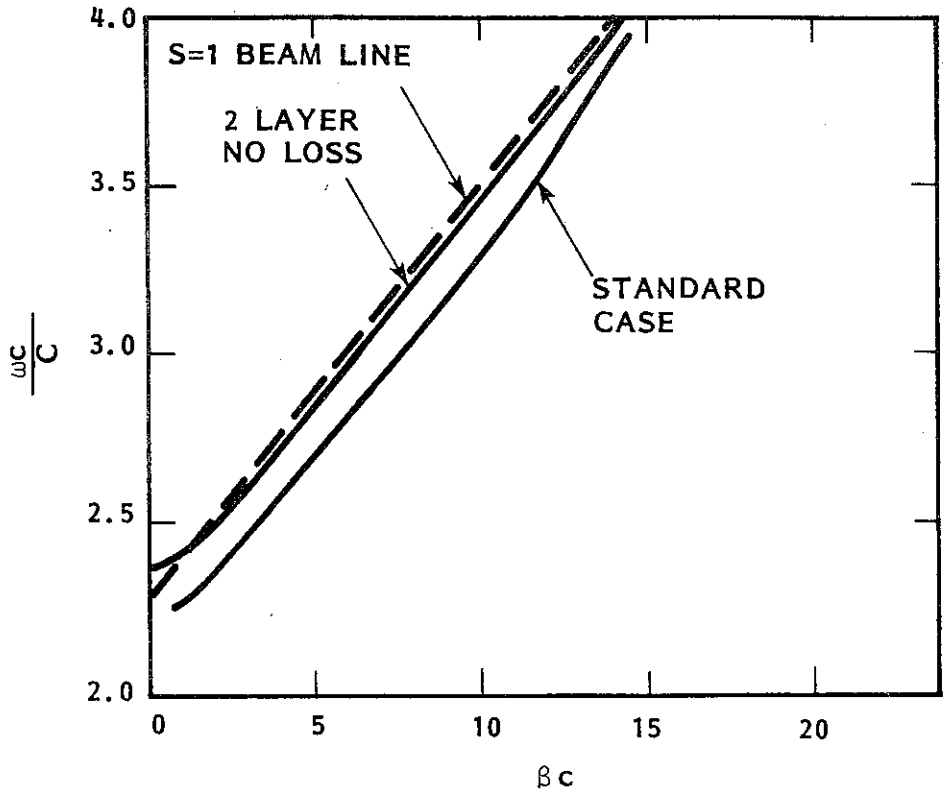

Figure 8-7. TE_{01} $\omega - \beta$ Plot for the Standard Case Parameters.

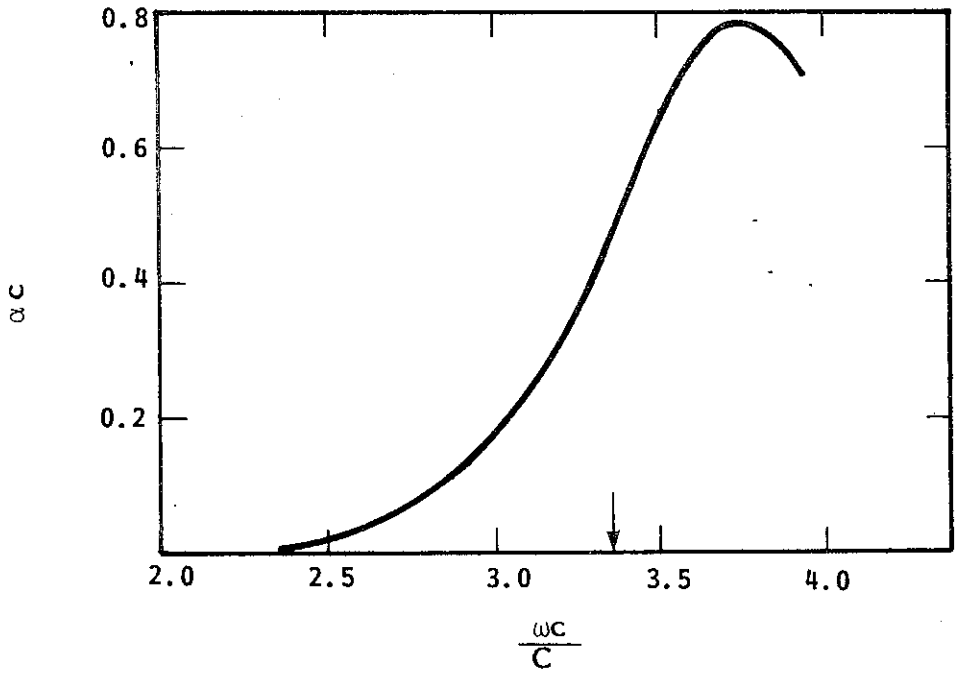

Figure 8-8. TE_{01} Attenuation vs Frequency for the Standard Case Parameters. Arrow Indicates the Position of Maximum μ''.

in Figure 8-8. The shape of this plot is remarkably similar to the shape of the μ'' vs frequency plot seen in Figure 8-2. What had not been anticipated, though, is the shift in frequency of the peak value of attenuation. Whereas, peak μ'' is chosen to occur at $\frac{\omega c}{C} = 3.35$, peak attenuation takes place at $\frac{\omega c}{C} = 3.75$.

Figure 8-7 is a plot of the $\omega - \beta$ diagram for the standard case parameters. It is seen that the addition of the ferrite layer causes the TE_{01} waveguide mode line to shift quite a bit to the right. This could result in problems with interaction if the beam line was not corrected to account for the shift. This amount of β shift appears to be a function of frequency. At higher frequencies, above $\frac{\omega c}{C} = 3.5$, the standard case line seems to be less displaced from the lossless case.

The manner in which αc and βc vary with changes in the thickness of the ferrite layer is shown in Figures 8-9 and 8-10. Figure 8-9 is a plot of $\Delta\beta c\ (w) = \beta c\ (w) - \beta c\ (w = 0)$, showing the same shift in βc seen in Figure 8-7. Two frequencies are shown, and, as was noted before, the amount of shift at a given thickness depends on the frequency considered. The shape of the curve is as expected, bending over so that a unit increase in w does not give quite as large an increase in $\Delta\beta c$ as the one before.

Figures 8-10 is a plot of attenuation vs frequency for various values of relative thickness. As a/c is increased the attenuation also increases. As with $\Delta\beta c$, the increase in αc with a

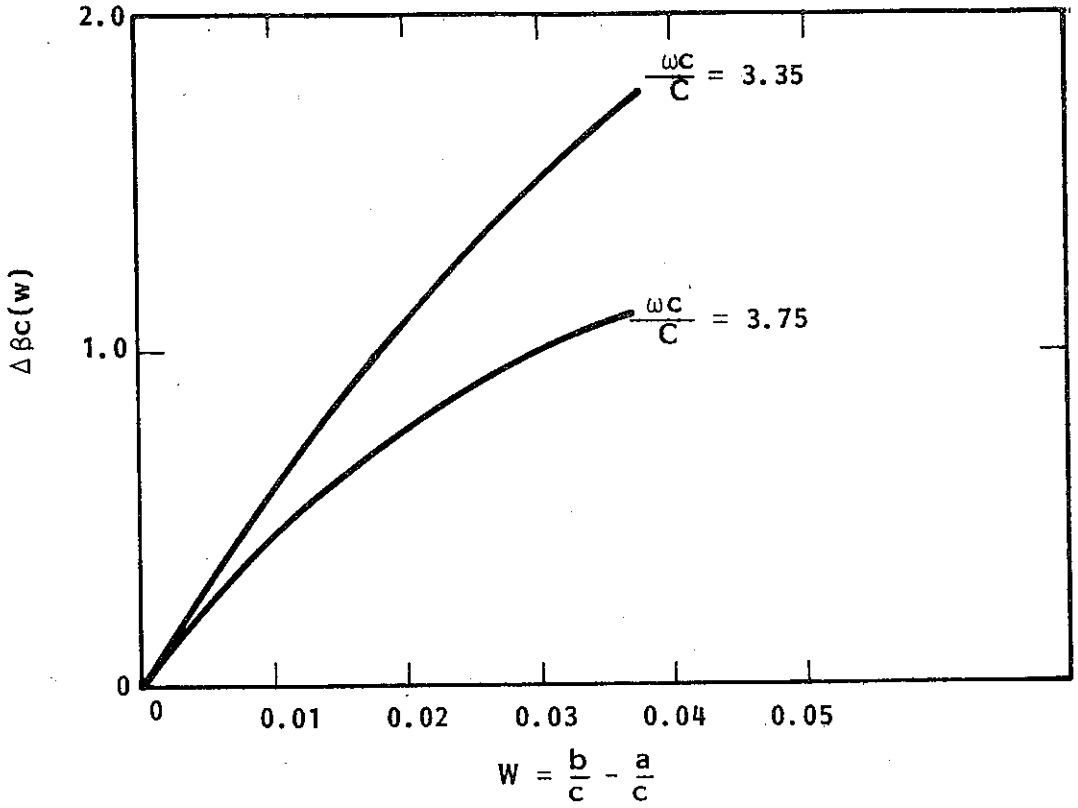

Figure 8-9. TE_{01} $\Delta\beta c\ (w) = \beta c\ (w) - \beta c\ (w = 0)$ vs Thickness for Various Frequencies.

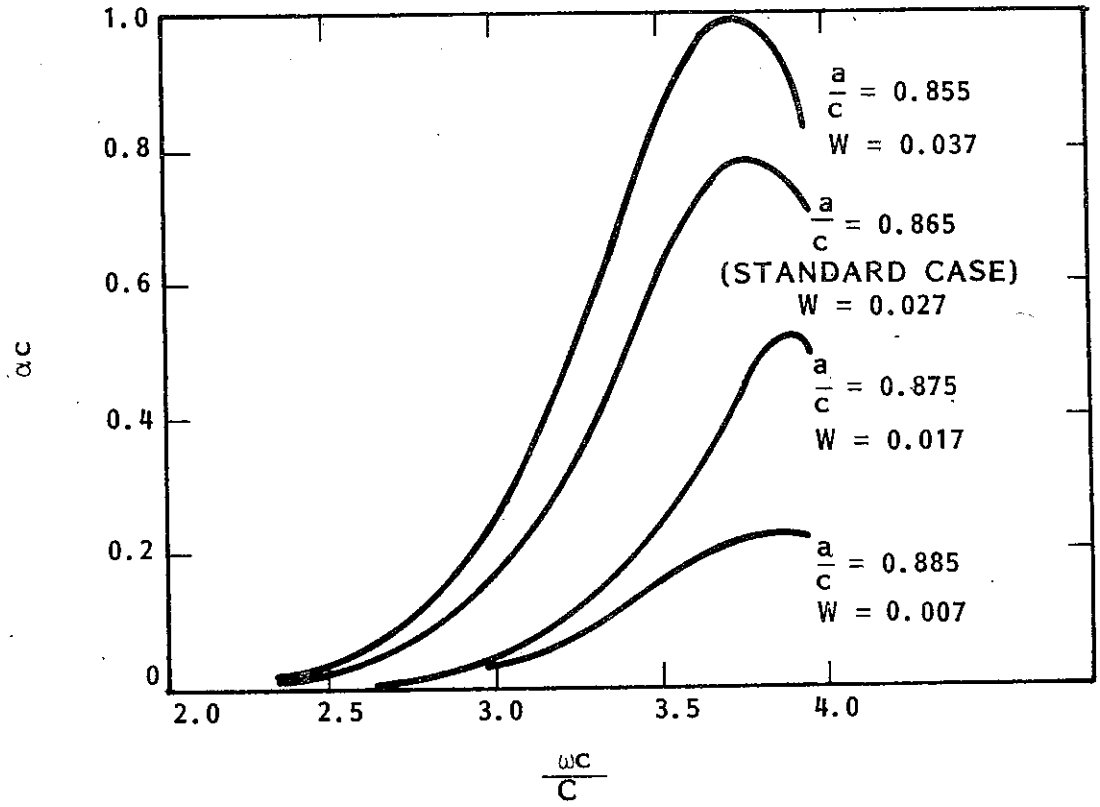

Figure 8-10. TE_{01} Attenuation vs Frequency for Various Relative Thicknesses.

unit increase in a/c is smaller for larger a/c. An interesting effect seen in this figure is that the position of the peak value of attenuation depends on a/c. As thickness is increased, the frequency of peak attenuation moves closer to the frequency of peak μ''.

The effects of various values of magnetization on the attenuation of the TE_{01} wave is shown in Figure 8-11. The results from Figure 8-6 revealed that a larger value of $4\pi M_s$ gave a larger peak μ''. This same effect is seen in Figure 8-11 where a larger $4\pi M_s$ results in a larger αc. In fact, the correspondence between the two is nearly one to one. A change in $4\pi M_s$ from 0.2 to 0.44 results in a change in μ''_{max} of about 2.0 times and a change in αc of about 2.2 times. In contrast, βc remains relatively constant with respect to changes in $4\pi M_s$. The same change in $4\pi M_s$ results in an increase in βc of only 2.5%. The dotted line in Figure 8-11 highlights another interesting observation. Increasing $4\pi M_s$ causes a shift in peak αc away from peak μ''. The dotted line shows the locus of this shift.

It has been mentioned that the frequencies of peak αc and peak μ'' do not coincide. The effect of varying the position of peak μ'' (by correctly choosing H_{an}) is shown vividly in Figure 8-12. As the frequency of peak μ'' is decreased, the frequency of peak αc follows close behind. Figure 8-13 displays the relationship between the two frequencies, which turns out to be fairly close to a straight line. This curve could be very helpful as a design aid. For example, if maximum attenuation is desired at a frequency of $\frac{\omega c}{C} = 3.35$, Figure 8-13 shows that the ferrite parameters should be chosen so as to put

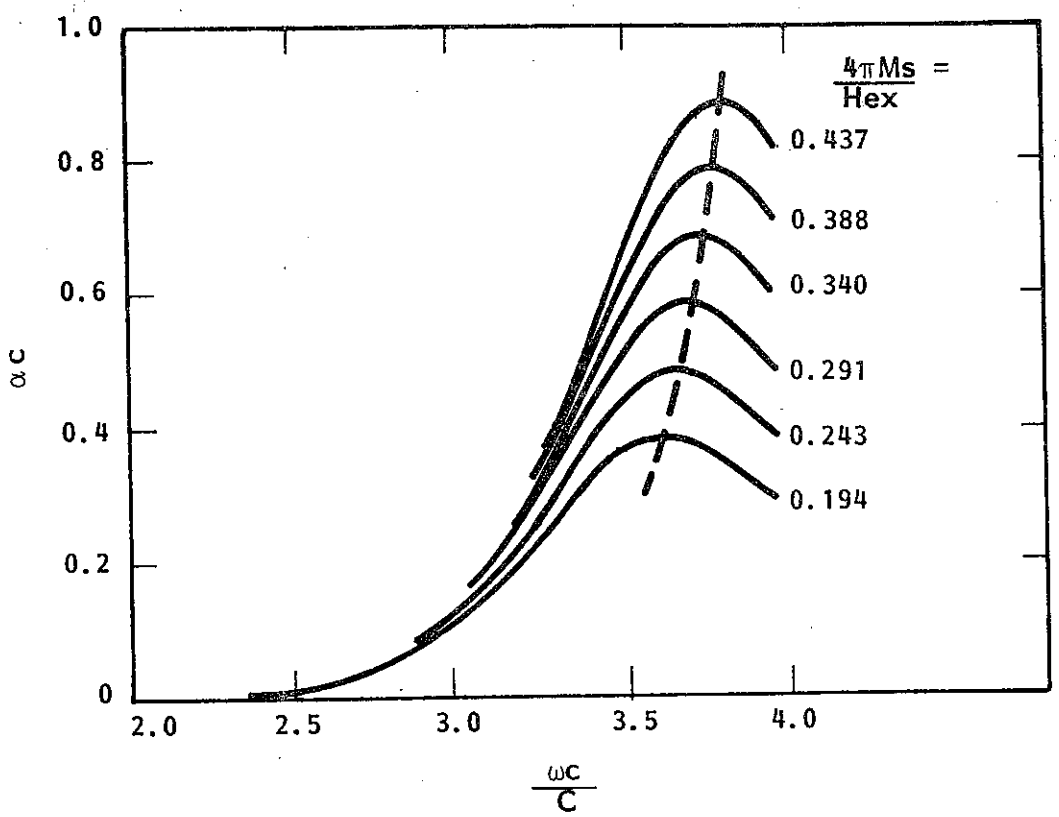

Figure 8-11. TE_{01} Attenuation vs Frequency for Various Magnetizations. Dotted Line Indicates Locus of Peak Attenuation.

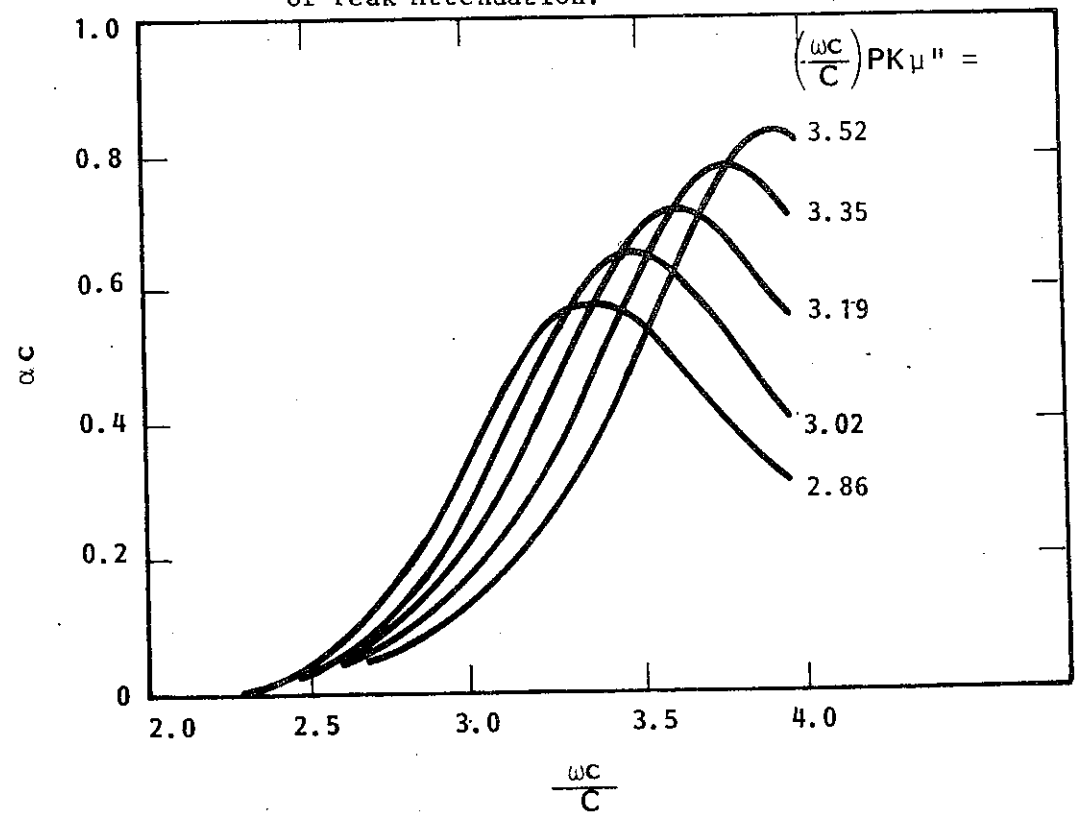

Figure 8-12. TE_{01} Attenuation vs Frequency for Various Values of $\left(\frac{\omega c}{C}\right)$ Peak μ".

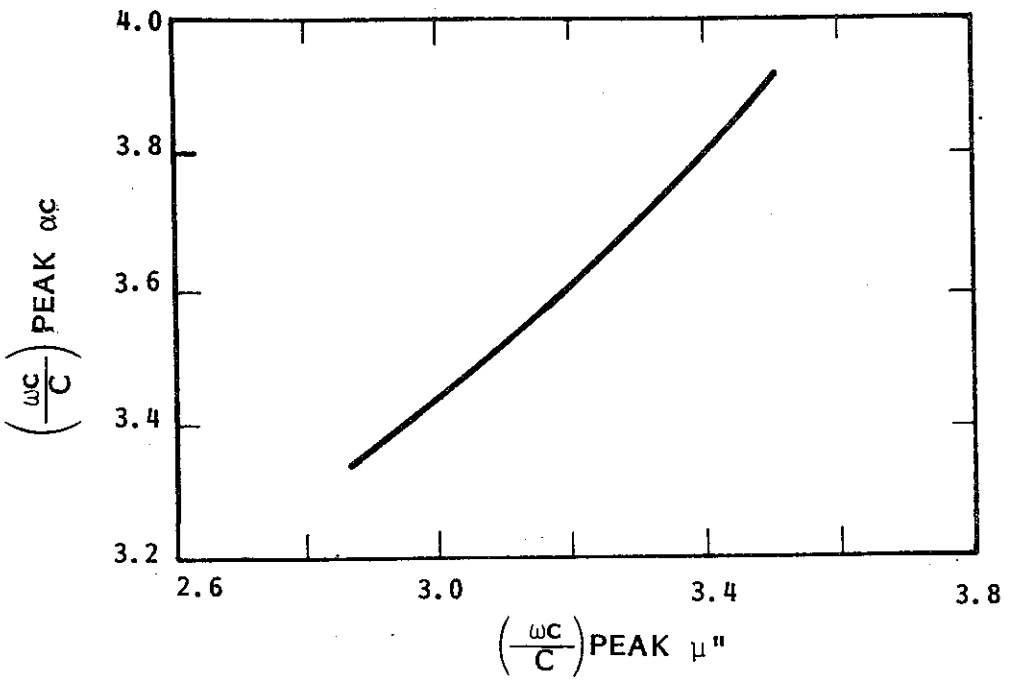

Figure 8-13. TE_{01} Prediction of Frequency of Peak Attenuation From Frequency of Peak μ".

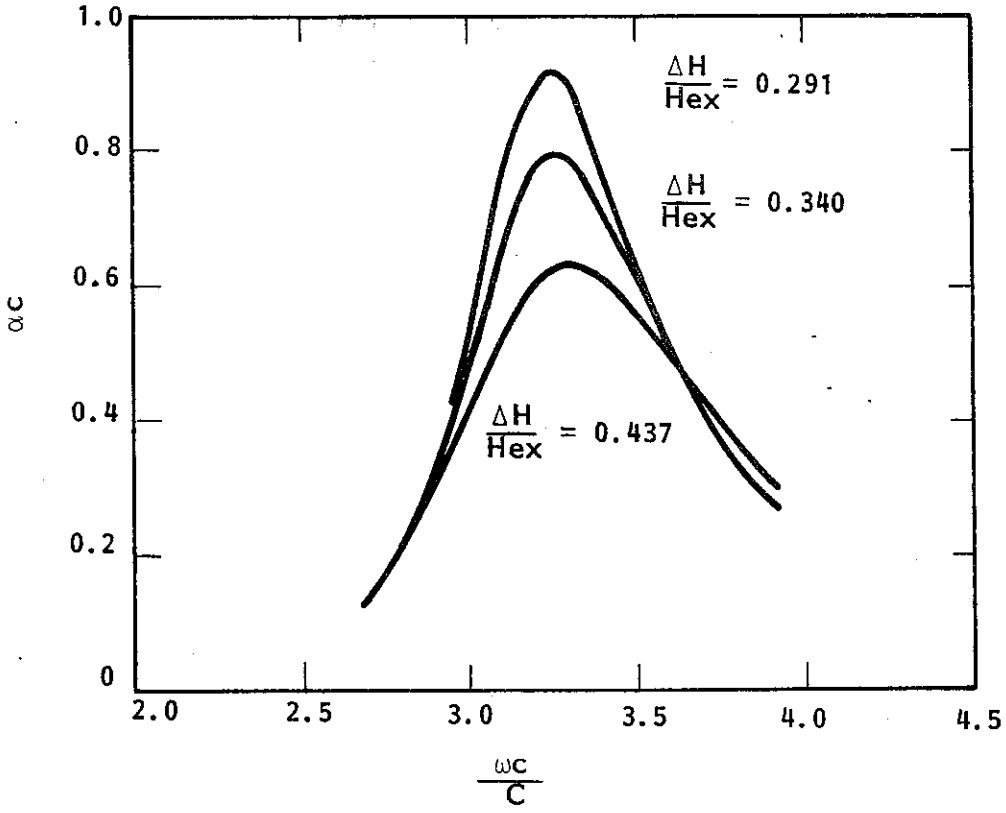

Figure 8-14. TE_{01} Attenuation vs Frequency for Various ΔH. $\left(\frac{\omega_c}{C}\right)$ Peak μ" = 2.88.

maximum μ'' at $\frac{\omega c}{C} = 2.88$. Another interesting fact brought out in Figure 8-12 is that the maximum value of αc is a function of the frequency at which it is maximized. This arises from the dependence of maximum αc on H_{an}.

Figure 8-14 shows the effect on αc of varying ΔH. Here μ'' has beem maximized at $\frac{\omega c}{C} = 2.88$, so Figure 8-13 indicates that peak αc should occur at $\frac{\omega c}{C} = 3.35$. For the standard case of $\frac{\Delta H}{H_{ex}} = 0.437$, this is seen to be so. As $\frac{\Delta H}{H_{ex}}$ is descreased below this value, the attenuation curve becomes taller and more narrow, and the frequency of its peak shifts slightly towards the frequency of peak μ''. This change in shape was predicted by Figure 8-5. Figure 8-15 is a plot of $\Delta\beta c\ (\Delta H) = \beta c\ (\Delta H) - \beta c\ (2\text{-layer})$ showing how the shift in βc changes with varying ΔH. This curve is interesting in that, at $\frac{\omega c}{C} = 2.95$, $\Delta\beta c$ decreases with increasing ΔH while at $\frac{\omega c}{C} = 3.35$ $\Delta\beta c$ increases with increasing ΔH. This is probably due to changes in μ_a' and μ' with frequency as shown in Figure 8-2. Here μ_a' and $\mu'-1$ are seen to cross the axis at about the same point where μ'' reaches its peak (at $\frac{\omega c}{C} = 2.88$, which is quite close to $\frac{\omega c}{C} = 2.95$).

Change in ε_2' and ε_2'' also affect the attenuation and phase constants. As might be expected, changing ε_2' has more of an

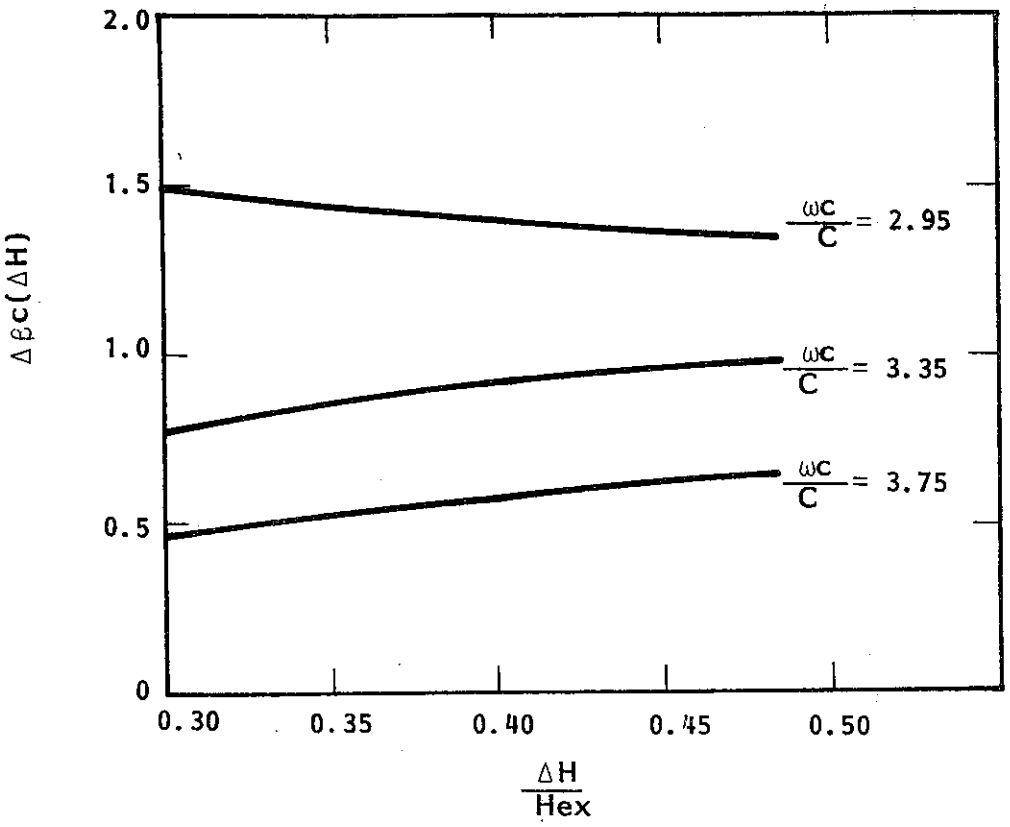

Figure 8-15. TE_{01} $\Delta\beta c\ (\Delta H) = \beta c\ (\Delta H) - \beta c\ (2\ \text{Layer})$ vs Linewidth for Various Frequencies. $\left(\frac{\omega c}{c}\right)$ Peak $\mu'' = 2.88$.

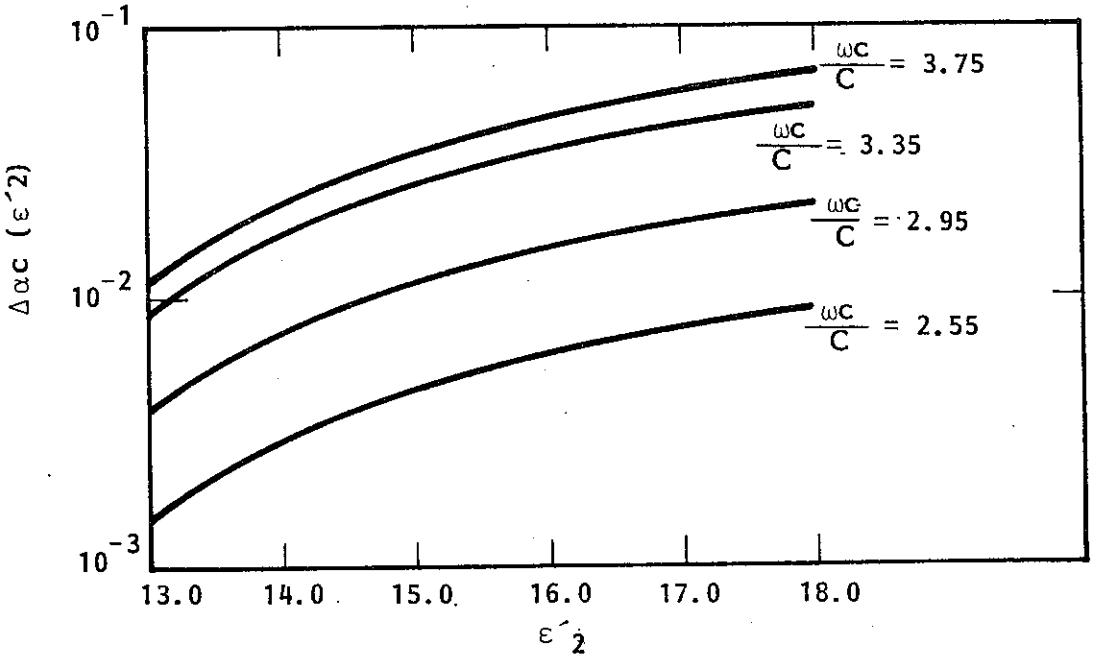

Figure 8-16. TE_{01} $\Delta\alpha c\ (\varepsilon_2') = \alpha c\ (\varepsilon_2') - \alpha c\ (\varepsilon_2' = 12)$ vs ε' for Various $\frac{\omega c}{c}$.

impact on βc than on αc. Figure 8-16 is a plot of $\Delta\alpha c\ (\varepsilon_2') = \alpha c\ (\varepsilon_2') - \alpha c\ (\varepsilon_2' = 12)$, showing the change in attenuation from the standard case as a function of ε_2'. The amount of change is a definite function of frequency, being nearly 10 times greater at $\frac{\omega c}{C} = 3.75$ than at $\frac{\omega c}{C} = 2.55$. However, even at $\frac{\omega c}{C} = 3.75$ and $\varepsilon' = 18$ the change amounts to only 0.07 -- about 9%.

The effect on βc is much more dramatic. Figure 8-17 demonstrates this with a plot of $\Delta\beta c\ (\varepsilon_2') = \beta c\ (\varepsilon_2') - \beta c$ (2-layer). It is seen that at $\frac{\omega c}{C} = 3.35$ a change in ε_2' from 12.0 to 18.0 changes $\Delta\beta c$ from 1.4 to 2.0 -- about 43%.

Figures 8-18 and 8-19 show the effects of various ε_2'' on the attenuation. Figure 8-18 plots αc against frequency for values of ε_2'' of 0.0, 1.0, and 2.0. The curves for $\varepsilon_2'' = 1.0$ and 2.0 display an interesting behavior at lower frequencies, curving sharply upward as they approach a certain limiting value of $\frac{\omega c}{C}$. This is much like the effect seen with the lossy dielectric cases where the attenuation usually took an abrupt upward leap as the frequency neared lossless cutoff.

Figure 8-19 is a plot of $\Delta\alpha c\ (\varepsilon_2'') = \alpha c\ (\varepsilon_2'') - \alpha c\ (\varepsilon_2'' = 0)$. The relationship between $\Delta\alpha c$ and ε_2'' is seen to be linear. This allows for a simple correction to be made in αc for changes in ε_2''.

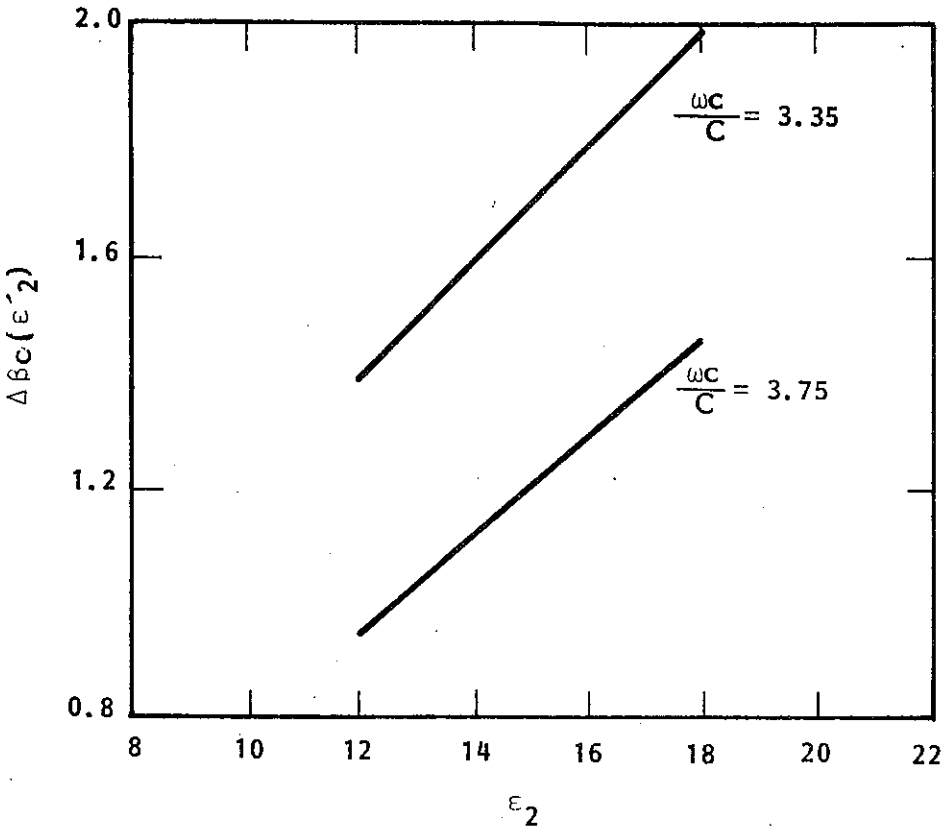

Figure 8-17. TE_{01} $\Delta\beta c\,(\varepsilon_2') = \beta c\,(\varepsilon_2') - \beta c\,(\varepsilon_2' = 12)$ vs ε' for Various $\frac{\omega c}{C}$.

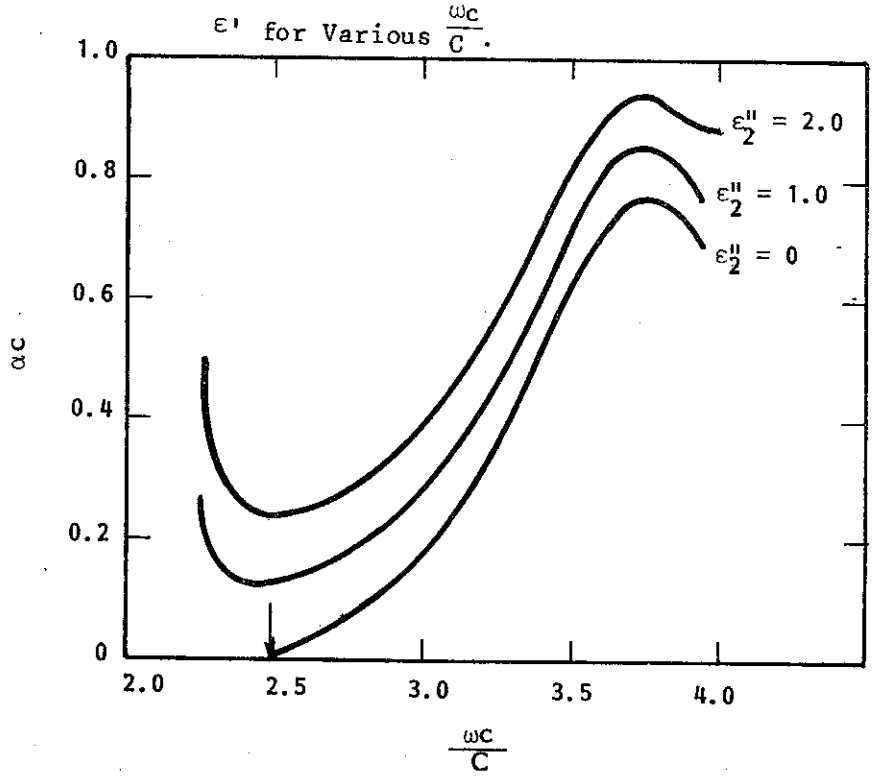

Figure 8-18. TE_{01} Attenuation vs Frequency for Various ε''. Arrow Shows Lossless Cutoff.

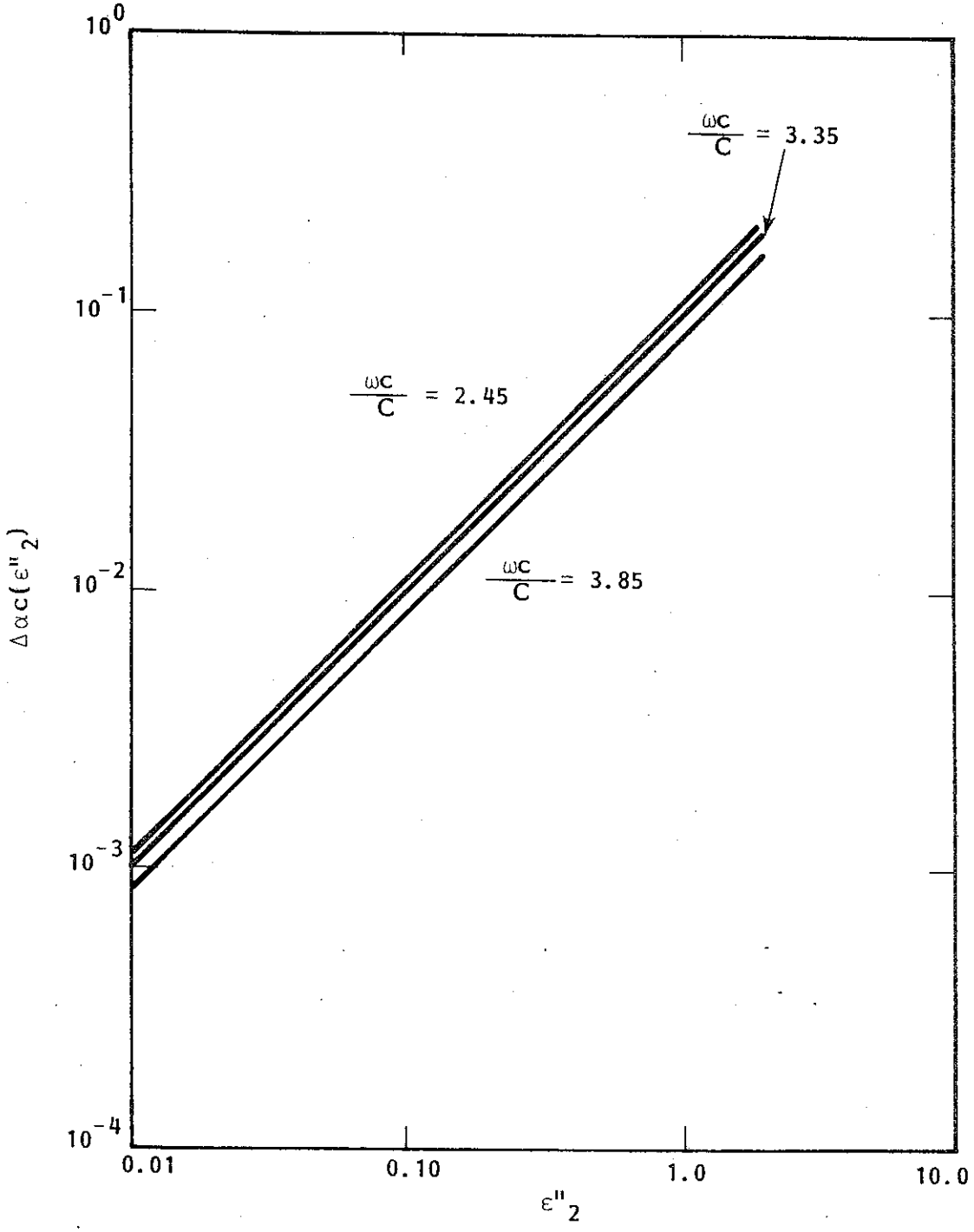

Figure 8-19. TE_{01} $\Delta\alpha_c$ (ε_2'') = α_c (ε_2'') - α_c ($\varepsilon_2'' = 0$) vs ε_2'' for Various Frequencies.

D. Comparison of Graphite and Ferrite for the Suppression of Fundamental Oscillations

There are a number of combinations of the ferrite parameters which would result in sufficient attenuation to suppress oscillation of the fundamental mode. Proper choice is determined primarily by the available materials. It is most important to make a correct choice of H_{an} to determine the frequency of peak attenuation. The linewidth is also an important factor. Smaller ΔH yields highly peaked attenuation while larger ΔH results in a wider, flatter spread. Other parameters are slightly less important. Smallest ε_2' is desired so that the shift in β is kept to a minimum, while highest ε_2'' results in more attenuation across the band. The magnetization affects both the position and the magnitude of the peak attenuation. A larger $4\pi M_s$ results in a larger αc which is shifted further away from the frequency of peak μ''. After all of these choices are made to determine the proper shape and position of the attenuation curve, w should be chosen so that oscillation could be prevented across the entire frequency band.

Two properties make the use of a ferrite liner less attractive than a graphite liner for attenuating the fundamental (TE_{01}) mode. First, a thicker sleeve of ferrite is required to provide an equivelant amount of attenuation. For example, at a frequency of $\frac{\omega c}{C} = 3.35$, Figure 8-14 shows that a thickness of ferrite of $w = 0.027$ is required to give $\alpha c = 0.92$, while Figure 7-15 shows that $\alpha c = 0.92$ is produced by a graphite thickness of $w = 0.000008$ (at $\varepsilon'' = 30{,}000$). Thus, an equivelant ferrite is nearly 4,000 times

thicker. A wider lossy layer might more severely perturb the waveguide fields, adversely affecting interaction.

Second, the thick ferrite layer causes a shift in the $\omega - \beta$ plot not seen in the graphite case. This removes the beam line from the waveguide mode line and reduces the fundamental interaction. Thus, if a ferrite layer is to be used, the amplifier should be redesigned so that the beam line would coincide with the shifted waveguide mode line.

A third property of the ferrite liner might prove either helpful or detrimental, depending on the behavior of the amplifier's lossless gain. If this gain is relatively flat across the band, the sharply peaked frequency response of the ferrite attenuator would result in an output that would be greater at the band edges than at the center frequency. However, if the lossless gain is more bell shaped, the attenuation would tend to smooth the resulting output.

The physical properties of the ferrite material are also an important consideration. When operated at high power levels the ferrite experiences large differences in temperature. The large temperature dependence of many of the ferrite parameters could cause a troublesome variation in attenuation with the power level used.

E. Solution for the TE_{02} Mode

It was suggested earlier that a useful application of frequency-dependent ferrite loss might lie in the attenuation of higher-order modes. The peak of the attenuation curve can be placed at the intersection of the TE_{02} waveguide mode and the s=2 beam line by selecting a proper value of H_{an}. The attenuation at this frequency

should be sufficient to prevent second-order oscillations while the attenuation at low frequencies will not adversely affect the TE_{01} mode.

To investigate this possibility, a three-layer dielectric/ferrite-loaded waveguide is considered. The waveguide is assumed to have the properties listed in Table 8-3 except that $\frac{\Delta H}{H_{ex}}$ is chosen to be 0.194 to give highest possible loss and the frequency of maximum μ'' is selected from Figure 8-13 to make the attenuation peak at $\frac{\omega c}{C} = 4.82$. It is found that peak attenuation occurs at $\frac{\omega c}{C} = 4.82$ when μ'' is made to peak at $\frac{\omega c}{C} = 4.3$. This necessitates a value of $\frac{H_{an}}{H_{ex}} = 0.654$. Figure 8-20 shows how the parameters μ', μ_a', and $\mu'' \cong \mu_a''$ vary with frequency under these conditions.

The dispersion equation (A4.17) has been solved for the TE_{02} mode using the conditions above and various values of $w = \frac{b}{c} - \frac{a}{c}$. Figure 8-21 is a plot of the resulting ω-β diagram for $w = 6.2 \times 10^{-2}$. As is usually seen to be the case, the ω-β curve has shifted to the right with the addition of loss. Figure 8-22 shows how the attenuation behaves as a function of frequency for two values of ferrite thickness. A peak in attenuation is very apparent near $\frac{\omega c}{C} = 4.82$, as predicted. A large amount of attenuation is also seen to occur at higher frequencies, giving the curves an interesting saddle shape. At lower frequencies, there is the usual rapid rise in αc near lossless cutoff. The values of attenuation being reached in these plots are much less than those achieved for the TE_{01} case.

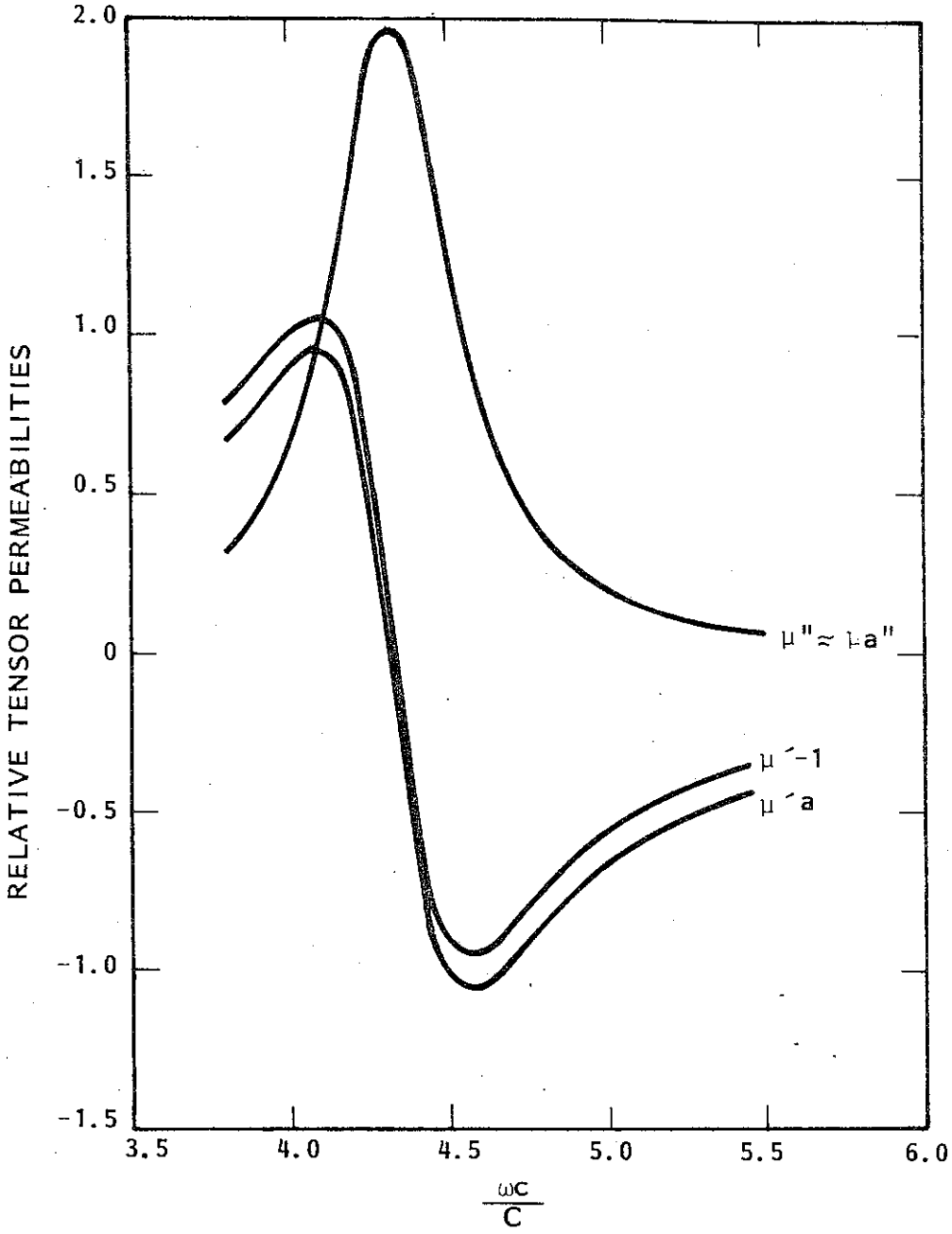

Figure 8-20. $\mu'-1$, μ_a', and μ'' vs Frequency. $\left(\frac{\omega c}{C}\right)$ Peak μ'' = 4.3, $\frac{\Delta H}{H_{ex}}$ = 0.194.

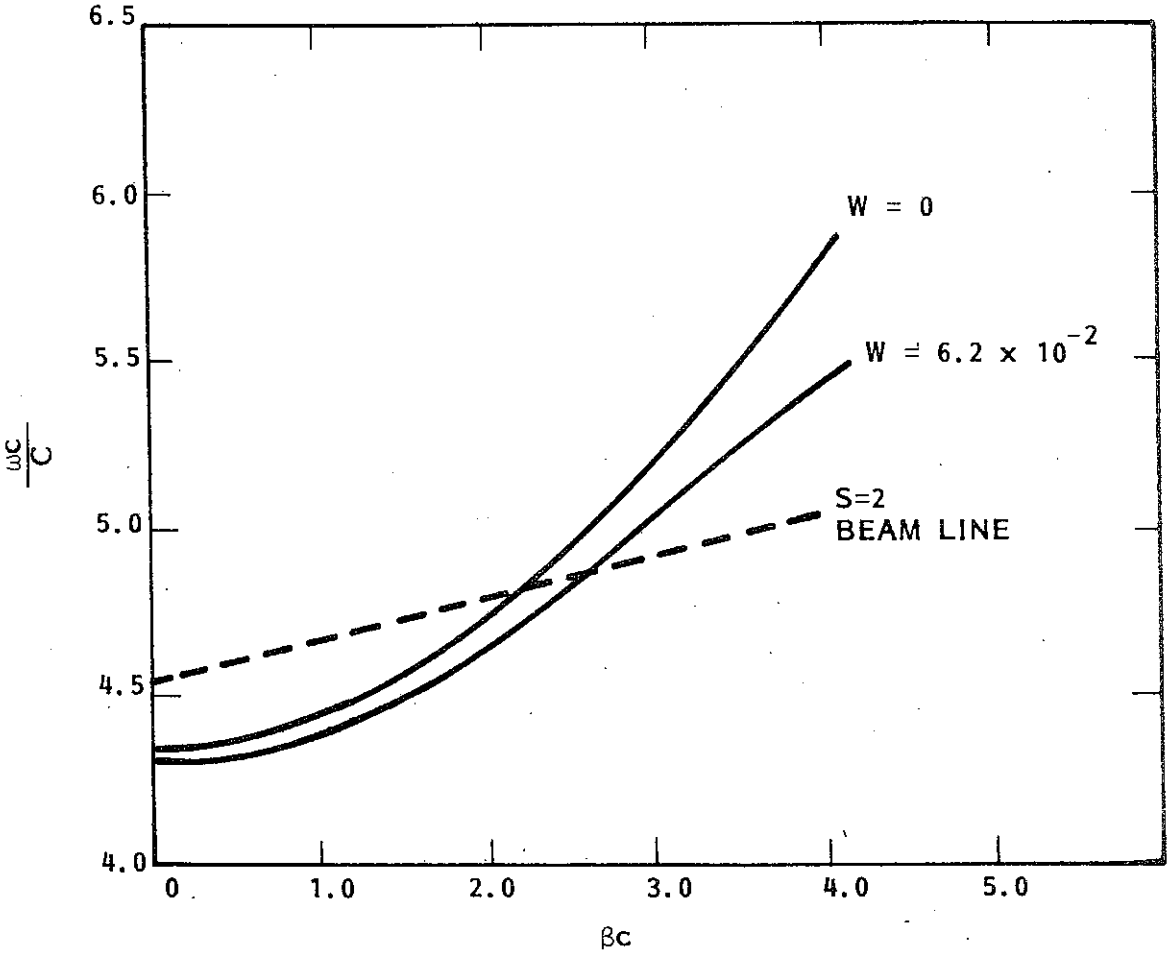

Figure 8-21. TE_{02} $\omega - \beta$ Plot for $\left(\frac{\omega c}{c}\right)$ Peak $\mu'' = 4.3$, $\frac{\Delta H}{H_{ex}} = 0.194$.

However, they are comparable to those produced by graphite. Figure 7-26 shows that a layer of graphite with $w = 6 \times 10^{-2}$ produces $\alpha c = 1.3 \times 10^{-2}$. For a similar layer of ferrite, $\alpha c = 1.6 \times 10^{-2}$.

F. Comparison of Graphite and Ferrite for the Suppression of TE_{02} Oscillations

Any amount of graphite that is used to attenuate the TE_{02} mode will also affect the TE_{01} mode -- and to a greater extent. Figure 7-17 shows that thicknesses of graphite only on the order of $w = 2 \times 10^{-6}$ can be used in the amplifier. Anything larger will have an overly detrimental effect on the fundamental interaction. Figure 7-25 reveals that for $\varepsilon'' = 30{,}000$, $w = 2 \times 10^{-6}$ produces a TE_{02} attenuation of only $\alpha c = 0.0005$. This small value, coupled with the fact that graphite must be applied in a pattern along just a portion of the tube, seems to shed doubt on its value as a TE_{02} attenuator.

A ferrite does not have this limitation. If the attenuation is centered on the $TE_{02}/s=2$ crossover, analysis shows that the TE_{01} mode will not be seriously attenuated. Figure 8-22 shows that a thickness of $w = 6.2 \times 10^{-2}$ gives a TE_{02} attenuation as large as $\alpha c = 0.016$. Even larger thicknesses can be used without adverse attenuation of the TE_{01} wave. Figure 8-23 shows a plot of TE_{02} attenuation vs thickness. It is seen that αc rises very quickly as w is increased. Thus, fairly large values of αc can probably be achieved without too much widening of the ferrite liner. To determine exactly the necessary value of αc to suppress oscillations, the amount of TE_{02} interaction needs to be known. As mentioned earlier, this has not been an objective of this investigation.

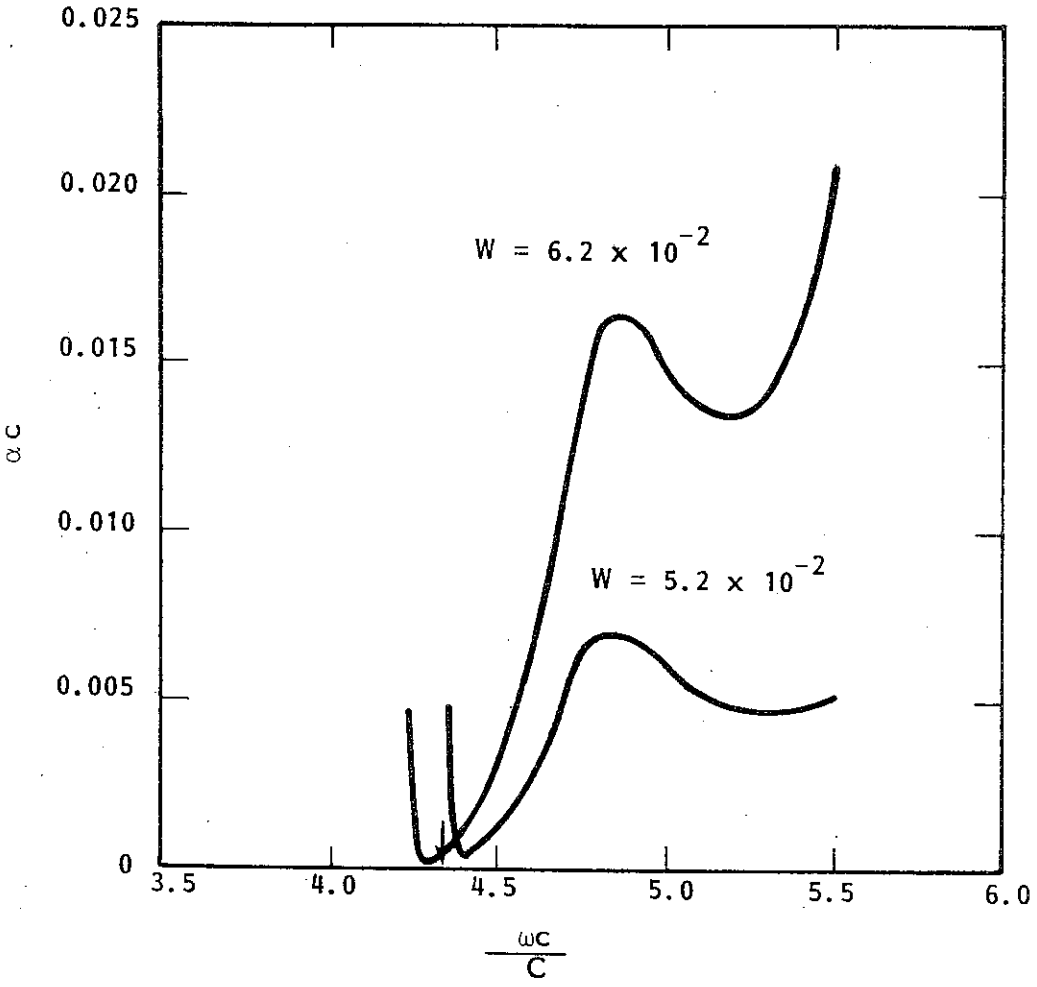

Figure 8-22. TE_{02} Attenuation vs Frequency for $\left(\frac{\omega c}{C}\right)$ Peak μ'' = 4.3, $\frac{\Delta H}{H_{ex}}$ = 0.194, and Various w. Arrow Indicates Lossless Cutoff.

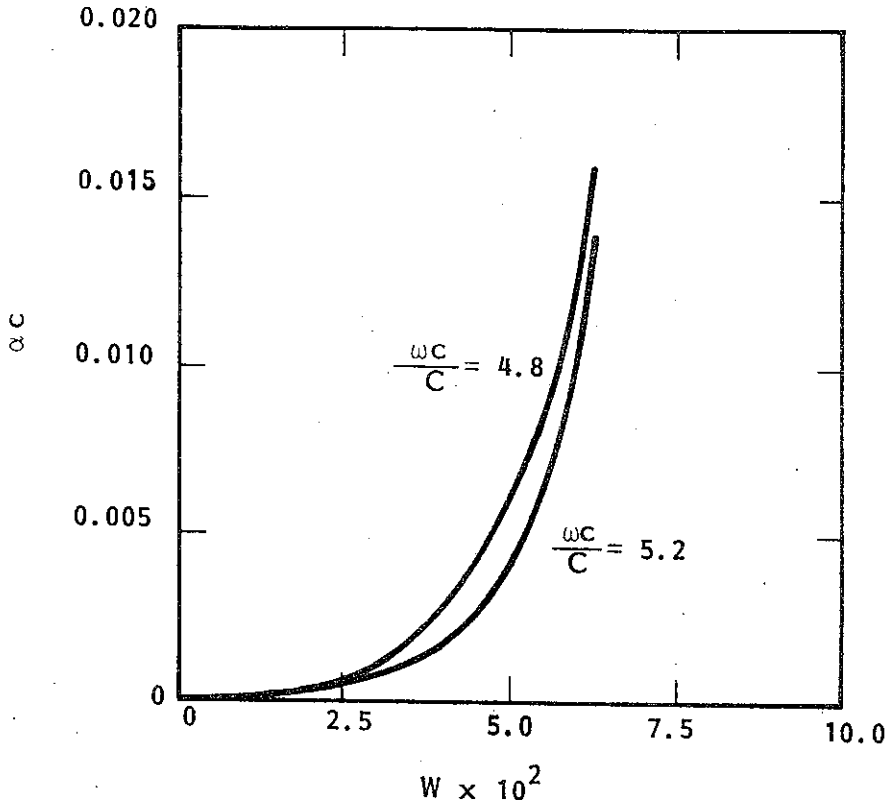

Figure 8-23. TE_{02} Attenuation vs Thickness for $\left(\frac{\omega c}{C}\right)$ Peak μ'' = 4.3, $\frac{\Delta H}{H_{ex}}$ = 0.194, and Various Frequencies.

The use of a ferrite layer is not without its drawbacks, however. Even though the TE_{01} mode is not overly attenuated by the addition of the ferrite, its phase constant is affected. Adding such a thick layer of material with a dielectric constant of 12 to 18 causes the TE_{01} ω-β plot to shift considerably to the right. The thicker the layer, the larger the shift. Thus, if a ferrite is to be used to attenuate the TE_{02} mode, the beam line must be adjusted to compensate for this shift, or fundamental interaction will cease.

IX. CONCLUSIONS

This study dealt with two major tasks: 1) to find the effect of a lossy charge suppression layer on the propagation characteristics of the dielectric-loaded waveguide slow-wave structure; 2) to determine the amount and form of loss needed to suppress various parasitic oscillations in an amplifier using the structure. To these ends, three separate analyses were employed: a two-layer analysis, a three-layer graphite analysis, and a three-layer ferrite analysis. In each case the proper dispersion relation was derived and solved for the phase and attenuation constants of the wave.

The three-layer graphite analysis determined that a graphite layer used to suppress charge build-up in the dielectric liner must be kept much less than a skin depth in thickness. A heavier layer would result in an unacceptable amount of attenuation of the fundamental mode. Since there exists a minimum depth of material which must be applied, it was decided that pure graphite is too lossy to use for this purpose. The effect of this layer on the phase constant of the wave was also determined. It was found that a thickness of a hundredth of a skin depth or so would cause only a negligible change in β.

The necessary thickness and conductivity of a lossy layer used to suppress oscillations of the fundamental mode was calculated by the three-layer analysis. Both the three- and two-layer analyses revealed that this loss would not affect the phase constant of the wave to the extent of threatening fundamental interaction. The two-layer analysis also showed that the shape of the radial component of the rf field distributions remained fairly constant with the addition of loss.

A three-layer ferrite analysis was employed to determine the feasibility of using a ferrite material as an attenuator. It was found that graphite is a better choice for attenuating the fundamental (TE_{01}) mode, while a ferrite would be well suited for attenuating higher-order modes where graphite is ineffective.

The peak of the frequency-dependent ferrite loss can be adjusted to nearly any desired frequency, thus producing a very useful selective loss.

Appendix 1: Derivation of the Three-Layer Dielectric-Loaded Waveguide Dispersion Relation

The derivation in this appendix paterns that of Harrington [10] who derives the two-layer n = 0 form of the dispersion relation.

The three-layer dielectric-loaded waveguide is analyzed as an infinitely long, circular structure as shown in Figure A1-1. Three separate dielectric regions, denoted by the subscripts 1, 2, and 3 from innermost to outermost, are surrounded by a thin, perfectly conducting metallic shell. The electromagnetic properties of region i (i = 1, 2, 3) are determined by the region's permeability, μ_i, and its permittivity, ε_i.

The scalar wave functions for this structure must obey the scalar Helmholz equation. Written in the cylindrical coordinate system of Figure A1-2, this is:

$$\frac{1}{\rho}\frac{\partial}{\partial\rho}\left(\rho\frac{\partial\psi}{\partial\rho}\right)+\frac{1}{\rho^2}\frac{\partial^2\psi}{\partial\phi^2}+\frac{\partial^2\psi}{\partial z^2}+k^2\psi=0 \qquad \text{(A1.1)}$$

where: ψ = scalar wave function

ρ = radial variable

ϕ = azimuthal variable

z = axial variable

k = propagation constant

The standard method for solving equation (A1.1) uses the separation of variables. This suggests a solution of the form:

$$\psi = R(\rho)\,\Phi(\phi)\,Z(z). \qquad \text{(A1.2)}$$

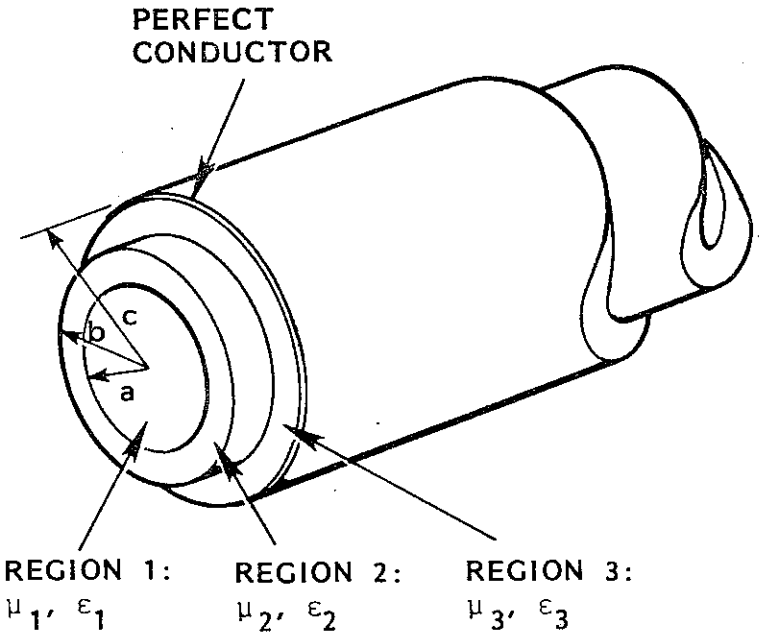

Figure A1-1. Infinitely Long Three-Layer Dielectric-Loaded Waveguide.

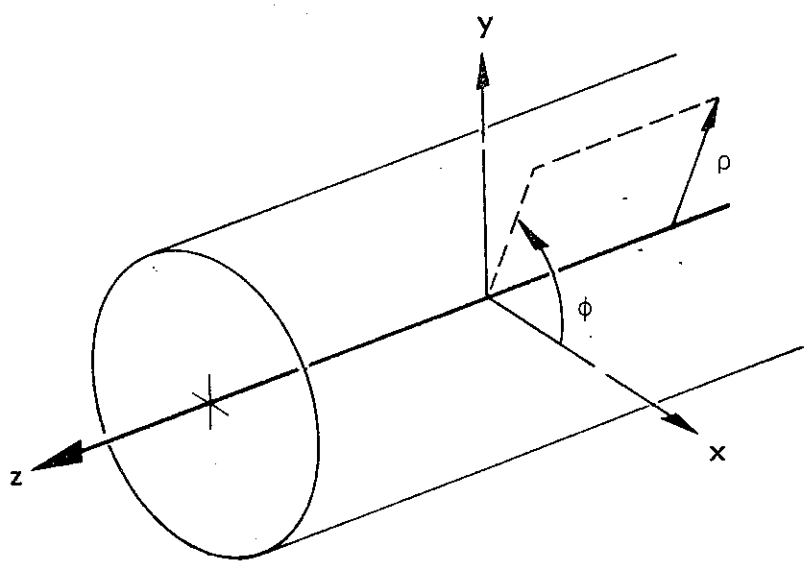

Figure A1-2. Cylindrical Coordinate System Used in Analyzing the Three-Layer Waveguide.

Upon substitution of (A1.2) and division by ψ, (A1.1) becomes:

$$\frac{1}{\rho R}\frac{d}{d\rho}\left(\rho\frac{dR}{d\rho}\right) + \frac{1}{\rho^2\Phi}\frac{d^2\Phi}{d\phi^2} + \frac{1}{Z}\frac{d^2Z}{dz^2} + k^2 = 0. \qquad \text{(A1.3)}$$

The third term of (A1.3) is independent of ϕ and z and so must be equal to a constant if the equation is to hold for all z. Thus:

$$\frac{1}{Z}\frac{d^2Z}{dz^2} = -k_z^2. \qquad \text{(A1.4)}$$

Substituting (A1.4) into (A1.3) and multiplying by ρ^2 gives:

$$\frac{\rho}{R}\frac{d}{d\rho}\left(\rho\frac{dR}{d\rho}\right) + \frac{1}{\Phi}\frac{d^2\Phi}{d\phi^2} + (k^2 - k_z^2)\rho^2 = 0. \qquad \text{(A1.5)}$$

Since the second term of (A1.5) is independent of ρ and z, let:

$$\frac{1}{\Phi}\frac{d^2\Phi}{d\phi^2} = -n^2. \qquad \text{(A1.6)}$$

Now, defining k_ρ by:

$$k_\rho^2 + k_z^2 = k^2, \qquad \text{(A1.7)}$$

and substituting it into (A1.5) results in the set of separated equations:

$$\rho\frac{d}{d\rho}\left(\rho\frac{dR}{d\rho}\right) + [(k_\rho\rho)^2 - n^2]R = 0 \qquad \text{(A1.8)}$$

$$\frac{d^2\Phi}{d\phi^2} + n^2\Phi = 0 \qquad \text{(A1.9)}$$

$$\frac{d^2Z}{dz^2} + k_z^2 Z = 0. \qquad \text{(A1.10)}$$

Equations (A1.9) and (A1.10) have simple solutions of harmonic functions. Equation (A1.8) is more complex. It is known as Bessel's equation of order n and argument $k_\rho\rho$. Solutions to Bessel's equation will be written in general as:

$$R = B_n(k_\rho\rho). \qquad \text{(A1.11)}$$

Common functions used for $B_n(k_\rho\rho)$ are: $J_n(k_\rho\rho)$, the Bessel function of the first kind; $Y_n(k_\rho\rho)$, the Bessel function of the second kind;

$H_n^{(1)}(k_\rho\rho)$, the Hankel function of the first kind; and $H_n^{(2)}(k_\rho\rho)$, the Hankel function of the second kind. Since the Hankel functions can be written as complex combinations of Y_n and J_n, any two of the above four functions can be taken as linearly independent solutions to (A1.8). The simplest choice is J_n and Y_n, so let:

$$B_n(k_\rho\rho) = C_1 J_n(k_\rho\rho) + C_2 Y_n(k_\rho\rho). \tag{A1.12}$$

Solutions to (A1.9) and (A1.10) can be written as:

$$Z(z) = e^{-jk_z z} \tag{A1.13}$$

$$\Phi(\phi) = \cos(n\phi) \text{ for TM waves} \tag{A1.14}$$

$$\Phi(\phi) = \sin(n\phi) \text{ for TE waves} \tag{A1.15}$$

and, from equation (A1.2), the scalar wave functions are written as:

$$\psi_n^m(k_\rho\rho) = C_1 B_n^m(k_\rho\rho)\cos(n\phi)\, e^{-jk_z z} \text{ for TM waves} \tag{A1.16}$$
$$\psi_n^e(k_\rho\rho) = C_2 B_n^e(k_\rho\rho)\sin(n\phi)\, e^{-jk_z z} \text{ for TE waves}$$

where C_1, C_2 are constants.

Equation (A1.7) can be written in each of the dielectric regions:

$$\begin{aligned} k_{\rho 1}^2 + k_z^2 &= k_1^2 = \omega^2 \mu_1 \varepsilon_1 \\ k_{\rho 2}^2 + k_z^2 &= k_2^2 = \omega^2 \mu_2 \varepsilon_2 \\ k_{\rho 3}^2 + k_z^2 &= k_3^2 = \omega^2 \mu_3 \varepsilon_3 \end{aligned} \tag{A1.17}$$

where ω is the wave's radian frequency.

Thus, the scalar wave function can be written in each region as:

$$\begin{aligned} \psi_n^{m1}(k_{\rho 1}\rho) &= A B_n^{m1}(k_{\rho 1}\rho)\cos(n\phi)\, e^{-jk_z z} \\ \psi_n^{e1}(k_{\rho 1}\rho) &= B B_n^{e1}(k_{\rho 1}\rho)\sin(n\phi)\, e^{-jk_z z} \\ \psi_n^{m2}(k_{\rho 2}\rho) &= C B_n^{m2}(k_{\rho 2}\rho)\cos(n\phi)\, e^{-jk_z z} \\ \psi_n^{e2}(k_{\rho 2}\rho) &= D B_n^{e2}(k_{\rho 2}\rho)\sin(n\phi)\, e^{-jk_z z} \\ \psi_n^{m3}(k_{\rho 3}\rho) &= E B_n^{m3}(k_{\rho 3}\rho)\cos(n\phi)\, e^{-kk_z z} \\ \psi_n^{e3}(k_{\rho 3}\rho) &= F B_n^{e3}(k_{\rho 3}\rho)\sin(n\phi)\, e^{-jk_z z} \end{aligned} \tag{A1.18}$$

where A, B, C, D, E, F are constants.

Here the solutions to Bessel's equation in each of the three regions are given by (A1.12) as:

$$
\begin{aligned}
A\ B_n^{m1}(k_{\rho 1}\rho) &= A_1 J_n(k_{\rho 1}\rho) + A_2 Y_n(k_{\rho 1}\rho) \\
B\ B_n^{e1}(k_{\rho 1}\rho) &= B_1 J_n(k_{\rho 1}\rho) + B_2 Y_n(k_{\rho 1}\rho) \\
C\ B_n^{m2}(k_{\rho 2}\rho) &= C_1 J_n(k_{\rho 2}\rho) + C_2 Y_n(k_{\rho 2}\rho) \\
D\ B_n^{e2}(k_{\rho 2}\rho) &= D_1 J_n(k_{\rho 2}\rho) + D_2 Y_n(k_{\rho 2}\rho) \\
E\ B_n^{m3}(k_{\rho 3}\rho) &= E_1 J_n(k_{\rho 3}\rho) + E_2 Y_n(k_{\rho 3}\rho) \\
F\ B_n^{e3}(k_{\rho 3}\rho) &= F_1 J_n(k_{\rho 3}\rho) + F_2 Y_n(k_{\rho 3}\rho)
\end{aligned}
\qquad \text{(A1.19)}
$$

Since region 1 contains the point $\rho = 0$ and $Y_n(0)$ is not defined, the constants A_2 and B_2 must be zero.

To derive the dispersion relation, it is necessary to know the electric and magnetic fields in each dielectric region. The partial fields can be obtained from the scalar wave function, ψ, by:

$$
\begin{aligned}
E_\rho &= \frac{1}{j\omega\varepsilon}\frac{\partial^2 \psi^m}{\partial\rho\,\partial z} & H_\rho &= \frac{1}{\rho}\frac{\partial \psi^m}{\partial \psi} \\
E\phi &= \frac{1}{j\omega\varepsilon\rho}\frac{\partial^2 \psi^m}{\partial\phi\,\partial z} & H_\phi &= -\frac{\partial \psi^m}{\partial\rho} \\
E_z &= \frac{1}{j\omega\varepsilon}\left(\frac{\partial^2}{\partial z^2} + k^2\right)\psi^m & H_z &= 0
\end{aligned}
\qquad \text{(A1.20)}
$$

for TM waves, and by:

$$
\begin{aligned}
E_\rho &= -\frac{1}{\rho}\frac{\partial \psi^e}{\partial\phi} & H_\rho &= \frac{1}{j\omega\mu}\frac{\partial^2 \psi^e}{\partial\rho\,\partial z} \\
E_\phi &= \frac{\partial \psi^e}{\partial\rho} & H_\phi &= \frac{1}{j\omega\mu\rho}\frac{\partial^2 \psi^e}{\partial\phi\,\partial z} \\
E_z &= 0 & H_z &= \frac{1}{j\omega\mu}\left(\frac{\partial^2}{\partial z^2} + k^2\right)\psi^e
\end{aligned}
\qquad \text{(A1.21)}
$$

For TE waves. The total electric and magnetic field in each region is given by the sum of the TE and TM fields in that region. Except

for the special case of n = 0, there will always be contributions from both TE and TM components. This leads to the propagation of hybrid modes, which are not purely TE or TM.

The important field components are those which will be used to impose the boundary conditions. These fields in region i (where i = 1, 2, 3) are found to be:

$$H_z = 0 + \frac{k_{\rho i}^2}{j\omega\mu_i} K B_n^{ei} (k_{\rho i}\rho) \sin(n\phi)\, e^{-jk_z z}$$

$$E_z = \frac{k_{\rho i}^2}{j\omega\varepsilon_i} K B_n^{mi} (k_{\rho i}\rho) \cos(n\phi)\, e^{-jk_z z} + 0$$

$$H\phi = -k_{\rho i} K B_n^{mi'} (k_{\rho i}\rho) \cos(n\phi)\, e^{-jk_z z} - \frac{nk_z}{\omega\mu_i \rho} K B_n^{ei} (k_{\rho i}\rho) \cos(n\phi)\, e^{-jk_z z} \qquad \text{(A1.22)}$$

$$E\phi = \frac{nk_z}{\omega\varepsilon_i \rho} K B_n^{mi} (k_{\rho i}\rho) \sin(n\phi)\, e^{-jk_z z} + k_{\rho i} K B_n^{ei'} (k_{\rho i}\rho) \sin(n\phi)\, e^{-jk_z z}$$

where: K = appropriate constant from (A1.19).

The boundary conditions require that the field components H_z, E_z, $H\phi$, and $E\phi$ be continuous at $\rho = a$ and at $\rho = b$. At $\rho = c$ the fields impinge on a perfect conductor so E_z and $E\phi$ must vanish. Equating these field components across the boundary and at the walls will yield ten simultaneous equations in the ten unknown constants, A_1,

B_1, C_1, C_2, D_1, D_2, E_1, E_2, F_1, and F_2. Using the boundary condition at $\rho = c$ to eliminate E_2 and F_2 gives a system of eight equations:

$$1. \quad \frac{k_{\rho 1}^2}{\mu_1} B_1 J_n(k_{\rho 1}a) - \frac{k_{\rho 2}^2}{\mu_2} [D_1 J_n(k_{\rho 2}a) + D_2 Y_n(k_{\rho 2}a)] = 0$$

$$2. \quad \frac{k_{\rho 1}^2}{\varepsilon_1} A_1 J_n(k_{\rho 1}a) - \frac{k_{\rho 2}^2}{\varepsilon_2} [C_1 J_n(k_{\rho 2}a) + C_2 Y_n(k_{\rho 2}a)] = 0$$

$$3. \quad -k_{\rho 1} A_1 J_n'(k_{\rho 1}a) - \frac{nk_z}{\omega \mu_1 a} B_1 J_n(k_{\rho 1}a) + k_{\rho 2} [C_1 J_n'(k_{\rho 2}a) + C_2 Y_n'(k_{\rho 2}a)] + \frac{nk_z}{\omega \mu_2 a} [D_1 J_n(k_{\rho 2}a) + D_2 Y_n(k_{\rho 2}a)] = 0 \qquad \text{(A1.23)}$$

$$4. \quad \frac{nk_z}{\omega \varepsilon_1 a} A_1 J_n(k_{\rho 1}a) + k_{\rho 1} B_1 J_n'(k_{\rho 1}a) - \frac{nk_z}{\omega \varepsilon_2 a} [C_1 J_n(k_{\rho 2}a) + C_2 Y_n(k_{\rho 2}a)] - k_{\rho 2} [D_1 J_n'(k_{\rho 2}a) + D_2 Y_n'(k_{\rho 2}a)] = 0$$

$$5. \quad \frac{k_{\rho 2}^2}{\mu_2} [D_1 J_n(k_{\rho 2}b) + D_2 Y_n(k_{\rho 2}b)] - \frac{k_{\rho 3}^2}{\mu_3} F_1 \left[J_n(k_{\rho 3}b) - Y_n(k_{\rho 3}b) \frac{J_n'(k_{\rho 3}c)}{Y_n'(k_{\rho 3}c)} \right] = 0$$

$$6. \quad \frac{k_{\rho 2}^2}{\varepsilon_2} [C_1 J_n(k_{\rho 2}b) + C_2 Y_n(k_{\rho 2}b)] - \frac{k_{\rho 3}^2}{\varepsilon_3} E_1 \left[J_n(k_{\rho 3}b) - Y_n(k_{\rho 3}b) \frac{J_n(k_{\rho 3}c)}{Y_n(k_{\rho 3}c)} \right] = 0$$

$$7.\quad -k_{\rho 2}\,[C_1\,J_n'\,(k_{\rho 2}b) + C_2\,Y_n'\,(k_{\rho 2}b)] - \frac{nk_z}{\omega\mu_{2b}}\,[D_1\,J_n\,(k_{\rho 2}b) + D_2\,Y_n\,(k_{\rho 2}b)] + k_{\rho 3}\,E_1\,[J_n'\,(k_{\rho 3}b) - Y_n'\,(k_{\rho 3}b)\,\frac{J_n\,(k_{\rho 3}c)}{Y_n\,(k_{\rho 3}c)}\,] + \frac{nk_z}{\omega\mu_{3b}}\,F_1\,[J_n\,(k_{\rho 3}b) - Y_n\,(k_{\rho 3}b)\,\frac{J_n'\,(k_{\rho 3}c)}{Y_n'\,(k_{\rho 3}c)}\,] = 0$$

$$8.\quad \frac{nk_z}{\omega\varepsilon_{2b}}\,[C_1\,J_n\,(k_{\ 2}b) + C_2\,Y_n\,(k_{\rho 2}b)] + k_{\rho 2}\,[D_1\,J_n'\,(k_{\rho 2}b) + D_2\,Y_n'\,(k_{\rho 2}b)] - \frac{nk_z}{\omega\varepsilon_{3b}}\,E_1\,[J_n\,(k_{\rho 3}b) - Y_n\,(k_{\rho 3}b)\,\frac{J_n\,(k_{\rho 3}c)}{Y_n\,(k_{\rho 3}c)}\,] - k_{\rho 3}\,F_1\,[J_n'\,(k_{\rho 3}b) - Y_n'\,(k_{\rho 3}b)\,\frac{J_n'\,(k_{\rho 3}c)}{Y_n'\,(k_{\rho 3}c)}\,] = 0.$$

Since all of these equations are equal to zero the only non-trivial solution will occur when the determinant of the coefficient matrix is zero. The equation which results from this condition is called the dispersion relation. This equation describes the relationship between ω, the radian frequency of the wave, and k_z, the axial propagation constant, which insures non-zero fields in the waveguide.

For compactness let:

$$\begin{aligned}
U_1 &= J_n\,(k_{\rho 1}a) & U_1' &= J_n'\,(k_{\rho 1}a)\\
U_2 &= J_n\,(k_{\rho 2}a) & U_2' &= J_n'\,(k_{\rho 2}a)\\
U_3 &= Y_n\,(k_{\rho 2}a) & U_3' &= Y_n'\,(k_{\rho 2}a)\\
U_4 &= J_n\,(k_{\rho 2}b) & U_4' &= J_n'\,(k_{\rho 2}b)\\
U_5 &= Y_n\,(k_{\rho 2}b) & U_5' &= Y_n'\,(k_{\rho 2}b)\\
U_6 &= J_n\,(k_{\rho 3}b) & U_6' &= J_n'\,(k_{\rho 3}b)\\
U_7 &= Y_n\,(k_{\rho 3}b) & U_7' &= Y_n'\,(k_{\rho 3}b)\\
U_8 &= J_n\,(k_{\rho 3}c) & U_8' &= J_n'\,(k_{\rho 3}c)\\
U_9 &= Y_n\,(k_{\rho 3}c) & U_9' &= Y_n'\,(k_{\rho 3}c).
\end{aligned} \qquad \text{(A1.24)}$$

Then, the determinant of equation (A1.25) provides the dispersion relation. The columns in the determinant marked TE arise from the TE contributions of the fields, and those marked TM come from the TM contributions. This determinant can be evaluated either numerically, by computer, or algebraically.

TM	TE	TM	TM	TE	TE	TM	TE
A_1	B_1	C_1	C_2	D_1	D_2	E_1	F_1
0	$\frac{k_{\rho 1}^2}{\mu_1} U_1$	0	0	$\frac{-k_{\rho 1}^2}{\mu_2} U_2$	$\frac{-k_{\rho 2}^2}{\mu_2} U_3$	0	0
$\frac{k_{\rho 1}^2}{\varepsilon_1} U_1$	0	$\frac{-k_{\rho 2}^2}{\varepsilon_2} U_2$	$\frac{-k_{\rho 2}^2}{\varepsilon_2} U_3$	0	0	0	0
$-k_{\rho 1} U_1'$	$\frac{-nk_z}{\omega \mu_1 a} U_1$	$k_{\rho 2} U_2'$	$k_{\rho 2} U_3'$	$\frac{nk_z}{\omega \mu_2 a} U_2$	$\frac{nk_z}{\omega \mu_2 a} U_3$	0	0
$\frac{nk_z}{\omega \varepsilon_1 a} U_1$	$k_{\rho 1} U_1'$	$\frac{-nk_z}{\omega \varepsilon_2 a} U_2$	$\frac{-nk_z}{\omega \varepsilon_2 a} U_3$	$-k_{\rho 2} U_2'$	$-k_{\rho 2} U_3'$	0	0
0	0	0	0	$\frac{k_{\rho 2}^2}{\mu_2} U_4$	$\frac{k_{\rho 2}^2}{\mu_2} U_5$	0	$\frac{-k_{\rho 3}^2}{\mu_3} [U_6 - U_7 \frac{U_8'}{U_9'}]$
0	0	$\frac{k_{\rho 2}^2}{\varepsilon_2} U_4$	$\frac{k_{\rho 2}^2}{\varepsilon_2} U_5$	0	0	$-k_{\rho 3}^2 [U_6 - U_7 \frac{U_8}{U_9}]$	0
0	0	$-k_{\rho 2} U_4'$	$-k_{\rho 2} U_5'$	$\frac{-nk_z}{\omega \mu_2 b} U_4$	$\frac{-nk_z}{\omega \mu_2 b} U_5$	$k_{\rho 3} [U_6' - U_7' \frac{U_8}{U_9}]$	$\frac{nk_z}{\omega \mu_3 b} [U_6 - U_7 \frac{U_8'}{U_9'}]$
0	0	$\frac{nk_z}{\omega \varepsilon_2 b} U_4$	$\frac{nk_z}{\omega \varepsilon_2 b} U_5$	$k_{\rho 2} U_4'$	$k_{\rho 2} U_5'$	$\frac{-nk_z}{\omega \varepsilon_3 b} [U_6 - U_7 \frac{U_8}{U_9}]$	$-k_{\rho 3} [U_6' - U_7' \frac{U_8'}{U_9'}]$

$= 0$ (A1.25)

The latter method yields an actual equation for the dispersion relation and shall be carried out here.

To make the calculation of the determinant simpler, the system of eight equations can be reduced to a system of four equations by the elimination of A_1, B_1, E_1, and F_1. Carrying this through yields the four by four determinant:

$$\begin{vmatrix} k_{\rho 2}\,[U_2'-G_4\,U_2] & k_{\rho 2}\,[U_3'-G_4\,U_3] & \frac{nk_z}{\omega\mu_{2a}}\,U_2\,K_1 & \frac{nk_z}{\omega\mu_{2a}}\,U_3\,K_1 \\ \frac{nk_z}{\omega\varepsilon_{2a}}\,U_2\,K_1 & \frac{nk_z}{\omega\varepsilon_{2a}}\,U_3\,K_1 & k_{\rho 2}\,[U_2'-G_3\,U_2] & k_{\rho 2}\,[U_3'-G_3\,U_3] \\ k_{\rho 2}\,[U_4'-G_2\,U_4] & k_{\rho 2}\,[U_5'-G_2\,U_5] & \frac{nk_z}{\omega\mu_{2b}}\,U_4\,K_3 & \frac{nk_z}{\omega\mu_{2b}}\,U_5\,K_3 \\ \frac{nk_z}{\omega\varepsilon_{2b}}\,U_4\,K_3 & \frac{nk_z}{\omega\varepsilon_{2b}}\,U_5\,K_3 & k_{\rho 2}\,[U_4'-G_1\,U_4] & k_{\rho 2}\,[U_5'-G_1\,U_5] \end{vmatrix} = 0$$

where:

$$G_1 = \frac{k_{\rho 2}\,\mu_3\,f_4}{k_{\rho 3}\,\mu_2\,f_3} \qquad G_2 = \frac{k_{\rho 2}\,\varepsilon_3\,f_2}{k_{\rho 3}\,\varepsilon_2\,f_1}$$

$$G_3 = \frac{k_{\rho 2}\,\mu_1\,U_1'}{k_{\rho 1}\,\mu_2\,U_1} \qquad G_4 = \frac{k_{\rho 2}\,\varepsilon_1\,U_1'}{k_{\rho 1}\,\varepsilon_2\,U_1} \qquad \text{(A1.26)}$$

$$f_1 = U_6\,U_9 - U_7\,U_8$$

$$f_2 = U_6'\,U_9 - U_7'\,U_8$$

$$f_3 = U_6\,U_9' - U_7\,U_8'$$

$$f_4 = U_6'\,U_9' - U_7'\,U_8'$$

$$K_1 = 1 - \frac{k_{\rho 2}^2}{k_{\rho 1}^2} \qquad K_3 = 1 - \frac{k_{\rho 2}^2}{k_{\rho 3}^2}\,.$$

This determinant can be evaluated very simply by expanding in minors. In schematic form, this is written as:

$$\begin{vmatrix} A & B & C & D \\ E & F & G & H \\ I & J & K & L \\ M & N & O & P \end{vmatrix} =$$

$$= (AF-EB)\,(KP-OL) + (EC-AG)\,(JP-LN) + (AH-ED)\,(JO-NK) \qquad \text{(A1.27)}$$
$$+ (MJ-IN)\,(GD-HC) + (IO-MK)\,(FD-HB) + (ML-IP)\,(FC-GB).$$

Carrying out the multiplications, grouping terms, and using the identity.

$$J_{n+1}(x)\,Y_n(x) - J_n(x)\,Y_{n+1}(x) = \frac{2}{\pi x} \qquad \text{(A1.28)}$$

yields the explicit form of the dispersion relation:

$$M\left[\frac{b}{a}\,\frac{k_{\rho 3}^2}{k_{\rho 1}^2}\,\frac{k_{\rho 1}^2 - k_{\rho 2}^2}{k_{\rho 3}^2 - k_{\rho 2}^2}\,(G_1 f_5 - f_7)(G_2 f_5 - f_7) + \frac{a}{b}\,\frac{k_{\rho 1}^2}{k_{\rho 3}^2}\cdot\right.$$

$$\left.\cdot\,\frac{k_{\rho 3}^2 - k_{\rho 2}^2}{k_{\rho 1}^2 - k_{\rho 2}^2}\,(G_4 f_5 - f_6)(G_3 f_5 - f_6) - \frac{8}{\pi^2 k_{\rho 2}^2\, ab} - M f_5^2\right] \qquad \text{(A1.29)}$$

$$= [G_3 (G_1 f_5 - f_7) - (G_1 f_6 - f_8)]\,[G_4 (G_2 f_5 - f_7) - (G_2 f_6 - f_8)]$$

where: $M = \overset{TE}{\frac{n^2 k_z^2}{\omega^2 \mu_2 \varepsilon_2 ab}}\;\overset{TM}{\frac{(k_{\rho 2}^2 - k_{\rho 1}^2)(k_{\rho 1}^2 - k_{\rho 3}^2)}{k_{\rho 1}^2 k_{\rho 2}^2 k_{\rho 3}^2}}$

$$f_5 = U_4\,U_3 - U_2\,U_5$$
$$f_6 = U_4\,U_3' - U_2'\,U_5$$
$$f_7 = U_4'\,U_3 - U_2\,U_5'$$
$$f_8 = U_4'\,U_3' - U_2'\,U_5'$$

A very useful property of equation (A1.29) is that all of its terms involve dimensionless ratios. This forgoes any worries about units when evaluating the dispersion relation.

A very special case of (A1.29) occurs when n = 0. In this case the entire left-hand side of the equation becomes zero and the right-hand side separates into a pair of solutions representing pure TE and TM modes. This can be seen to be true by considering determinant (A1.25). If the waveguide is propagating a pure TE mode all the field components due to the TM partial fields must be zero. Thus, (A1.25) becomes:

$$\begin{vmatrix} \frac{k_{\rho 1}^2}{\mu_1} U_1 & -\frac{k_{\rho 1}^2}{\mu_2} U_2 & -\frac{k_{\rho 1}^2}{\mu_2} U_3 & 0 \\ k_{\rho 1} U_1' & -k_{\rho 2} U_2' & -k_{\rho 2} U_3' & 0 \\ 0 & \frac{k_{\rho 2}^2}{\mu_2} U_4 & \frac{k_{\rho 2}^2}{\mu_2} U_5 & -\frac{k_{\rho 3}^2}{\mu_3}\left[U_6 - U_7 \frac{U_8'}{U_9'}\right] \\ 0 & k_{\rho 2} U_4' & k_{\rho 2} U_5' & -k_{\rho 3}\left[U_6' - U_7' \frac{U_8'}{U_9'}\right] \end{vmatrix} = 0 \qquad \text{(A1.30)}$$

Carrying out the multiplication according to equation (A1.27) yields:

$$\left(-U_2' + \frac{k_{\rho 2}\,\mu_1\,U_1'}{k_{\rho 1}\,\mu_2\,U_1} U_2\right)\left(-\frac{k_{\rho 2}\,\mu_3\,f_4}{k_{\rho 3}\,\mu_2\,f_3} U_5 + U_5'\right) \qquad \text{(A1.31)}$$

$$+ \left(-\frac{k_{\rho 2}\,\mu_1\,U_1'}{k_{\rho 1}\,\mu_2\,U_1} U_3 + U_3'\right)\left(-\frac{k_{\rho 2}\,\mu_3\,f_4}{k_{\rho 3}\,\mu_2\,f_3} U_4 + U_4'\right) = 0,$$

or:

$$(G_3\,U_2 - U_2')\,(U_5' - G_1\,U_5) + (U_3' - G_3\,U_3)\,(U_4' - G_1\,U_4) = 0, \qquad \text{(A1.32)}$$

which is rearranged to:

$$[G_3\,(G_1\,f_5 - f_7) - (G_1\,f_6 - f_8)] = 0. \qquad \text{(A1.33)}$$

This is simply the first multiplying term on the right-hand side of the three-layer dispersion equation (A1.29). A similar consideration of pure TM fields leads to the second multiplying term.

Appendix 2. Derivation of the Two-Layer Dispersion Relation as a Simplification of the Three-Layer Dispersion Relation

The two-layer dielectric-loaded waveguide dispersion relation can be derived from either the boundary-value problem, as in Appendix One, or as a limiting case of the three-layer problem. The latter is much simpler and can be accomplished by allowing the thickness of the middle layer to go to zero while $k_{\rho 2}$ goes to $k_{\rho 1}$. This transformation is shown in Figure A2-1. Under these conditions the following relations result:

$$\begin{aligned} k_{\rho 1},\ k_{\rho 2} &\longrightarrow k_{\rho A} & a,\ b &\longrightarrow A \\ k_{\rho 3} &\longrightarrow k_{\rho B} & c &\longrightarrow B \end{aligned} \tag{A2.1}$$

$$\begin{aligned} \varepsilon_1,\ \varepsilon_2 &\longrightarrow \varepsilon_A & \mu_1,\ \mu_2 &\longrightarrow \mu_A \\ \varepsilon_3 &\longrightarrow \varepsilon_B & \mu_3 &\longrightarrow \mu_B \ . \end{aligned}$$

Using these will yield:

$$\begin{aligned} U_1,\ U_2,\ U_4 &\longrightarrow J_n\,(k_{\rho A}A) = \tilde{U}_4 \\ U_3,\ U_5 &\longrightarrow Y_n\,(k_{\rho A}A) = \tilde{U}_3 \\ U_6 &\longrightarrow J_n\,(k_{\rho B}A) = \tilde{U}_6 \\ U_7 &\longrightarrow Y_n\,(k_{\rho B}A) = \tilde{U}_7 \\ U_8 &\longrightarrow J_n\,(k_{\rho B}B) = \tilde{U}_8 \\ U_9 &\longrightarrow Y_n\,(k_{\rho B}B) = \tilde{U}_9 \ . \end{aligned} \tag{A2.2}$$

Thus:

$$\begin{aligned} f_1 &\longrightarrow \tilde{f}_1 = \tilde{U}_6\ \tilde{U}_9 - \tilde{U}_7\ \tilde{U}_8 \\ f_2 &\longrightarrow \tilde{f}_2 = \tilde{U}_6'\ \tilde{U}_9 - \tilde{U}_7'\ \tilde{U}_8 \\ f_3 &\longrightarrow \tilde{f}_3 = \tilde{U}_6\ \tilde{U}_9' - \tilde{U}_7\ \tilde{U}_8' \\ f_4 &\longrightarrow \tilde{f}_4 = \tilde{U}_6'\ \tilde{U}_9' - \tilde{U}_7'\ \tilde{U}_8' \end{aligned} \tag{A2.3}$$

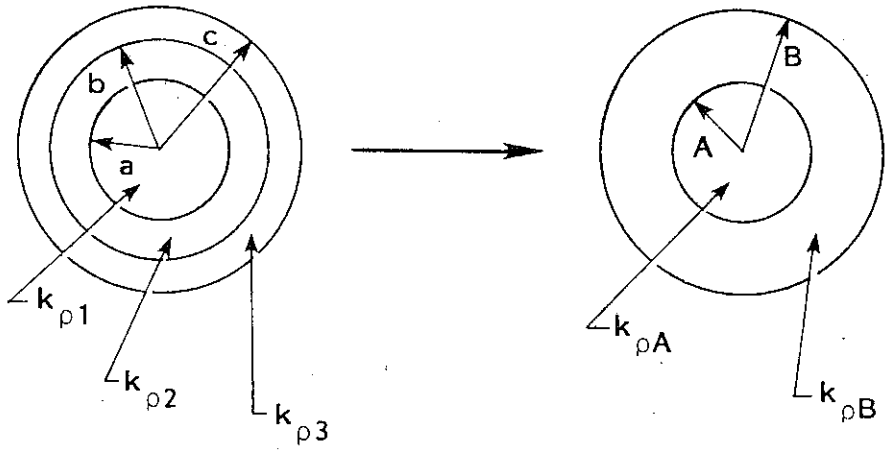

Figure A2-1. Transformation of the Three-Layer Waveguide to the Two-Layer Waveguide.

$$
\begin{aligned}
f_5 \longrightarrow \tilde{f}_5 &= \tilde{U}_4\,\tilde{U}_3 - \tilde{U}_3\,\tilde{U}_4 = 0 \\
f_6 \longrightarrow \tilde{f}_6 &= \tilde{U}_4\,\tilde{U}_3' - \tilde{U}_3\,\tilde{U}_4' \qquad \text{(A2.3)} \\
f_7 \longrightarrow \tilde{f}_7 &= \tilde{U}_4'\,\tilde{U}_3 - \tilde{U}_3'\,\tilde{U}_4 = -\tilde{f}_6 \qquad \text{(Cont'd)} \\
f_8 \longrightarrow \tilde{f}_8 &= \tilde{U}_4'\,\tilde{U}_3' - \tilde{U}_3'\,\tilde{U}_4' = 0,
\end{aligned}
$$

and:

$$
\begin{aligned}
G_1 \longrightarrow \tilde{G}_1 &= \frac{k_{\rho A}\,\mu_B\,\tilde{f}_4}{k_{\rho B}\,\mu_A\,\tilde{f}_3} \\
G_2 \longrightarrow \tilde{G}_2 &= \frac{k_{\rho A}\,\varepsilon_B\,\tilde{f}_2}{k_{\rho B}\,\varepsilon_A\,\tilde{f}_1} \qquad \text{(A2.4)} \\
G_3 \longrightarrow \tilde{G}_3 &= \frac{\tilde{U}_4'}{\tilde{U}_4} \\
G_4 \longrightarrow \tilde{G}_4 &= \frac{\tilde{U}_4'}{\tilde{U}_4} = \tilde{G}_3 .
\end{aligned}
$$

With (A2.2), equation (A1.29) reduces to:

$$
\frac{n^2 k_z^2}{\omega^2 \mu_A \varepsilon_A A^2} \quad \frac{(k_{\rho A}^2 - k_{\rho B}^2)^2}{k_{\rho A}^2 k_{\rho B}^4} \quad (\tilde{G}_4\,\tilde{f}_5 - \tilde{f}_6)\,(\tilde{G}_3\,\tilde{f}_5 - \tilde{f}_6) \qquad \text{(A2.5)}
$$

$$
= [\tilde{G}_3\,(\tilde{G}_1\,\tilde{f}_5 - \tilde{f}_7) - (\tilde{G}_1\,\tilde{f}_6 - \tilde{f}_8)]\,[\tilde{G}_4\,(\tilde{G}_2\,\tilde{f}_5 - \tilde{f}_7) - (\tilde{G}_2\,\tilde{f}_6 - \tilde{f}_8)].
$$

Substituting (A2.3) and (A2.4) into (A2.5) yields the two-layer dielectric-loaded waveguide dipsersion relation:

$$
\frac{n^2 k_z^2}{\omega^2 \mu_A \varepsilon_A A^2} \quad \frac{(k_{\rho A}^2 - k_{\rho B}^2)^2}{k_{\rho A}^2 \quad k_{\rho B}^4} = \underbrace{\left(\frac{k_{\rho A}\,\mu_B\,\tilde{f}_4}{k_{\rho B}\,\mu_A\,\tilde{f}_3} - \frac{J_n'\,(k_{\rho A}A)}{J_n\,(k_{\rho A}A)}\right)}_{\text{TE}} \cdot
$$

$$
\cdot \underbrace{\left(\frac{k_{\rho A}\,\varepsilon_B\,\tilde{f}_2}{k_{\rho B}\,\varepsilon_A\,\tilde{f}_1} - \frac{J_n'\,(k_{\rho A}A)}{J_n\,(k_{\rho A}A)}\right)}_{\text{TM}}. \qquad \text{(A2.6)}
$$

As with equation (A1.29), all terms in (A2.6) involve ratios of like dimensions.

When n = 0, the right-hand side of equation (A2.6) splits into pure TE and TM modes. The first multiplying term describes TE mode propagation, and the second term describes TM progagation.

Appendix 3. Derivation of the Two-Layer Waveguide Field Values

To derive the values of the electric and magnetic fields for the case of the two-layer dielectric-loaded waveguide, it is necessary to set up the boundary-value matrix as was done for the three-layer case in Appendix One. For the structure of Figure A3-1, remembering that the outer wall is considered a perfect conductor, the scalar wave functions can be written as:

$$\psi^{m1} = A_1 \, J_n \, (k_{\rho 1}\rho) \cos (n\phi) \, e^{-jk_z z}$$

$$\psi^{e1} = B_1 \, J_n \, (k_{\rho 1}\rho) \sin (n\phi) \, e^{-jk_z z} \qquad \text{(A3.1)}$$

$$\psi^{m2} = C_1 \left[J_n \, (k_{\rho 2}\rho) - \frac{J_n \, (k_{\rho 2}b)}{Y_n \, (k_{\rho 2}b)} Y_n \, (k_{\rho 2}\rho) \right] \cos (n\phi) \, e^{-jk_z z}$$

$$\psi^{e2} = D_1 \left[J_n \, (k_{\rho 2}\rho) - \frac{J_n' \, (k_{\rho 2}b)}{Y_n' \, (k_{\rho 2}b)} Y_n \, (k_{\rho 2}\rho) \right] \sin (n\phi) \, e^{-jk_z z} .$$

Letting:

$$U_1 = J_n \, (k_{\rho 1}a) \qquad f_1 = U_3 \; U_4 \; - U_2 \; U_5$$

$$U_2 = J_n \, (k_{\rho 2}a) \qquad f_2 = U_3' \; U_4 \; - U_2' \; U_5$$

$$U_3 = Y_n \, (k_{\rho 2}a) \qquad f_3 = U_3 \; U_4' - U_2 \; U_5' \qquad \text{(A3.2)}$$

$$U_4 = J_n \, (k_{\rho 2}b) \qquad f_4 = U_3' \; U_4' - U_2' \; U_5'$$

$$U_5 = Y_n \, (k_{\rho 2}b)$$

and applying the boundary conditions at ρ = a results in the matrix:

$$\begin{bmatrix} 0 & \frac{k_{\rho 1}^2}{\mu_1} U_1 & 0 & \frac{-k_{\rho 2}^2}{\mu_2} \left[U_2 - \frac{U_4'}{U_5'} U_3 \right] \\ \frac{k_{\rho 1}^2}{\varepsilon_1} U_1 & 0 & \frac{-k_{\rho 2}^2}{\varepsilon_2} \left[U_2 - \frac{U_4}{U_5} U_3 \right] & 0 \\ -k_{\rho 1} \, U_1' & \frac{-nk_z}{\omega \mu_1 a} U_1 & k_{\rho 2} \left[U_2' - \frac{U_4}{U_5} U_3' \right] & \frac{nk_z}{\omega \mu_2 a} \left[U_2 - \frac{U_4'}{U_5'} U_3 \right] \\ \frac{nk_z}{\omega \varepsilon_1 a} & k_{\rho 1} & \frac{-nk_z}{\omega \varepsilon_2 a} \left[U_2 - \frac{U_4}{U_5} U_3 \right] & -k_{\rho 2} \left[U_2' - \frac{U_4'}{U_5'} U_3' \right] \end{bmatrix} \begin{bmatrix} A_1 \\ B_1 \\ C_1 \\ D_1 \end{bmatrix} = \begin{bmatrix} 0 \\ 0 \\ 0 \\ 0 \end{bmatrix} \qquad \text{(A3.3)}$$

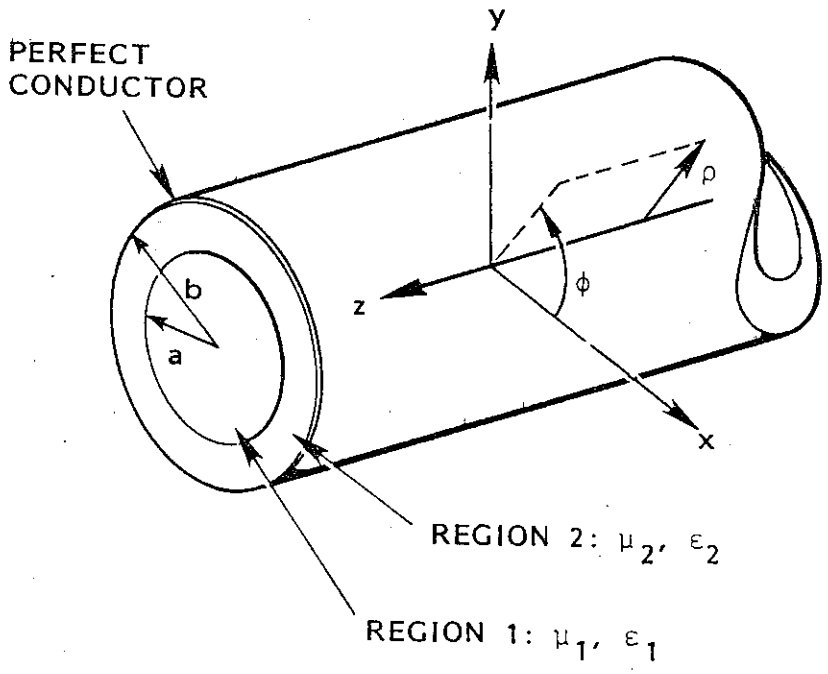

Figure A3-1. Infinitely Long Two-Layer Dielectric-Loaded Waveguide and Cylindrical Coordinate System.

Solving for B_1, C_1, and D_1 in terms of A_1 yields:

$$\frac{C_1}{A_1} = - \frac{\varepsilon_2 \, k_{\rho 1}^2}{\varepsilon_1 \, k_{\rho 2}^2} \frac{U_1 \, U_5}{f_1} \tag{A3.4}$$

$$\frac{B_1}{A_1} = \frac{nk_z}{k_{\rho 1} \, \omega \mu_1 a} \frac{\frac{U_1'}{U_1} - \frac{k_{\rho 1} \, \varepsilon_2 \, f_2}{k_{\rho 2} \, \varepsilon_1 \, f_1}}{\frac{k_{\rho 1}^2}{k_{\rho 2}^2} - 1} \tag{A3.5}$$

$$\frac{D_1}{A_1} = \frac{B_1}{A_1} \frac{C_1}{A_1} \frac{\mu_2 \, \varepsilon_1}{\mu_1 \, \varepsilon_2} \, . \tag{A3.6}$$

Substituting (A3.1) into (A1.20) and (A1.21) and using (A3.4), (A3.5), and (A3.6) allows explicit formulas to be written for the fields in each region. Here, A_1 remains a constant which can be determined knowing the power in the guide. Thus:

REGION ONE

$$\text{Let: } R_1 = \frac{B_1}{A_1} \text{ (from equation (A3.5))} \tag{A3.7}$$

$$E_\rho = -A_1 \left[\frac{k_z \, k_{\rho 1}}{\omega \varepsilon_1} J_n' (k_{\rho 1} \rho) + R_1 \frac{n}{\rho} J_n (k_{\rho 1} \rho) \right] \cos (n\phi) \, e^{-jk_z z}$$

$$E_\phi = A_1 \left[\frac{nk_z}{\omega \varepsilon_1 \rho} J_n (k_{\rho 1} \rho) + R_1 \, k_{\rho 1} \, J_n' (k_{\rho 1} \rho) \right] \sin (n\phi) \, e^{-jk_z z}$$

$$E_z = A_1 \frac{k_{\rho 1}^2}{j\omega \varepsilon_1} J_n (k_{\rho 1} \rho) \cos (n\phi) \, e^{-jk_z z} \tag{A3.8}$$

$$H_\rho = -A_1 \left[\frac{n}{\rho} J_n (k_{\rho 1}\rho) + R_1 \frac{k_z k_{\rho 1}}{\omega \mu_1} J_n' (k_{\rho 1}\rho) \right] \sin (n\phi) e^{-jk_z z}$$

$$H_\phi = -A_1 \left[k_{\rho 1} J_n' (k_{\rho 1}\rho) + R_1 \frac{nk_z}{\omega \mu_1 \rho} J_n (k_{\rho 1}\rho) \right] \cos (n\phi) e^{-jk_z z}$$

$$H_z = A_1 \frac{k_{\rho 1}^2}{j\omega\mu_1} R_1 J_n (k_{\rho 1}\rho) \sin (n\phi) e^{-jk_z z} \qquad \text{(A3.8) (Cont'd)}$$

REGION TWO

Let: $R_2 = \frac{C_1}{A_1}$ (from equation (A3.4)) (A3.9)

$R_3 = \frac{D_1}{A_1}$ (from equation (A3.6)) (A3.10)

$$\begin{aligned} f_{\rho 1} &= J_n (k_{\rho 2}\rho) Y_n (k_{\rho 2} b) - J_n (k_{\rho 2} b) Y_n (k_{\rho 2}\rho) \\ f_{\rho 2} &= J_n (k_{\rho 2}\rho) Y_n' (k_{\rho 2} b) - J_n' (k_{\rho 2} b) Y_n (k_{\rho 2}\rho) \\ f_{\rho 3} &= J_n' (k_{\rho 2}\rho) Y_n (k_{\rho 2} b) - J_n (k_{\rho 2} b) Y_n' (k_{\rho 2}\rho) \\ f_{\rho 4} &= J_n' (k_{\rho 2}\rho) Y_n' (k_{\rho 2} b) - J_n' (k_{\rho 2} b) Y_n' (k_{\rho 2}\rho) \end{aligned} \qquad \text{(A3.11)}$$

$$E_\rho = -A_1 \left[R_2 \frac{k_z k_{\rho 2}}{\omega \varepsilon_2} \frac{f_{\rho 3}}{U_5} + R_3 \frac{n}{\rho} \frac{f_{\rho 2}}{U_5'} \right] \cos (n\phi) e^{-jk_z z}$$

$$E_\phi = A_1 \left[\frac{nk_z}{\omega \varepsilon_2 \rho} R_2 \frac{f_{\rho 1}}{U_5} + R_3 k_{\rho 2} \frac{f_{\rho 4}}{U_5'} \right] \sin (n\phi) e^{-jk_z z}$$

$$E_z = A_1 \frac{k_{\rho 2}^2}{j\omega\varepsilon_2} R_2 \frac{f_{\rho 1}}{U_5} \cos (n\phi) e^{-jk_z z} \qquad \text{(A3.12)}$$

$$H_\rho = -A_1 \left[R_2 \frac{n}{\rho} \frac{f_{\rho 1}}{U_5} + R_3 \frac{k_z k_{\rho 2}}{\omega \mu_2} \frac{f_{\rho 4}}{U_5'} \right] \sin (n\phi) e^{-jk_z z}$$

$$H_\phi = -A_1 \left[k_{\rho 2} R_2 \frac{f_{\rho 3}}{U_5} + \frac{nk_z}{\omega \mu_2 \rho} \frac{f_{\rho 2}}{U_5'} \right] \cos (n\phi) e^{-jk_z z}$$

$$H_z = A_1 R_3 \frac{k_{\rho 2}^2}{j\omega\mu_2} \frac{f_{\rho 2}}{U_5'} \sin (n\phi) e^{-jk_z z} .$$

The TE_{0m} fields can be found by letting n = 0 in equations (A3.12). In this case the fields will have no azimuthal variations. They are given by:

REGION ONE

$$E_\rho = 0 \qquad E_z = 0 \qquad H_\phi = 0$$

$$H_\rho = -A_1 R_1 \frac{k_z k_{\rho 1}}{\omega \mu_1} Jo'(k_{\rho 1}\rho) e^{-jk_z z}$$

$$E_\phi = A_1 R_1 k_{\rho 1} Jo'(k_{\rho 1}\rho) e^{-jkz_z} \qquad \text{(A3.13)}$$

$$H_z = -j A_1 R_1 \frac{k_{\rho 1}^2}{\omega \mu_1} Jo(k_{\rho 1}\rho) e^{-jk_z z}$$

REGION TWO

$$E_\rho = 0 \qquad E_z = 0 \qquad H_\phi = 0$$

$$H_\rho = -A_1 \frac{k_z k_{\rho 2}}{\omega \mu_2} R_3 \frac{f_{\rho 4}}{U_5'} e^{-jk_z z}$$

$$E_\phi = A_1 k_{\rho 2} R_3 \frac{f_{\rho 4}}{U_5'} e^{-jk_z z} \qquad \text{(A3.14)}$$

$$H_z = -j A_1 R_3 \frac{k_{\rho 2}^2}{\omega \mu_2} \frac{f_{\rho 2}}{U_5'} e^{-jk_z z} .$$

Equations (A3.13) and (A3.14) can be put in a much simpler form by making them dimensionally normalized. The simplest way to normalize the fields is to define the H_z magnetic field component to be one on the axis. This yields a normalizing factor of:

$$\frac{j \omega \mu_1}{A_1 R_1 k_{\rho 1}^2} e^{jk_z z}, \qquad \text{(A3.15)}$$

which will multiply all of the field components to give their normalized counterparts.

The value of R_3 from equation (A3.10) can be found by writing:

$$R_3 = \frac{D_1}{A_1} = \frac{B_1}{A_1}\,\frac{D_1}{B_1} = R_1\,\frac{D_1}{B_1}. \qquad \text{(A3.16)}$$

Letting n = 0 in the fourth equation of (A3.3) yields:

$$\frac{D_1}{B_1} = \frac{k_{\rho 1}\, U_5'\, U_1'}{k_{\rho 2}\, f_4}. \qquad \text{(A3.17)}$$

Substituting (A3.16) and (A3.17) into equations (A3.13) and (A3.14) and multiplying by (A3.15) gives the normalized TE_{0m} field components:

REGION ONE

$$\hat{E}_\rho = 0 \qquad \hat{E}_z = 0 \qquad \hat{H}_\phi = 0$$

$$\hat{H}_z = Jo\,(k_{\rho 1}\rho)$$

$$\hat{H}_\rho = -j\,\frac{k_z}{k_{\rho 1}}\,Jo'\,(k_{\rho 1}\rho) \qquad \text{(A3.18)}$$

$$\hat{E}\phi = j\,\mu_{1R}\,\frac{\frac{\omega}{C}\,b}{k_{\rho 1} b}\,\eta_o\,Jo'\,(k_{\rho 1}\rho)$$

REGION TWO

$$\hat{E}_\rho = 0 \qquad \hat{E}_z = 0 \qquad \hat{H}_\phi = 0$$

$$\hat{H}_z = \frac{\mu_1\, k_{\rho 2}}{\mu_2\, k_{\rho 1}}\,Jo'\,(k_{\rho 1} a)\,\frac{f_{\rho 2}}{f_4} \qquad \text{(A3.19)}$$

$$\hat{H}_\rho = -j\,\frac{\mu_1\, k_z}{\mu_2\, k_{\rho 1}}\,Jo'\,(k_{\rho 1} a)\,\frac{f_{\rho 4}}{f_4}$$

$$\hat{E}\phi = j\,\mu_{1R}\,\frac{\frac{\omega}{C}\,b}{k_{\rho 1} b}\,\eta_o\,Jo'\,(k_{\rho 1} a)\,\frac{f_{\rho 4}}{f_4}$$

where: $\eta_o = \sqrt{\frac{\mu_o}{\varepsilon_o}}$

$$\mu_{1R} = \frac{\mu_1}{\mu_o}.$$

In the above equations, a hat ("^") indicates a normalized field component.

Appendix 4: Derivation of the Three-Layer Dispersion Equation with a Ferrite Layer

The three-layer dielectric/ferrite-loaded waveguide is analyzed as an infinitely long, circular structure as shown in Figure A1-1. The first and third regions are dielectric in nature and can be described by their scalar permeability, μ_1 or μ_3, and by their scalar permittivity, ε_1 or ε_3. The second region is composed of a ferrite material which is described by a tensor permeability, $\mu_0 \overleftrightarrow{\mu_2}$, and a scalar permittivity, $\varepsilon_0 \varepsilon_2$. Surrounding these three layers is a perfectly conducting, metallic shell.

The expressions for the field components in regions one and three can be obtained in the same manner as that used in Appendix One. The fields in the ferrite region are obtained similarly, and by considering region two to exhibit the tensor permeability:

$$\overleftrightarrow{\mu_2} = \begin{bmatrix} \mu & j\,\mu_a & 0 \\ -j\,\mu_a & \mu & 0 \\ 0 & 0 & \mu_{11} \end{bmatrix}, \qquad \text{(A4.1)}$$

and, thus, to have the vector fields:

$$\vec{B_2} = \mu_0 \overleftrightarrow{\mu_2} \vec{H_2} \qquad \text{(A4.2)}$$

$$\vec{D_2} = \varepsilon_0 \varepsilon_2 \vec{E_2} .$$

As with the scalar wave functions in the dielectric regions, those in the ferrite region must obey the Helmholz equation:

$$\frac{1}{\rho}\frac{\partial}{\partial\rho}\left(\rho\frac{\partial\psi}{\partial\rho}\right) + \frac{1}{\rho^2}\frac{\partial^2\psi}{\partial\phi^2} + \frac{\partial^2\psi}{\partial z^2} + \chi_{1,2}^{\,2}\ \psi = 0 \qquad \text{(A4.3)}$$

which is written in the cylindrical coordinate system of Figure A1-2. Using the method of separation of variables as in Appendix One, ψ can be written as:

$$\psi = [C_1 J_n (\chi_{1,2}\rho) + C_2 Y_n (\chi_{1,2}\rho)] e^{jn\phi} e^{-jk_z z} . \qquad (A4.4)$$

Gurevich [9] has shown that the fields in the ferrite region can be found from the relations:

$$E_\rho = j S \frac{\partial\psi}{\partial\rho} + T \frac{1}{\rho}\frac{\partial\psi}{\partial\phi}$$

$$E_\phi = -T \frac{\partial\psi}{\partial\rho} + j S \frac{1}{\rho}\frac{\partial\psi}{\partial\phi}$$

$$E_z = j W \frac{\partial\psi}{\partial z} \qquad (A4.5)$$

$$H_\rho = j M \frac{\partial^2\psi}{\partial\rho\partial z} + N \frac{1}{\rho}\frac{\partial^2\psi}{\partial\phi\partial z}$$

$$H_\phi = -N \frac{\partial^2\psi}{\partial\rho\partial z} + j M \frac{1}{\rho}\frac{\partial^2\psi}{\partial\phi\partial z}$$

$$H_z = j R \frac{\partial^2\psi}{\partial z^2}$$

where S, T, W, M, N, and R are differential operators arrising from the fact that $\overleftrightarrow{\mu_2}$ is a tensor quantity. For the tensor of (A5.1), Gurevich derives these factors to be:

$$T_{1,2} = \frac{\omega^2}{c^2} \varepsilon_2 \mu_\perp - k_z^2 - \chi_{1,2}^2$$

$$S = \frac{\mu_a}{\mu} k_z^2$$

$$W_{1,2} = -\frac{\mu_a}{\mu} \chi_{1,2}^2 \qquad (A4.6)$$

$$M_{1,2} = \frac{1}{\mu\left(\frac{\omega}{c}\right)}\left(\frac{\omega^2}{c^2}\ \varepsilon_2\ \mu - k_z^2 - \chi_{1,2}^2\right) \qquad \text{(A4.6) (Cont'd.)}$$

$$N = \frac{\omega}{c}\ \varepsilon_2\ \frac{\mu_a}{\mu}$$

$$R_{1,2} = -\frac{T_{1,2}\ \chi_{1,2}^2}{\frac{\omega}{c}\ \mu_{11}\ k_z^2}$$

where: $\mu_\perp = \mu - \frac{\mu_a^2}{\mu}$. (A4.7)

He also finds the separation relation between the axial propagation constant, k_z, and the radial propagation constant, $\chi_{1,2}$, to be:

$$\chi_{1,2}^2 = \frac{1}{2}\left[\frac{\omega^2}{c^2}\ \varepsilon_2\ (\mu_\perp + \mu_{11}) - \left(1 + \frac{\mu_{11}}{\mu}\right) k_z^2\right]$$

$$\pm\sqrt{\frac{1}{4}\left[\frac{\omega^2}{c^2}\ \varepsilon_2\ (\mu_\perp - \mu_{11}) - \left(1 - \frac{\mu_{11}}{\mu}\right) k_z^2\right] + k_z^2\ \frac{\omega^2}{c^2}\ \varepsilon_2\ \mu_{11}\ \frac{\mu_a^2}{\mu_2}}. \qquad \text{(A4.8)}$$

It is noted that if $\mu = \mu_{11}$ and $\mu_a = 0$, the tensor μ_2 reduces to a scalar, $\mu_2 = \mu$, and equation (A4.8) becomes:

$$\chi_{1,2}^2 = \frac{\omega^2}{c^2}\ \mu_2\ \varepsilon_2 - k_z^2 = \chi_1^2 = \chi_2^2, \qquad \text{(A4.9)}$$

and the case reduces to the three-layer dielectric case considered in Appendix One.

In the ferrite region, the Helmolz equation (A4.3) is solved using the function ψ of (A4.4). This solution holds for ψ using either χ_1 or χ_2. Thus, ψ must be written in region two as:

$$\psi_2 = [C_1\ J_n(\chi_1\rho) + C_2\ J_n(\chi_2\rho) + D_1\ Y_n(\chi_1\rho) + D_2\ Y_n(\chi_2\rho)] \cdot$$
$$\cdot\ e^{-jk_z z}\ e^{jn\phi} \qquad \text{(A4.10)}$$

or:

$$\psi_2 = [C_1 J_n(\chi_1\rho) + D_1 Y_n(\chi_1\rho)]\, e^{-jk_z z}\, e^{jn\phi} + [C_2 J_n(\chi_1\rho) + D_2 Y_n(\chi_2\rho)]\, e^{-jk_z z}\, e^{jn\phi} \quad \text{(A4.11)}$$

The field components in region one are found from (A1.19), (A1.20), and (A1.21) to be:

$$E_{z1} = k_{\rho 1}^2 [A_1 J_n(k_{\rho 1}\rho)]$$

$$E_{\phi 1} = j \mu_{1R} \frac{\omega}{c} k_{\rho 1} [B_1 J_n'(k_{\rho 1}\rho)] + \frac{nk_z}{\rho} [A_1 J_n(k_{\rho 1}\rho)]$$

$$H_{z1} = k_{\rho 1}^2 [B_1 J_n(k_{\rho 1}\rho)] \quad \text{(A4.12)}$$

$$H_{\phi 1} = \frac{nk_z^2}{\rho} [B_1 J_n(k_{\rho 1}\rho)] - j \varepsilon_{1R} \frac{\omega}{c} k_{\rho 1} [A_1 J_n'(k_{\rho 1}\rho)]$$

where they vary with $e^{-jk_z}\, e^{jn\phi}$ $\left(\text{not with } \begin{matrix}\sin(n\phi)\\ \cos(n\phi)\end{matrix}\right)$. In region two, the field components are found from (A4.5) and (A4.11) to be:

$$E_{z2} = k_z W_1 [C_1 J_n(\chi_1\rho) + D_1 Y_n(\chi_1\rho)] + k_z W_2 [C_2 J_n(\chi_2\rho) + D_2 Y_n(\chi_2\rho)]$$

$$E_{\phi 2} = -T_1 \chi_1 [C_1 J_n'(\chi_1\rho) + D_1 Y_n'(\chi_1\rho)] - T_2 \chi_2 [C_2 J_n'(\chi_2\rho) + D_2 Y_n'(\chi_2\rho)]$$

$$- S_1 \frac{n}{\rho} [C_1 J_n(\chi_1\rho) + D_1 Y_n(\chi_1\rho)] - S_2 \frac{n}{\rho} [C_2 J_n(\chi_2\rho) + D_2 Y_n(\chi_2\rho)]$$

$$H_{z2} = -j k_z^2 R_1 [C_1 J_n(\chi_1\rho) + D_1 Y_n(\chi_1\rho)] - j k_z^2 R_2 [C_2 J_n(\chi_2\rho) + D_2 Y_n(\chi_2\rho)]$$

$$H_{\phi 2} = j k_z N \chi_1 [C_1 J_n'(\chi_1\rho) + D_1 Y_n'(\chi_1\rho)] + j k_z N \chi_2 [C_2 J_n'(\chi_2\rho) + D_2 Y_n'(\chi_2\rho)]$$

$$+ j \frac{nk_z}{\rho} M_1 [C_1 J_n(\chi_1\rho) + D_1 Y_n(\chi_1\rho)] + j \frac{nk_z}{\rho} M_2 [C_2 J_n(\chi_2\rho) + D_2 Y_n(\chi_2\rho)]. \quad \text{(A4.13)}$$

In region three, the field components are:

$$E_{z3} = k_{\rho 3}^2 \left[E_1 J_n (k_{\rho 1}\rho) + E_2 Y_n (k_{\rho 1}\rho)\right]$$

$$E_{\phi 3} = j \mu_{3R} \frac{\omega}{C} k_{\rho 3} \left[F_1 J_n' (k_{\rho 3}\rho) + F_2 Y_n' (k_{\rho 3}\rho)\right] + \frac{nk_z}{\rho} \left[E_1 J_n (k_{\rho 3}\rho) + E_2 Y_n (k_{\rho 3}\rho)\right]$$

$$H_{z3} = k_{\rho 3}^2 \left[F_1 J_n (k_{\rho 3}\rho) + F_2 Y_n (k_{\rho 3}\rho)\right] \qquad \text{(A4.14)}$$

$$H_{\phi 3} = \frac{nk_z}{\rho} \left[F_1 J_n (k_{\rho 3}\rho) + F_2 Y_n (k_{\rho 3}\rho)\right] - j \varepsilon_{3R} \frac{\omega}{C} k_{\rho 3} \left[E_1 J_n' (k_{\rho 3}\rho) + E_2 Y_n' (k_{\rho 3}\rho)\right].$$

Here all fields vary with $e^{-jk_z z} e^{jn\phi}$. Applying the boundary conditions at $\rho = a$, $\rho = b$, and $\rho = c$ as in Appendix One yields a set of eight simultaneous equations in the eight unknowns A_1, B_1, C_1, C_2, D_1, D_2, E_1, and F_1. A non-trivial solution is guaranteed by setting the determinant of the coefficient matrix to zero. The resulting equation yields the dispersion relation for the waveguide, relating ω and k_z. Letting:

$$V_1 = J_n (k_{\rho 1}a) \qquad V_1' = J_n' (k_{\rho 1}a)$$

$$V_2 = J_n (\chi_1 a) \qquad V_2' = J_n' (\chi_1 a)$$

$$V_3 = Y_n (\chi_1 a) \qquad V_3' = Y_n' (\chi_1 a)$$

$$V_4 = J_n (\chi_2 a) \qquad V_4' = J_n' (\chi_2 a)$$

$$V_5 = Y_n (\chi_2 a) \qquad V_5' = Y_n' (\chi_2 a)$$

$$V_6 = J_n (\chi_1 b) \qquad V_6' = J_n' (\chi_1 b)$$

$$V_7 = Y_n (\chi_1 b) \qquad V_7' = Y_n' (\chi_1 b)$$

$$V_8 = J_n (\chi_2 b) \qquad V_8' = J_n' (\chi_2 b)$$

$$V_9 = Y_n (\chi_2 b) \qquad V_9' = Y_n' (\chi_2 b)$$

$$V_{10} = J_n\,(k\rho_3 b) \qquad V_{10}' = J_n'\,(k\rho_3 b)$$

$$V_{11} = Y_n\,(k\rho_3 b) \qquad V_{11}' = Y_n'\,(k\rho_3 b)$$

$$V_{12} = J_n\,(k\rho_3 c) \qquad V_{12}' = J_n'\,(k\rho_3 c)$$

$$V_{13} = Y_n\,(k\rho_3 c) \qquad V_{13}' = Y_n'\,(k\rho_3 c)$$

$$\begin{aligned} g_1 &= V_{10}\,V_{13} - V_{11}\,V_{12} \\ g_2 &= V_{10}'\,V_{13} - V_{11}'\,V_{12} \\ g_3 &= V_{10}\,V_{13}' - V_{11}\,V_{12}' \\ g_4 &= V_{10}'\,V_{13}' - V_{11}'\,V_{12}', \end{aligned} \tag{A4.15}$$

the determinant (A4.16) results. This is a very complicated determinant. In this form it is best evaluated on a computer.

A much simpler case to analyze is that for which n = 0. Putting n = 0 into (A4.16), substituting in equations (A4.6) and eliminating A_1, B_1, E_1, and F_1 yields the much simpler determinant:

$$\begin{vmatrix} V_2'-H_1 V_2 & V_4'-H_2 V_4 & V_3'-H_1 V_3 & V_5'-H_2 V_5 \\ T_1\,[V_2'-I_1 V_2] & T_2\,[V_4'-I_2 V_4] & T_1\,[V_3'-I_1 V_3] & T_2\,[V_5'-I_2 V_5] \\ V_6'-H_3 V_6 & V_8'-H_4 V_8 & V_7'-H_3 V_7 & V_9'-H_4 V_9 \\ T_1\,[V_6'-I_3 V_6] & T_2\,[V_8'-I_4 V_8] & T_1\,[V_7'-I_3 V_7] & T_2\,[V_9'-I_4 V_9] \end{vmatrix} = 0 \tag{A4.17}$$

where:
$$H_{1,2} = \frac{\varepsilon_1 \chi_{1,2} V_1'}{\varepsilon_2 k\rho_1 V_1}$$

$$I_{1,2} = \frac{\mu_1 \chi_{1,2} V_1'}{\mu_{11} k\rho_1 V_1} \tag{A4.18}$$

$$H_{3,4} = \frac{\varepsilon_3 \chi_{1,2} g_2}{\varepsilon_2 k\rho_3 g_1}$$

$$I_{3,4} = \frac{\mu_3 \chi_{1,2} g_4}{\mu_{11} k\rho_3 g_3}\,.$$

$$
\begin{array}{|c|c|c|c|c|c|c|c|}
\hline
A_1 & B_1 & C_1 & C_2 & D_1 & D_2 & E_1 & F_1 \\
\hline
0 & k_{\rho 1}^2 V_1 & j k_z^2 R_1 V_2 & j k_z^2 R_2 V_4 & j k_z^2 R_1 V_3 & j k_z^2 R_2 V_5 & 0 & 0 \\
\hline
-k_{\rho 1}^2 V_1 & 0 & k_z W_1 V_2 & k_z W_2 V_4 & K_z W_1 V_3 & k_z W_2 V_5 & 0 & 0 \\
\hline
j\varepsilon_{1R} \frac{\omega}{c} k_{\rho 1} V_1' & -\frac{nk_z}{a} V_1 & \begin{array}{l} j k_z N \chi_1 V_2' \\ +j \frac{nk_z}{a} M_1 V_2 \end{array} & \begin{array}{l} j k_z N \chi_2 V_4' \\ +j \frac{nk_z}{a} M_2 V_4 \end{array} & \begin{array}{l} j k_z N \chi_1 V_3' \\ +j \frac{nk_z}{a} M_1 V_3 \end{array} & \begin{array}{l} j k_z N \chi_2 V_5' \\ +j \frac{nk_z}{a} M_2 V_5 \end{array} & 0 & 0 \\
\hline
\frac{nk_z}{a} V_1 & j \mu_{1R} \frac{\omega}{c} k_{\rho 1} V_1' & \begin{array}{l} T_1 \chi_1 V_2' \\ + S_1 \frac{n}{a} V_2 \end{array} & \begin{array}{l} T_2 \chi_2 V_4' \\ + S_2 \frac{n}{a} V_4 \end{array} & \begin{array}{l} T_1 \chi_1 V_3' \\ + S_1 \frac{n}{a} V_3 \end{array} & \begin{array}{l} T_2 \chi_2 V_5' \\ + S_2 \frac{n}{a} V_5 \end{array} & 0 & 0 \\
\hline
0 & 0 & j k_z^2 R_1 V_6 & j k_z^2 R_2 V_8 & j k_z^2 R_1 V_7 & j k_z^2 R_2 V_9 & 0 & \frac{k_{\rho 3}^2}{V_{13}'} g_3 \\
\hline
0 & 0 & k_z W_1 V_6 & k_z W_2 V_8 & k_z W_1 V_7 & k_z W_2 V_9 & -\frac{k_{\rho 3}^2}{V_{13}} g_1 & 0 \\
\hline
0 & 0 & \begin{array}{l} j k_z N \chi_1 V_6' \\ +j \frac{nk_z}{b} M_1 V_6 \end{array} & \begin{array}{l} j k_z N \chi_2 V_8' \\ +j \frac{nk_z}{b} M_2 V_8 \end{array} & \begin{array}{l} j k_z N \chi_1 V_7' \\ +j \frac{nk_z}{b} M_1 V_7 \end{array} & \begin{array}{l} j k_z N \chi_2 V_9' \\ +j \frac{nk_z}{b} M_2 V_9 \end{array} & j \varepsilon_{3R} \frac{\omega}{c} k_{\rho 3} \frac{g_2}{V_{13}} & -\frac{nk_z}{b} \frac{g_3}{V_{13}'} \\
\hline
0 & 0 & \begin{array}{l} T_1 \chi_1 V_6' \\ + S_1 \frac{n}{b} V_6 \end{array} & \begin{array}{l} T_2 \chi_2 V_8' \\ + S_2 \frac{n}{b} V_8 \end{array} & \begin{array}{l} T_1 \chi_1 V_7' \\ + S_2 \frac{n}{b} V_9 \end{array} & \begin{array}{l} T_2 \chi_2 V_9' \\ + S_2 \frac{n}{b} V_9 \end{array} & \frac{nk_z}{b} \frac{g_1}{V_{13}} & j \mu_{3R} \frac{\omega}{c} k_{\rho 3} \frac{g_4}{V_{13}'} \\
\hline
\end{array}
= 0
$$

(A4.16)

This determinant is very easy to handle. All of its entries are dimensionless quantities, the I's and H's being ratios of like units. It can be evaluated very simply by using equation (A1.27).

Appendix 5. Methods of Numerical Solution

A. Lossless Two-Layer Dispersion Solution

In the absence of loss, the two-layer dispersion equation is a function of a real variable. A variety of methods are available for solving such functions. Because of the complicated behavior of the Bessel functions, the very simple method of halving the interval was chosen. Although convergence is not very rapid, it avoids the pitfalls of more complicated techniques. It is not prone to divergence and no derivative need be calculated. The Bessel functions are calculated in a subroutine which uses the infinite series representation for small arguments and an asymptotic expansion for an argument larger than thirty.

A numerical problem is encountered when the phase velocity of the wave is less than the speed of light. In this frequency region k_ρ^2 is negative and the arguments of the Bessel functions are imaginary. The dispersion equation must then be recalculated using the relations $J_n(j z) = j^n I_n(z)$ and $Y_n(j z) = j^{n+1} I_n(z) - \frac{2}{\pi} j^{-n} K_n(z)$. Substitution of these into the dispersion relation results in a new equation for this region, which is still a real function of a real variable.

The algorithm developed for this problem can be used in two ways. Given a value of $k_z b$, it will step up through $\frac{\omega b}{c}$, solving for the first m roots at a desired n. At a given $\frac{\omega b}{c}$ the program will step through $k_z b$, solving for the first m roots at a desired n.

B. Lossy Dielectric Dispersion Solution

Each of the three lossy dielectric problems are solved in a similar manner. The presence of loss makes each dispersion equation a function of a complex variable (a result of the complex dielectric constant or permeability tensor). The Bessel functions will thus have arguments which are complex. These are calculated in much the same way as the real Bessel functions. If the magnitude of the argument is small, an infinite series of complex terms is used. If the magnitude of the argument is greater than thirty, a complex assymptotic expansion is used.

Since the dispersion equation is a function of a complex variable, its numerical solution will involve convergence in two dimensions. The routine chosen uses Muller's technique with deflation to eliminate prviously obtained roots. The convergence of this method can be either very fast or very slow, depending on the behavior of the function near the root. The quickly varying nature of the Bessel functions makes it necessary to begin with a seed value quite near the actual root. Also, the dispersion equation must be analytic in the region containing both the root and the initial guess.

The algorithm developed for the solution of the lossy problem starts at a given frequency and inputs an initial seed value of k_z. Upon converging to the actual root, the program increments the frequency and projects ahead to the next seed value by linear interpolation. Thus, the routine follows along the mode line of interest.

The program can also be adapted to increment the thickness of the lossy layer rather than the frequency. Starting from the lossless case the layer is slowly increased from zero until the desired value of thickness is reached. This allows the mode line and attenuation to be monitored as it is perturbed from the lossless case.

In the two-layer lossy problem only the first method was used. In each of the three-layer cases, both methods were used to provide an added check. Results from each were in agreement.

Bibliography

1. Bacon, L.C.: "Ferrite Attenuators for Travelling-Wave Tubes," Technical Report No. 26 (Project 202), Stanford Electronics Laboratories, February 11, 1958.

2. Baird, J.M.; Barnett, L.R.; Park, S.Y.: "Experimental Investigation of Fast and Slow Wave Cyclotron Amplifier," B.K. Dynamics Technical Report on Contract N00173-79-C-0447, September, 1980.

3. Chu, K.R.: "Cyclotron Resonance Radiation Processes Involving Energetic Electron Streams, " Research Seminar Series, Yale University, January, 1980.

4. Chu, K.R.; Drobot, A.T.; Szu, H.H.; Sprangle, P.: "Theory and Simulation of the Gyrotron Travelling Wave Amplifier Operating at Cyclotron Harmonics," I.E.E.E. Trans. on Microwave Theory and Techniques, pp. 313-317, 1980.

5. Chu, K.R.; Hirshfield, J.L.: "Comparative Study of the Axial and Azimuthal Bunching Mechanisms in Electromagnetic Cyclotron Instabilities," N.R.L. Memorandum Report 3607, Naval Research Laboratory, November, 1980.

6. Clarricoats, P.J.B.: Microwave Ferrites, John Wiley and Sons, 1961.

7. Flesher, G.T.; Cohn, G.I.: "Dielectric Loading for Waveguide Linear Accelrators," A.I.E.E. Transactions, pp. 887-893, 195, Vol. 70, 1951.

8. Gittins, J.F.: Power Traveling-Wave Tubes, American Elsevier Publishing Co., 1965.

9. Gurevich, A.G.: Ferrites at Microwave Fequencies, Trans. by A. Tybulewicz, Consultants Bureau Enterprises, Inc., 1963.

10. Harrington, R.F.: Time Harmonic Electromagnetic Fields, McGraw-Hill, 1961.

11. Lau, Y.Y.; Chu, K.R.; Barnett, L.: "Effects of Velocity Spread and Wall Resistivity on the Gain and Bandwidth of the Gyrotron Travelling-Wave Amplifier," N.R.L. Memorandum Report 4304, Naval Research Laboratory, November, 1980.

12. Ramo, S.; Winnery, J.; Van Duzer, T.: Fields and Waves in Communication Electronics, John Wiley and Sons, 1965.

13. Lau, Y.Y.; Chu, K.R.; Barnett, L.; Granastein, V.L.: "Analysis of Oscillations in the Gyrotron Traveling Wave amplifier," N.R.L. Memorandum Report 4304, Naval Research Laboratory, October 29, 1980.

14. Stegun, I.A.; Abramowitz, M., ed., Handbook of Mathematical Functions, Dover Publications Inc., 1972.

List of Symbols

A:	Signal amplitude
a, b, c:	Waveguide dimensions
Bo:	External magnetic field in the waveguide
C:	Speed of light in a vacuum
$E\phi$, $E\rho$, E_z:	Waveguide electric field components
e:	Electronic charge
f:	Wave frequency
f_1 f_2 f_3 f_4:	Various combinations of Bessel functions
G:	Amplifier gain
$H\phi$, $H\rho$, H_z:	Waveguide magnetic field components
H_{res}:	Ferrite resonant magnetic field
H_{an}:	Ferrite anisotropy field
H_{ex}:	External magnetic field in the waveguide = $\frac{Bo}{\mu_o}$
I:	Amplifier Beam current
j:	$\sqrt{-1}$
$K_{\alpha 2L}$, $K_{\alpha c01}$:	Constants relating αc or βc and ϵ''
$K_{\alpha c02}$, $K_{\beta c01}$:	Constants relating αc and ϵ''
$k\rho$:	Radial propagation constant
k_z:	Axial propagation constant = $\beta - j\alpha$
L:	Cold circuit loss
L_F:	Forward warm circuit loss
L_R:	Reverse warm circuit loss
ℓ:	Length of the amplifier loss pattern
m, n:	Waveguide mode designators
m_o:	Electron rest mass

List of Symbols (Continued)

N_x, N_y, N_z: Ferrite demagnetizing shape factors

P_m, α_m, σ_m: Ferrite loss factors

R_g: Electron orbit guiding center radius

R_I: Input reflection coefficient

R_O: Output Reflection Coefficient

r_L: Larmor radius

s: Cyclotron harmonic number

t: Time Variable

$U_1 \cdots U_9$: Shorthand notation for various Bessel functions

V: Amplifier beam potential

v_p: Wave phase velocity

v_z: Electron axial velocity

v_{11}: Radial electron velocity

$v_\perp$: Azimuthal electron velocity

w: Lossy layer thickness = $\frac{b}{c} - \frac{a}{c}$

z: Axial variable

$4\pi M_s$: Ferrite magnetization

α: Wave attenuation constant

β: Wave phase constant

γ: Gyromagnetic ratio

γ_o: Relativistic beam parameter

$\Delta\alpha$: Change in attenuation constant

$\Delta\beta$: Change in phase constant

ΔH: Ferrite line width

List of Symbols (Continued)

δ: Dielectric loss tangent = $\frac{\varepsilon''}{\varepsilon'}$

ε_o: Permittivity of free space

ε_1, ε_2, ε_3: Permittivity of various dielectric regions; dielectric constants

ε_{1R}, ε_{2R}, ε_{3R}: Relative permittivity = $\frac{\varepsilon_1}{\varepsilon_o} \ldots \frac{\varepsilon_3}{\varepsilon_o}$

ε': Real part of the dielectric constant

ε'': Imaginary part of the dielectric constant

η_o: Impedance of free space $\cong 120\,\pi$

μ_o: Permeability of free space

$\overleftrightarrow{\mu_2}$: Tensor permeability

μ, μ_a, μ_{11}: Entries of $\overleftrightarrow{\mu_2}$

μ_1, μ_2, μ_3: Permeability of various dielectric regions

μ_{1R}, μ_{2R}, μ_{3R}: Relative permeabilities = $\frac{\mu_1}{\mu_o} \ldots \frac{\mu_3}{\mu_o}$

ρ: Radial variable

σ: Dielectric Conductivity

ϕ: Azimuthal variable

Ω_e: Non-relativistic cyclotron frequency = $\frac{e\,B_o}{m_o}$

ω: Wave radian frequency

ω_c: Waveguide cutoff frequency